

**Strengthening of concrete structures with
near-surface mounted CFRP laminate strips**

**Reforço de estruturas com laminados de
CFRP inseridos no betão de recobrimento**

Tese apresentada por

José Manuel de Sena Cruz

à Universidade do Minho para a obtenção do grau de
Doutor em Engenharia Civil

Publicação subsidiada pela Fundação para a Ciência e a Tecnologia

Orientador:

Doutor Joaquim António Oliveira de Barros, Universidade do Minho

Co-orientadores:

Doutor Álvaro Ferreira Marques Azevedo, Universidade do Porto

Doutor Rui Manuel Carvalho Marques de Faria, Universidade do Porto

Membros do Júri:*Presidente*

Presidente da Escola de Engenharia da Universidade do Minho (por delegação reitoral)

Vogais

Doutor Álvaro Ferreira Marques Azevedo, Professor Auxiliar, Universidade do Porto

Doutor Joaquim António Oliveira de Barros, Professor Auxiliar, Universidade do Minho

Doutor Joaquim de Azevedo Figueiras, Professor Catedrático, Universidade do Porto

Doutor Paulo Barbosa Lourenço, Professor Associado com Agregação, Universidade do Minho

Doutor Paulo Jorge de Sousa Cruz, Professor Associado, Universidade do Minho

Doutor Ravindra Gettu, Investigador Sénior, Universidade Politécnica da Catalunha

Doutor Rui Manuel Carvalho Marques de Faria, Professor Associado, Universidade do Porto

Copyright © 2005 J.M. Sena Cruz

All rights reserved. No part of this publication may be reproduced, stored in a retrieval system, or transmitted in any form or by means, electronic, mechanical, photocopying, recording or otherwise, without the prior written permission of the publisher:

Universidade do Minho, Departamento de Engenharia Civil, Azurém, 4800-058 Guimarães, Portugal

ISBN 972-8692-21-8

Printed in Portugal

To my family

ACKNOWLEDGEMENTS

The present work was mainly developed at the Civil Engineering Department of the University of Minho, Portugal. The experimental programs were developed at the Laboratory of the Structural Division of the Civil Engineering Department of the University of Minho, Portugal, and at the Structural Technology Laboratory of the Technical University of Catalonia, Spain.

This research was carried out under the supervision of Prof. Joaquim Barros, Prof. Álvaro Azevedo and Prof. Rui Faria. I express my gratitude to Prof. Joaquim Barros and Prof. Álvaro Azevedo for their support, several interesting discussions, their advice and their friendship. I would also like to express my thanks to Prof. Rui Faria for his contribution to this work.

I express my gratitude to Dr. Ravindra Gettu for his interest, suggestions, care and for making my stay at Technical University of Catalonia possible.

The financial support provided by the Fundação para a Ciência e a Tecnologia (Foundation for the Science and Technology) and the Fundo Social Europeu (European Social Fund), grant SFRH/BD/3259/2000, is gratefully acknowledged. The experimental tests performed at the Structural Technology Laboratory were partially supported by the Spanish Ministry of Science and Technology, grant PB98-0293.

The help of António Matos (Laboratory of the Structural Division), Miguel Angel Martín and Ernesto Diaz (Structural Technology Laboratory) and the other technicians of both laboratories during the experimental work, is gratefully appreciated.

I would also like to thank to the S&P, Bettor MBT, SECIL and SOLUSEL companies for providing the materials used in the experimental programs. The contribution of the Composite Materials Unit of INEGI, CEMACOM, in the characterization of the laminates, is appreciated.

The contribution of the researchers Ventura Gouveia, Victor Cunha and Alberto Ribeiro in the validation of the developed numerical tools is appreciated. I am grateful to Prof. Daniel Oliveira and to the other colleagues from the Civil Engineering Department of the University of Minho, for their support, interesting discussions and friendship. Thanks to Prof. Laura de Lorenzis, University of Lecce, Italy, and Dr. Francesco Focacci, University IUAV of Venice, Italy, for the fruitful discussions about topics related to this work.

I am also very grateful to all my friends that always encouraged and supported me during the execution of this work.

Finally, my gratitude to my family, in particular to Inês, my daughter, Cátia, my wife, José and Lúcia, my parents and Susana, my sister, for their love and unconditional support.

This research was co-financed by the European Social Fund, through the Program of Educational Development for Portugal, namely the Measure 5/ Action 5.3 - Advanced teacher training for higher education, and by the Department of Civil Engineering of the University of Minho.



ABSTRACT

In recent years, the near-surface mounted (NSM) strengthening technique has been used to increase the load carrying capacity of concrete structures. This technique consists in the insertion of carbon fiber reinforced polymer (CFRP) laminate strips into pre-cut slits opened in the concrete cover of the elements to be strengthened. The laminates are fixed to concrete with an epoxy adhesive. This technique, in some cases, presents substantial advantages with respect to externally bonded laminates. The present work intends to contribute to a better knowledge of the behavior of concrete structures strengthened with NSM CFRP laminate strips. The study carried out is composed of an experimental, an analytical and a numerical part.

The experimental research was developed at the Laboratory of the Structural Division of the Civil Engineering Department of the University of Minho, Portugal, and at the Structural Technology Laboratory of the Technical University of Catalonia, Spain. The main objective of the experimental work was to assess the bond behavior between the CFRP and concrete. With this purpose, pullout-bending tests were carried out. The influence of bond length, concrete strength and load history on the bond behavior was investigated.

Using the results of the pullout-bending tests and a numerical strategy, an analytical local bond stress-slip relationship was obtained. The numerical strategy was developed with the aim of solving the second-order differential equation that governs the slip phenomenon. This numerical strategy was also used to calculate the critical anchorage length for this type of reinforcement.

Numerical tools were developed for the simulation of the nonlinear behavior of concrete structures strengthened with NSM CFRP laminate strips. These tools were implemented in a computer code named FEMIX, which is a general purpose finite element software system. In the context of this work, the following capabilities were added: an elasto-plastic multi-fixed smeared crack model to simulate concrete, interface elements and a constitutive material model for the simulation of the nonlinear behavior of the interface between CFRP and concrete.

RESUMO

Nos últimos anos, a técnica baseada na inserção de laminados no betão de recobrimento tem sido utilizada no reforço de estruturas de betão. Esta técnica consiste na introdução de laminados de CFRP (compósitos reforçados com fibras de carbono) em ranhuras pré-executadas nos elementos a reforçar. Os laminados são fixos ao betão por intermédio de um adesivo epoxy. Esta técnica, em alguns casos, apresenta vantagens substanciais comparativamente com a técnica que recorre à colagem externa dos laminados de CFRP. O presente trabalho pretende dar um contributo para a compressão do comportamento de estruturas de betão reforçadas com laminados de CFRP inseridos no betão de recobrimento. O trabalho realizado é composto por uma parte experimental, uma parte analítica e uma parte numérica.

O programa experimental foi realizado no Laboratório de Estruturas da Universidade do Minho, Portugal, e no Laboratório Estrutural da Universidade Politécnica de Catalunha, Espanha. O principal objectivo do trabalho experimental foi procurar compreender o comportamento da ligação entre o laminado e o betão. Com este propósito foram efectuados ensaios de arrancamento em flexão. Foi investigada a influência do comprimento de aderência, da classe de resistência do betão e da historia do carregamento no comportamento da ligação.

A partir dos resultados experimentais e da implementação de uma estratégia numérica, obteve-se uma lei analítica local tensão de corte *versus* deslizamento. A estratégia numérica foi desenvolvida com o objectivo de resolver a equação diferencial de segunda ordem que rege o fenómeno do deslizamento. Esta estratégia numérica foi também utilizada na determinação do comprimento de ancoragem crítico associado à técnica de reforço em estudo.

Foram desenvolvidas ferramentas numéricas para simular estruturas de betão reforçadas com laminados de CFRP inseridos no betão de recobrimento. Estas ferramentas foram implementadas no software de elementos finitos designado FEMIX. No contexto do presente trabalho, foram acrescentadas ao código computacional as seguintes funcionalidades: um modelo elasto-plástico que inclui a possibilidade de ocorrência de múltiplas fendas fixas distribuídas, para simular o betão, elementos de interface e uma lei material para simular o comportamento não linear da interface entre o CFRP e o betão.

CONTENTS

Acknowledgements.....	<i>i</i>
Abstract.....	<i>iii</i>
Resumo	<i>iv</i>
Contents	<i>v</i>
List of symbols	<i>ix</i>
Glossary	<i>xiii</i>
Chapter 1 - Introduction	1
1.1 Near-surface mounted CFRP laminate strips technique.....	2
1.2 Previous research.....	3
1.3 Objectives	9
1.4 Outline of the thesis.....	11
Chapter 2 - Bond between near-surface mounted CFRP laminate strips and concrete: experimental tests	13
2.1 Experimental program	17
2.1.1 Specimen and test configuration	17
2.1.2 Test program	20
2.2 Material characterization	23
2.2.1 Concrete	23
2.2.2 CFRP laminate strip.....	26
2.2.3 Epoxy adhesive	28
2.3 Preparation of specimen	30
2.4 Results	33
2.4.1 Identification of failure modes	34
2.4.2 Monotonic loading results.....	35
2.4.2.1 Pullout force.....	35
2.4.2.2 Slip at free and loaded ends	36
2.4.2.3 Pullout force <i>versus</i> slip.....	39
2.4.2.4 Discussion of results	40
2.4.3 Cyclic loading results.....	44
2.4.3.1 Pullout force, free end and loaded end slips	44
2.4.3.2 Pullout force <i>versus</i> slip.....	46
2.4.3.3 Discussion of results	49
2.5 Summary and conclusions	51
Chapter 3 - Analytical modeling of bond between near-surface mounted CFRP laminate strips and concrete	53
3.1 Differential equation governing the slip.....	54
3.2 Determination of the local bond stress-slip relationship	56
3.2.1 Analytical expressions for the local bond stress-slip relationship	56
3.2.2 Description of the method.....	57
3.2.3 Example	62

3.3	Local bond stress-slip relationship for near-surface mounted CFRP laminate strips...	63
3.4	Anchorage length.....	66
3.5	Summary and conclusions	69

Chapter 4 - Numerical model for concrete structures strengthened with near-surface mounted CFRP laminate strips		71
4.1	Nonlinear finite element analysis	74
4.1.1	Iterative techniques for the solution of nonlinear problems.....	74
4.1.2	FEMIX computer code.....	78
4.2	Crack concepts.....	80
4.2.1	Smeared crack concept.....	80
4.2.1.1	Crack strains and crack stresses	81
4.2.1.2	Concrete constitutive law.....	83
4.2.1.3	Constitutive law of the crack	83
4.2.1.4	Constitutive law of the cracked concrete	83
4.2.1.5	Crack fracture parameters	84
4.2.2	Multi-fixed smeared crack concept.....	90
4.2.2.1	Crack initiation	91
4.2.2.2	Crack evolution history.....	91
4.2.3	Algorithmic aspects.....	92
4.2.3.1	Stress update	93
4.2.3.2	Crack status.....	97
4.2.3.3	Singularities	104
4.2.4	Model appraisal.....	105
4.3	Plasticity	108
4.3.1	Basic assumptions.....	108
4.3.2	Integration of the elasto-plastic constitutive equations	111
4.3.3	Evaluation of the tangent operator	112
4.3.4	Elasto-plastic concrete model	113
4.3.4.1	Yield surface	113
4.3.4.2	Hardening behavior.....	114
4.3.4.3	Return-mapping algorithm.....	116
4.3.4.4	Consistent tangent operator.....	119
4.3.5	Model appraisal.....	119
4.3.5.1	Uniaxial compressive tests.....	119
4.3.5.2	Biaxial compressive test	120
4.4	Elasto-plastic multi-fixed smeared crack model	122
4.4.1	Yield surface	122
4.4.2	Integration of the constitutive equations	123
4.4.2.1	Constitutive equations from the multi-fixed smeared crack model ...	123
4.4.2.2	Constitutive equations from the elasto-plastic model.....	124
4.4.2.3	Return-mapping algorithm.....	124
4.4.2.4	Method proposed by de Borst and Nauta.....	127
4.4.3	Consistent tangent operator.....	129
4.4.4	Model appraisal.....	130
4.4.4.1	Traction-compression-traction (TCT) numerical test	131
4.4.4.2	Compression-traction-compression (CTC) numerical test	131
4.4.4.3	Biaxial numerical test	132

4.4.4.4	Beam failing by shear.....	132
4.5	Line interface finite element.....	135
4.5.1	Finite element formulation.....	136
4.5.2	Model appraisal.....	141
4.6	Summary and conclusions.....	142
Chapter 5 - Numerical applications		145
5.1	Concrete properties.....	145
5.1.1	Uniaxial behavior of plain concrete	145
5.1.2	Uniaxial behavior of reinforced concrete.....	148
5.2	Steel reinforcement properties.....	150
5.3	Modeling of beams with flexural strengthening.....	152
5.4	Modeling of shear-strengthened beams	160
5.5	Summary and conclusions	168
Chapter 6 - Summary and conclusions		171
References		175
Appendix A - Experimental results.....		189
Appendix B - Runge-Kutta-Nyström method		193
Appendix C - Hardening/softening law for concrete.....		195
Appendix D - Consistent tangent operator.....		197

LIST OF SYMBOLS

A_f	Cross section area of the CFRP
D^I	Mode I stiffness modulus
D^{II}	Mode II stiffness modulus
\underline{D}^{cr}	Crack constitutive matrix
\underline{D}^e	Elastic constitutive matrix
\underline{D}^{ecr}	Elasto-cracked constitutive matrix
\underline{D}^{ep}	Elasto-plastic constitutive matrix
E_c	Young's modulus of concrete
E_f	CFRP Young's modulus
F_l	CFRP pullout force at the loaded end
F_{lmax}	Maximum CFRP pullout force
G_c	Shear modulus of concrete
G_f	Mode I fracture energy of concrete
L_{an}	Anchorage length
L_b	Bond length
\underline{T}^{cr}	Transformation matrix of a crack
$f(\underline{\sigma}, \kappa) = 0$	Yield surface
f_c	Compressive strength of concrete
f_{cm}	Mean value of the uniaxial compressive strength of concrete
f_{ct}	Tensile strength of concrete
f_{fu}	CFRP tensile strength
h	Crack band-width, Hardening modulus
h_c	Scalar parameter that amplifies the plastic strain vector
m	Number of critical crack status changes
n	Combination

x

n_{cr}	Number of distinct smeared crack orientations at each integration point
p	Hydrostatic pressure
q	Iteration
s_1	Parameter defining the local bond stress-slip relationship
s_f	Free end slip
s_l	Loaded end slip
s_{lmax}	Loaded end slip at maximum CFRP pullout force
s_m	Slip at peak bond stress defining the local bond stress-slip relationship
t_f	CFRP thickness
w_f	CFRP width

$\Delta \underline{\underline{\varepsilon}}$	Incremental strain vector
$\Delta \underline{\underline{\varepsilon}}_l^{cr}$	Incremental crack strain vector (in CrCS)
$\Delta \underline{\underline{\sigma}}_l^{cr}$	Incremental crack stress vector (in CrCS)
α_{th}	Threshold angle
α	Parameter defining the local bond stress-slip relationship
α'	Parameter defining the local bond stress-slip relationship
α''	Parameter defining the local bond stress-slip relationship
β	Shear retention factor
γ_t^{cr}	Crack shear strain
$\underline{\underline{\varepsilon}}$	Strain vector
ε_f	CFRP strain
$\underline{\underline{\varepsilon}}^{cr}$	Crack strain vector
$\underline{\underline{\varepsilon}}_l^{cr}$	Crack strain vector (in CrCS)
ε_n^{cr}	Crack normal strain
θ	Angle between the x_1 global axis and the crack normal axis
κ	Hardening parameter
σ_n^{cr}	Crack normal stress
τ_m	Bond strength defining the local bond stress-slip relationship

τ_{\max}	Average bond strength at the peak pullout force
τ_r	Residual bond stress at the end of the test
τ_t^{cr}	Crack shear stress
$\underline{\sigma}$	Stress vector
$\bar{\sigma}$	Yield stress
$\underline{\sigma}_t^{cr}$	Crack stress vector (in CrCS)
$\sigma_{l\max}$	Maximum CFRP stress
ν_c	Poisson's ratio of concrete

GLOSSARY

Adhesive – Substance applied to mating surfaces to bond them together by surface attachment. An adhesive can be in liquid, film or paste form.

Carbon fiber – Fiber produced by high temperature treatment of an organic precursor fiber based on PAN (polyacrylonitrile) rayon or pitch in an inert atmosphere at temperatures about 980 °C. Fibers can be graphitized by removing still more of the non-carbon atoms by heat treating above 1650 °C.

CFRP – Carbon fiber reinforced polymer.

Composite – A material that combines fiber and a binding matrix to maximize specific performance properties. Neither element merges completely with the other. Advanced polymer composites use only continuous oriented fibers in a polymer matrix.

Cure – To change the molecular structure and physical properties of a thermosetting resin by chemical reaction via heat and catalyst in combination with or without pressure.

Debonding – Local failure in the bond zone between concrete and the externally bonded reinforcement.

EBR – Externally bonded FRP reinforcement.

Epoxy adhesive – A polymer resin characterized by epoxy molecule groups.

Fabric – A material formed from fibers or yarns without interlacing.

Fiber – A general term used to refer to filamentary materials. Fiber is often used synonymously with filament.

FRP – Fiber reinforced polymer.

GFRP – Glass fiber reinforced polymer.

Glass fiber – Reinforcing fiber made by drawing molten glass through brushings. The predominant reinforcement for polymer matrix composites. Known for its good strength, processability and low cost.

Groove – Long narrow channel.

Laminate – To unite layers of material with an adhesive. Also, a structure resulting from bonding multiple plies of reinforcing fiber or fabric.

Lay-up – Placement of layers of reinforcement in a mould.

LVDT – Linear voltage differential transducer.

Matrix – Binder material in which reinforcing fibers are embedded. Usually a polymer but may also be metal or ceramic.

NSM – Near-surface mounted.

Polymer – Large molecule formed by combining many smaller molecules or monomers in a regular pattern.

Pot life – Length of time in which a catalyzed thermosetting resin retains sufficiently low viscosity for processing.

RC – Reinforced concrete.

Rebar – Steel reinforcement bar placed in concrete.

Reinforced concrete – Concrete strengthened with steel.

Resin – Polymer with indefinite and often high molecular weight and a softening or melting range that exhibits a tendency to flow when subjected to stress. As composite matrices, resin binds together reinforcement fibers.

Sheet – A material formed from fibers or yarns without interlacing.

Slit – Strait and narrow cut.

Unidirectional – A strip or fabric with all fibers oriented in the same direction.

Wet lay-up – Fabrication step involving application of a resin to dry reinforcement.

CHAPTER 1

INTRODUCTION

In the last decade, fiber reinforced polymer materials (FRP) have progressively replaced conventional concrete and steel in the strengthening of concrete structures (FIB 2001, ACI 2002). These new materials are available in the form of unidirectional strips made by pultrusion, or in the form of sheets or fabrics consisting of fibers in one or more directions. Carbon (C) and glass (G) are the main types of fibers composing the fibrous phase of these materials (CFRP and GFRP), whereas epoxy adhesive is generally used in the matrix phase. Wet lay-up (sheets and fabrics) and prefabricated strips (designated by laminates) are the main types of FRP strengthening systems available in the market. In the last years the significant and increasing demand of FRP to be used in structural repair and/or strengthening is due to the following main advantages of these composites: low weight, easy installation procedures, high durability and tensile strength, electromagnetic permeability and practically unlimited availability in terms of geometry and size (FIP 2001).

The most common strengthening technique is based on the application of the FRP on the surface of the elements to be strengthened and is designated as externally bonded reinforcement (EBR) technique. Recent research has revealed that this technique cannot mobilize the full tensile strength of FRP materials due to premature debonding (Mukhopadhyaya and Swamy 2001, Nguyen et al. 2001). The reinforcing performance of FRP materials can be diminished by the effect of freeze/thaw cycles (Toutanji and Balaguru 1998) and decreases significantly when submitted to high or low temperatures (Pantuso et al. 2000). Furthermore, EBR systems are susceptible to damage caused by vandalism and mechanical malfunctions.

Several attempts have been made to overcome the aforementioned drawbacks. Strengthening with near-surface mounted (NSM) FRP rods is one of the most promising techniques. This approach is based on the concept of bonding glass or carbon FRP rods into pre-cut grooves opened in the concrete cover of the elements to be strengthened

(De Lorenzis et al. 2000). However, the NSM concept is not new, since it started to be used in Europe, for the strengthening of reinforced concrete structures, in the 1940s. This pioneering technique consisted on placing rebars in grooves located in the concrete cover. These grooves were then filled with cement mortar (Asplund 1949). In the present, FRP rods can take the place of rebars and an epoxy adhesive can replace the cement mortar. This “reinvented” technique has been used in some applications and several benefits have been pointed out, namely, high levels of strengthening efficacy and, when compared with EBR, a significant decrease of the probability of harm resulting from fire, acts of vandalism, mechanical damages and aging effects (Warren 1998, Alkhrdaji et al. 1999, Hogue et al. 1999, Tumialan et al. 1999, Warren 2000, Emmons et al. 2001, Täljsten and Carolin 2001, De Lorenzis 2002, Täljsten et al. 2003).

Also recently, another similar strengthening technique was proposed, consisting in the utilization of laminate strips of CFRP instead of rods. Since this technique is the main subject of the present work, the following sections are dedicated to a more detailed description of its characteristics, and to refer the most relevant research available in the literature.

1.1 NEAR-SURFACE MOUNTED CFRP LAMINATE STRIPS TECHNIQUE

The near-surface mounted (NSM) technique using laminate strips of carbon fiber reinforced polymer (CFRP) as a strengthening system is proposed as means to increase the load carrying capacity of concrete members. The term ‘near-surface’ is used to distinguish this technique of structural strengthening from the case where externally bonded FRP composites are utilized. With the NSM technique, laminate strips of CFRP are introduced into saw-cut slits on the concrete cover of the elements to be strengthened. These slits are previously filled with an epoxy adhesive (see Figure 1.1). Typically, the CFRP laminate strip has a cross section of about 1.4 mm thick and 10 mm width, while the width and depth of the slit vary between 3 and 5 mm, and 12 and 15 mm, respectively.

This practice requires no surface preparation work and, after cutting the slit, requires a minimal installation time, when compared with the externally bonded reinforcement

technique. The following steps are usually adopted in the application of the NSM technique:

- open slits in the concrete cover using a saw-cut machine;
- clean the slits with compressed air;
- clean the CFRP laminate with an appropriate cleaner (e.g., acetone);
- prepare the epoxy adhesive according to the supplier recommendations;
- fill the slits and cover the lateral faces of the CFRP with the epoxy adhesive;
- insert the CFRP laminate into the slit, and slightly press it to force the epoxy adhesive to flow between the CFRP and the slit borders. This phase requires a special care in order to assure that the slits are completely filled with epoxy adhesive. When this is not the case the formation of voids might occur.

The time of cure of the epoxy adhesive, indicated by the supplier, must be respected before its expected performance becomes fully available.

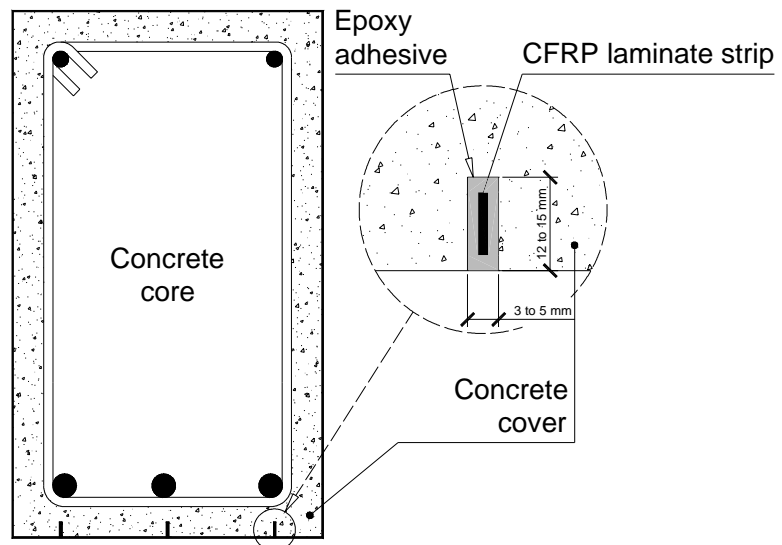


Figure 1.1 – Near-surface mounted CFRP reinforcement technique used to increase the beam bending capacity.

1.2 PREVIOUS RESEARCH

The first known experiments with near-surface mounted CFRP laminate strips as a strengthening technique were published by Baschko and Zilch in 1999. In this work, the authors compared externally bonded reinforcement with NSM CFRP laminate strips as strengthening techniques. With this purpose, Baschko and Zilch carried out the bond and

mechanical tests schematically represented in Figure 1.2. The properties of the utilized CFRP laminates and the dimensions of the slits are included in Table 1.1. The three different specimen configurations, represented in Figure 1.2(a), were used in the bond tests (D1, D2 and D3). A crack was induced in the center of the $200 \times 200 \times 900 \text{ mm}^3$ concrete block, in order to concentrate all damage in the bonded zones between the CFRP and the concrete. Figure 1.2(b) shows the cross sections of the four 3.0 m long beams that were also tested. Based on the results obtained in the bond tests, the authors concluded that the NSM technique has provided a higher ductility and load carrying capacity than the EBR technique. The bending tests performed with the beams shown in Figure 1.2(b) indicated that the NSM technique was capable of almost double the load carrying capacity of the corresponding beams strengthened with the EBR technique.

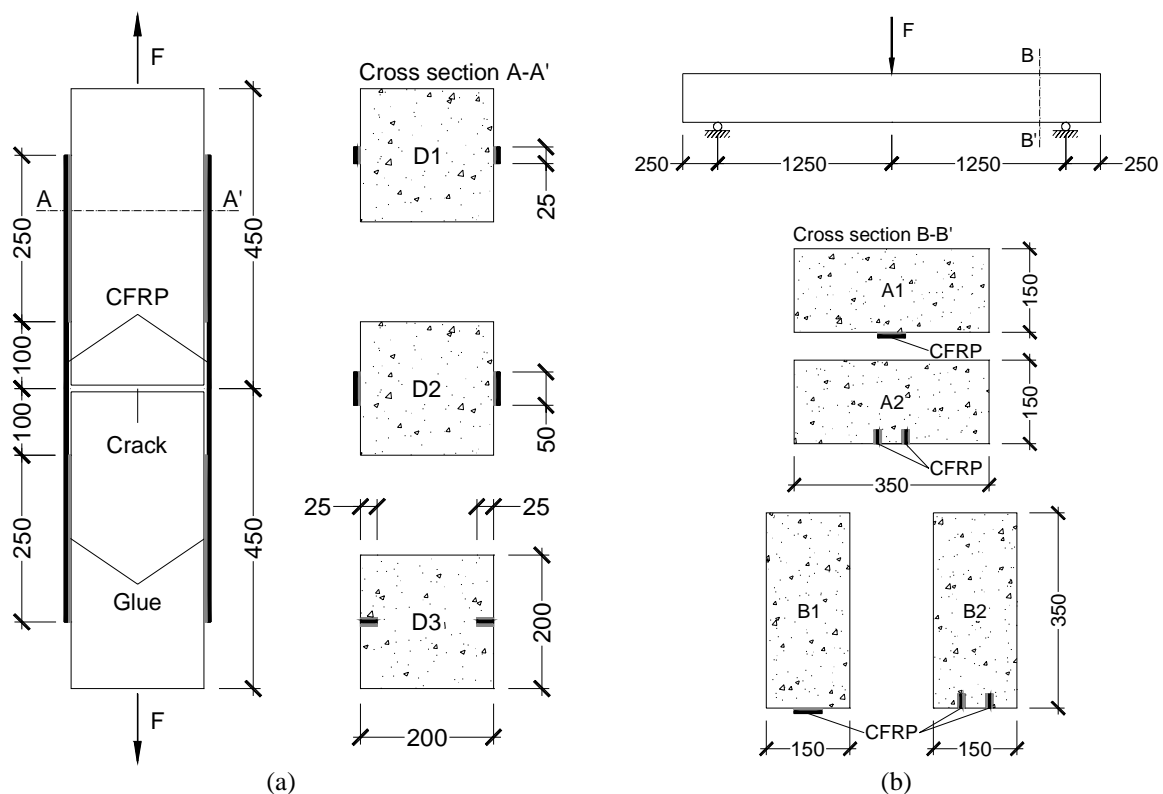


Figure 1.2 – Experimental program performed by Blaschko and Zilch (1999): (a) bond tests; (b) beam tests. Note: all dimensions are in millimeters.

With the purpose of analyzing the performance of the NSM technique in concrete columns, Barros et al. (2000) carried out some tests. Figure 1.3 shows the geometry of the columns and the reinforcement configurations considered in those tests. Six CFRP

laminates strips were used to strengthen each specimen. The laminates were fixed in the slits using an epoxy adhesive, whereas epoxy mortar was used to fix the CFRP to the foundation. The properties of the CFRP laminate strips and the dimensions of the slits are indicated in Table 1.1. With the setup shown in Figure 1.3, eighteen tests were performed under quasi-constant axial compression, N , and a lateral cyclic force. The strengthening efficiency provided by this technique was high, due to the fact that peeling was prevented and the tensile strain on the CFRP laminates has attained values close to its ultimate strain (Ferreira 2001).

Table 1.1 – Properties of the CFRP laminate strips and dimensions of the slits used in the experimental programs.

Experimental work	CFRP properties				Slit dimensions	
	Thickness [mm]	Width [mm]	Young's modulus [GPa]	Tensile strength [MPa]	Width [mm]	Depth [mm]
Blaschko and Zilch (1999)	1.2	25	2600	n.a.	3	26
Barros et al. (2000)	1.5	10	1573	159	5	15
Barros and Fortes (2002)	1.45	9.6	2700	158	4	12
Tan et al. (2002)	1.4	10	2490	173	3	15
Barros and Dias (2003)	1.45	9.6	2200	150	5	12

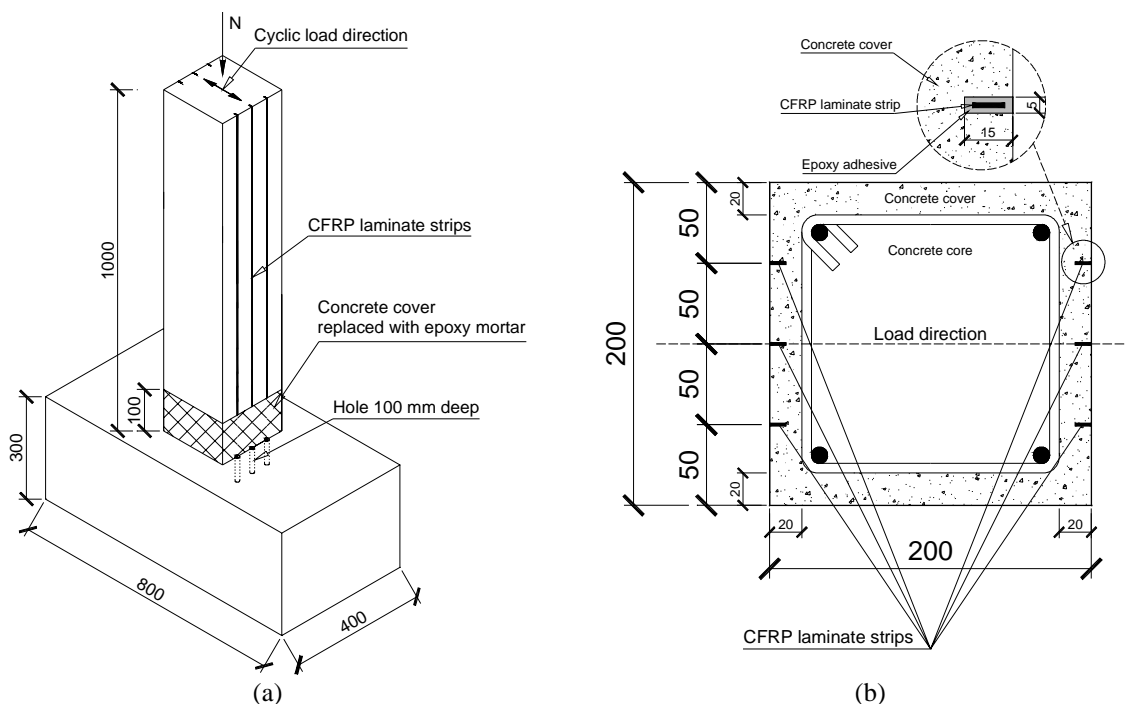


Figure 1.3 – NSM technique applied to reinforced concrete columns: (a) test specimen; (b) cross section of the columns (Ferreira 2001). Note: all dimensions are in millimeters.

In order to evaluate the efficiency of the NSM CFRP laminate strips technique for increasing the flexural capacity of reinforced concrete beams, an experimental program was carried out by Barros and Fortes (2002). Figure 1.4 shows the concrete beam, while Figure 1.5 depicts the cross section of the beams of the four tested series. Each series had a reference beam (V1, V2, V3 and V4) and the corresponding strengthened beam (V1R1, V2R2, V3R2 and V4R3). According to the experience of the authors, this technique is easier and faster to apply than the EBR technique. The test results have shown that the strengthening configurations adopted in the test series were capable of almost double the load carrying capacity of the corresponding reference beams. High efficacy was obtained, since at the failure of the beams, the stress on the CFRP has reached values ranging between 60 % and 90 % of its tensile strength.

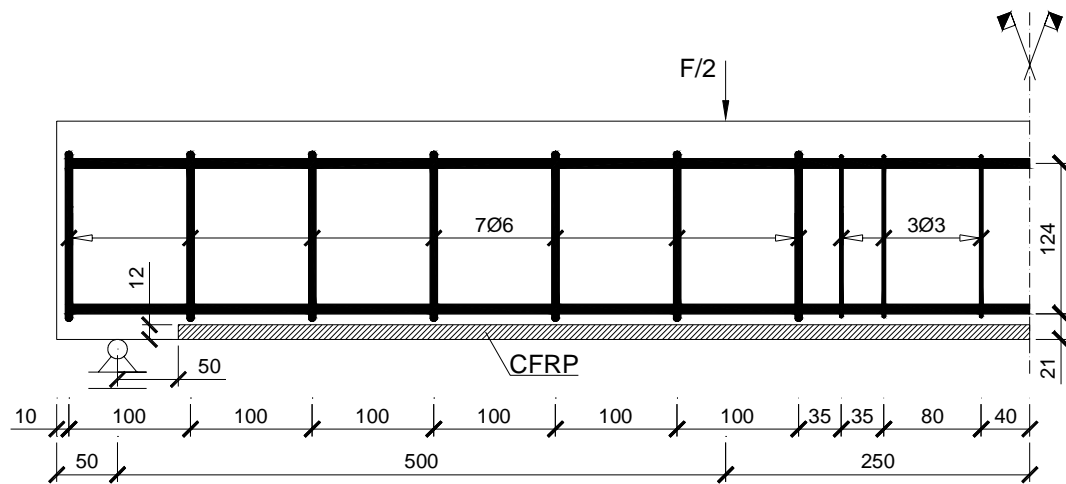


Figure 1.4 – NSM technique applied to reinforced concrete beams (Barros and Fortes 2002): specimen geometry, reinforcement arrangement, supports and loading. Note: all dimensions are in millimeters.

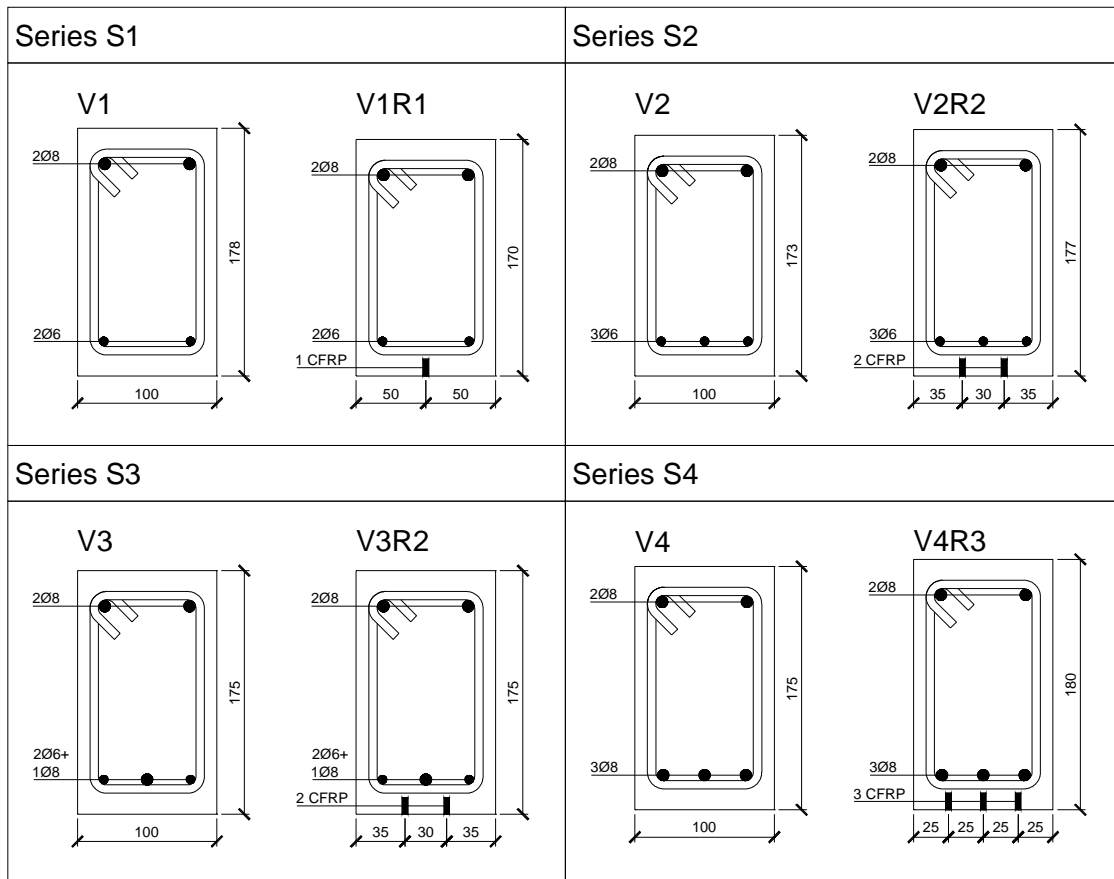


Figure 1.5 – Cross section of the tested beams (Barros and Fortes 2002). Note: all dimensions are in millimeters.

Tan et al. (2002) carried out an experimental program in order to study and compare the efficiency of different CFRP strengthening systems and techniques for the flexural strengthening of reinforced concrete slabs. Figure 1.6 shows the details of the slabs analyzed in this research. Two laminate strips of CFRP were used to reinforce slabs A and B. The strips of the latter were pre-stressed. In slabs C and D the strengthening system was composed of a CFRP sheet and several CFRP laminate strips, respectively. The time required to apply these distinct strengthening systems was measured. The shortest period of time was obtained in slab C. However, the authors recognized not having used appropriate tools for sawing the concrete, in order to apply the strengthening system of slab D. The test results showed that slab D exhibited the highest load carrying capacity. In this case the CFRP laminate strips were fully utilized prior to failure.

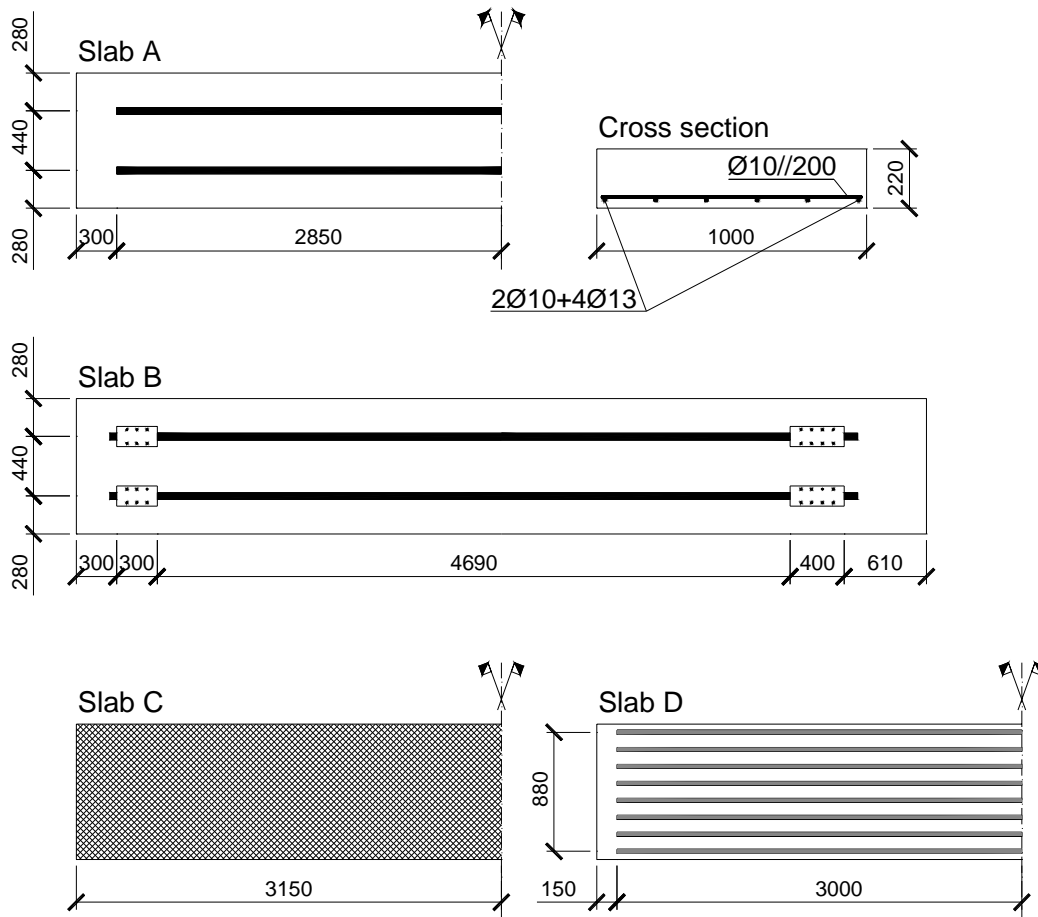


Figure 1.6 – Geometry and reinforcement details of the tested slabs (Tan et al. 2002). Note: all dimensions are in millimeters.

The performance of the NSM technique as a means of increasing the shear strength of reinforced concrete beams was also assessed. For this purpose an experimental program was carried out by Barros and Dias (2003). Figure 1.7 and Figure 1.8 show the analyzed series. Four different strengthening techniques were used: conventional steel stirrups (VAE-30 and VBE-15); NSM CFRP laminate vertical strips (VACV-20 and VBCV-10); NSM CFRP laminate strips at 45 degrees (VACI-30 and VBCI-15); and strips of CFRP sheets (VAM-19 and VBM-8). Two beams without shear reinforcement were also included in the experimental program for comparison purposes (VA10 and VB10). In order to assure that all beams failed by shear with a similar load carrying capacity, the amount of shear reinforcement applied to the beams was conveniently estimated. From the results obtained, it can be pointed out that of all CFRP systems, the NSM technique was the most effective, not only in terms of load carrying capacity, but also in terms of ductility. More ductile failure modes occurred in the beams strengthened with NSM technique. This technique had the easiest and fastest application procedure.

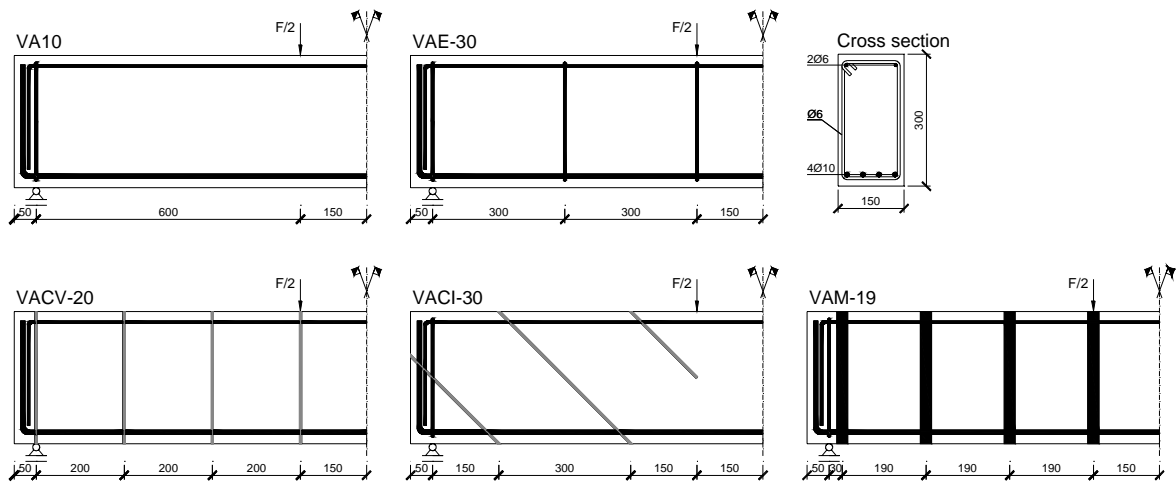


Figure 1.7 – Beams of series VA (Barros and Dias 2003). Note: all dimensions are in millimeters.

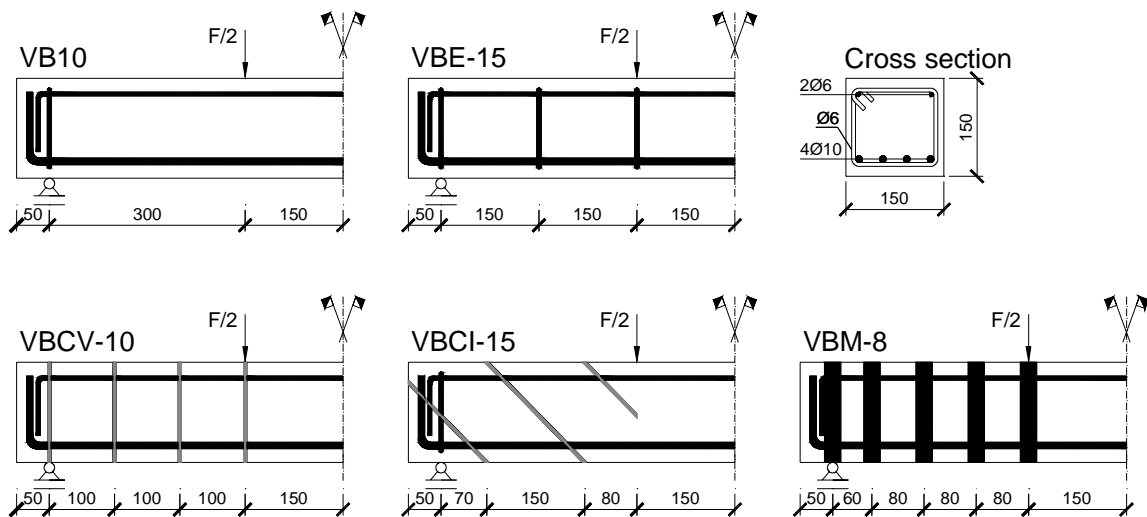


Figure 1.8 – Beams of series VB (Barros and Dias 2003). Note: all dimensions are in millimeters.

1.3 OBJECTIVES

Since the NSM CFRP laminate strips strengthening technique is quite recent, there are several important aspects deserving deep research in order to provide the necessary knowledge for a rational and safe strengthening design. The research carried out on this subject has been essentially dedicated to the assessment of the applicability and economical advantages of the NSM technique in structural applications where EBR is currently the selected strengthening technique. Research is still required in several areas, such as long term behavior of structural elements strengthened with NSM technique, effects of

temperature, humidity and freeze/thaw cycles, and implications of fatigue and cyclic loadings on the strengthening performance, and the concrete-FRP bond behavior.

The experimental research efforts to be undertaken on these subjects should always be followed by the development of robust analytical and numerical tools. The results obtained from the experimental research can significantly contribute to the quality of the analytical/numerical research, and vice-versa. If the suggested approach is followed, the knowledge derived from this global research strategy can be used to elaborate design guidelines.

In the present work the aforementioned research methodology was followed. In fact, the research carried out is composed of an experimental, an analytical and a numerical part. Understanding the FRP-concrete bond behavior is very important, not only to justify the relative performance of the NSM technique, but also to obtain information required by the analytical formulations and numerical models. This experimental program should provide enough information in order to define precise bond relationships, based on a strategy that will also involve analytical and numerical tools. Finally, the prediction of the load carrying capacity, deformability and crack pattern of a strengthened concrete structure can be performed with nonlinear material models, integrated in a finite element computer code. These models should take into account the information provided by the aforementioned experimental program and by the analytical model. Therefore, the main objectives of the present study are:

- the proposal of a test methodology intended to investigate the bond behavior between CFRP and concrete and to evaluate the influence of the variables which play a significant role in the phenomenon;
- the development of an analytical formulation for the prediction of the bond behavior, thus enabling the design of the critical anchorage length of NSM CFRP laminate strips;
- the development of a numerical model for the simulation, with high accuracy, of the nonlinear behavior of concrete structures strengthened with NSM CFRP laminate strips.

1.4 OUTLINE OF THE THESIS

In Chapter 2 a test methodology is proposed and applied to the characterization of the bond between CFRP and concrete. The specimen configuration and preparation, as well as the test setup and program, are described in detail. The characterization of the properties of the materials used in the experimental program is presented in this chapter. The test results are presented and analyzed, and a physical interpretation of the bond mechanisms is given.

In Chapter 3 a methodology for the prediction of the bond behavior associated with the near-surface mounted strengthening technique is presented. The analytical and numerical research is described. This methodology uses the results that were obtained in the experimental program, which was presented in Chapter 2. The developed tool is used to calculate the critical anchorage length of concrete elements strengthened with NSM CFRP laminate strips.

In Chapter 4 the developed numerical model, whose objective is to simulate concrete structures strengthened with NSM CFRP laminate strips, is presented. Some aspects of the developed finite element computer code, and also the solution procedures used in nonlinear finite element analysis are briefly described. All relevant aspects of the developed elasto-plastic multi-fixed smeared crack material model are described in detail. Another developed model, whose purpose is the simulation of the nonlinear behavior of the interface between CFRP and concrete, is also presented in this chapter. The performance and the accuracy of the developed numerical tools are assessed using results available in the literature and from the experimental results obtained in Chapter 2.

In Chapter 5 some applications of the developed numerical tools are presented. The numerical simulation of the experimental tests carried out with concrete beams strengthened with NSM CFRP laminate strips is described in detail. The most relevant results are presented and interpreted, and the main conclusions are pointed out.

Finally, in Chapter 6, an extended summary and the final conclusions of the present work are given. Some suggestions for future research are also indicated.

CHAPTER 2

BOND BETWEEN NEAR-SURFACE MOUNTED CFRP LAMINATE STRIPS AND CONCRETE: EXPERIMENTAL TESTS

In the current context, the word bond means the transfer of stresses between the concrete and the reinforcement in order to develop the composite action of both materials, during the loading process of reinforced concrete elements. The bond performance influences the ultimate load carrying capacity of a reinforced element, as well as some serviceability aspects, such as crack width and crack spacing. Since structural strengthening with NSM CFRP laminate strips is an emerging technique, the bond behavior is an important issue that needs to be focused. Literature treating the bond between laminate strips and concrete is very scarce. Only one experimental work, already summarized in Chapter 1, could be found after an extensive bibliographic search. Since bond of NSM CFRP laminate strips to concrete has similarities with the bond of rebars or FRP rods to concrete, a brief overview of both is presented in the following paragraphs.

Several researchers have studied the bond between rebars and concrete. Useful information can be found elsewhere (Tassios 1979, Bartos 1982, CEB 1982, Eligehausen et al. 1983, FIB 2000). Typically, bond performance of a smooth rebar embedded in concrete is due to the adhesion between concrete and rebar, and a small amount of friction. Both mechanisms disappear at higher load levels, due to the decrease of the cross section area of the rebar as a consequence of the Poisson's effect. If sufficient embedment length exists, the full carrying capacity of the rebar can be attained. Otherwise the pullout of the rebar occurs. In deformed rebars the bond transfer mechanisms are more complex and are not treated in the present work, since only smooth bars are similar to the laminate strips used in the studied technique. Bond behavior depends on a variety of factors and parameters related, basically, to the rebar characteristics, to the concrete properties and to the stress state in both the rebar and the surrounding concrete. Technological aspects such as concrete cover, clear space between rebars, number of rebar layers and bundled rebars, casting direction with respect to rebar orientation and rebar position also contribute to the bond behavior. Finally, the load history should also be taken into account (FIB 2000).

With the advent of the FRP rods several researchers investigated the characteristics of the bond of FRP rods to concrete (Al-Zahrani 1995, Cosenza et al. 1997, Bakis et al. 1998, Tepfers 1998, Focacci et al. 2000). These researches showed that friction is the dominant mechanism for smooth FRP bars. Furthermore, the other main factors that affect the bond performance are the longitudinal stiffness, transverse stiffness and, in particular, the Poisson's ratio of the bar.

With the emergence of the NSM FRP rod reinforcement technique, its bond behavior started to be investigated. The corresponding main references are the works of Warren (1998 and 2000), Yan et al. (1999), and, specially, De Lorenzis (2002). The main parameters influencing the bond performance are the material type and the surface configuration of the rod, the bond length, the size and surface characteristics of the groove, and the groove-filling material.

In the last decades several test methods have been proposed and used on the bond research. The most common are the direct and the beam pullout tests. The beam pullout test is recognized by the research community as the most representative of the behavior of flexural members. For each test method, several test setups have been proposed (FIB 2000). Figure 2.1 shows two tests setup examples for direct and beam pullout tests.

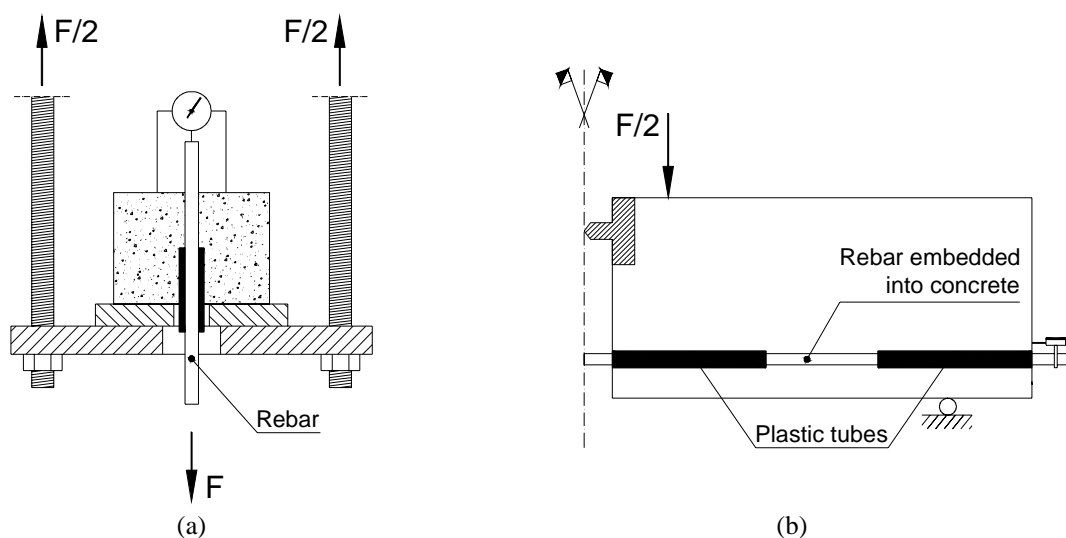


Figure 2.1 – (a) Direct pullout test; (b) pullout-bending test (FIB 2000).

De Lorenzis (2002) proposed the pullout tests A and B shown in Figure 2.2 and Figure 2.3, respectively, to investigate the bond between the NSM FRP rod and concrete. The pullout-bending test A had a hinge at the top and a transverse saw cut at the bottom, both located at the mid-span of the specimen. The saw cut had the intention of causing the formation of a crack at the center of the beam. The FRP rod was installed in a groove, carved at the bottom face, and oriented along the longitudinal axis of the beam. The test region was located on the left side of the beam, with a pre-defined bond length (see Figure 2.2). An extensive bond length was considered on the right side of the beam, guaranteeing the occurrence of bond failure on the other part. The beam was loaded under four-point bending with a shear span of 483 mm. Two LVTD's were used, being the first located at mid-span, in order to measure the vertical deflection, and the other placed at the lateral face of the beam, in order to measure the free end slip*. A load cell was used to measure the applied force. Along the bond length of the test region, gages were applied to the rod in order to measure the strains. The test was performed under displacement control, using the LVDT located at the specimen mid-span, until failure. The FRP pullout force (at the loaded end) was calculated using the force values measured at the load cell and taking into account the internal lever arm, i.e., the distance between the longitudinal axis of the FRP and the contact point at the hinge. According to De Lorenzis (2000) this test setup has the following limitations:

- the specimen has a considerable mass (about 150 kg) and dimensions, which is a disadvantage in extensive experimental programs;
- the test setup does not provide the possibility of measuring the loaded end slip;
- the test control system was not suitable to capture the softening branch of the load-slip behavior;
- the propagation of the crack located at the specimen mid-span disturbs the computation of the rod stress;
- the presence of gages locally disturbs the bond behavior.

* The important relationship between bond stress and slip can be obtained from the information supplied by the instrumentation of the specimen. The bond stress is the shear stress developed along the bond length, in the contact surface between the rebar and the concrete. The slip is the relative displacement between the rebar and the surrounding concrete. Usually, the bond length extremities are designated free and loaded end, being the former the extremity where the force at the reinforcement is null.

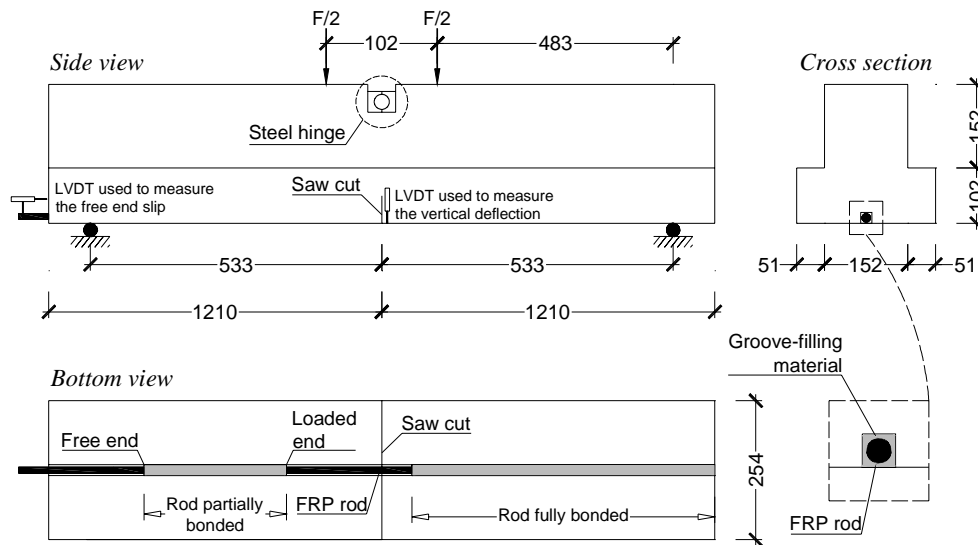


Figure 2.2 – Pullout test A (De Lorenzis 2002). Note: all dimensions are in millimeters.

Due to the aforementioned drawbacks of the pullout test A, De Lorenzis (2002) proposed an alternative pullout test, which is represented in Figure 2.3. In this test setup, the problems associated with the pullout test A are avoided. The free and loaded end slips, as well as the pullout force, can be measured directly. Due to space limitations in the specimen, the rod is fixed in a preformed square groove, rather than in a groove carved after concrete curing. The surface characteristics of the groove walls in both alternatives are very different and might significantly influence the bond performance. In addition, preformed grooves cannot simulate the bond conditions associated with the practice of repairing and/or strengthening real life concrete structures, since in these cases the rods are fixed in grooves cut in the concrete.

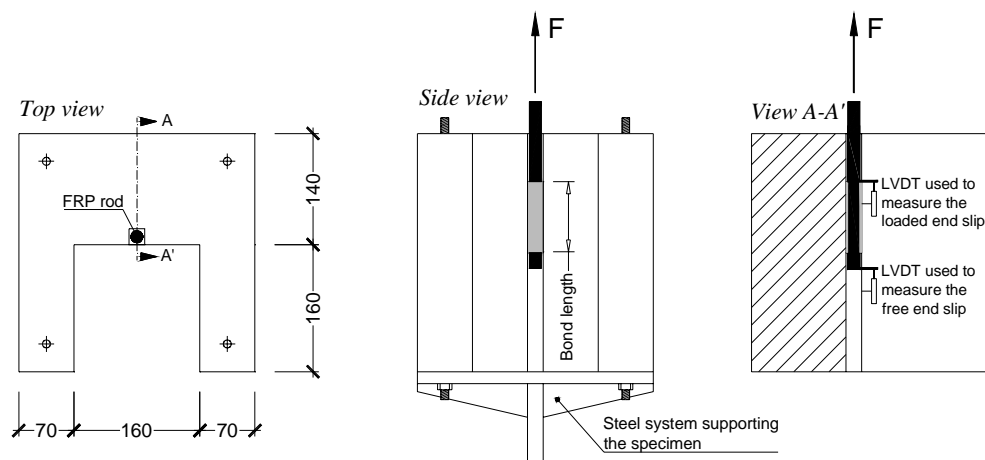


Figure 2.3 – Pullout test B (De Lorenzis 2002). Note: all dimensions are in millimeters.

The experimental research dealing with the bond of rebars or FRP rods to concrete, which was summarized before, indicated that the slit size, bond length, concrete strength, slit-filling material, type of FRP and load history are, probably, the main variables affecting the bond performance between laminate strips and concrete in near-surface mounted (NSM) strengthening technique. To assess the influence of bond length, concrete strength and load history on the bond performance, an experimental program was carried out in the context of the present work.

This chapter describes the tests, and also presents and analyzes the obtained results. The first part is dedicated to the description of the specimen, test configuration and test program. The characterization of the materials used in the experimental program and the preparation of the specimens are detailed. Finally, a physical interpretation of the bond mechanisms is given, and the results of the tests are presented and analyzed.

2.1 EXPERIMENTAL PROGRAM

The experimental program carried out to assess bond performance between CFRP and concrete was composed of two parts: the first one was carried out at the Laboratory of the Structural Division of the Civil Engineering Department of the University of Minho (LEST), Portugal, whereas the second one was developed at the Structural Technology Laboratory of the Technical University of Catalonia (LTE), Spain. In the first part, the influence of bond length and concrete strength on the bond behavior was analyzed, whereas in the second one the influence of load history and bond length was investigated. *S1* and *S2* series are the designations of the experimental works carried out at LEST and LTE, respectively.

2.1.1 Specimen and test configuration

As mentioned in the introduction of this chapter, several test configurations were used to investigate the bond performance between rebars or FRP rods and concrete. After a preliminary evaluation of the advantages and disadvantages of these test configurations, a test layout similar to the one proposed by RILEM for assessing the bond characteristics of conventional steel rods (RILEM 1982) was adopted in the present work.

the adopted displacement transducers, strain gages and load cells are described elsewhere (Sena-Cruz and Barros 2002, Sena-Cruz et al. 2004).

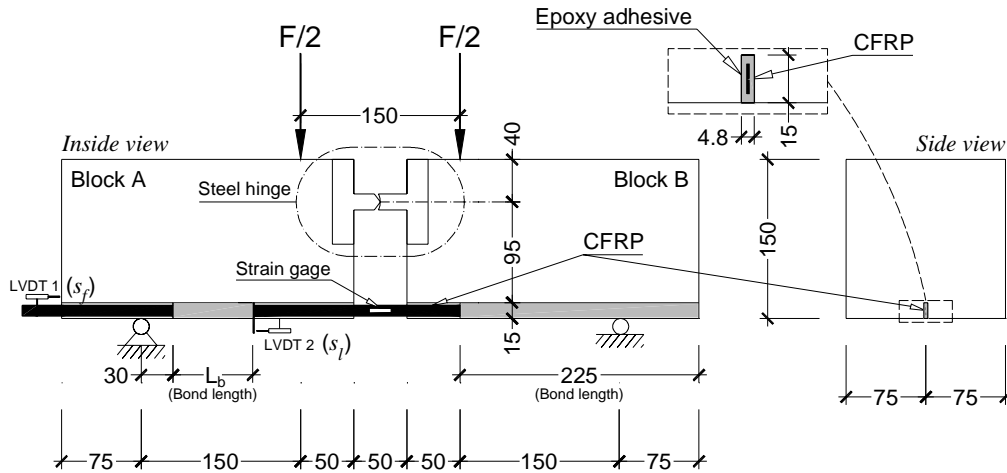


Figure 2.5 – Specimen geometry and pullout-bending test configuration for the *S2* series. Note: all dimensions are in millimeters.

Figure 2.6 shows the setup of the pullout-bending test. The following servo-controlled equipments were used in the experimental program: Sentur (Freitas et al. 1998) for the *S1* series and Instron (series 8505) for the *S2* series.

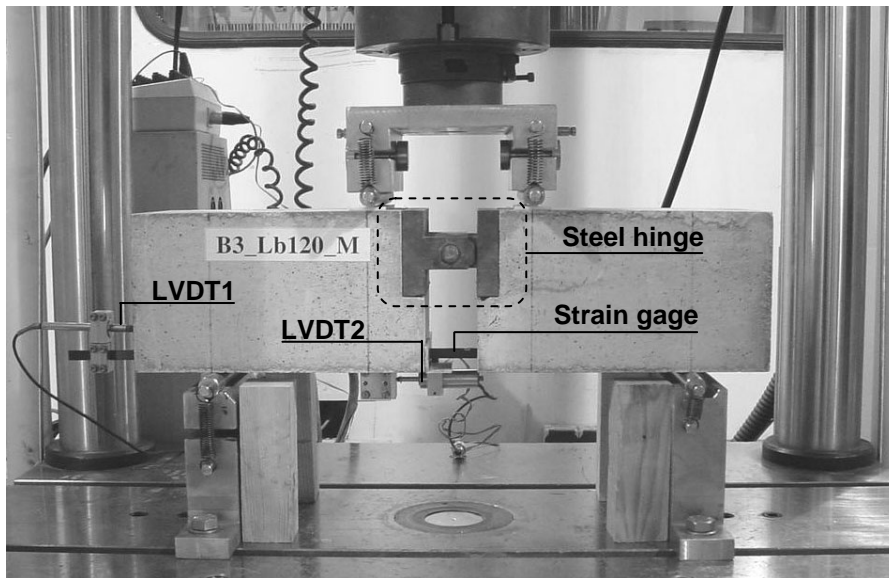


Figure 2.6 – Layout of the pullout-bending tests.

2.1.2 Test program

Assuming that for concrete structures needing strengthening intervention the concrete compressive strength usually ranges between 30 MPa and 50 MPa, concrete mixes were designed to have an average compressive strength (f_{cm}) within this range. To appraise the influence of concrete strength on CFRP bond behavior, a high strength concrete (70 MPa) was also designed.

In order to avoid the failure of the CFRP during the pullout-bending test, suitable bond lengths were adopted. For this evaluation preliminary tests were carried out. Bond lengths ranging between 40 and 120 mm were used in order to assess its influence on the bond behavior. The lower value, 40 mm, was considered since the bond length must be large enough to be representative of the different CFRP-concrete interface conditions and to make negligible the unavoidable end effects. The upper bound, 120 mm, was considered due to limitations associated to the specimen geometry.

In the last decades, the influence of the loading history on the bond performance between rebars and concrete has been extensively analyzed and, the work of Eligehausen et al. (1983) is one of the most extensive researches in this topic. This work supplied important recommendations regarding the selection of loading configurations used in the present research. According to the author's knowledge, the influence of the loading history on the bond performance associated with the NSM strengthening technique has not yet been investigated. This subject has been treated in the present study by means of the consideration of three types of load configurations: monotonic loading (M), one cycle of unloading/reloading at different slip levels (C1) and ten cycles of unloading/reloading for a fixed load level (C10).

Table 2.1 indicates the denominations adopted for the sixteen series of the selected experimental program, each one consisting of three specimens. The generic denomination of a series is $f_{cm}XX_LbYY_Z$, where XX is the strength class of compressed concrete, in megapascal, YY is the CFRP bond length, in millimeters, and Z is the type of load configuration (M, C1 or C10). In $S1$ series the influence of the bond length (40, 60 or 80 mm) and of the concrete strength (35, 45 or 70 MPa) were investigated. In the $S2$ series

the concrete compressive strength was always 40 MPa, and the main investigated parameters were the bond length and the load configuration.

Preliminary tests performed in the *S2* series have shown that, using the bond lengths of the *S1* series, lower bond strength and higher slip at peak pullout force values were obtained. In an attempt to define an experimental program with similar values of the bond strength and slip at peak pullout force, the bond lengths of the *S2* series were increased to 60, 90 and 120 mm.

Three distinct C10 load configurations were adopted (see Figure 2.7): in the fcm40_Lb60_C10 series, ten unloading/reloading cycles at 90 % of the peak pullout force ($F_{l0}/F_{lmax} = 0.90$); in the fcm40_Lb90_C10 series, ten unloading/reloading cycles at 60 % of the peak pullout force ($F_{l0}/F_{lmax} = 0.60$); in the fcm40_Lb120_C10 series, ten unloading/reloading cycles at 75 % of the peak pullout force ($F_{l0}/F_{lmax} = 0.75$). The unloading/reloading cycles performed before the peak pullout force were applied with the purpose of assessing the influence of the cyclic loading in the degradation of the bond stress. Carrying out cycles at different bond stress levels (60 %, 75 % or 90 %), before the occurrence of the peak pullout force, had the intention of evaluating the influence of this parameter on the bond stress degradation and on the variation of the bond strength.

In the C1 load configuration (see Figure 2.8) one unloading/reloading cycle was performed at a slip of 250 μm , 500 μm , 750 μm , 1000 μm , 1500 μm , 2000 μm , 3000 μm and 4000 μm . This load configuration was selected in order to investigate the influence of the cyclic loading on the stiffness variation. Due to some limitations in the software of the servo-controlled equipment, all unloading phases were performed under load control, with an average slip rate of 5 $\mu\text{m/s}$.

Table 2.1 – Denominations of the studied test series.

Series	Concrete strength [MPa]	Bond length [mm]	Load configuration	Denomination
S1	35	40	Monotonic (M)	fcm35_Lb40_M
	45			fcm45_Lb40_M
	70			fcm70_Lb40_M
	35	60		fcm35_Lb60_M
	45			fcm45_Lb60_M
	70			fcm70_Lb60_M
	35	80		fcm35_Lb80_M
	45			fcm45_Lb80_M
	70			fcm70_Lb80_M
S2	40	60	Monotonic (M)	fcm40_Lb60_M
			Cyclic (C10)	fcm40_Lb60_C10
		90	Monotonic (M)	fcm40_Lb90_M
			Cyclic (C10)	fcm40_Lb90_C10
		120	Monotonic (M)	fcm40_Lb120_M
			Cyclic (C10)	fcm40_Lb120_C10
		Cyclic (C1)	fcm40_Lb120_C1	

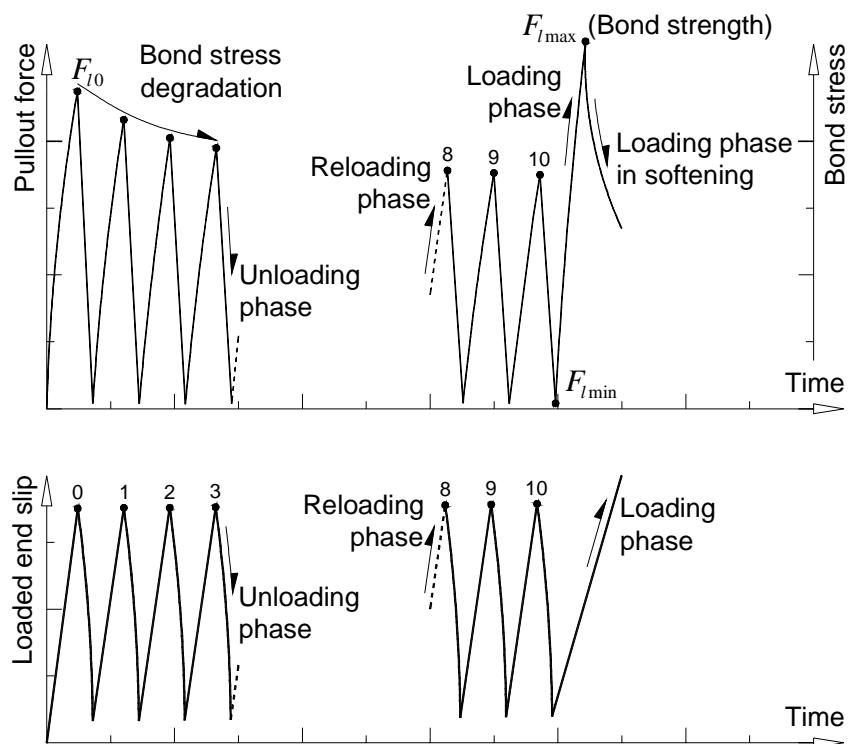


Figure 2.7 – Configuration of the C10 cyclic tests.

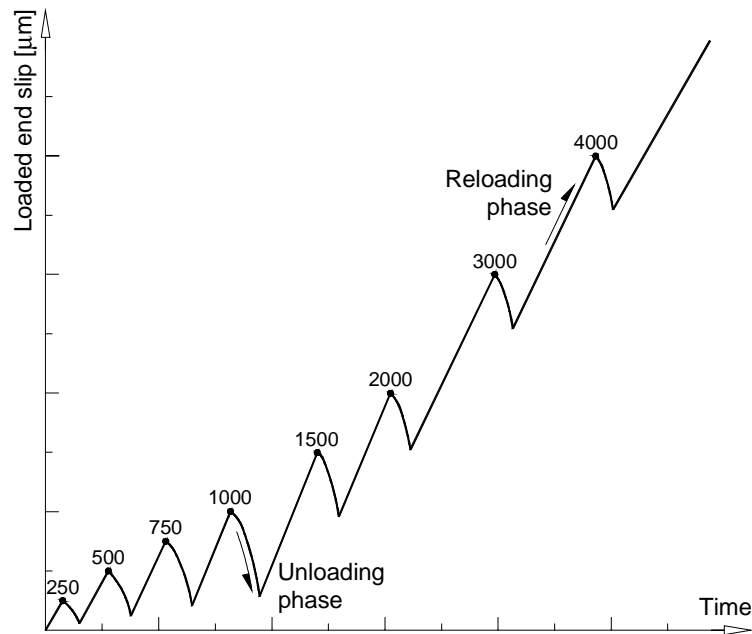


Figure 2.8 – Configuration of the C1 cyclic tests.

2.2 MATERIAL CHARACTERIZATION

In the following sections the characterization of concrete, CFRP laminate and epoxy adhesive used in the experimental research is described.

2.2.1 Concrete

The granulometric analyses of sand and gravel used in the concrete aggregate skeleton are included in Figure 2.9 and Figure 2.10. These analyses were carried out according to the NP 1379 (1976) and UNE-EN 933-1 (1998) recommendations for the *S1* and *S2* series, respectively.

Concrete compositions are included in Table 2.2. In preliminary tests, shear failure occurred due to the lack of shear reinforcement in the specimen (Sena-Cruz et al. 2001). To avoid shear failure of the specimen, 60 kg/m^3 of hooked end steel fibers were added to the concrete composition. For this content of fibers, only the concrete post-cracking tensile residual strength is significantly affected by fiber reinforcement mechanisms (Rossi 1998, Barros and Figueiras 1999). Since concrete cracking is not expected to occur in the

bonding zone, the influence of adding fibers to concrete is marginal in terms of bond behavior (Ezeldin and Balaguru 1989).

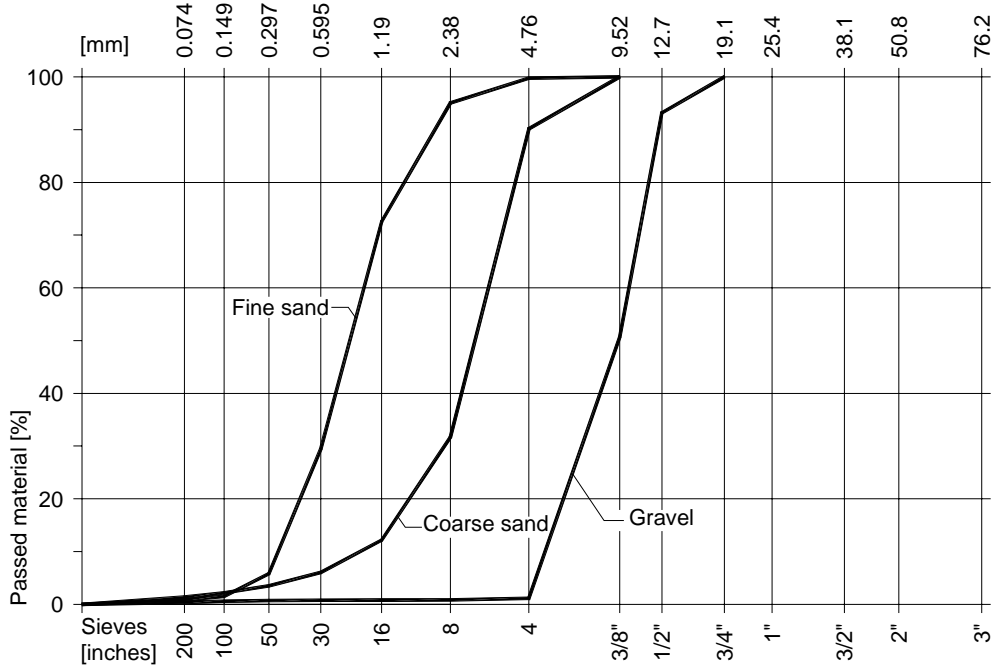


Figure 2.9 – Granulometric curves of the concrete aggregate components used in the *S1* series.

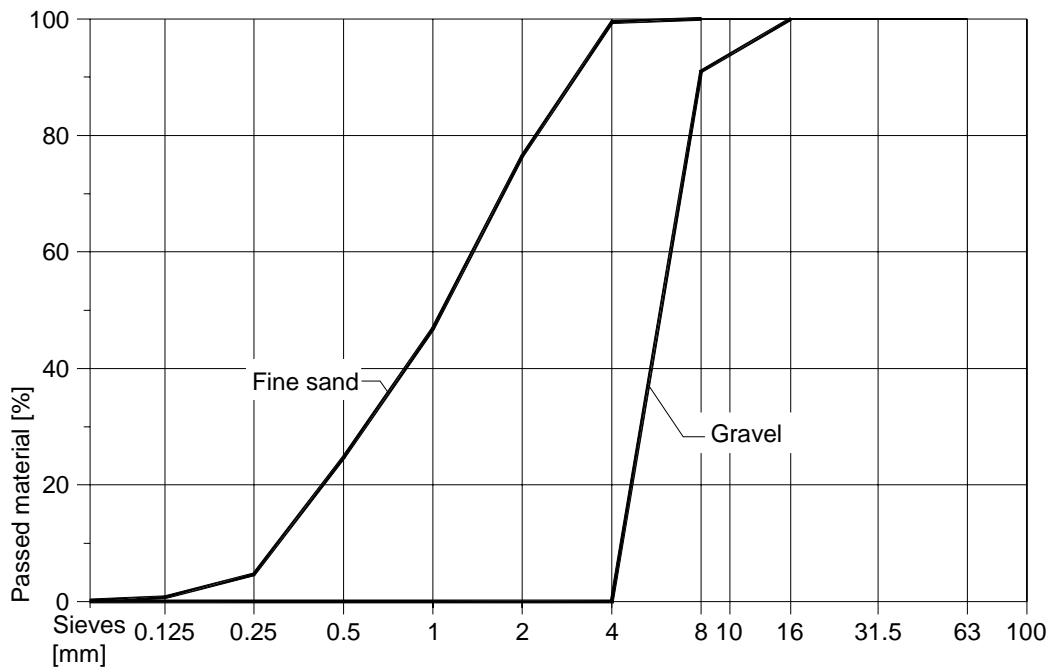


Figure 2.10 – Granulometric curves of the concrete aggregate components used in the *S2* series.

In the concrete manufacturing, vertical-axis forced-action mixers were used. The mixing procedures were the following:

- the coarse and fine aggregates, and the cement were mixed during 1 minute;
- water was added and the mix continued for another minute;
- superplasticizer was incorporated and the mixing continued for another minute;
- steel fibers were gradually added and the concrete was mixed for another 2 minutes.

The mix had satisfactory homogeneity and no balling of fibers was observed.

Table 2.2 – Mix compositions and average compressive strength of the concrete used in the test series.

Series	Composition [kg/m ³]					f_{cm} [MPa]
	FS	CS	CA	C	W	
fcm35_Lb40_M	–	745	943	350	210	34.5 (6.9 %)
fcm35_Lb60_M						33.0 (4.2 %)
fcm35_Lb80_M						37.2 (1.5 %)
fcm45_Lb40_M		627	1049	400	200	46.2 (0.5 %)
fcm45_Lb60_M						41.4 (2.3 %)
fcm45_Lb80_M						47.1 (1.7 %)
fcm70_Lb40_M	427	419	848	500	150	69.9 (0.9 %)
fcm70_Lb60_M						70.3 (8.2 %)
fcm70_Lb80_M						69.2 (7.5 %)
fcm40_Lb60_M	–	990	705	350	203	41.0 (2.3 %)
fcm40_Lb60_C10						
fcm40_Lb90_M						
fcm40_Lb90_C10						
fcm40_Lb120_M						
fcm40_Lb120_C10						
fcm40_Lb120_C1						

Notes: FS – Fine Sand (0-3 mm); CS – Coarse Sand (0-5 mm); CA – Coarse Aggregate (5-15 mm); C – Secil Cement 42.5 type I; W – Water. In series fcm70, 7.8 l/m³ of Rheobuild 1000 superplasticizer were applied; in series fcm40, 3.4 l/m³ of DARACEM® 205 superplasticizer were applied. The values within parentheses are the coefficients of variation.

Cylinder specimens with a diameter of 150 mm and a height of 300 mm were used to obtain the compressive strength of the concrete. The compression tests were carried out in a universal test machine, under load control, at a rate of 0.5 MPa/s. The average

compressive strength (f_{cm}) was obtained from, at least, three specimens at the age of the pullout-bending tests (see Table 2.2).

2.2.2 CFRP laminate strip

The CFRP laminate produced by S&P[®] was provided in rolls, and was composed of unidirectional carbon fibers, agglutinated with an epoxy adhesive. The laminate properties provided by the supplier are included in Table 2.3.

To verify the CFRP cross section geometry, twenty measurements of the laminates were carried out for each series. The average values obtained for the width and thickness are included in Table 2.3.

Table 2.3 – CFRP laminate properties.

Property	<i>S1</i> series		<i>S2</i> series	
	Supplier	Laboratory	Supplier	Laboratory
Width [mm]	10.0	9.34 (1.0 %)	10.0	10.0 (0.1 %)
Thickness [mm]	1.4	1.39 (0.2 %)	1.4	1.40 (0.5 %)
Tensile strength [MPa]	> 2200	2740 (3.1 %)	2500	2833 (5.7 %)
Young's modulus [GPa]	150	159 (1.6 %)	150	171 (0.9 %)
Ultimate strain [%]	1.4	1.70 (2.4 %)	1.25	1.55 (6.2 %)

Note: values within parentheses are the coefficients of variation.

Evaluation of the Young's modulus, tensile strength and ultimate strain was carried out with tensile tests, following ISO 527-5 (1997) recommendations. The specimen's length was 250 mm, and tabs of 50 mm length were glued to the ends to avoid premature failure of the specimen due to stress concentrations introduced by the machine fixtures. The end-tabs were built with the same material used in the tested specimen. The test was controlled with a constant displacement rate of 2 mm/min. To evaluate the strain of the laminate, clip and strain gages were used, for the *S1* and *S2* series, respectively. The applied force was measured by a load cell with a static load carrying capacity of ± 100 kN. Figure 2.11(a) shows the test layout of the *S2* series.

At about 75 % of the ultimate tensile strength, the rupture of the fibers located at the edges of the laminate started to occur. The brittle failure took place, accompanied by a loud sound. Figure 2.11(b) depicts the appearance of the specimens of the *S2* series after being tested. Similar failure was observed in the specimens used in the *S1* series. In some specimens the failure region was not located in the central part of the specimen; this can be justified by the difficulty of ensuring homogeneity in terms of fiber distribution, fiber alignment and laminate cross sectional area.

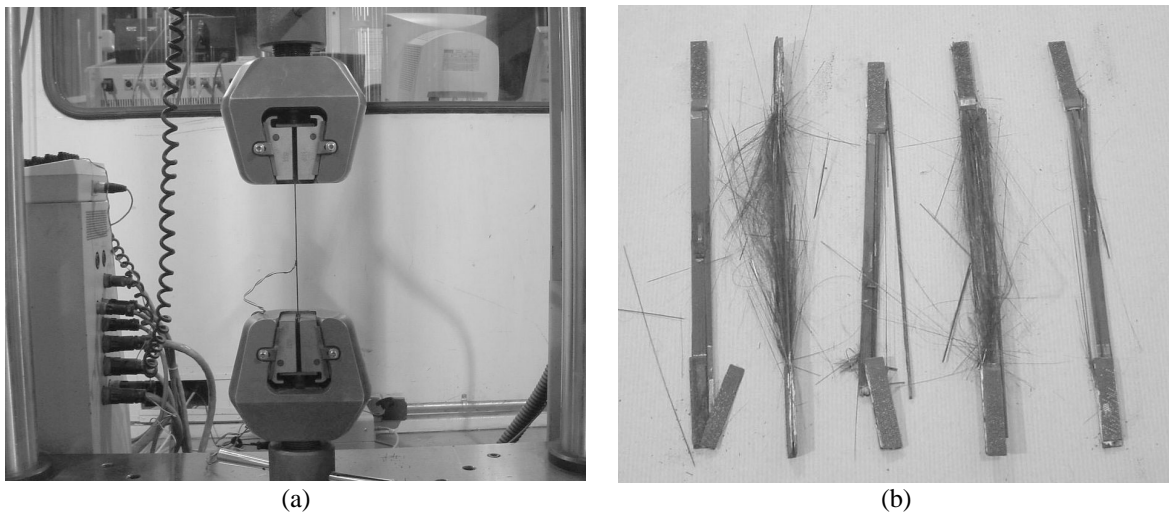


Figure 2.11 – (a) Layout of the CFRP tensile tests of the *S2* series. (b) Failure of the *S2* series CFRP specimens.

Figure 2.12 shows the uniaxial stress-strain relationship obtained in the tests of the specimens. A linear stress-strain relation up to the peak load is observed. Table 2.3 includes the average values obtained for the tensile strength, Young's modulus and ultimate strain (at the peak stress). Low coefficient of variation values were obtained.

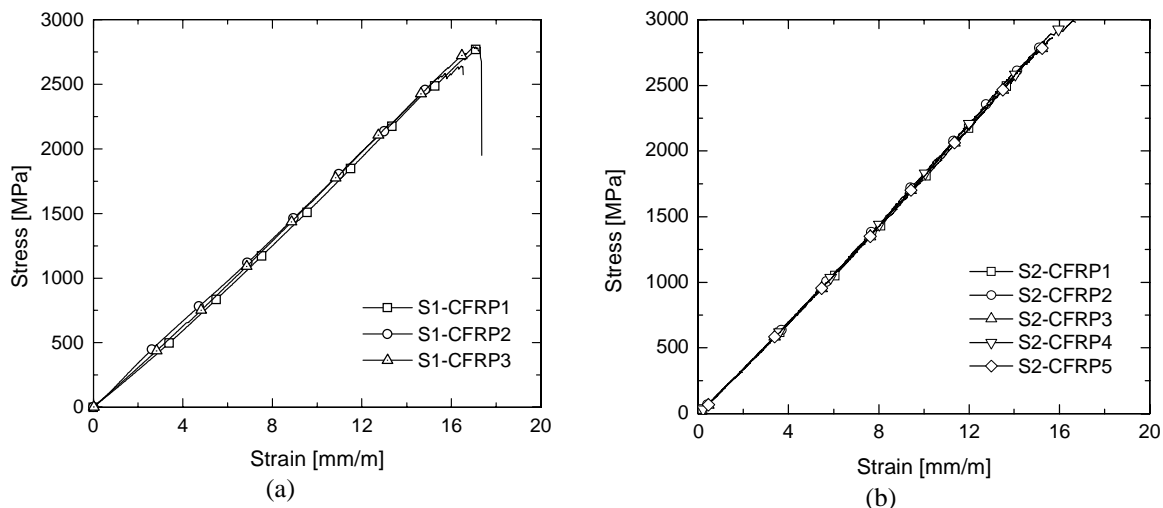


Figure 2.12 – Stress-strain relationship of the CFRP tensile specimens of *S1* (a) and *S2* (b) series.

2.2.3 Epoxy adhesive

The low viscosity epoxy adhesive used to bond the CFRP laminate to concrete, produced by Bettor-MBT[®], had the trademark *Mbrace Epoxikleber* and *Mbrace Epoxikleber 220*, respectively, for the *S1* and *S2* series. This adhesive is composed of two parts (A and B) and, according to the supplier, its properties are those indicated in Table 2.4.

Table 2.4 – Main properties of the epoxy adhesive.

Property	Mbrace Epoxikleber (<i>S1</i> series)	Mbrace Epoxikleber 220 (<i>S2</i> series)
Compressive strength [MPa]	90	40
Tensile strength [MPa]	n.a.	7
Flexural tensile strength [MPa]	30	n.a.
Young's modulus [GPa]	8.15	7
Bond strength to concrete [MPa]	> 3.5	3.0
Bond strength to laminate [MPa]	n.a.	3.0
Pot life at 20 °C [min]	80	60
Time of cure [days]	3	3
Mixing ratio (Part A to Part B)	2 to 1 by weight	3 to 1 by weight

To characterize the epoxy adhesive, three point-bending tests and compression tests were carried out, following NP-EN 196-1 (1987) recommendations. The preparation of the

epoxy specimens, with dimensions $160 \times 40 \times 40 \text{ mm}^3$, was accomplished in the following steps: both components were homogenized individually; component B was added to component A and both were mixed for 2 minutes in a mixer machine at 1800 rpm; the procedure was then interrupted in order to homogenize the mix, using a spoon; the mixing procedure continued for another two minutes. A visual inspection of the result leads to the conclusion that this procedure ensured mixtures with the desired quality. The molds were cast in two layers each one compacted by 120 jolts. The specimens were removed from the moulds 24 hours after casting and were placed in a curing chamber, at $20 \text{ }^\circ\text{C}$ and 50 % RH.

The bending tests were undertaken in a universal test machine under load control, at a rate of 50 N/s (see Figure 2.13(a)). The appearance of the *S2* series specimens after they had been tested is shown in Figure 2.14. Several voids were observed in the fracture surface of the specimens, which can be responsible for the large coefficients of variation obtained (see values within parentheses indicated in Table 2.5).

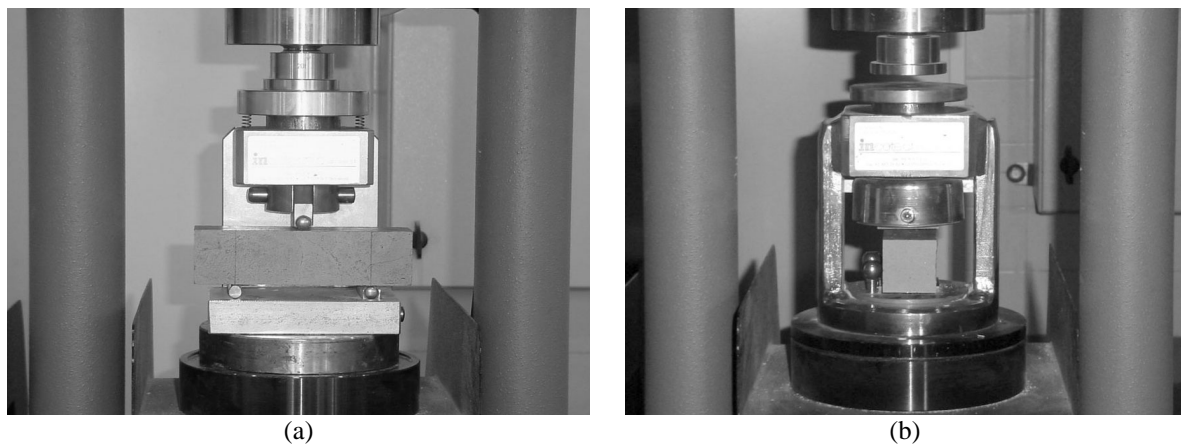


Figure 2.13 – Layout of the three point bending (a) and compression (b) tests of the epoxy adhesive.

Compression tests were carried out with the two parts resulting from the prismatic specimens after the bending tests. These compression tests were performed in a universal testing machine under load control at a rate of 2.4 kN/s (see Figure 2.13(b)). From these tests, average compressive strengths of 44.4 MPa and 67.5 MPa, with a low coefficients of variation, were obtained for the *S1* and *S2* series, respectively (see Table 2.5).

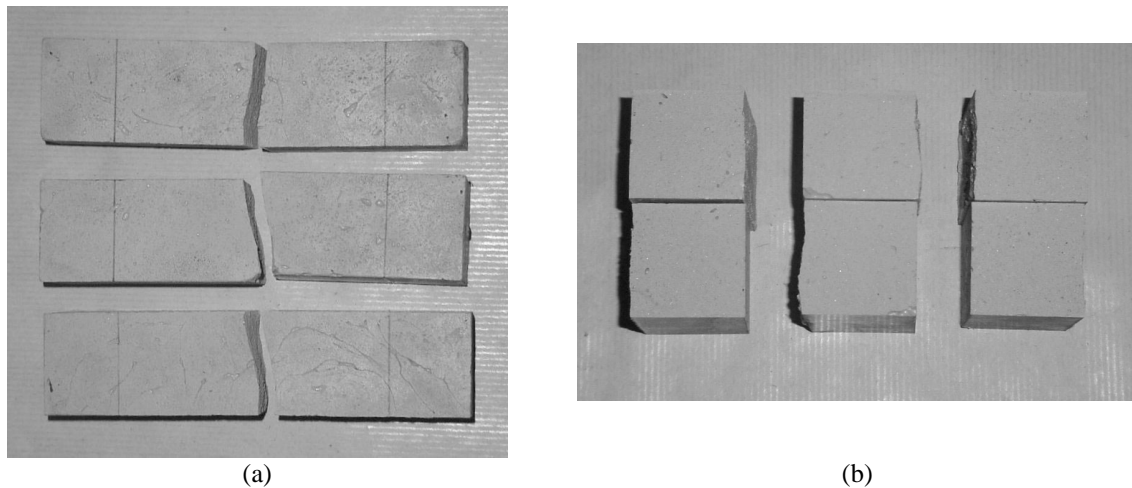


Figure 2.14 – Specimens of the S2 series after the bending test: (a) lateral view; (b) top view.

Table 2.5 – Results from the three point bending and compression tests of epoxy adhesive specimens.

Series	Flexural tensile strength [MPa]	Compressive strength [MPa]
<i>S1</i>	25.8 (8.0 %)	44.4 (11.9 %)
<i>S2</i>	21.8 (25.2 %)	67.5 (5.3 %)

2.3 PREPARATION OF SPECIMEN

Figure 2.15 shows the main steps adopted in the preparation of the pullout-bending specimens, which are detailed in the following paragraphs.

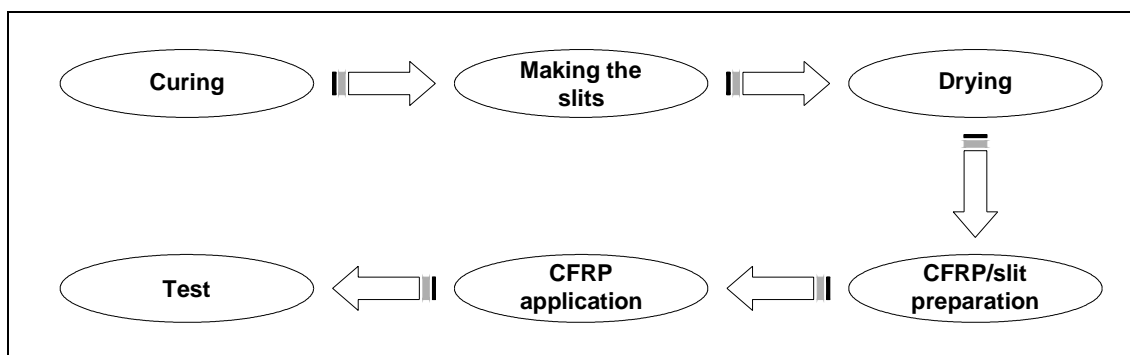


Figure 2.15 – Main steps used in the preparation of a specimen.

At the age of 28 days, blocks A and B of each specimen (see Figure 2.4 and Figure 2.5) were removed from the curing room to make the slits using a table-mounted saw (Figure 2.16(a)). In order to eliminate the remaining dust induced by the sawing process, the slits were cleaned with compressed water (Figure 2.16(b)). To guarantee a dry surface before bonding the laminate to the concrete, the specimens were air-dried in the laboratory environment during at least one week.

Before bonding the CFRP, the slits were cleaned with compressed air (see Figure 2.16(c)). To avoid the presence of epoxy adhesive in undesirable zones, a masking procedure was adopted, as shown in Figure 2.16(d). Preparation of the CFRP itself involved the following steps:

- a small tab, built with the same CFRP material, was fixed at the loaded end to measure the loaded end slip (see Figure 2.16(e));
- small plastic pieces were fixed at the free and loaded ends of the bonded zone in order to ensure the desired length of the test region (see Figure 2.16(e));
- the CFRP was cleaned with acetone;
- a strain gage was glued to the CFRP at the mid-span of the specimen (see Figure 2.16(f));
- finally, in the zones to be bonded, the CFRP was again cleaned with acetone.

The laminate was fixed to the concrete using the epoxy adhesive described in Section 2.2.3. In the regions where the laminate was bonded to concrete, the slit was filled with the epoxy adhesive (see Figure 2.16(g)). In the corresponding lateral surfaces the laminate was covered with a thin layer of the epoxy adhesive (see Figure 2.16(h)). Then, the CFRP was inserted into the slit, and slightly pressed to force the epoxy adhesive to flow between the CFRP and the slit sides. Finally, the epoxy adhesive in excess was removed and the surface was leveled. Figure 2.17 shows the final appearance of the specimen. The specimens were kept in the laboratory environment before being tested.



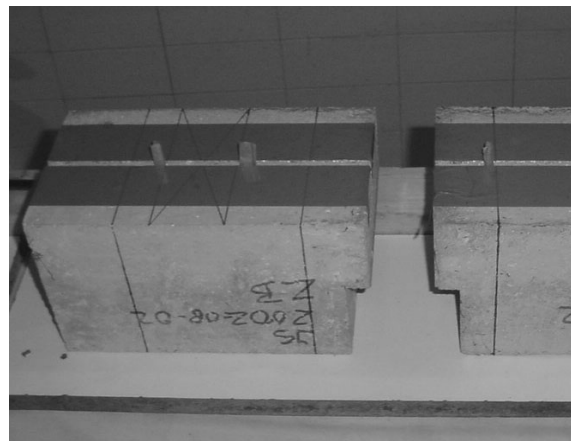
(a)



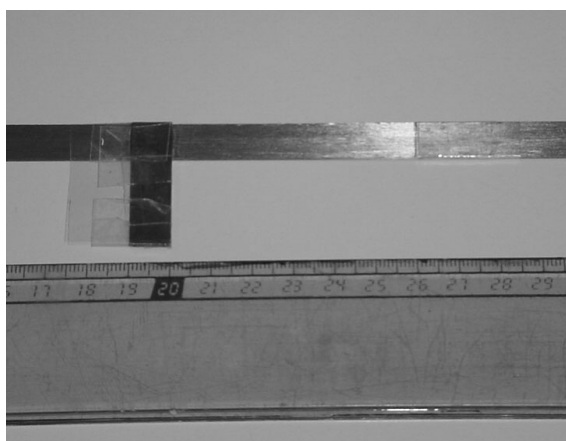
(b)



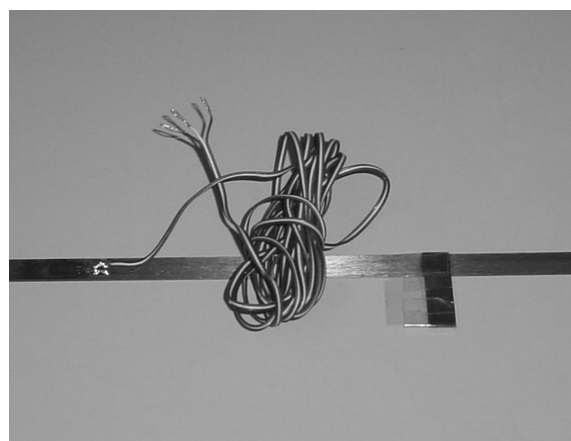
(c)



(d)



(e)



(f)

Figure 2.16 – Specimen preparation: (a) making the slits; (b) cleaning the slits with compressed water; (c) cleaning the slits with compressed air; (d) specimen final state before the CFRP reinforcement; (e) final state of the laminate bond zone; (f) final state of the CFRP laminate.



Figure 2.16 (cont.) – Specimen preparation: (g) slit filled with epoxy adhesive; (h) epoxy adhesive on the CFRP surface at the bond zone.

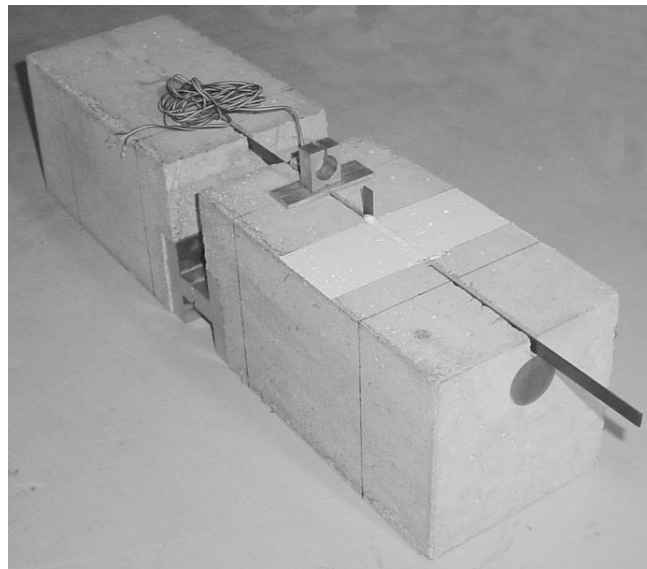


Figure 2.17 – Final state of the specimen before testing.

2.4 RESULTS

In the following sections the results obtained from the tested specimens are presented. These results include evaluation of the failure modes and influences of the bond length, concrete strength and load history on the bond performance.

2.4.1 Identification of failure modes

In the tested specimens, a large slip in the laminate-adhesive interface was observed. In fact, assuming that the adhesive-concrete and laminate-adhesive bond properties are similar (see Section 2.2.3), and considering that the concrete surface is rougher than the laminate surface, a larger slip in the laminate-adhesive interface was expected.

Photos of the laminate-adhesive-concrete bonding zone, included in Figure 2.18, were obtained with an optical microscope. They put in evidence that failure is caused by epoxy adhesive cracking, and debonding and sliding at the adhesive-concrete and laminate-adhesive interfaces. A fish spine crack pattern can be observed in the epoxy adhesive, which is explainable in terms of the deformations imposed by the CFRP during the pullout, as schematically shown in Figure 2.19. This figure depicts the developed micro-mechanism consisting on tensile forces, F_t , and compressive forces, F_c , in the epoxy adhesive, due to the shear stresses developed at the adhesive-concrete and CFRP-adhesive interfaces as a consequence of the stress transfer between concrete and CFRP.

From the information provided by the photos shown in Figure 2.18, an average angle between the crack surface and the CFRP direction of 33 degrees was observed. No cracks on the concrete surface were formed, justifying the previous hypothesis that concrete tensile strength does not influence the results in this specific bond test.

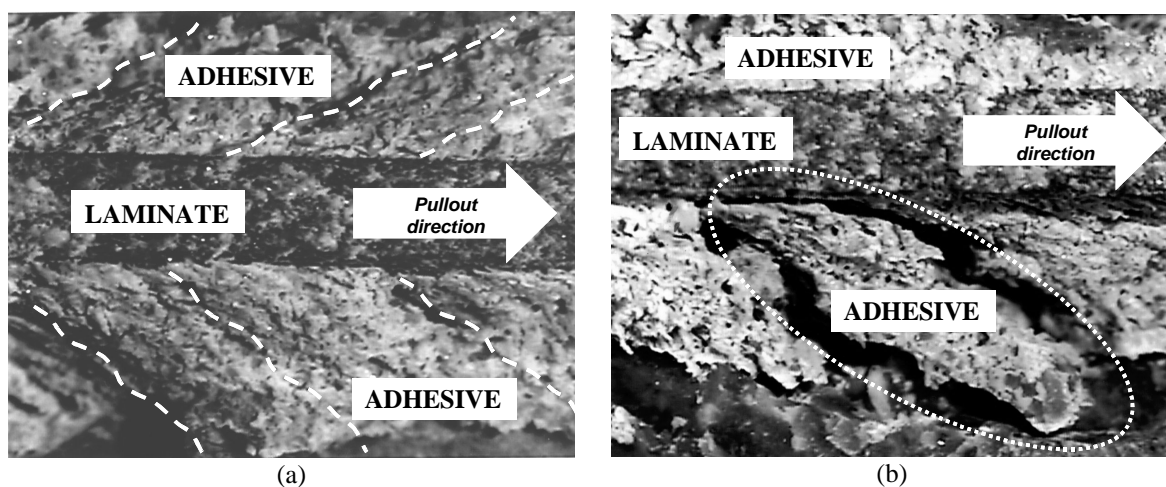
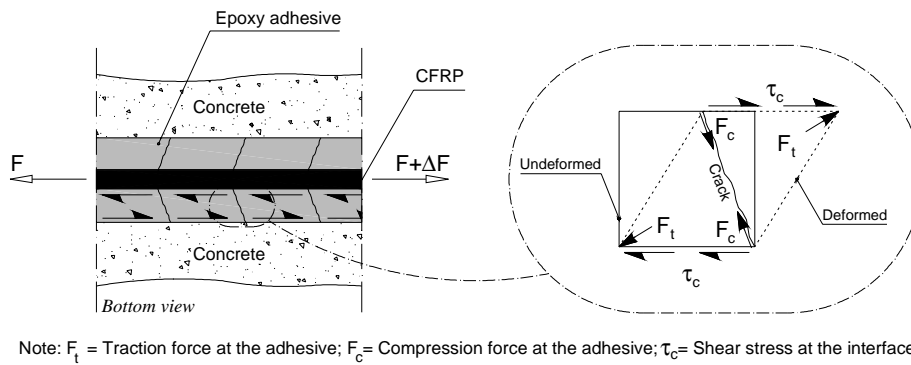


Figure 2.18 – Photos of the laminate-adhesive-concrete bonding zone: crack pattern (a) and failure of the epoxy adhesive (b).



Note: F_t = Traction force at the adhesive; F_c = Compression force at the adhesive; τ_c = Shear stress at the interface

Figure 2.19 – Force distribution corresponding to the crack pattern in the epoxy adhesive. Note: F_t is the traction force at the adhesive; F_c is the compression force at the adhesive; τ_c is the shear stress at the interface.

2.4.2 Monotonic loading results

2.4.2.1 Pullout force

Two different approaches were adopted in order to evaluate the pullout force in the CFRP, F_t , at the loaded end of the bond length. The first one is based on the force values measured at the load cells and takes into account the internal lever arm, i.e., the distance between the longitudinal axis of the CFRP and the contact point at the steel hinge (see Figure 2.4 and Figure 2.5). The second approach is based on the values recorded by the strain gage glued to the CFRP and takes into account the CFRP Young's modulus ($E_f = 160$ GPa for the *S1* series and $E_f = 171$ GPa for the *S2* series) and its cross sectional area ($A_f = 12.98$ mm² for the *S1* series and $A_f = 14.04$ mm² for the *S2* series).

Figure 2.20 shows a typical evolution of the pullout force for the *S1* and *S2* series calculated using the first and second approaches. In general, similar results were obtained with both approaches in the *S1* series. For the *S2* series it can be observed that up to the peak load the difference in the forces derived from both approaches increases, and remains constant in the softening phase. The differences in the force values obtained by both approaches, in the *S2* series, are probably justified by the variation of the internal lever arm during the test. Friction between the specimen and the load system also contributed to this difference, as demonstrated elsewhere (Sena-Cruz et al. 2004). In the following sections the pullout force is calculated with the strain gage approach, in order to avoid the cause of the aforementioned errors.

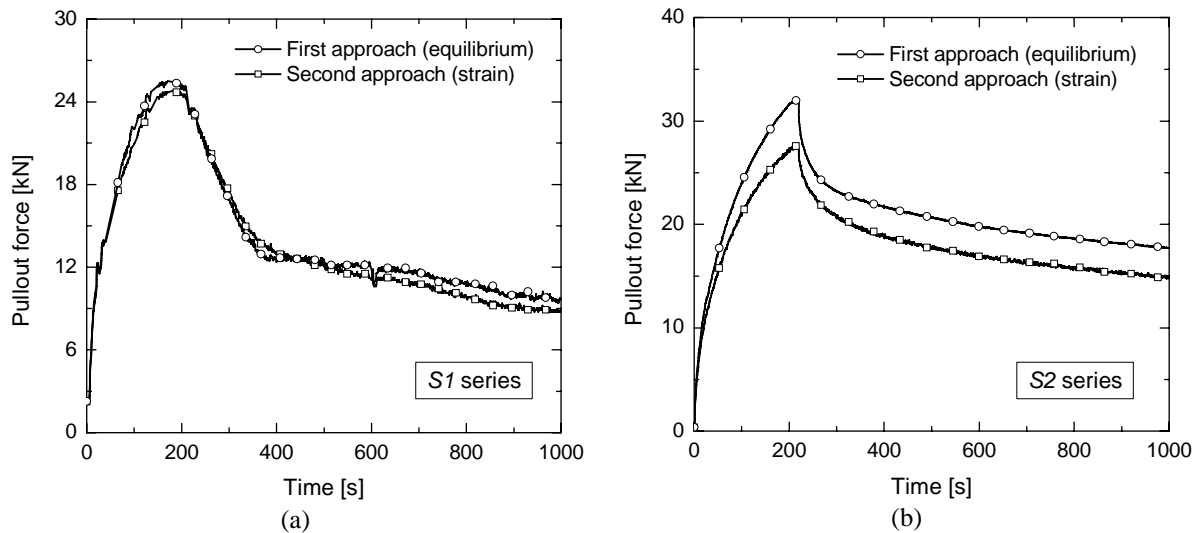


Figure 2.20 – Evolution of the pullout force in the specimens B3_fcm45_Lb80_M (a) and B3_fcm40_Lb120_M (b). Note: B3 means third beam of the series.

2.4.2.2 Slip at free and loaded ends

Figure 2.21 depicts a typical evolution of the slip measured at the free and loaded ends, and also the evolution of the pullout force. As expected, the slip at the loaded end, measured by the controller LVDT2, has a linear evolution. The slip at the free end, recorded by LVDT1 exhibits a nonlinear evolution. By analyzing simultaneously the curves corresponding to the evolution of both slips and of the pullout force, the following four branches can be identified in the pullout force curve:

- path AB, where slip occurs only at loaded end;
- path BC, where slip occurs at the loaded and free ends, with a higher slip rate at the loaded end;
- path CD, where the slip rate at the free end is higher than the slip rate at the loaded end;
- path DE, where slip rates are similar at the free and loaded ends.

Point B corresponds to the onset of the free end slip. In the *S1* series the free end slip slowly increased while in the *S2* series it has a negligible value up to the peak pullout force. Point C corresponds to the highest difference between the slip at the free and loaded ends. During the stage corresponding to the branch BC, both the pullout force and the free end slip have a nonlinear evolution. This can be justified by the nonlinear behavior of the epoxy adhesive as well as the debonding process at laminate-adhesive and adhesive-concrete

interfaces. Point D separates two branches of the pullout force curve, with a distinct slope. This transition is more pronounced in the S1 series. Due to the degradation of the bonding mechanisms at the laminate-adhesive-concrete interfaces, as well as to the adhesive cracking, a significant decay of the pullout force can be observed from point C to point D. Due to this load decrease, an elastic strain release on the CFRP occurs, thereby justifying the slip rate at the free end being higher than the slip rate at the loaded end. After point D, the pullout force is mainly due to friction mechanisms at both the laminate-adhesive and the adhesive-concrete interfaces, resulting in a quasi-rigid body movement of the CFRP at the bonded zone, with similar slip rates at both free and loaded ends.

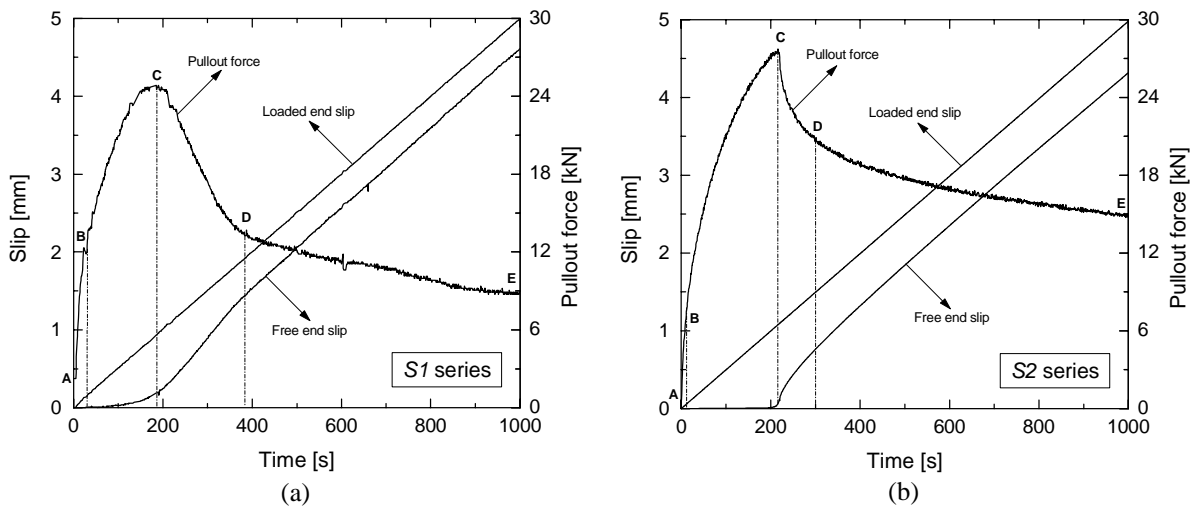


Figure 2.21 – Evolution of the slip at the free and loaded ends and of the pullout force in the specimens B3_fcm45_Lb80_M (a) and B3_fcm40_Lb120_M (b). Note: B3 means third beam of the series.

Ratios F_l/F_{lmax} for the points B, C and D are evaluated from the obtained experimental results, where F_l is the pullout force at points B, C or D and F_{lmax} is the maximum registered pullout force. These results are included in Table 2.6 and Table 2.7, from which it can be remarked that: the force at point C is near the F_{lmax} value; the forces at points B and D are about 70 % of F_{lmax} for the S1 series and about 20 % and 65 %, respectively, for the S2 series, but exhibiting a large scatter for the case of point B; concrete strength has a marginal influence on the F_l/F_{lmax} values for these points.

Table 2.6 – Average values of the F_l/F_{lmax} ratio for points B, C and D of the *S1* series.

Series	Ratio F_l/F_{lmax}		
	B	C	D
fcm35_Lb40_M	0.563 (30.0 %)	0.978 (0.7 %)	0.805 (2.9 %)
fcm35_Lb60_M	0.662 (12.0 %)	0.996 (0.7 %)	0.798 (11.2 %)
fcm35_Lb80_M	0.677 (9.0 %)	0.971 (0.9 %)	0.730 (7.4 %)
fcm45_Lb40_M	0.817 (6.0 %)	0.991 (1.0 %)	0.601 (9.3 %)
fcm45_Lb60_M	0.654 (24.3 %)	0.987 (1.0 %)	0.661 (7.0 %)
fcm45_Lb80_M	0.705 (18.8 %)	0.981 (2.0 %)	0.759 (2.2 %)
fcm70_Lb40_M	0.767 (5.3 %)	0.987 (1.4 %)	0.663 (6.4 %)
fcm70_Lb60_M	0.657 (23.3 %)	0.942 (9.0 %)	0.584 (7.0 %)
fcm70_Lb80_M	0.669 (31.9 %)	0.990 (0.9 %)	0.708 (5.8 %)

Note: the values within parentheses are the coefficients of variation.

Table 2.7 – Average values of the F_l/F_{lmax} ratio for points B, C and D of the *S2* series.

Series	Ratio F_l/F_{lmax}		
	B	C	D
fcm40_Lb60_M	0.180 (43.9 %)	0.996 (0.5 %)	0.598 (3.5 %)
fcm40_Lb90_M	0.246 (66.1 %)	0.989 (0.5 %)	0.654 (1.4 %)
fcm40_Lb120_M	0.229 (20.9 %)	0.993 (0.5 %)	0.669 (2.4 %)

Note: the values within parentheses are the coefficients of variation.

The large scatter obtained for the point B can be justified by the difficulty to assure the homogeneity of the epoxy adhesive in terms of thickness and physical properties along the bond length. Consequently, nonlinear deformations of the epoxy adhesive may have occurred during the stage corresponding to branch AB, especially at the loaded end, thereby contributing to the scatter of F_l/F_{lmax} obtained at point B. It was observed that the epoxy adhesive stiffness and strength depend on the presence of inevitable and unpredictable voids, as already reported (Sena-Cruz et al. 2001). Since the uncertainty of these epoxy properties influences the stress transfer between the laminate and the concrete, this may also have contributed to the scatter of F_l/F_{lmax} at point B.

2.4.2.3 Pullout force versus slip

Figure 2.22 and Figure 2.23 show typical relationships between the pullout force and slip at the free and loaded ends ($F_l - s_f$ and $F_l - s_l$) of the *S1* and *S2* series, respectively, for a monotonic loading configuration. Curves corresponding to the results of all the tested specimens are included in APPENDIX A.

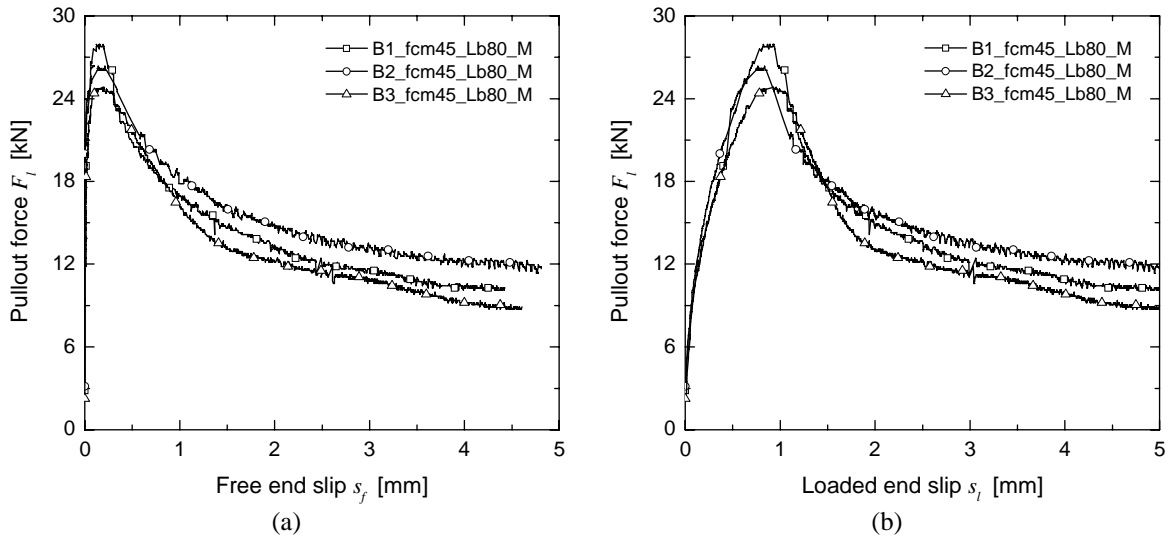


Figure 2.22 – Pullout force vs. free end slip (a) and vs. loaded end slip (b), of the fcm45_Lb80_M series.

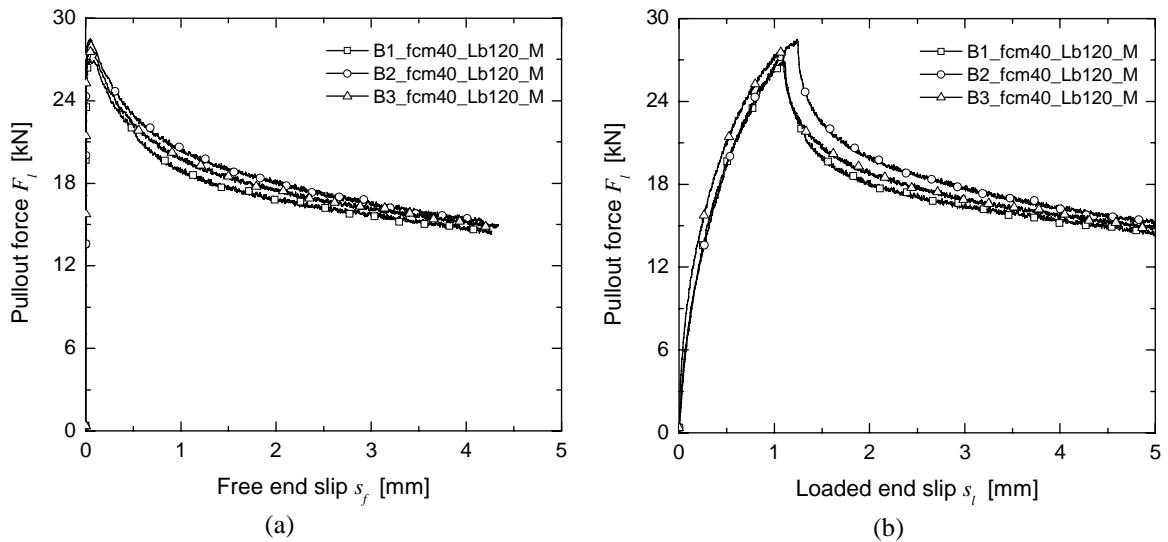


Figure 2.23 – Pullout force vs. free end slip (a) and vs. loaded end slip (b), of the fcm40_Lb120_M series.

The analysis of the $F_l - s_l$ and $F_l - s_f$ curves shows that after a short linear branch the response becomes nonlinear. Peak loads occurred for loaded end slips in the range of 0.27 mm to 1.24 mm. After a sudden decay beyond the peak, the pullout force decreases smoothly with the slip increment, describing a nonlinear softening branch. Residual pullout forces, which are quite significant, indicate that frictional mechanisms in the laminate-adhesive-concrete interfaces are mobilized. The aspect of the curves and the registered responses were similar in all the tested specimens (see APPENDIX A).

2.4.2.4 Discussion of results

In order to assess the bond performance of the monotonic tests, the entities included in Table 2.8 and Table 2.9 were analyzed. The meaning of each of those entities is the following:

- $s_{l_{\max}}$ is the slip at the loaded end at the peak pullout force ($F_{l_{\max}}$);
- τ_{\max} is the average bond strength, which is obtained dividing the peak pullout force by the contact area between the CFRP and epoxy adhesive, $F_{l_{\max}} / (2(w_f + t_f)L_b)$, where w_f and t_f are the width and the thickness of the CFRP and L_b is the bond length;
- the expression $\sigma_{l_{\max}} / f_{fu}$ is the ratio between the CFRP normal stress at peak pullout force and the CFRP tensile strength;
- τ_r / τ_{\max} is the residual bond stress ratio, defined as the ratio between the average bond stress at the end of the test (loaded end slip with a 5 mm displacement) and τ_{\max} .

The influence of the bond length and concrete strength on the loaded end slip at peak pullout force, $s_{l_{\max}}$, can be observed in Figure 2.24(a) and (b), respectively. In these graphs each dot represents an experimental result, and each curve is the average of three specimens. An almost linear relationship between $s_{l_{\max}}$ and the bond length can be observed in Figure 2.24(a). The value of $s_{l_{\max}}$ is practically independent of the concrete strength, as shown in Figure 2.24(b).

Table 2.8 – Average values of the main entities of the S1 series (monotonic loading).

Series	$s_{l_{max}}$ [mm]	$F_{l_{max}}$ [kN]	τ_{max} [MPa]	$\sigma_{l_{max}}/f_{fu}$ [%]	τ_r/τ_{max} [-]
fcm35_Lb40_M	0.29 (21.5 %)	15.0 (5.8 %)	17.5	42.1	0.41 (11.3 %)
fcm35_Lb60_M	0.49 (5.8 %)	22.8 (8.7 %)	17.7	64.0	0.47 (9.4 %)
fcm35_Lb80_M	0.65 (16.0 %)	22.4 (5.0 %)	13.0	62.1	0.37 (8.2 %)
fcm45_Lb40_M	0.27 (26.8 %)	15.5 (2.0 %)	18.1	43.5	0.39 (17.1 %)
fcm45_Lb60_M	0.46 (8.8 %)	19.9 (3.7 %)	15.5	55.8	0.33 (9.7 %)
fcm45_Lb80_M	0.84 (30.6 %)	26.4 (4.2 %)	15.4	73.9	0.41 (3.7 %)
fcm70_Lb40_M	0.32 (10.5 %)	15.7 (8.8 %)	18.3	44.0	0.50 (7.2 %)
fcm70_Lb60_M	0.40 (10.0 %)	18.9 (5.8 %)	14.7	52.9	0.39 (11.8 %)
fcm70_Lb80_M	0.74 (3.0 %)	25.6 (6.2 %)	14.9	71.6	0.48 (3.2 %)

Note: the values within parentheses are the coefficients of variation.

Table 2.9 – Average values of the main entities of the S2 series (monotonic loading).

Series	$s_{l_{max}}$ [mm]	$F_{l_{max}}$ [kN]	τ_{max} [MPa]	$\sigma_{l_{max}}/f_{fu}$ [%]	τ_r/τ_{max} [-]
fcm40_Lb60_M	0.43 (11.3 %)	18.7 (5.1 %)	13.6	47.5	0.45 (4.9 %)
fcm40_Lb90_M	0.79 (9.0 %)	23.9 (4.1 %)	11.6	60.7	0.52 (2.2 %)
fcm40_Lb120_M	1.13 (8.1 %)	27.7 (2.8 %)	10.1	70.5	0.54 (0.9 %)

Note: the values within parentheses are the coefficients of variation.

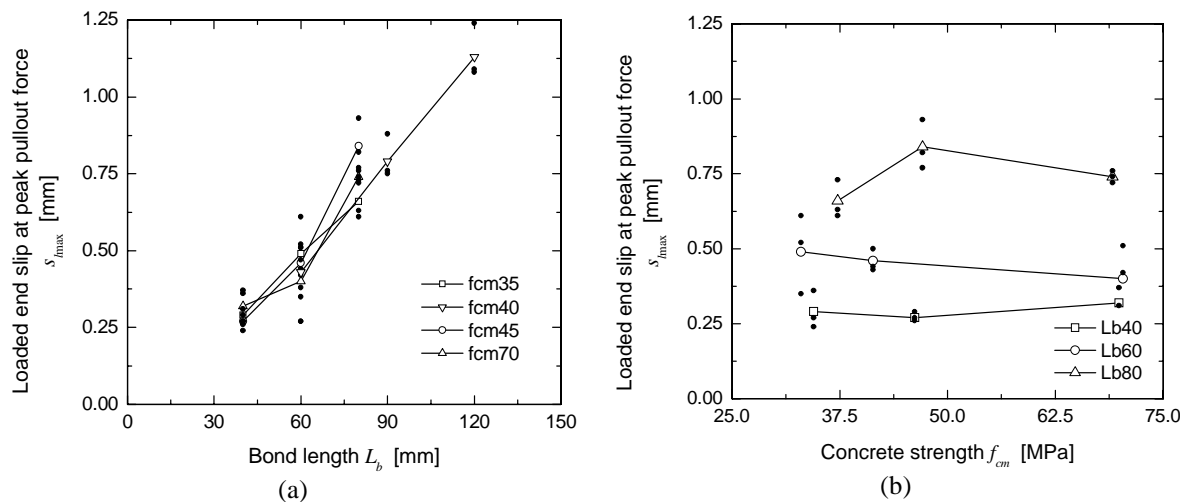


Figure 2.24 – Influence of the bond length (a) and concrete strength (b) on the loaded end slip at peak pullout force.

Figure 2.25(a) and (b) show the evolution of the peak pullout force, $F_{l_{\max}}$, with the bond length and the concrete strength, respectively. As expected, $F_{l_{\max}}$ increases with the bond length, L_b . Since the epoxy adhesive volume increases with L_b , the nonlinear branch before the peak pullout force also increases with L_b . The analysis of Figure 2.25 (b) and Table 2.8 leads to the conclusion that the influence of the concrete strength on $F_{l_{\max}}$ is marginal. The increase of the peak pullout force with L_b was higher in series *S1* than in series *S2*. Since the width of the slit was 3.3 mm and 4.8 mm for the *S1* and *S2* series, respectively, the larger volume of epoxy adhesive in the *S2* series seems to be the main reason for the aforementioned more significant increase.

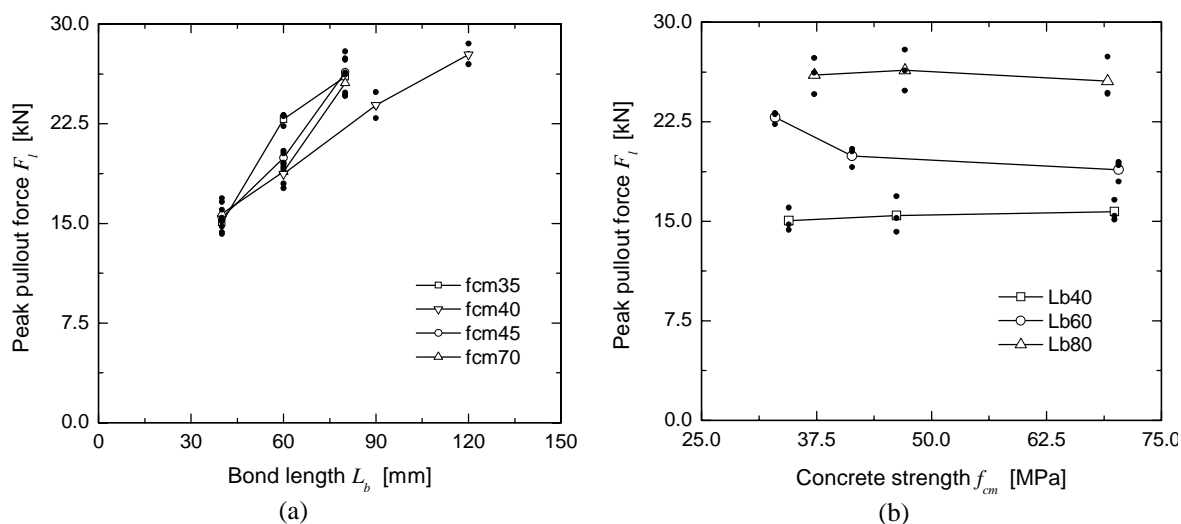


Figure 2.25 – Influence of bond length (a) and concrete strength (b) on the pullout force.

Figure 2.26(a) illustrates the relationship between τ_{\max} and the bond length for the series of different concrete strength classes, whereas Figure 2.26(b) depicts the evolution of τ_{\max} with the concrete strength for different bond lengths. The average peak bond stress, τ_{\max} , decreases with the bond length, being practically independent of the concrete strength (see Table 2.8 and Table 2.9). In the *S2* series values of τ_{\max} were lower than those of the *S1* series. This was predictable since τ_{\max} is linearly dependent of the peak pullout force, and lower values of $F_{l_{\max}}$ in the *S2* series were obtained.

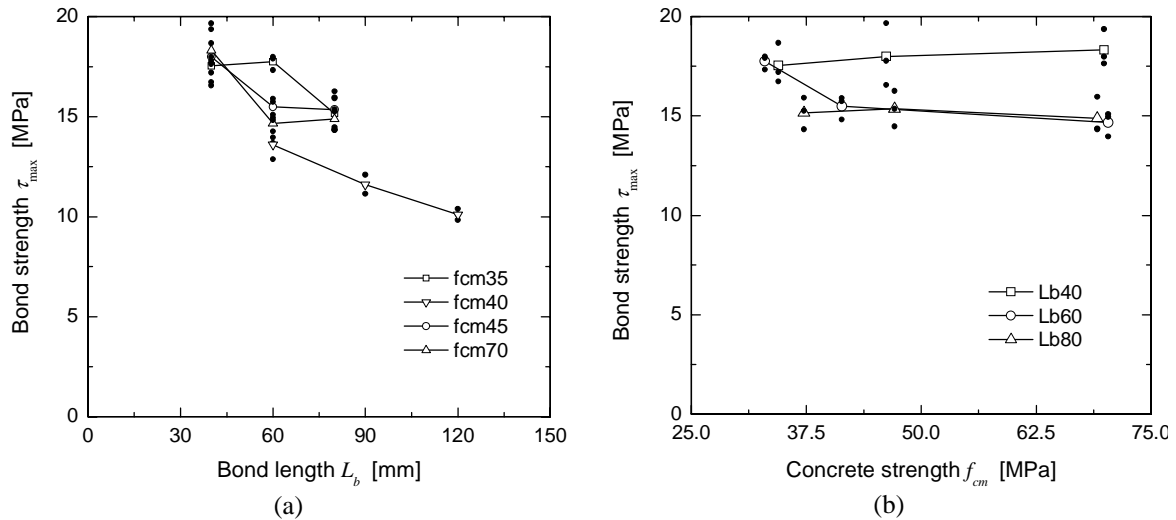


Figure 2.26 – Influence of bond length (a) and concrete strength (b) on the average bond strength.

The influence of the bond length and concrete strength on the CFRP normal stress at peak pullout force, σ_{lmax} , are represented in Figure 2.27(a) and (b), respectively, where σ_{lmax} is normalized by the CFRP tensile strength, f_{fu} . These influences can also be assessed from the results included in Table 2.8 and Table 2.9. Figure 2.27 reveals that, in general, σ_{lmax}/f_{fu} increases with the bond length and is independent of the concrete strength. For a given σ_{lmax}/f_{fu} , the *S1* series required a lower bond length than in the case of the *S2* series, which means that the *S1* series provides a higher bond efficiency. The larger volume of epoxy adhesive applied in the *S2* series, already pointed out in the justification for the smaller increase of the peak pullout force with L_b in comparison with what was observed in the *S1* series, is also the reason for the smaller increase of σ_{lmax}/f_{fu} with L_b .

Analyzing the influence of the bond length and the concrete strength in Table 2.8 (*S1* series) a clear trend of τ_r/τ_{max} ratio values was not found. The values of τ_r/τ_{max} in the *S2* series (see Table 2.9) seem to be bond length dependent.

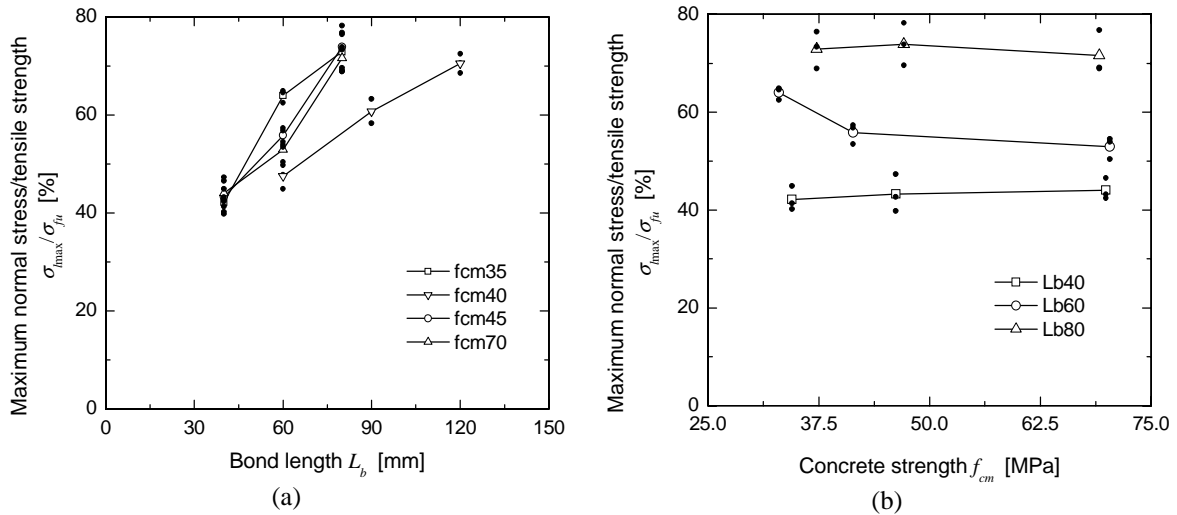


Figure 2.27 – Influence of bond length (a) and concrete strength (b) on the tensile ratio $\sigma_{l_{max}}/f_{fu}$.

2.4.3 Cyclic loading results

2.4.3.1 Pullout force, free end and loaded end slips

Figure 2.28(a) presents the typical evolution of the slip at the free and loaded ends of the C10 series. As this figure shows, in the unloading/reloading branches, the free end slip remains with a negligible value. The loaded end slip has a nonlinear evolution in the unloading branches since the tests were performed under load control in the unloading phase (see section 2.1.2). In the monotonic phase of the test both slips have similar variation.

Figure 2.28(b) shows the typical evolution of the pullout force in the C10 series. During the reloading branches the pullout force has a nonlinear evolution since in this phase the tests were performed under displacement control. A residual pullout force can be observed at the end of the unloading branches. This residual value was imposed in order to guarantee the stability of the test. In all the ten unloading/reloading cycles, the pullout force at the end of the reloading branches has decreased.

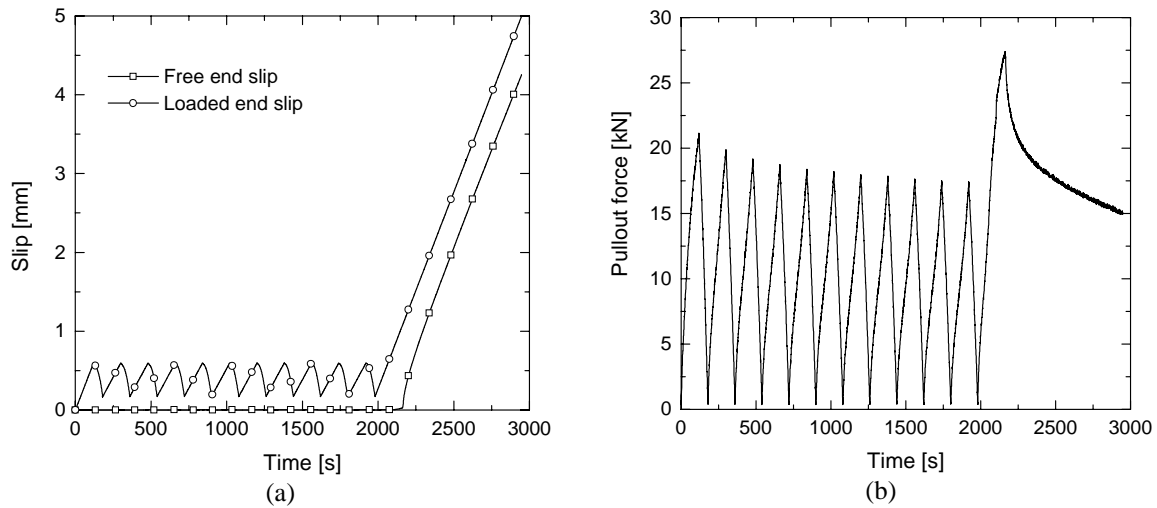


Figure 2.28 – Evolution of the slip at the free end (s_f) and loaded end (s_l) (a), and evolution of the pullout force (F_l) of the specimen B1_fcm40_Lb120_C10.

Figure 2.29 illustrates the typical evolution of the slip at the free and loaded ends and the pullout force in the C1 series. In the unloading branches the free end slip has remained practically constant whereas the loaded end slip has decreased. In the reloading branches after peak pullout force, the slip at both the free and loaded ends has increased with the pullout force. The loaded end slip has a nonlinear evolution in the unloading branches since the tests were performed under load control in the unloading phase.

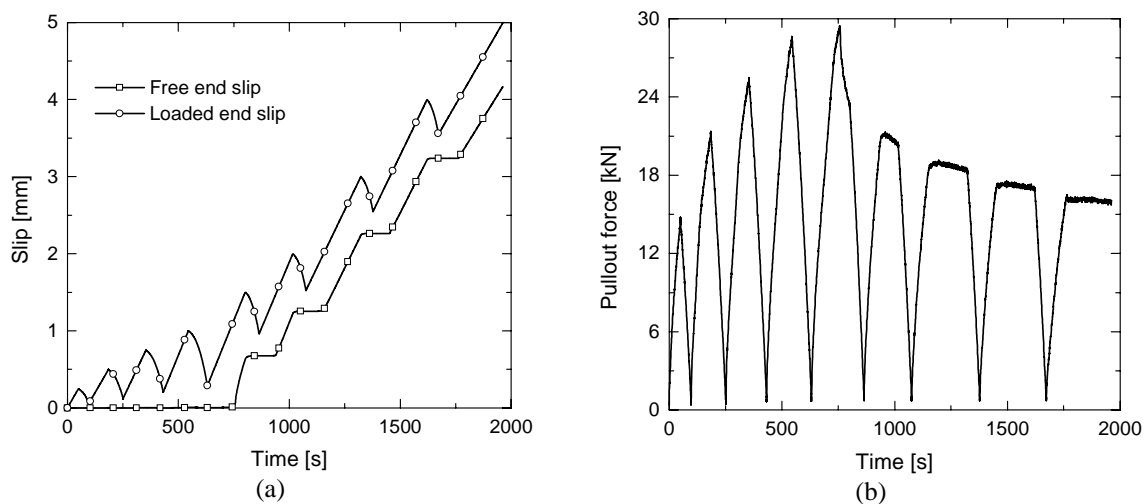


Figure 2.29 – Evolution of the slip at the free end (s_f) and loaded end (s_l) (a), and evolution of the pullout force (F_l) of the specimen B1_fcm40_Lb120_C1. Note: B1 means first beam of the series.

2.4.3.2 Pullout force *versus* slip

Figure 2.30 to Figure 2.32 reproduce the relationships between the pullout force and the slip at the free and loaded ends ($F_l - s_f$ and $F_l - s_l$) for the C10 series. For the series having the same bond length, the monotonic curve was also included. This curve is the average response of the monotonic tests composing the homologous series (with the same bond length).

For all the C10 series, the envelope of the cyclic tests is similar to the curve of the corresponding monotonic test. In the series having 60 mm and 90 mm bond length, the monotonic curve corresponds to the upper bound, while in the series having 120 mm bond length the monotonic curve is approximately a lower bound.

Figure 2.33 illustrates the typical behavior of the loaded end slip and pullout force relationship for the C10 series at the cycle loading phase. In Figure 2.33(a) a single cycle is shown, where two distinct behaviors can be identified: in the unloading branch nonlinear behavior occurs and the curve presents an upward-concavity; in the initial part of the reloading branch the behavior is nonlinear, followed by a linear relationship up to the end of this branch. This linear relationship, however, no longer occurs when the number of cycles is increased (see Figure 2.33(b)). This tendency has already been observed in concrete elements submitted to uniaxial cyclic loadings (Sinha et al. 1964, Karsan and Jirsa 1969).

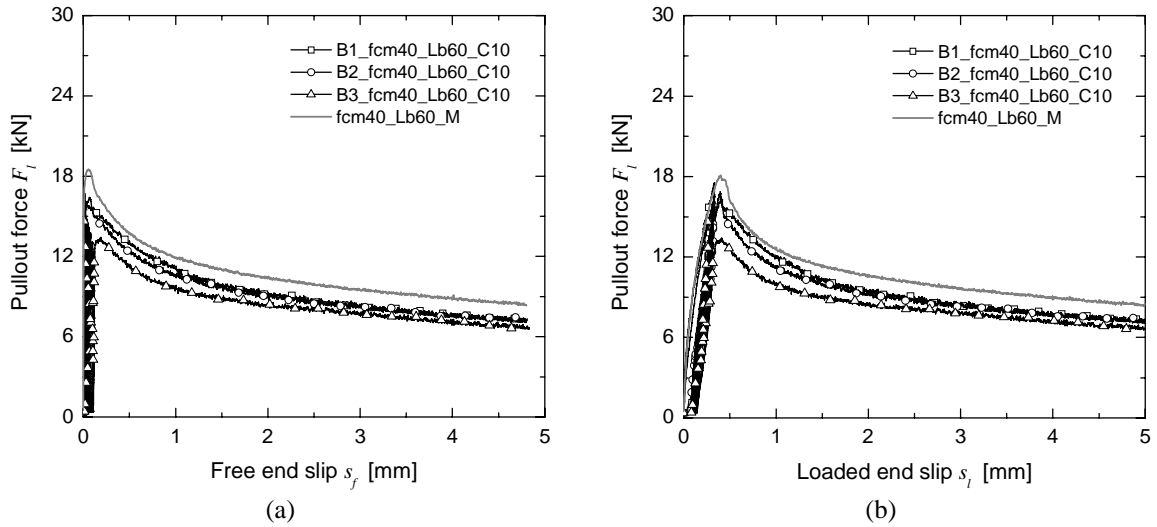


Figure 2.30 – Pullout force vs. free end slip (a) and vs. loaded end slip (b), of the fcm40_Lb60_C10 series.

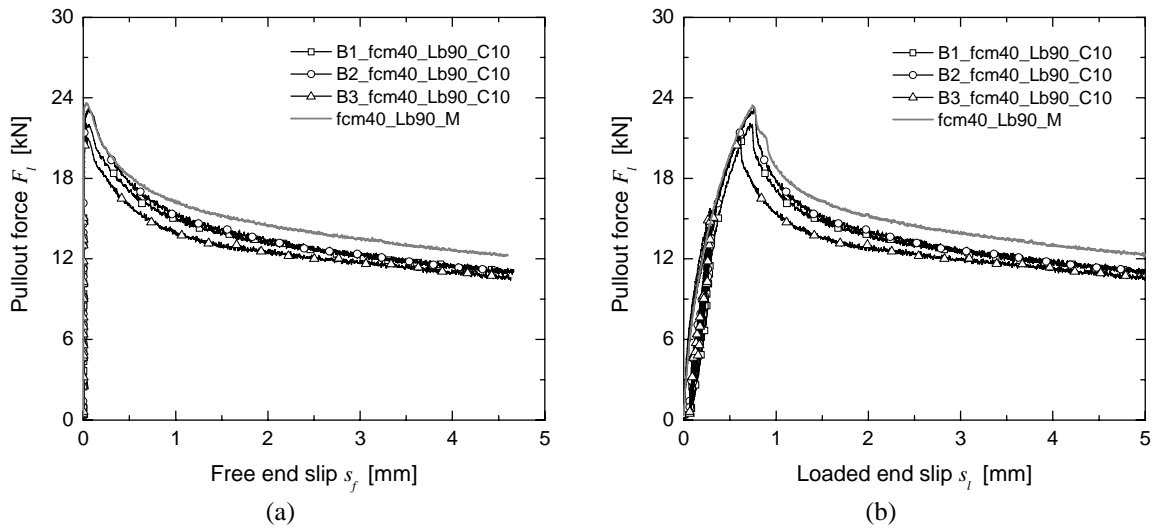


Figure 2.31 – Pullout force vs. free end slip (a) and vs. loaded end slip (b), of the fcm40_Lb90_C10 series.

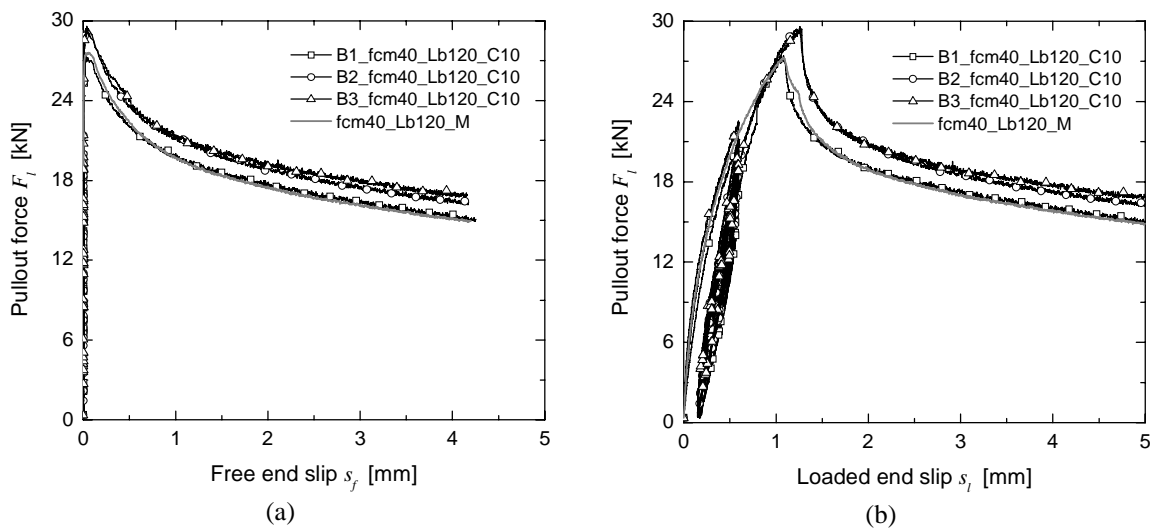


Figure 2.32 – Pullout force vs. free end slip (a) and vs. loaded end slip (b), of the fcm40_Lb120_C10 series.

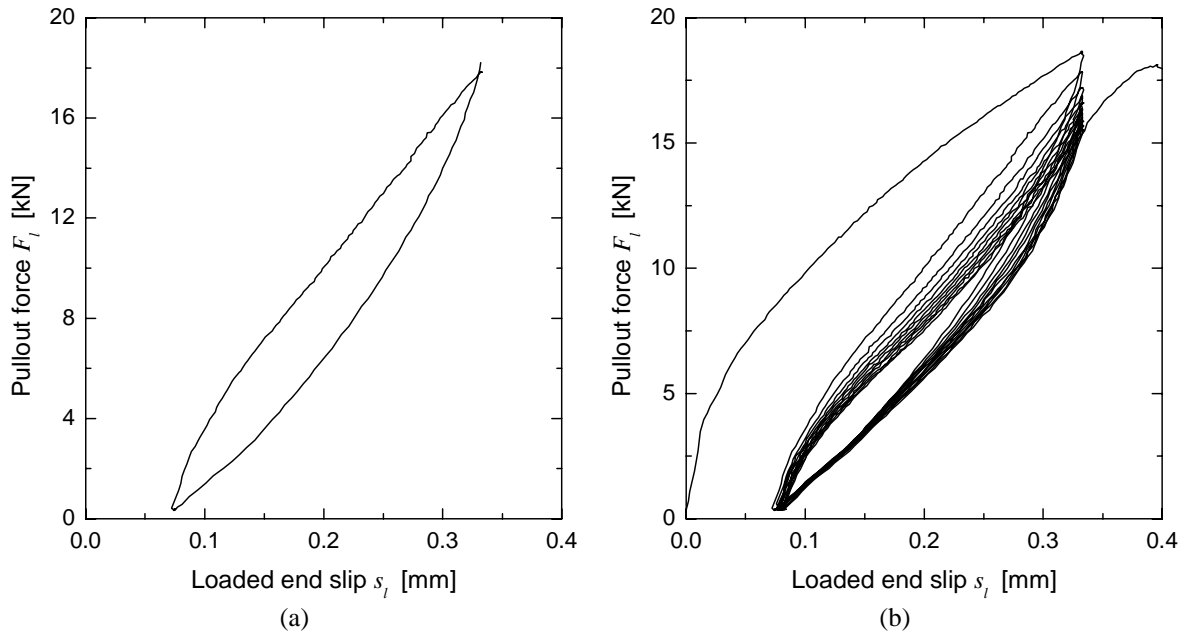


Figure 2.33 – Pullout force vs. loaded end slip of B1_fcm40_Lb60_C10 specimen: (a) typical cycle; (b) all performed cycles. Note: B1 means first beam of the series.

Figure 2.34 shows the relationships between the pullout force and the slip at the free and loaded ends ($F_l - s_f$ and $F_l - s_l$) for the C1 series, where the monotonic curve was also included. As expected, the envelopes of the cyclic tests are similar to the monotonic ones. Like in Lb120_C10 series, the monotonic curve seems to be the lower bound of the corresponding cyclic tests. During the unloading and reloading phase, the free end slip has not varied. In this phase, the relationship between the pullout force and the loaded end slip is nonlinear.

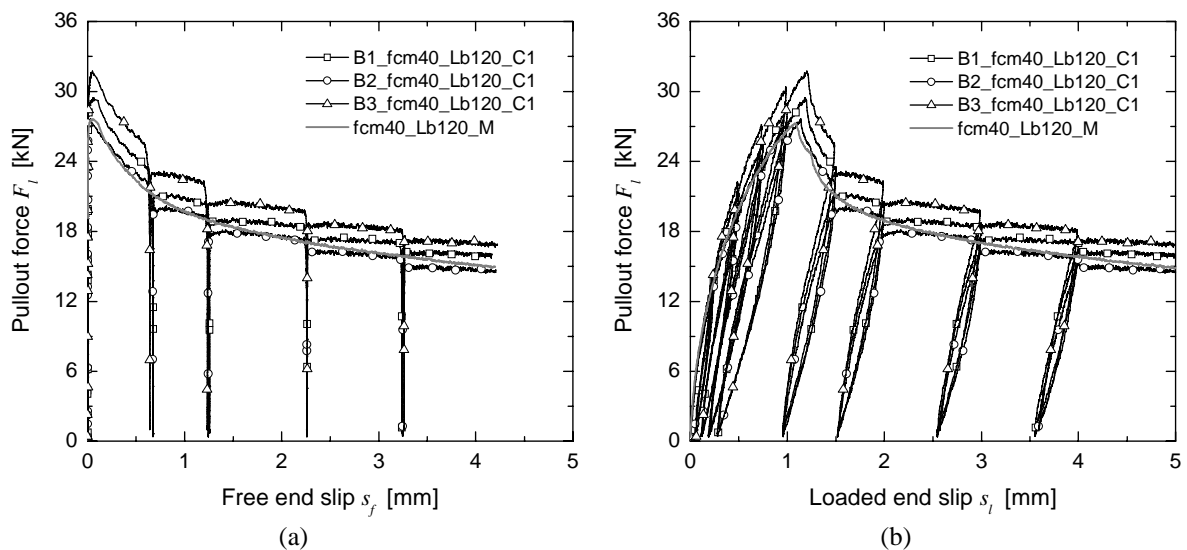


Figure 2.34 – Pullout force vs. free end slip (a) and vs. loaded end slip (b), of the fcm40_Lb120_C1 series.

2.4.3.3 Discussion of results

Table 2.10 includes the main entities analyzed (the meaning of each entity is indicated in Section 2.4.2.4). Comparing these values with those obtained for the monotonic tests of the homologous series, it is observed that the former are smaller, in general. Series Lb120 is the only exception to this tendency. During the epoxy adhesive application of the series Lb120_M a shorter pot life was observed, due probably to the elevated temperature. This fact might have adversely affected the bond performance of this series. The entities $s_{l_{max}}$, $F_{l_{max}}$, $\sigma_{l_{max}}/f_{fu}$ and τ_r/τ_{max} revealed a tendency to increase with the bond length, L_b , whereas τ_{max} decreased with L_b .

Table 2.10 – Average values of the main entities evaluated in the cyclic loading series.

Series	$s_{l_{max}}$ [mm]	$F_{l_{max}}$ [kN]	τ_{max} [MPa]	$\sigma_{l_{max}}/f_{fu}$ [%]	τ_r/τ_{max} [-]
fcm40_Lb60_C10	0.35 (13.43 %)	16.6 (5.2 %)	12.1 (5.2 %)	42.22 (5.19 %)	0.43 (3.59 %)
fcm40_Lb90_C10	0.69 (11.96 %)	22.2 (4.7 %)	10.8 (4.7 %)	56.35 (4.67 %)	0.49 (3.09 %)
fcm40_Lb120_C10	1.20 (8.36 %)	28.8 (4.1 %)	10.5 (4.1 %)	73.15 (4.09 %)	0.56 (2.61 %)
fcm40_Lb120_C1	1.18 (2.81 %)	29.6 (6.9 %)	10.8 (6.9 %)	75.53 (6.89 %)	0.54 (1.35 %)

Note: the values within parentheses are the coefficients of variation.

The influence of the number of cycles in the normalized pullout force is represented in Figure 2.35, for the C10 series. For each test, F_{i} is the pullout force at the end of the i -th reloading branch, while F_{i0} is the pullout force at the beginning of the first unloading branch. Figure 2.35(a) shows that the cycles did not occur at the pre-defined level of ratio between F_{i0} and $F_{l_{max}}$ (60 % for Lb90 series, 75 % for Lb120 series and 90 % for Lb60 series). Since F_{i0} was estimated from the homologous series, these discrepancies were expected. The influence of the load cycles on the strength degradation was similar in all series. An average value of 17 % for the strength degradation was observed. After the fifth cycle, a larger degradation occurred in the specimen B3_Lb60_C10, since these cycles were performed in the post-peak regime, while in the remaining specimens all cycles were carried out before the peak load. Figure 2.35(b) shows that the variation of the ration F_{i}/F_{i0} at the 10th cycle of all specimens is small.

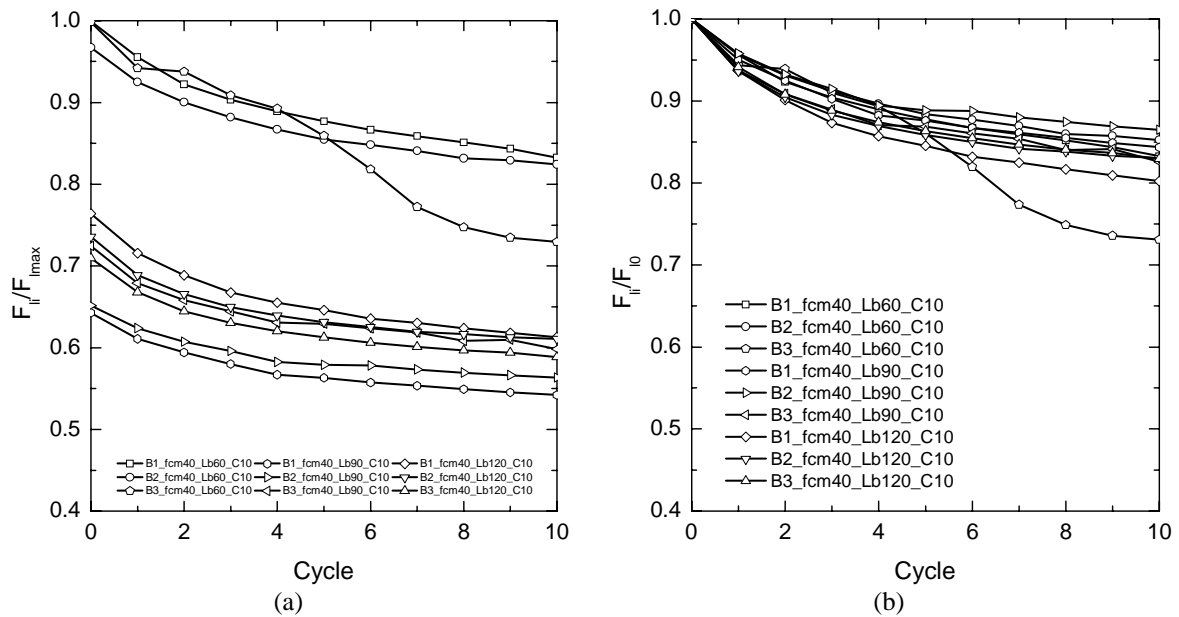


Figure 2.35 – Normalized pullout force as a function of the number of cycles.

The influence of the loading cycles on the stiffness degradation of the C1 series is represented in Figure 2.36. The stiffness is defined as the slope of the line connecting two points corresponding to unloading and reloading initiation. These points are signaled in Figure 2.36(a) with circles. Figure 2.36(b) represents, for the C1 series, the stiffness evolution with the loaded end slip. This chart shows that up to the peak pullout force the stiffness decreases significantly, while in the first phase of the softening branch a slight increase was registered, followed by a small decrease. The mechanisms involved at the pre-peak and post-peak pullout forces dictate this distinct behavior. Up to the peak pullout force, significant CFRP-adhesive and adhesive-concrete debonding occurs, accompanied with adhesive cracking, leading to a significant decrease of the bond stiffness. In the post-peak regime, the sudden decay of the pullout force induces the typical increase of stiffness that occurs when materials are submitted to large instantaneous load or displacement variations as reported by Otter and Naaman (1986). When this phase stabilizes, the bond stiffness is governed by friction between the failing surfaces (adhesive-concrete and laminate-adhesive) along the bond length, decreasing smoothly as slip increases.

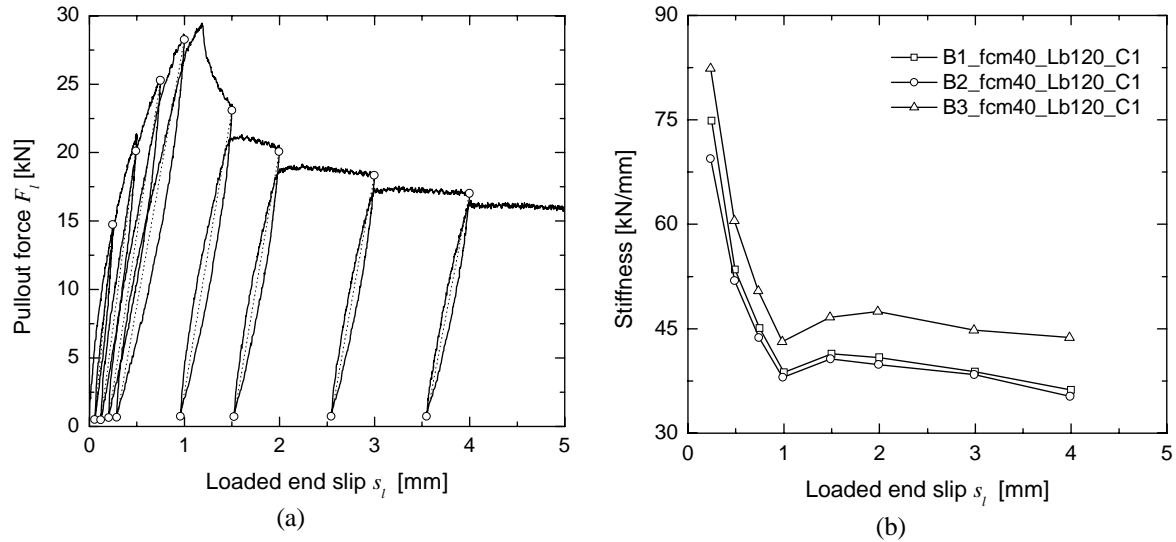


Figure 2.36 – Pullout force vs. loaded end slip relationship of the specimen B1_fcm40_Lb120_C1 (a) and stiffness degradation of the fcm40_Lb120_C1 series (b). Note: B1 means first beam of the series.

2.5 SUMMARY AND CONCLUSIONS

To assess the bond performance of laminate strips of CFRP to concrete using the near-surface mounted technique, pullout-bending tests under monotonic and cyclic loading were carried out. The influence of the bond length, L_b , the concrete strength, f_{cm} , and the load history was analyzed, by means of a series of tests with $L_b = 40, 60, 80, 90$ or 120 mm, $f_{cm} = 35, 45$ or 70 MPa, under monotonic or cyclic loadings.

A physical interpretation of the evolution of the pullout force and slip at the free and loaded ends was given based on the involved micro-mechanisms.

Since the tensile stress of the CFRP laminate is measured with strain devices, the bond test setup used in this experimental program seems to be adequate for the evaluation of the bond performance.

Based on the results obtained in the monotonic tests, the following remarks can be pointed out: the nonlinear branch before the peak pullout force and the peak pullout force increased with L_b ; the influence of the concrete strength on the pullout behavior was marginal; the bond strength ranged from 10 MPa to 18 MPa, having revealed a tendency to decrease with the increase of L_b and was practically insensitive to the concrete strength;

the ratio between the maximum tensile stress in the CFRP laminate and its tensile strength increased with L_b and is practically independent of the concrete strength; the loaded end slip at peak pullout force exhibited a linear increasing trend with L_b and was not affected by the concrete strength.

The ten cycle unloading/reloading tests with a fixed load level lead to the following main conclusions: the envelope of the pullout force *versus* slip relationships of the cyclic tests and the curve obtained in the homologous monotonic tests had a similar shape; a continuous decrease of the pullout force at the end of the reloading branches in the unloading/reloading cycles, carried out before the peak pullout force, was observed. The peak pullout force, however, was not influenced by this effect; in the unloading branches of the load cycles, no slip at the free end was observed.

In the single cycle unloading/reloading tests at different slip levels the stiffness, i.e., the average inclination of a complete cycle, decreased significantly up to the peak pullout force. At the initiation of the softening phase the stiffness increased slightly, followed by a smooth decrease.

CHAPTER 3

ANALYTICAL MODELING OF BOND BETWEEN NEAR-SURFACE MOUNTED CFRP LAMINATE STRIPS AND CONCRETE

Bond of reinforcement in concrete is intrinsically a three-dimensional problem. Typically, due to its complexity and for the purpose of developing analytical formulations, the three-dimensional problem is split up into two unidimensional or bidimensional problems. Usually, bond behavior along the reinforcement is analyzed as a uniaxial problem, and can be modeled by solving the differential equation that governs the behavior of bond between reinforcement and concrete. In order to solve this equation the local bond stress-slip relationship must be known. The bond behavior along the reinforcement depends on the stress state in the surrounding concrete (lateral stress state) which can be analyzed as a plane strain problem. In this analysis, the cover depth and the confining pressure level must be taken into account. The simultaneous consideration of both behaviors (longitudinal and lateral) can also be performed (FIB 2000).

Several researchers have modeled the longitudinal bond behavior of rebars, assuming that the slip and the bond stress are constant along the bond length, which is quite acceptable for rebars (FIB 2000). Many researchers have proposed empirical nonlinear equations for the local bond stress-slip relationship. The proposal of Eligehausen et al. (1983) is the most commonly used.

In early works on the analytical modeling of the bond of FRP bars, the methodology already adopted for the rebars was followed. Several researchers have considered a constant slip and bond stress throughout the bond length and, with this assumption, have proposed different local bond stress-slip relationships in order to model the bond behavior (Larralde et al. 1993, Malvar 1995, Cosenza et al. 1997, De Lorenzis et al. 2002). For FRP reinforcement, however, this approach should not be considered, since the distribution of the slip and bond stress along the bond length is markedly nonlinear (Focacci et al. 2000).

In the present chapter, an analytical bond stress-slip relationship was determined for the NSM technique. With this purpose, a numerical method was developed, which uses the results obtained in the experimental program (see Chapter 2). This method solves the differential equation that governs the slip evolution of the near-surface mounted CFRP laminate strips technique, and takes into account the distribution of the slip and the bond stress along the bond length. In the following sections this differential equation is deduced, the corresponding numerical method is detailed and its performance is assessed. Using this numerical tool, the parameters that define the local bond stress-slip relationship are obtained, as well as the critical anchorage length for this type of reinforcement.

3.1 DIFFERENTIAL EQUATION GOVERNING THE SLIP

The equilibrium of an infinitesimal length dx of a CFRP laminate bonded to concrete can be expressed by (see Figure 3.1)

$$\sigma_f t_f w_f + \tau 2w_f dx = (\sigma_f + d\sigma_f) t_f w_f \quad (3.1)$$

where $\tau = \tau(s(x))$ is the bond stress on the contact surface between the CFRP and the epoxy adhesive, and σ_f , t_f and w_f are the normal stress, thickness and width of the CFRP, respectively.

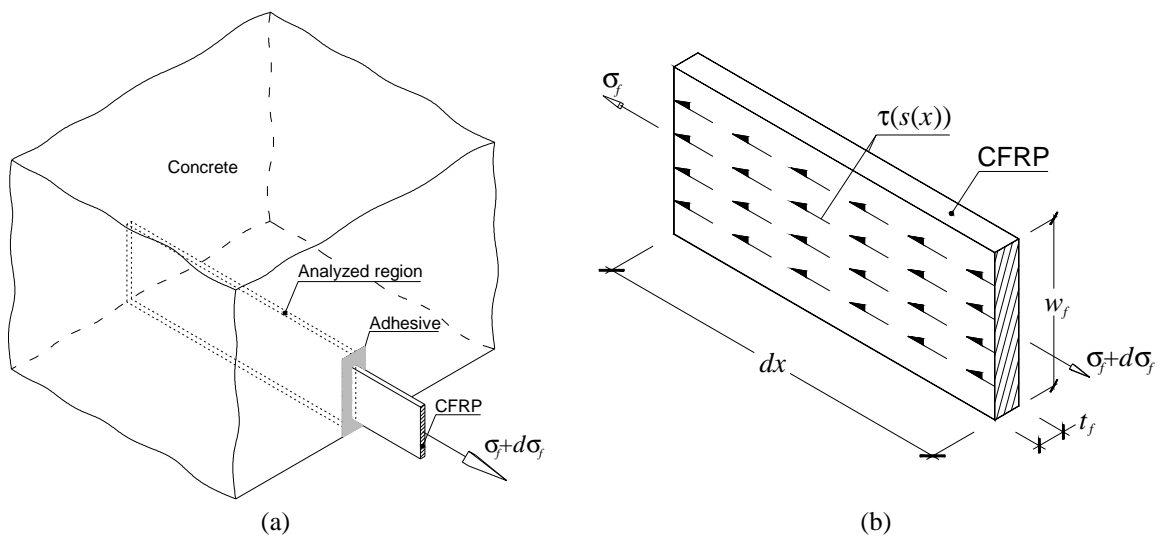


Figure 3.1 – (a) Laminate strip bonded to concrete; (b) Equilibrium of the CFRP laminate strip.

Assuming that the CFRP laminate has a linear elastic behavior ($d\sigma_f = E_f d\varepsilon_f$), equation (3.1) leads to

$$\tau = \frac{E_f t_f}{2} \frac{d\varepsilon_f}{dx} \tag{3.2}$$

where E_f and ε_f are the Young's modulus and the normal strain of the CFRP, respectively.

In a representative region of the CFRP-adhesive-concrete bonding phenomenon, the strain components indicated in Figure 3.2 are present. Neglecting the concrete and the adhesive deformability in the slip evaluation, the CFRP strain can be obtained from the slip variation, ds , which leads to

$$\varepsilon_f = \frac{ds}{dx} \tag{3.3}$$

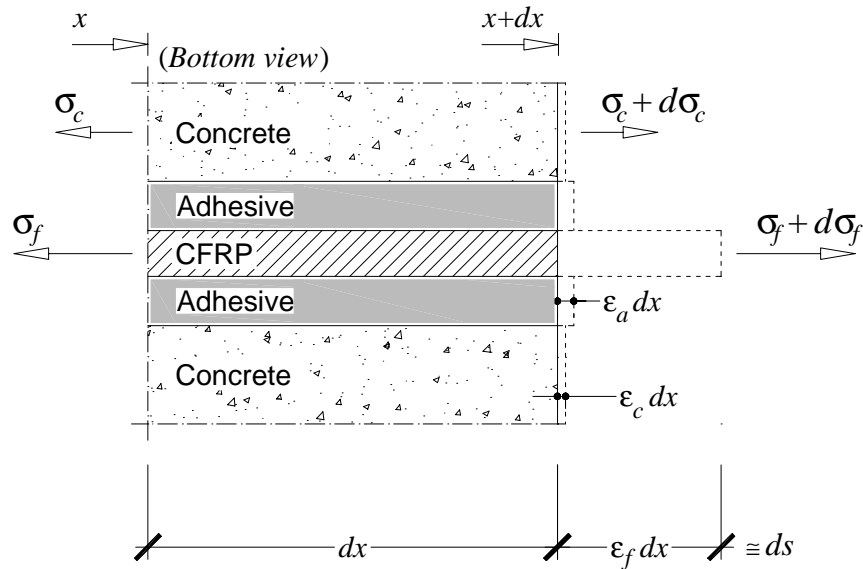


Figure 3.2 – Stresses and strains in the materials surrounding the bond region.

Incorporating (3.3) into (3.2), the differential equation that governs the slip of CFRP bonded into concrete is derived, and reads

$$\frac{d^2s}{dx^2} = \frac{2}{t_f E_f} \tau \quad (3.4)$$

With expressions similar to (3.4), important aspects associated with concrete behavior, such as anchorage length of the reinforcement, tension-stiffening, crack spacing and crack opening, can be simulated. The accuracy of the local bond stress-slip relationship, $\tau-s$, has decisive importance on the quality of the simulation of these phenomena.

3.2 DETERMINATION OF THE LOCAL BOND STRESS-SLIP RELATIONSHIP

The method adopted to determine the local bond stress-slip relationship, $\tau-s$, is based on the work developed by Focacci et al. (2000). Modifications were implemented in order to take into account the specificities of the present strengthening technique and to improve the performance of the method. In the following sections, the method developed in the present study is described in detail.

3.2.1 Analytical expressions for the local bond stress-slip relationship

In the present work the local bond stress-slip relationship for the *SI* series (see Chapter 2), is defined by the following function,

$$\tau(s) = \begin{cases} \tau_m \left(\frac{s}{s_m} \right)^\alpha & \text{if } s \leq s_m \\ \tau_m \left(\frac{s}{s_m} \right)^{-\alpha'} & \text{if } s > s_m \end{cases} \quad (3.5a)$$

$$(3.5b)$$

where τ_m and s_m are the bond strength and its corresponding slip, being α and α' the parameters that define the shape of the curves. Equation (3.5a) was used by Eligehausen et al. (1983) and defines the bond behavior up to peak stress (ascending branch). Equation (3.5b) was adopted by De Lorenzis et al. (2002) and characterizes the post-peak

bond behavior (descending branch). These relationships were selected due to its simplicity and ability to simulate the local bond stress-slip behavior.

In the *S2* series a higher initial post-peak stress decay was observed, when compared with the *S1* series (see Chapter 2). For this reason, the proposal of Stang and Aarre (1992) was selected for the branch with $s > s_m$. With these assumptions and for the case of the *S2* series, the local bond stress-slip relationship is defined by

$$\tau(s) = \begin{cases} \tau_m \left(\frac{s}{s_m} \right)^\alpha & \text{if } s \leq s_m \\ \tau_m \frac{1}{1 + \left(\frac{s - s_m}{s_1} \right)^{\alpha''}} & \text{if } s > s_m \end{cases} \quad (3.6a)$$

$$(3.6b)$$

where α'' and s_1 are parameters that define the shape of the post-peak branch of the curve.

3.2.2 Description of the method

Figure 3.3 represents a CFRP fixed to concrete with an epoxy adhesive over a bond length L_b . When the CFRP is slipping due to an applied pullout force, \bar{N} , the following entities can be evaluated along the CFRP bond length: slip, $s(x)$; bond stress between the CFRP and the epoxy adhesive, $\tau(x)$; strain, $\varepsilon_f(x)$; and the axial force, $N(x)$. For the particular case of the bond length extremities, designated free and loaded ends, the conditions are

$$x = 0 \Rightarrow \begin{cases} s(0) = s_f \\ N(0) = 0 \\ \varepsilon_f(0) = 0 \end{cases} ; \quad x = L_b \Rightarrow \begin{cases} s(L_b) = s_l \\ N(L_b) = \bar{N} \\ \varepsilon_f(L_b) = \bar{N}/(E_f A_f) \end{cases} \quad (3.7)$$

where s_f and s_l are the slips at the free and loaded ends, respectively, and A_f is the cross section area of the laminate. In the present method, numerical and experimental entities

will be involved, being the latter differentiated by a strikeover. For instance, \bar{N}^i represents the pullout force experimentally measured in the i -th scan reading.

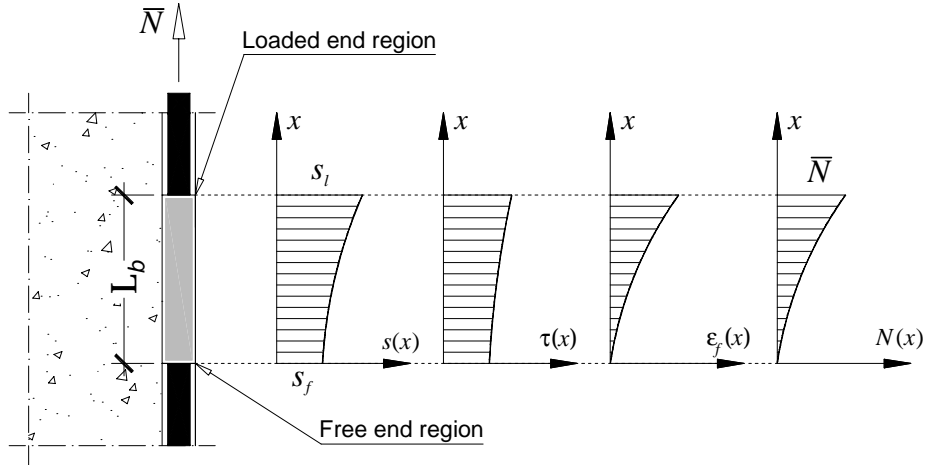


Figure 3.3 – Entities involved in the developed method.

By means of a pullout-bending test, the slip at the free end, \bar{s}_f , the slip at the loaded end, \bar{s}_l , and the pullout force, \bar{N} , were obtained for several scan readings, being \bar{s}_f^i , \bar{s}_l^i and \bar{N}^i the values of reading i . Using these experimental results, the main purpose was to obtain the parameters s_m , τ_m , α and α' of equation (3.5) and s_m , τ_m , α , α'' and s_l of equation (3.6), that fit the differential equation (3.4) as accurately as possible. With this aim, a computational code was developed, based on the algorithm described in Figure 3.4. In this algorithm the second order differential equation (3.4) is solved by the Runge-Kutta-Nyström (RKN) method (Kreyszig 1993), which is detailed in APPENDIX B. The following main steps constitute the algorithm:

1. the $\tau-s$ relationship is defined attributing values to its parameters. For instance, the values of s_m , τ_m , α and α' must be imposed to define equation (3.5). The error, e , defined as the area between the experimental and analytical curves, is initialized;
2. the loaded end slip is calculated at the onset of the free end slip, \tilde{s}_l , (see *Module A* in Figure 3.5);
3. for the experimental i -th scan reading, the free end slip, \bar{s}_f^i , the loaded end slip, \bar{s}_l^i , and the pullout force, \bar{N}^i are read;

4. taking the free end slip, \bar{s}_f^i , and solving (3.4), the numerical pullout force at the loaded end, $N^i(\bar{s}_f^i)$, is calculated (see *Module B* in Figure 3.5);
5. the error associated with $N^i(\bar{s}_f^i)$ is calculated. This error is the area between the experimental ($A_{\text{exp},f}^i$) and numerical ($A_{\text{num},f}^i$) curves. The points $(\bar{s}_f^{i-1}, N^{i-1}(\bar{s}_f^{i-1}))$ and $(\bar{s}_f^i, N^i(\bar{s}_f^i))$ are used to define the numerical curve, while the experimental curve is represented by the points $(\bar{s}_f^{i-1}, \bar{N}^{i-1})$ and (\bar{s}_f^i, \bar{N}^i) ;
6. the error is updated;
7. taking the loaded end slip, \bar{s}_l^i , and using (3.4), the pullout force at the loaded end, $N^i(\bar{s}_l^i)$, is evaluated. In this case the following two loaded end slip conditions must be considered: i) if $\bar{s}_l^i < \tilde{s}_l$, the determination of $N^i(\bar{s}_l^i)$ must take into account that the effective bond length is smaller than L_b (see *Module C* in Figure 3.5); ii) if $\bar{s}_l^i \geq \tilde{s}_l$, the evaluation of $N^i(\bar{s}_l^i)$ is based on *Module D* (see Figure 3.5);
8. the error associated with $N^i(\bar{s}_l^i)$ is calculated. This error is the area between the experimental ($A_{\text{exp},f}^i$) and numerical ($A_{\text{num},f}^i$) curves. The points $(\bar{s}_l^{i-1}, N^{i-1}(\bar{s}_l^{i-1}))$ and $(\bar{s}_l^i, N^i(\bar{s}_l^i))$ are used to define the numerical curve, whereas the experimental curve is represented by the points $(\bar{s}_l^{i-1}, \bar{N}^{i-1})$ and (\bar{s}_l^i, \bar{N}^i) ;
9. the error is updated.

In *Modules C* and *D* the Newton-Raphson method is used. When the Newton-Raphson method fails, the bisection method is used as an alternative.

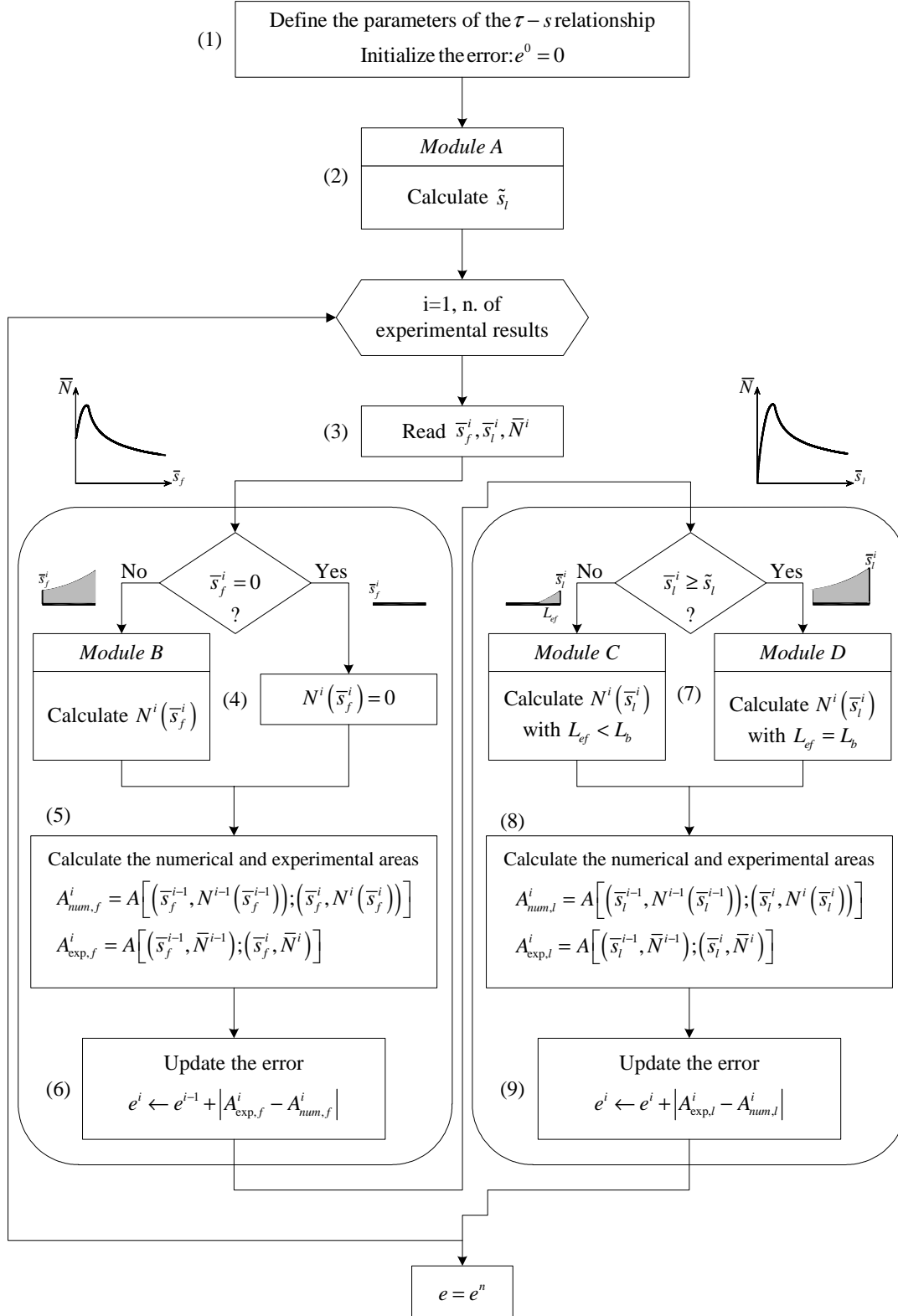


Figure 3.4 – Implemented algorithm to obtain the local bond-stress slip relationship.

The determination of the parameters defining the $\tau-s$ relationship with a minimum error, e , was also conditioned by the restriction of ensuring similar values for the numerical and experimental peak pullout force and its corresponding slip (with a tolerance

smaller than 1 %). For this purpose, an exhaustive search was performed, based on a predefined range and a predefined step for the values of the independent parameters. The algorithm described in Figure 3.4 was adopted for each set of parameters.

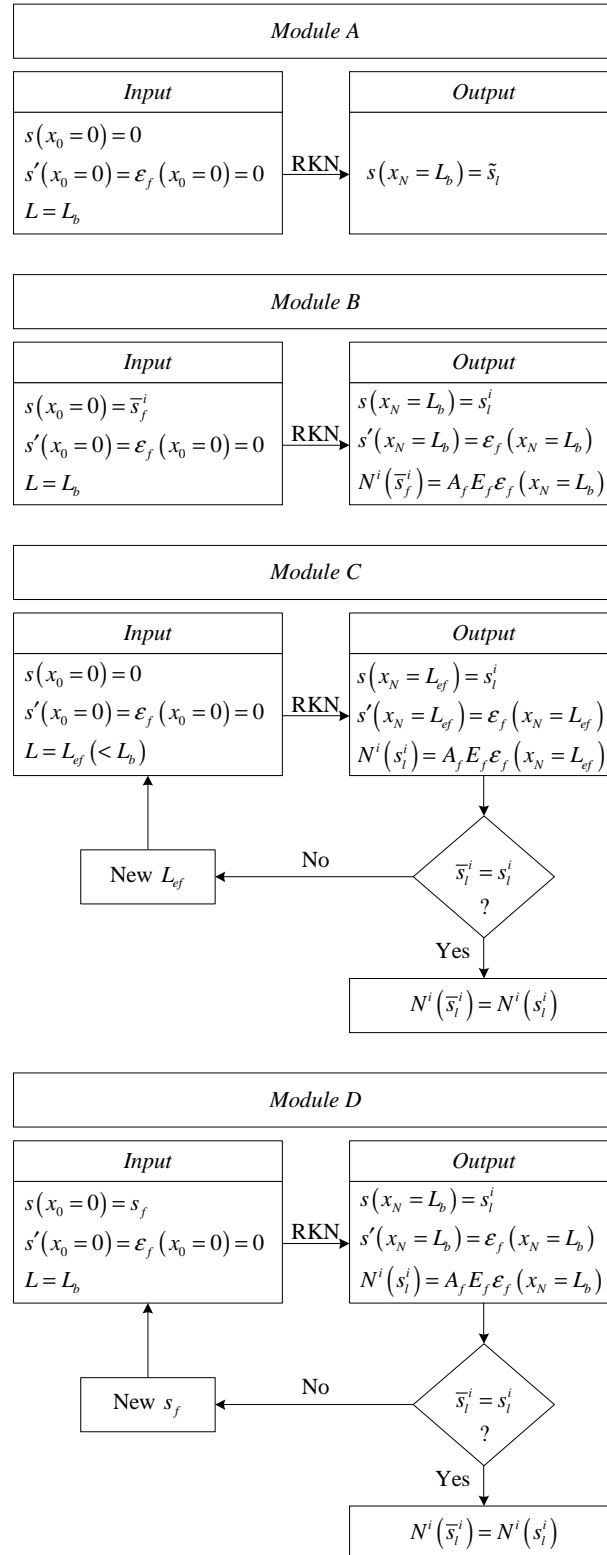


Figure 3.5 – Modules A, B, C and D of the algorithm shown in Figure 3.4.

3.2.3 Example

Of all the pullout-bending tests carried out (see Chapter 2), the beam B2_fcm45_Lb80_M was selected to exemplify the application of the method described in the previous section. The excellent performance of the developed method is well illustrated in Figure 3.6, where the experimental and numerical pullout force *versus* slip relationships are compared. The variation of the slip, bond stress and axial force along the bond length, at the peak pullout force, is shown in Figure 3.7. At this loading stage the bond behavior is essentially nonlinear, and in one half of the bond length the softening phase of the constitutive relation was reached.

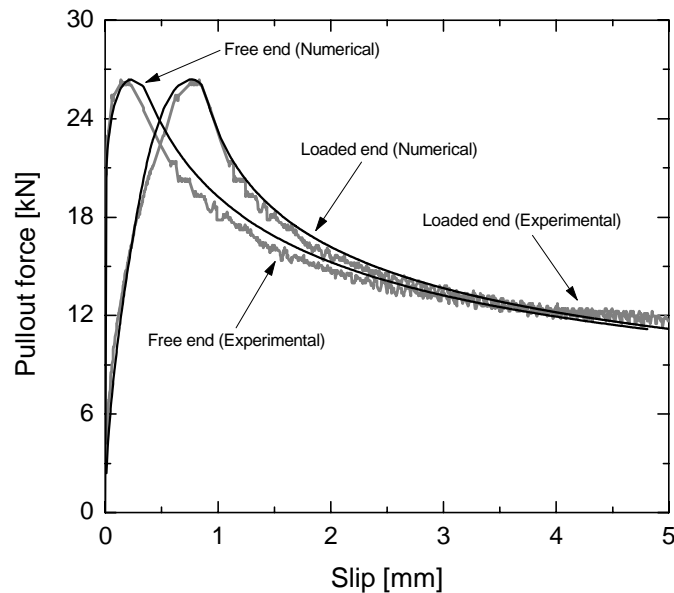


Figure 3.6 – Specimen B2_fcm45_Lb80_M: experimental and numerical pullout force vs. slip relationships.

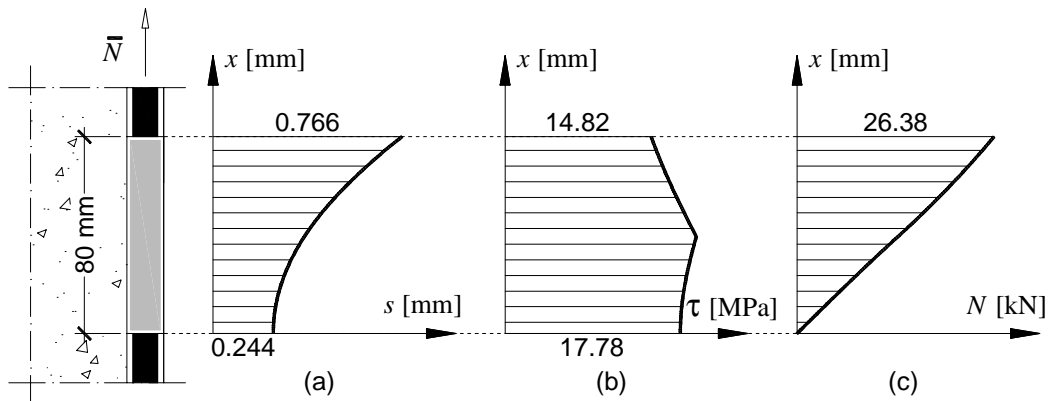


Figure 3.7 – Variation of the slip (a), bond stress (b) and axial force (c) along the bond length in the specimen B2_fcm45_Lb80_M.

A sensitivity analysis was performed in order to evaluate the influence of the parameters that define the local bond stress-slip relationship on the $N-s$ response. This analysis lead to the following conclusions:

- the peak pullout force is controlled by τ_m ;
- the slip at the peak pullout force is controlled by s_m ;
- all the other parameters have a negligible influence on the definition of the peak values (peak pullout force and its corresponding slip), but strongly affect the shape of the pre- and post-peak branches.

3.3 LOCAL BOND STRESS-SLIP RELATIONSHIP FOR NEAR-SURFACE MOUNTED CFRP LAMINATE STRIPS

Using the results obtained in the experimental program described in Chapter 2, the values of the parameters s_m , τ_m , α , α' , α'' and s_1 of the local bond stress-slip relationships (see equations (3.5) and (3.6) of the *S1* and *S2* series) were determined using the numerical strategy described in Section 3.2.2 and applied in Section 3.2.3. For each series (composed of three specimens), the average relationship between the loaded end slip and the pullout force was used to calibrate the relationship. Table 3.1 includes the CFRP properties used in the model.

Table 3.1 – Main properties of the CFRP laminate strip used in the model.

Series	t_f [mm]	w_f [mm]	E_f [MPa]
<i>S1</i>	1.39	9.34	160000
<i>S2</i>	1.40	10.03	171000

Figure 3.8 to Figure 3.11 show that the pullout force *versus* loaded end slip relationship obtained numerically (thick line) accurately fits the corresponding experimental envelop (shaded area) for both the *S1* and *S2* series.

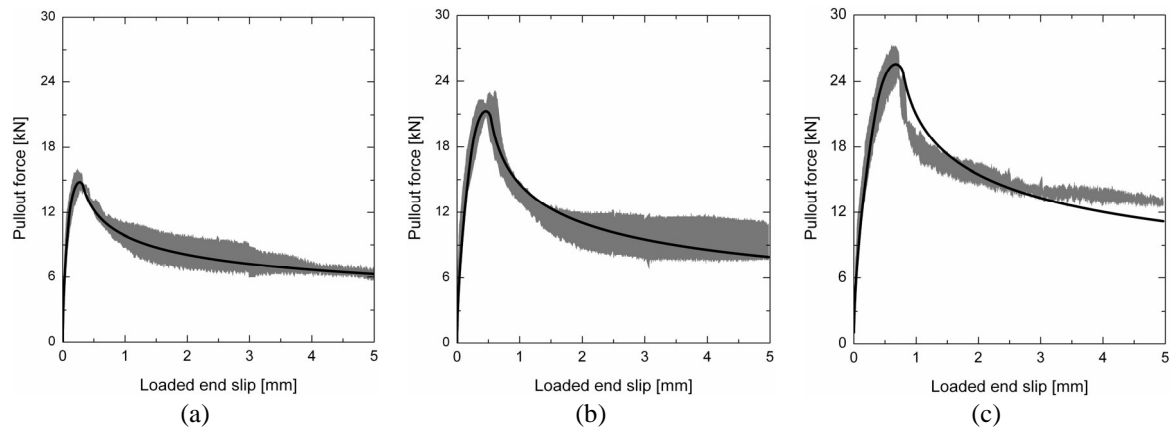


Figure 3.8 – Simulation of the series fcm35_Lb40_M (a), fcm35_Lb60_M (b) and fcm35_Lb80_M (c).

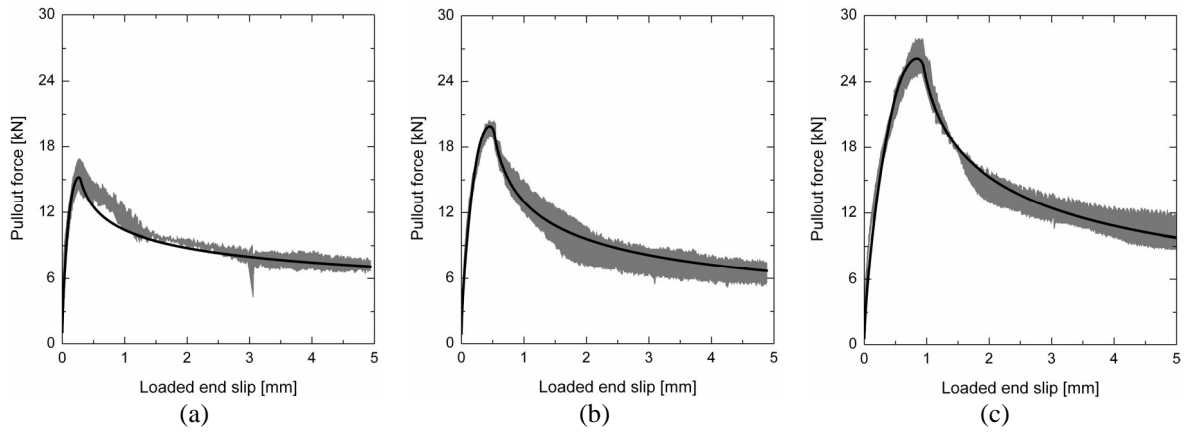


Figure 3.9 – Simulation of the series fcm45_Lb40_M (a), fcm45_Lb60_M (b) and fcm45_Lb80_M (c).

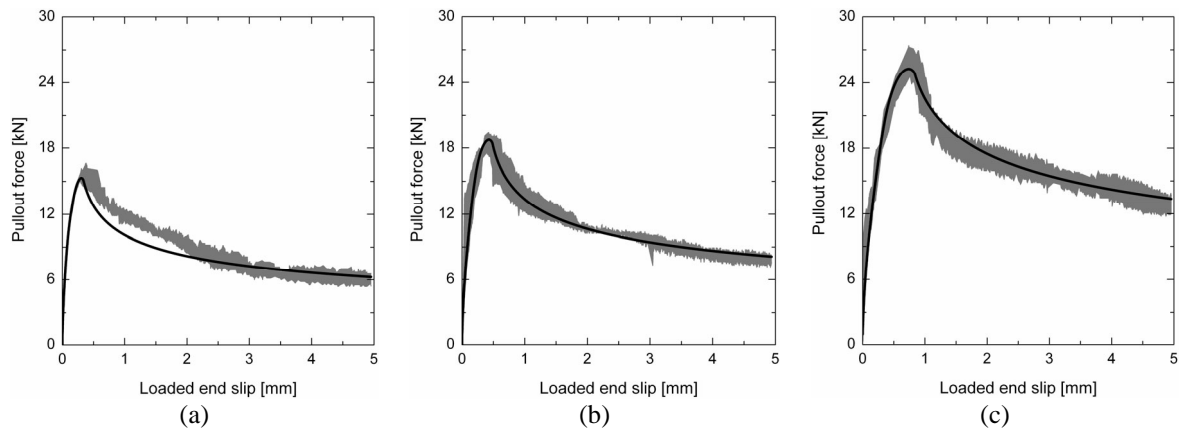


Figure 3.10 – Simulation of the series fcm70_Lb40_M (a), fcm70_Lb60_M (b) and fcm70_Lb80_M (c).

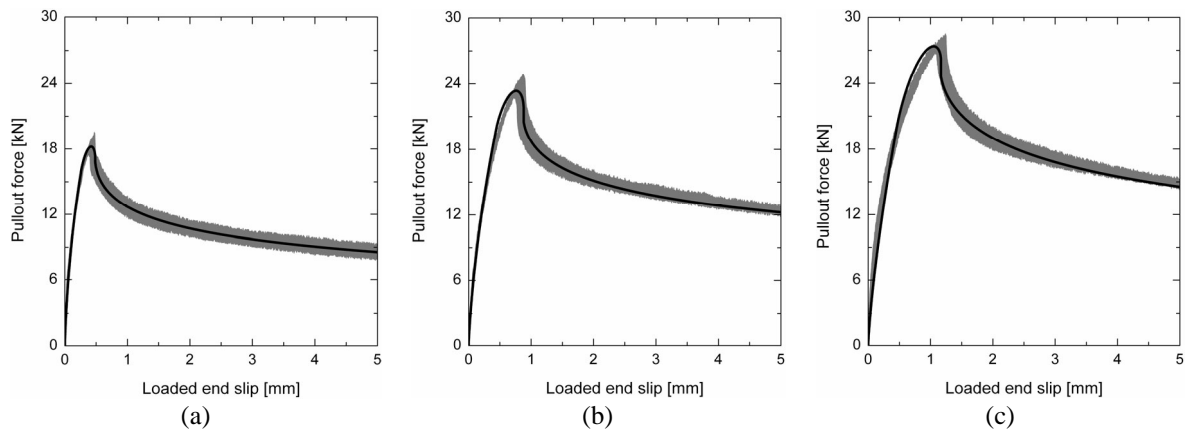


Figure 3.11 – Simulation of the series fcm40_Lb60_M (a), fcm40_Lb90_M (b) and fcm40_Lb120_M (c).

The values of the parameters defining the $\tau-s$ relationship and the values of the normalized errors obtained in each exhaustive search are included in Table 3.2 (*S1* series) and Table 3.3 (*S2* series). The normalized error, \bar{e} , is the ratio between e and the area under the experimental curve, being e the area between the experimental and numerical curves. From Table 3.2 and Table 3.3 the following observations can be pointed out:

- the normalized error in each series is acceptable;
- a reasonable coefficient of variation was obtained for the average bond strength. No correlation between the bond strength and the bond length can be observed in the *S1* series, whereas in the *S2* series τ_m decreases when the bond length increases;
- in the *S2* series, τ_m values were smaller than the values obtained in the *S1* series. The distinct width of the slit used in both series is probably the main justification of this behavior;
- a large scatter in the values of s_m , α (only in the *S1* series) and α' was obtained;
- as expected, s_m increases with the bond length, since the adhesive deformability was neglected in the present approach (see Section 3.1). In order to obtain a local $\tau-s$ relationship with more accuracy, an independent registration of the CFRP-adhesive slip, of the adhesive-concrete slip and of the adhesive deformability is required. However, the implementation of this procedure with the equipments available in most laboratories is considered too complex.

Table 3.2 – Values of the parameters defining the local bond stress-slip relationship of the *S1* series.

Series	s_m [mm]	τ_m [MPa]	α	α'	\bar{e} [%]
fcm35_Lb40_M	0.18	20.6	0.13	0.27	2.0
fcm35_Lb60_M	0.23	20.7	0.19	0.35	5.9
fcm35_Lb80_M	0.29	18.9	0.17	0.33	6.7
fcm45_Lb40_M	0.14	21.4	0.21	0.23	4.7
fcm45_Lb60_M	0.23	19.5	0.24	0.39	3.0
fcm45_Lb80_M	0.43	19.5	0.35	0.45	2.8
fcm70_Lb40_M	0.19	21.5	0.24	0.29	7.8
fcm70_Lb60_M	0.21	18.0	0.21	0.29	3.4
fcm70_Lb80_M	0.35	18.2	0.19	0.27	2.4
Average	0.25 (36.2 %)	19.8 (6.6 %)	0.21 (29.1 %)	0.32 (21.5 %)	–

Note: the values in parentheses are the coefficients of variation of the corresponding series.

Table 3.3 – Values of the parameters defining the local bond stress-slip relationship of the *S2* series.

Series	s_m [mm]	s_1 [mm]	τ_m [MPa]	α	α''	\bar{e} [%]
fcm40_Lb60_M	0.26	1.8	17.5	0.40	0.40	1.2
fcm40_Lb90_M	0.45	2.0	15.7	0.45	0.35	1.6
fcm40_Lb120_M	0.47	2.0	14.3	0.50	0.41	2.5
Average	0.39 (29.5 %)	1.9 (6.0 %)	15.8 (10.1 %)	0.45 (11.1 %)	0.39 (8.3 %)	–

Note: the values in parentheses are the coefficients of variation of the corresponding series.

3.4 ANCHORAGE LENGTH

Due to safety and economic reasons, the anchorage length L_{an} of the CFRP should be calculated, taking into account the requirements imposed by service and ultimate limit state analysis, i.e.,

$$L_{an} = \max \{ L_{an,S}, L_{an,U} \} \quad (4.8)$$

where $L_{an,S}$ and $L_{an,U}$ are the anchorage length that fulfills the requirements of the service and ultimate limit state analyses, respectively. In order to determine the anchorage length,

the local bond stress-slip relationship must be known. In the present analysis the average values of τ_m , α , α' , α'' and s' are used (see Table 3.2 and Table 3.3). For the bond lengths considered in the carried out experimental program, a linear relationship between s_m and L_b was observed. However, additional experimental research with larger bond lengths should be undertaken in order to establish a more general relationship. Taking into account the available experimental data, the linear relationships $s_m = 0.0042L_b$ and $s_m = 0.0043L_b$ are assumed, for the *S1* and *S2* series, respectively.

For load levels at the service limit state it is desired that the free end does not slip (Focacci et al. 2000, De Lorenzis et al. 2002). For this reason, the value of the pullout force at the onset of the free end slip, $N(\tilde{s}_l)$, is of practical interest. The value of $N(\tilde{s}_l)$ can be calculated with the method described in Section 3.2.2. Figure 3.12 depicts $N(\tilde{s}_l)$ and \tilde{s}_l as a function of the bond length, for the *S1* and *S2* series. The experimental results are signaled with circles. Comparing the bond performance of the *S1* and *S2* series (see Figure 3.12), it is evident that the former is considerably higher. Using these diagrams, the anchorage length for a given pullout service load, $L_{an,S}$, can be calculated. For instance, for a 200 mm bond length, the pullout force at the onset of free end slip is 53 kN and 17 kN for the *S1* and *S2* series, respectively. From this observation, and assuming a similar performance of the epoxy adhesive used in both series, higher bond efficiency can be obtained when the slit width decreases.

The prediction of the peak pullout force requires the availability of the entire local bond stress-slip relationship (see Figure 3.7). Figure 3.13 shows the relationship between the peak pullout force and the bond length, which can be used to determine $L_{an,U}$. The curve that best fits the experimental results and the curve that corresponds to the numerical results are slightly different (see Figure 3.13), since τ_m was considered independent of the bond length.

As a design example, a CFRP strip is assumed to be submitted to 10 kN and 30 kN in the service and ultimate limit state analysis, respectively. Using the charts represented in Figure 3.12(a) and Figure 3.13(a), the anchorage lengths thus determined are equal to

50 mm and 89 mm, in order to accomplish the service and ultimate limit state requirements, respectively. In order to satisfy both criteria, the latter value of the anchorage length must be adopted.

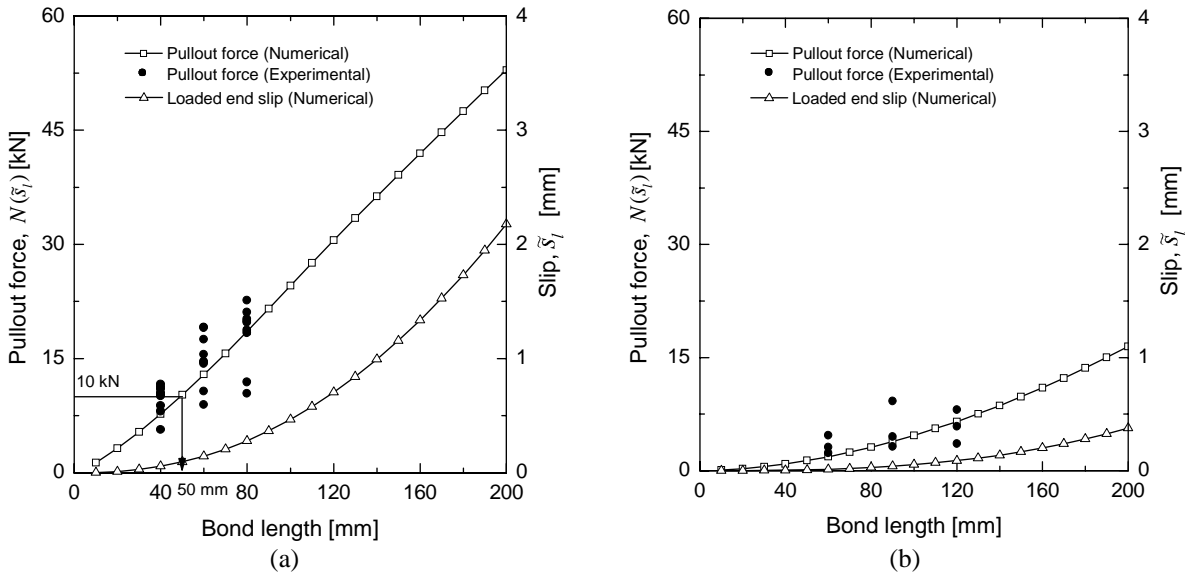


Figure 3.12 – Pullout force at the onset of the free end slip, $N(\tilde{s}_l)$ and loaded end slip, \tilde{s}_l , as a function of the bond length: (a) S1 series; (b) S2 series.

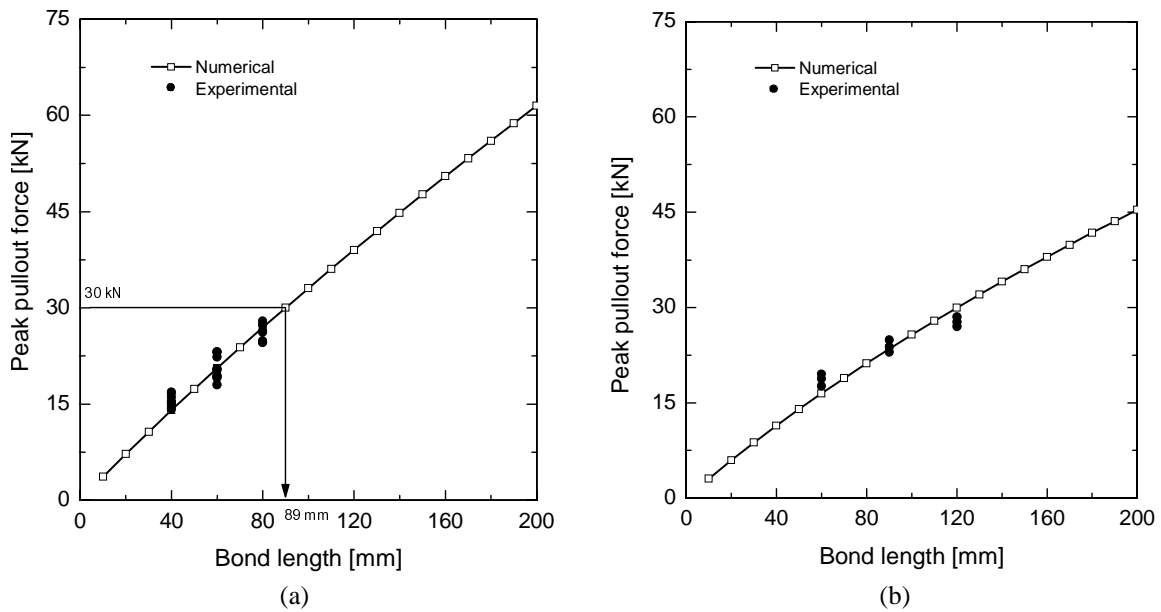


Figure 3.13 – Relationship between the pullout force and the bond length: (a) S1 series; (b) S2 series.

3.5 SUMMARY AND CONCLUSIONS

A research was developed with the aim of calibrating the analytical local bond stress-slip relationship between laminate strips of CFRP and concrete, considering a near-surface mounted strengthening technique. With this purpose, a numerical strategy was developed to solve the second-order differential equation that governs the slip phenomenon. The developed numerical method can also be used in the evaluation of the anchorage length of the CFRP which is required in both service and ultimate limit state analyses. Due to some limitations in the experimental equipments, the deformability of the epoxy adhesive, the CFRP-adhesive slip and the adhesive-concrete slip could not be measured, resulting in a local bond stress-slip relationship which is dependent on the bond length. In order to use this relationship in design practice, the influence of the bond length and thickness of the epoxy adhesive must be assessed experimentally.

CHAPTER 4

NUMERICAL MODEL FOR CONCRETE STRUCTURES STRENGTHENED WITH NEAR-SURFACE MOUNTED CFRP LAMINATE STRIPS

The finite element method is the basis of a powerful computational tool, which can be used to simulate the response of structures, structural components and materials, when submitted to a specified load. This tool has been extensively used to assess the behavior of concrete structures.

In order to simulate the structural response of concrete structures under the finite element framework, a mathematical idealization of the material behavior is required. This mathematical approach is commonly named constitutive or material model, and provides the relation between the stress and strain tensors in a material point of the body. In order to predict with high accuracy the behavior of concrete structures, appropriate constitutive models must be used. These constitutive models must be capable of simulating the most relevant nonlinear phenomena of the intervening materials.

The nonlinear fracture mechanics theory has been used to simulate the quasi-brittle failure of concrete (ACI 1991, ACI 1997). The discrete and the smeared crack concepts are the most used to model the concrete fracture under the framework of the finite element method. For concrete structures with a reinforcement ratio that assures crack stabilization, the smeared crack approach is more appropriate than the discrete approach, since several cracks can be formed in the structure. The discrete approach is especially suitable to simulate concrete structures where the failure is governed by the occurrence of a small number of cracks with a path that can be predicted. The discrete approach is not treated in the present work. Nevertheless, a comprehensive description of the discrete approach can be found elsewhere, e.g., Ngo and Scordelis (1967), Hillerborg et al. (1976), Rots (1988) and Bittencourt et al. (1992).

In smeared crack models, the fracture process is initiated when the maximum principal stress in a material point exceeds its tensile strength. The crack propagation is mainly controlled by the shape of the tensile-softening diagram and the material fracture energy. In order to assure mesh objectivity, the energy dissipated in the crack propagation process is associated with a characteristic length of the finite element (Bazant and Oh 1983). In the original smeared crack or single-fixed smeared crack concept, the orientation of the crack, i.e., the direction which is normal to the crack plane is coincident with the maximum principal stress orientation at crack initiation, and remains fixed throughout the loading process. However, due to aggregate interlock and dowel action of the reinforcement (Chen 1982), the principal stresses can change their orientation and, once more, exceed the tensile strength. In this case, the single-fixed smeared crack approach predicts a numerical response that is stiffer than the experimental observations. To avoid this inconvenience, rotating single smeared crack or multi-fixed smeared crack models have been developed. In the former, the local crack coordinate system is continuously rotating with the modification of the direction of the principal axes. In the multi-fixed smeared crack models, several fixed smeared cracks are allowed to form, according to a crack initiation criterion.

Plasticity theory has been extensively used to model the concrete behavior, particularly under compressive states of stress (ASCE 1982, Chen and Han 1988). Plasticity theory is based on a micromechanical or a phenomenological approach. In the micromechanical approach, also named fundamental approach, the constitutive relations are established for the microstructural behavior. In contrast, the phenomenological approach, also known as the mathematical theory of plasticity, establishes the constitutive model directly based on observed features from experimental tests. Plasticity theory is a natural constitutive description for metals (Hill 1950), but it can also be used for cementitious materials. In the 1980s several tools were developed for mathematical plasticity, e.g., implicit Euler backward algorithms and consistent tangent operators (e.g., Ortiz and Popov 1985, Simo and Taylor 1985), which made this theory even more attractive to model the concrete behavior.

Hybrid models derived from fracture mechanics and plasticity theories have been proposed by several researchers. In these models, fracture mechanics theory is used to

simulate the tensile post-cracking behavior of concrete, whereas plasticity theory is used to simulate its compressive behavior. Elasto-plastic multi-fixed smeared crack models seem to be suitable for the simulation of concrete structures, but due to their conceptual complexities and severe computational difficulties, only a few researchers were successful in the implementation of these models (de Borst and Nauta 1985, Crisfield and Wills 1989, Barros 1995).

Interface elements are commonly used to model geometrical discontinuities. In the context of concrete structures, interface elements can be used to model discrete cracking (Ngo and Scordelis 1967, Rots 1988), aggregate interlock (Feenstra et al. 1990) and bond between steel reinforcement and concrete (Ingraffea et al. 1984, Mehlhom et al. 1985, Lundgren and Gylltoft 2000, Girard and Bastien 2002). Interface elements have also been used to model the interface between CFRP and concrete (Silva 1999, Henriques et al. 2001, Wong and Vecchio 2003).

The numerical tools developed for the simulation of concrete structures strengthened with near-surface mounted CFRP laminate strips are detailed in this chapter. These tools include the development of constitutive models for the simulation of concrete and the CFRP-concrete interface, as well as a finite element formulation for interface elements. In the first part of this chapter, the solution procedures used in nonlinear finite element analysis, and also the most significant aspects of the developed finite element computer code are briefly described. Next, all relevant aspects of the developed elasto-plastic multi-fixed smeared crack model are described in detail. The description of the model is divided in three parts: the first part deals with the smeared crack model (Section 4.2); the second describes the elasto-plastic model (Section 4.3); and, finally, the third part presents the elasto-plastic multi-fixed smeared crack model (Section 4.4). Finally, a finite element formulation for interface elements, as well as the corresponding constitutive model are presented. The main purpose of this model is the simulation of the nonlinear behavior of the interface between CFRP and concrete. All the developed numerical tools are validated with results available in the literature and with the experimental results presented in Chapter 2.

4.1 NONLINEAR FINITE ELEMENT ANALYSIS

In the first part of this section, a brief introduction to the nonlinear analysis of structures using the finite element method is given. A comprehensive description of this method can be found elsewhere, e.g., Zienkiewicz and Taylor (1989, 1991) and Bathe (1996). In the second part of this section, the finite element computer code used in this study is briefly described.

4.1.1 Iterative techniques for the solution of nonlinear problems

The displacement formulation of the finite element method leads to (Zienkiewicz and Taylor 1989)

$$\underline{K} \underline{a} = \underline{F} \quad (4.1)$$

where \underline{K} is the stiffness matrix, \underline{a} is the vector of the nodal displacements and \underline{F} is the vector of the nodal forces which are equivalent to the loads acting on the finite element. The stiffness matrix can be computed with the following expression

$$\underline{K} = \int_V \underline{B}^T \underline{D} \underline{B} dV \quad (4.2)$$

where \underline{D} is the constitutive matrix, \underline{B} is a matrix that depends on the finite element type and V is the volume of the finite element. Commonly, numerical integration is used to evaluate the integral in (4.2). When Gaussian or Newton-Cotes quadrature is adopted, the integrand function is evaluated in predefined integration points.

In linear elasticity equation (4.1) corresponds to a system of linear equations, whose solution can be obtained using several techniques. The most common algorithms are based on direct methods, such as Gaussian elimination (Zienkiewicz and Taylor 1989) or iterative methods, like the conjugate gradient method (Azevedo and Barros 1990).

In the context of nonlinear analysis, equation (4.1) is no longer linear, since the stiffness matrix depends on the values of the displacements, \underline{a} . In order to obtain the

evolution of the structural response, \underline{F} must be applied in small steps. In the present work the total load at the end of each step is named combination. The solution at combination n can be computed by solving the system of nonlinear equations,

$$\underline{\Psi}_n = \underline{\Psi}(\underline{a}_n) = \underline{F}_n - \underline{F}'(\underline{a}_n) = \underline{0} \quad (4.3)$$

where $\underline{\Psi}_n$ is the residual force vector, which is calculated as the difference between $\underline{F}_n = \underline{F}_{n-1} + \Delta\underline{F}_n$ and the internal equivalent nodal forces, $\underline{F}'(\underline{a}_n)$. Equation (4.3) can be solved by the Newton-Raphson method. The first two terms of the Taylor series expansion of $\underline{\Psi}(\underline{a}_n)$ can be used in (4.3) as an approximation, yielding

$$\underline{\Psi}(\underline{a}_n^q) \approx \underline{\Psi}(\underline{a}_n^{q-1}) + \left(\frac{\partial \underline{\Psi}}{\partial \underline{a}} \right)_n^{q-1} \delta \underline{a}_n^q = \underline{0} \quad (4.4)$$

In this equation q is the iteration counter. The initial solution of the Newton-Raphson method is $\underline{a}_n^0 = \underline{a}_{n-1}$. In equation (4.4)

$$\left(\frac{\partial \underline{\Psi}}{\partial \underline{a}} \right)_n^{q-1} = - \left(\frac{\partial \underline{F}'}{\partial \underline{a}} \right)_n^{q-1} = - (\underline{K}_T)_n^{q-1} \quad (4.5)$$

is the Jacobian matrix, which in this context corresponds to the tangential stiffness matrix. The iterative correction $\delta \underline{a}_n^q$ is obtained by solving the system of linear equations (4.4), i.e.,

$$(\underline{K}_T)_n^{q-1} \delta \underline{a}_n^q = \underline{\Psi}(\underline{a}_n^{q-1}) \quad (4.6)$$

The vector of the displacements is updated with

$$\underline{a}_n^q = \underline{a}_{n-1} + \Delta \underline{a}_n^q = \underline{a}_n^{q-1} + \delta \underline{a}_n^q \quad (4.7)$$

where

$$\Delta \underline{a}_n^q = \sum_{i=1}^q \delta \underline{a}_n^i \quad (4.8)$$

The Newton-Raphson method is illustrated in Figure 4.1.

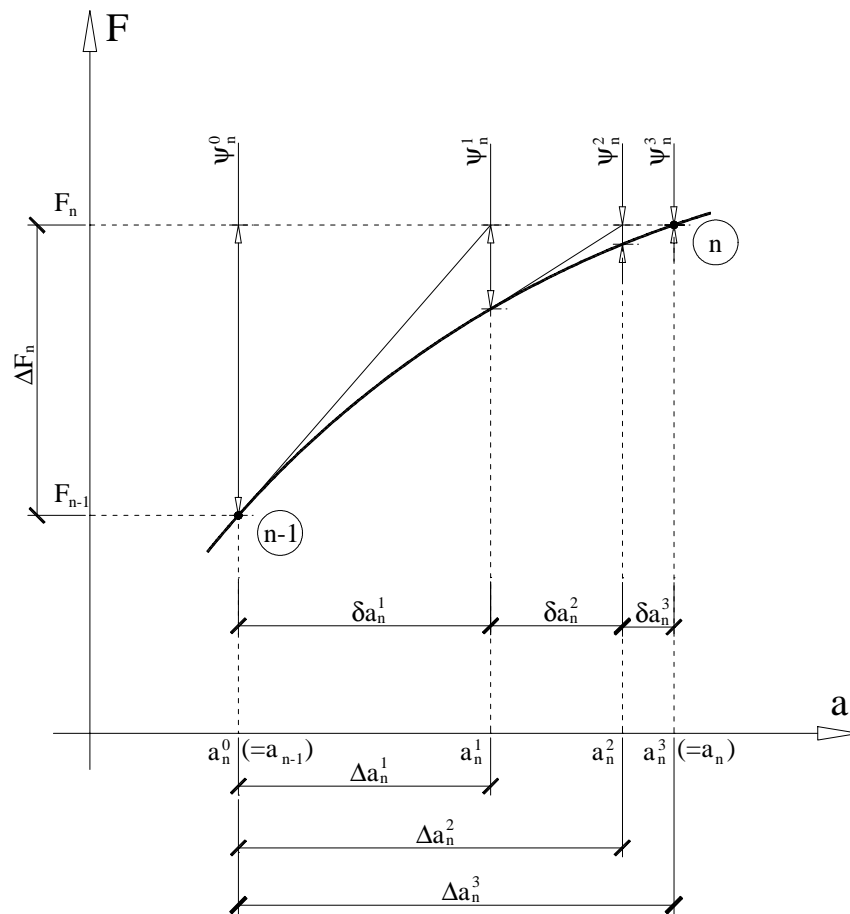


Figure 4.1 – Newton-Raphson method.

The iterative procedure described above is interrupted when a certain parameter becomes smaller than a predefined tolerance. The convergence criterion can be based on the force norm, the displacement norm or the energy norm (Zienkiewicz and Taylor 1991). In the present work a force norm is adopted, and the iterative procedure is successfully terminated when the following condition is verified

$$\frac{\sqrt{(\underline{\Psi}_n^i)^T \underline{\Psi}_n^i}}{\sqrt{(\underline{F}_n)^T \underline{F}_n}} < 10^{-3} \quad (4.9)$$

In the incremental-iterative procedure two stress update strategies were implemented, which lead to a path dependent (PD) or to a path independent (PI) behaviors (see Figure 4.2 and Figure 4.3). In the former (PD) the iterative variation of the displacements of the current iteration, $\delta \underline{a}_n^q$, is calculated using information of the previous iteration, $q-1$. The new stress state, $\underline{\sigma}^q$, is calculated as an update of the stress state at the previous iteration, $\underline{\sigma}^{q-1}$ (see Figure 4.2). When a path independent (PI) strategy is adopted, the iterative variation of the displacements of the current iteration, $\delta \underline{a}_n^q$, is also calculated using the information of the previous iteration, $q-1$. The new stress state, $\underline{\sigma}^q$, is calculated as an update of the stress state at the end of the iterative process of the previous combination, $\underline{\sigma}_{n-1}$ (see Figure 4.3).

1. Calculate the iterative displacements: $\underline{K}_T^{q-1} \delta \underline{a}^q = \underline{\psi}^{q-1}$
2. Calculate the iterative strain: $\delta \underline{\epsilon}^q = \underline{B} \delta \underline{a}^q$
3. Calculate the iterative stress: $\delta \underline{\sigma}^q = \underline{D}_T \delta \underline{\epsilon}^q$
4. Update the stress: $\underline{\sigma}^q = \underline{\sigma}^{q-1} + \delta \underline{\sigma}^q$

Figure 4.2 – Path dependent strategy.

1. Calculate the iterative displacements: $\underline{K}_T^{q-1} \delta \underline{a}^q = \underline{\psi}^{q-1}$
2. Update the incremental displacements: $\Delta \underline{a}^q = \Delta \underline{a}^{q-1} + \delta \underline{a}^q$
3. Calculate the incremental strain: $\Delta \underline{\epsilon}^q = \underline{B} \Delta \underline{a}^q$
4. Calculate the incremental stress: $\Delta \underline{\sigma}^q = \underline{D}_T \Delta \underline{\epsilon}^q$
5. Update the stress: $\underline{\sigma}^q = \underline{\sigma}_{n-1} + \Delta \underline{\sigma}^q$

Figure 4.3 – Path independent strategy.

According to Crisfield (1991), the path dependent strategy is not recommended since it may lead to “spurious unloading” during the iterative process. In spite of both strategies

(PD and PI) being available in the finite element computer code used in the present study, only the latter is adopted in the numerical simulations.

4.1.2 FEMIX computer code

All the numerical models and strategies described in the present work were implemented in version 4.0 of the FEMIX computer code (Azevedo et al. 2003). This version started to be developed in late 2000, by Álvaro Azevedo, Joaquim Barros and José Sena Cruz. Two years later Ventura Gouveia joined the original team. The present version also includes the contributions of Alberto Ribeiro (2004) and Vitor Cunha (2004).

Table 4.1 lists the types of finite elements available in the present version of the computer code. For some types of elements a materially nonlinear analysis can be performed. Several nonlinear models are available, in order to simulate concrete and steel. The systems of nonlinear equations arising from the incremental-iterative procedure are solved by the Newton-Raphson method (see Section 4.1.1). The analyses can be performed using a path dependent or a path independent strategy, with load or displacement control. Other techniques, such as arc-length control or indirect displacement control, are also available.

In the present study the following types of elements were used: plane stress elements to simulate the concrete, embedded cable and cable elements to simulate the reinforcements, and line interface elements to model the interface between the reinforcement and concrete.

Table 4.1 – Types of finite elements available in FEMIX 4.0 computer code.


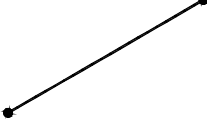
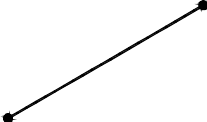
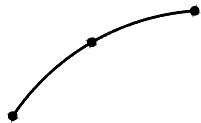
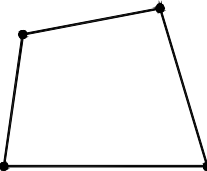
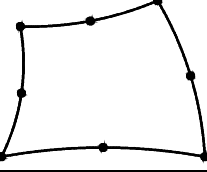
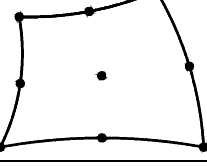
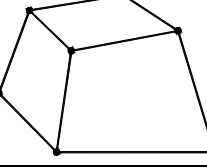
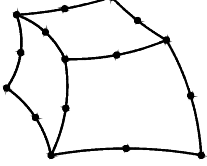
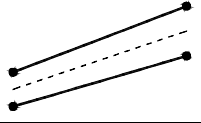
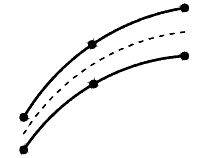
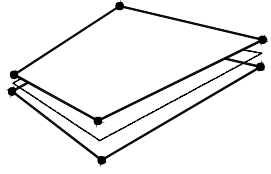
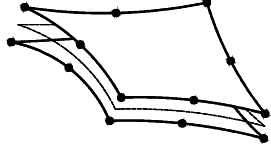
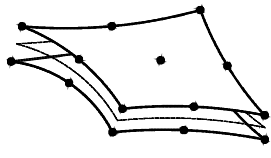
Applicability	Description	Shape
Point spring (2D or 3D)	1-node	
Truss (2D or 3D) Beam (2D or 3D)	Linear 2-node	
Timoshenko beam (2D or 3D) Embedded cable (2D or 3D) Cable (2D or 3D) Line spring (2D or 3D)	Linear 2-node	
	Quadratic 3-node	
Plane stress (2D) Mindlin slab (2D) Mindlin shell (3D) Ahmad shell (3D) Surface spring (2D or 3D)	Lagrangian 4-node	
	Serendipity 8-node	
	Lagrangian 9-node	
Solid (3D)	Lagrangian 8-node	
	Serendipity 20-node	
Line interface (2D)	Linear 4-node	
	Quadratic 6-node	

Table 4.1 (cont.) – Types of finite elements available in FEMIX 4.0 computer code.

Surface interface (3D)	Lagrangian 8-node	
	Serendipity 16-node	
	Lagrangian 18-node	

4.2 CRACK CONCEPTS

In this section, firstly, the single-fixed smeared crack concept is described, followed by the generalization to the multi-fixed smeared crack concept. The most relevant algorithmic aspects are detailed. Finally, the developed numerical model is validated using results available in the literature.

4.2.1 Smeared crack concept

After crack initiation, the basic assumption of smeared crack models, is the decomposition of the incremental strain vector, $\Delta \underline{\varepsilon}$, into an incremental crack strain vector, $\Delta \underline{\varepsilon}^{cr}$, and an incremental strain vector of the concrete between cracks, $\Delta \underline{\varepsilon}^{co}$:

$$\Delta \underline{\varepsilon} = \Delta \underline{\varepsilon}^{cr} + \Delta \underline{\varepsilon}^{co} \quad (4.10)$$

The decomposition expressed by (4.10) has been adopted by several researchers (Litton 1974, Bazant and Gambarova 1980, de Borst and Nauta 1985, Rots et al. 1985, Rots 1988).

4.2.1.1 Crack strains and crack stresses

Figure 4.4 shows the morphology of a crack for the case of plane stress. Two relative displacements define the relative movement of the crack lips: the crack opening displacement, w , and the crack sliding displacement, s . Axes n and t define the local coordinate system of the crack ($CrCS$), being n and t the crack normal and tangential directions, respectively.

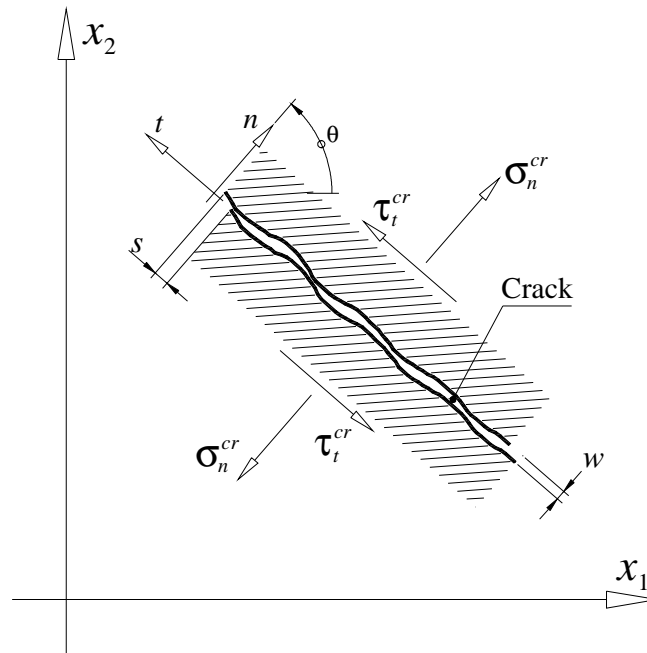


Figure 4.4 – Crack stresses, relative displacements and local coordinate system of the crack.

In the smeared crack approach w is replaced with a crack normal strain defined in $CrCS$, ε_n^{cr} , and s is replaced with a crack shear strain also defined in $CrCS$, γ_t^{cr} . The same approach can be applied to the incremental normal and shear crack strains ($\Delta\varepsilon_n^{cr}$ and $\Delta\gamma_t^{cr}$). The incremental crack strain vector in $CrCS$, $\Delta\underline{\varepsilon}_t^{cr}$, is defined by

$$\Delta\underline{\varepsilon}_t^{cr} = \begin{bmatrix} \Delta\varepsilon_n^{cr} & \Delta\gamma_t^{cr} \end{bmatrix}^T \quad (4.11)$$

The incremental crack strain vector in the global coordinate system (GCS), $\Delta\underline{\varepsilon}^{cr}$, has the following three components,

$$\Delta \underline{\varepsilon}^{cr} = \left[\Delta \varepsilon_1^{cr} \quad \Delta \varepsilon_2^{cr} \quad \Delta \gamma_{12}^{cr} \right]^T \quad (4.12)$$

The transformation of the incremental crack strain vector from *CrCS* to *GCS* reads

$$\begin{bmatrix} \Delta \varepsilon_1^{cr} \\ \Delta \varepsilon_2^{cr} \\ \Delta \gamma_{12}^{cr} \end{bmatrix} = \begin{bmatrix} \cos^2 \theta & -\sin \theta \cos \theta \\ \sin^2 \theta & \sin \theta \cos \theta \\ 2 \sin \theta \cos \theta & \cos^2 \theta - \sin^2 \theta \end{bmatrix} \begin{bmatrix} \Delta \varepsilon_n^{cr} \\ \Delta \gamma_t^{cr} \end{bmatrix} \quad (4.13)$$

or

$$\Delta \underline{\varepsilon}^{cr} = \left[\underline{T}^{cr} \right]^T \Delta \underline{\varepsilon}_\ell^{cr} \quad (4.14)$$

being $\left[\underline{T}^{cr} \right]^T$ the crack strain transformation matrix and θ the angle between x_1 and n (see Figure 4.4). The incremental local crack stress vector, $\Delta \underline{\sigma}_\ell^{cr}$, is defined by

$$\Delta \underline{\sigma}_\ell^{cr} = \left[\Delta \sigma_n^{cr} \quad \Delta \tau_t^{cr} \right]^T \quad (4.15)$$

where $\Delta \sigma_n^{cr}$ and $\Delta \tau_t^{cr}$ are the incremental crack normal and shear stresses in the crack, respectively. The relationship between $\Delta \underline{\sigma}_\ell^{cr}$ and the incremental stress vector (in *GCS*), $\Delta \underline{\sigma}$, can be defined as

$$\begin{bmatrix} \Delta \sigma_n^{cr} \\ \Delta \tau_t^{cr} \end{bmatrix} = \begin{bmatrix} \cos^2 \theta & \sin^2 \theta & 2 \sin \theta \cos \theta \\ -\sin \theta \cos \theta & \sin \theta \cos \theta & \cos^2 \theta - \sin^2 \theta \end{bmatrix} \begin{bmatrix} \Delta \sigma_1 \\ \Delta \sigma_2 \\ \Delta \tau_{12} \end{bmatrix} \quad (4.16)$$

or

$$\Delta \underline{\sigma}_\ell^{cr} = \underline{T}^{cr} \Delta \underline{\sigma} \quad (4.17)$$

4.2.1.2 Concrete constitutive law

Assuming linear elastic behavior for the concrete between cracks (undamaged concrete), the constitutive relationship between $\Delta \underline{\underline{\epsilon}}^{co}$ and $\Delta \underline{\underline{\sigma}}$ is given by,

$$\Delta \underline{\underline{\sigma}} = \underline{\underline{D}}^{co} \Delta \underline{\underline{\epsilon}}^{co} \quad (4.18)$$

where $\underline{\underline{D}}^{co}$ is the constitutive matrix according to Hooke's law,

$$\underline{\underline{D}}^{co} = \frac{E_c}{1-\nu_c^2} \begin{bmatrix} 1 & \nu_c & 0 \\ \nu_c & 1 & 0 \\ 0 & 0 & (1-\nu_c)/2 \end{bmatrix} \quad (4.19)$$

being E_c and ν_c the Young's modulus and Poisson's ratio of plain concrete, respectively.

4.2.1.3 Constitutive law of the crack

In a similar way, a relationship between $\Delta \underline{\underline{\sigma}}_l^{cr}$ and $\Delta \underline{\underline{\epsilon}}_l^{cr}$ is established to simulate the crack opening and the shear sliding using,

$$\Delta \underline{\underline{\sigma}}_l^{cr} = \underline{\underline{D}}^{cr} \Delta \underline{\underline{\epsilon}}_l^{cr} \quad (4.20)$$

where $\underline{\underline{D}}^{cr}$ is the crack constitutive matrix including mode I and mode II crack fracture parameters.

4.2.1.4 Constitutive law of the cracked concrete

Combining the equations presented in the previous sections, a constitutive law for cracked concrete is obtained. Hence, incorporating equations (4.10) and (4.14) into (4.18) yields,

$$\Delta \underline{\underline{\sigma}} = \underline{\underline{D}}^{co} \left(\Delta \underline{\underline{\epsilon}} - [\underline{\underline{T}}^{cr}]^T \Delta \underline{\underline{\epsilon}}_l^{cr} \right) \quad (4.21)$$

Pre-multiplying both members of equation (4.21) by \underline{T}^{cr} leads to

$$\underline{T}^{cr} \Delta \underline{\sigma} = \underline{T}^{cr} \underline{D}^{co} \Delta \underline{\epsilon} - \underline{T}^{cr} \underline{D}^{co} \left[\underline{T}^{cr} \right]^T \Delta \underline{\epsilon}_l^{cr} \quad (4.22)$$

Substituting (4.17) into the left side of equation (4.22) yields

$$\Delta \underline{\epsilon}_l^{cr} + \underline{T}^{cr} \underline{D}^{co} \left[\underline{T}^{cr} \right]^T \Delta \underline{\epsilon}_l^{cr} = \underline{T}^{cr} \underline{D}^{co} \Delta \underline{\epsilon} \quad (4.23)$$

Including (4.20) into the left side of equation (4.23), the following equation defining the incremental crack strain vector in *CrCS* is obtained

$$\Delta \underline{\epsilon}_l^{cr} = \left(\underline{D}^{cr} + \underline{T}^{cr} \underline{D}^{co} \left[\underline{T}^{cr} \right]^T \right)^{-1} \underline{T}^{cr} \underline{D}^{co} \Delta \underline{\epsilon} \quad (4.24)$$

The inclusion of (4.24) in (4.21) leads to the constitutive law of the cracked concrete, which reads

$$\Delta \underline{\sigma} = \left(\underline{D}^{co} - \underline{D}^{co} \left[\underline{T}^{cr} \right]^T \left(\underline{D}^{cr} + \underline{T}^{cr} \underline{D}^{co} \left[\underline{T}^{cr} \right]^T \right)^{-1} \underline{T}^{cr} \underline{D}^{co} \right) \Delta \underline{\epsilon} \quad (4.25)$$

or

$$\Delta \underline{\sigma} = \underline{D}^{crco} \Delta \underline{\epsilon} \quad (4.26)$$

where \underline{D}^{crco} is the following constitutive matrix for the cracked concrete

$$\underline{D}^{crco} = \underline{D}^{co} - \underline{D}^{co} \left[\underline{T}^{cr} \right]^T \left(\underline{D}^{cr} + \underline{T}^{cr} \underline{D}^{co} \left[\underline{T}^{cr} \right]^T \right)^{-1} \underline{T}^{cr} \underline{D}^{co} \quad (4.27)$$

4.2.1.5 Crack fracture parameters

In the present model, the crack constitutive matrix, \underline{D}^{cr} , is assumed to be diagonal

$$\underline{D}^{cr} = \begin{bmatrix} D_I^{cr} & 0 \\ 0 & D_{II}^{cr} \end{bmatrix} \quad (4.28)$$

In this matrix D_I^{cr} and D_{II}^{cr} are the mode I and mode II stiffness modulus associated with the crack behavior.

The crack-dilatancy effect and the shear-normal stress coupling is not considered in the present approach. The shear-normal stress coupling, however, may be simulated indirectly, allowing non-orthogonal cracks to form and relating D_{II}^{cr} with the crack normal strain (Rots 1988). This strategy is adopted in the present model.

The crack initiation in the present model is governed by the Rankine yield surface (see Figure 4.5), i.e., when the maximum principal stress, σ_I , exceeds the uniaxial tensile strength, f_{cr} , a crack is formed. This assumption is justified by the experimental results obtained by Kupfer et al. (1969) when the tensile cracking is not accompanied by significant lateral compression.

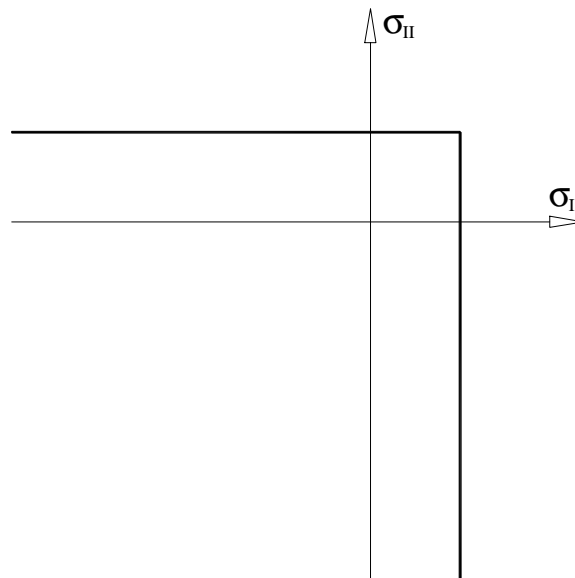


Figure 4.5 – Rankine yield surface in the 2D principal stress space.

According to Bazant and Oh (1983), the most suitable approach to simulate the crack propagation under the finite element framework is by taking into account the concrete fracture parameters, namely, the shape of the tensile-softening diagram and the fracture energy.

Two distinct tensile-softening diagrams are available in the developed computational code: tri-linear and exponential diagrams (see Figure 4.6). The tri-linear diagram shown in Figure 4.6(a) is defined by the following expressions

$$\sigma_n^{cr}(\varepsilon_n^{cr}) = \begin{cases} f_{ct} + D_{I,1}^{cr} \varepsilon_n^{cr} & \text{if } 0 < \varepsilon_n^{cr} \leq \xi_1 \varepsilon_{n,ult}^{cr} \\ \alpha_1 f_{ct} + D_{I,2}^{cr} (\varepsilon_n^{cr} - \xi_1 \varepsilon_{n,ult}^{cr}) & \text{if } \xi_1 \varepsilon_{n,ult}^{cr} < \varepsilon_n^{cr} \leq \xi_2 \varepsilon_{n,ult}^{cr} \\ \alpha_2 f_{ct} + D_{I,3}^{cr} (\varepsilon_n^{cr} - \xi_2 \varepsilon_{n,ult}^{cr}) & \text{if } \xi_2 \varepsilon_{n,ult}^{cr} < \varepsilon_n^{cr} \leq \varepsilon_{n,ult}^{cr} \\ 0 & \text{if } \varepsilon_n^{cr} > \varepsilon_{n,ult}^{cr} \end{cases} \quad (4.29)$$

with,

$$D_{I,i}^{cr} = -k_i \frac{h f_{ct}^2}{G_f} \quad (4.30)$$

where

$$\begin{aligned} k_1 &= \frac{(1 - \alpha_1)(\xi_1 + \alpha_1 \xi_2 - \alpha_2 \xi_1 + \alpha_2)}{2\xi_1} \\ k_2 &= \frac{(\alpha_1 - \alpha_2)(\xi_1 + \alpha_1 \xi_2 - \alpha_2 \xi_1 + \alpha_2)}{2(\xi_2 - \xi_1)} \\ k_3 &= \frac{\alpha_2(\xi_1 + \alpha_1 \xi_2 - \alpha_2 \xi_1 + \alpha_2)}{2(1 - \xi_2)} \end{aligned} \quad (4.31)$$

The ultimate crack normal strain, $\varepsilon_{n,ult}^{cr}$, is given by,

$$\varepsilon_{n,ult}^{cr} = k_4 \frac{G_f}{f_{ct} h} \quad (4.32)$$

where

$$k_4 = \frac{2}{\xi_1 + \alpha_1 \xi_2 - \alpha_2 \xi_1 + \alpha_2} \quad (4.33)$$

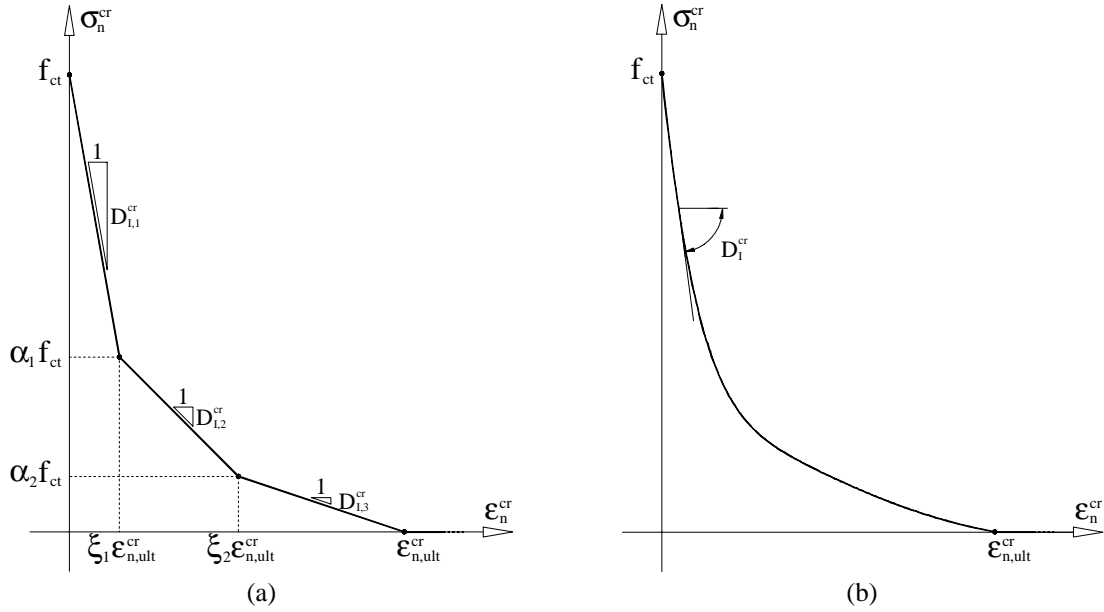


Figure 4.6 – Tensile-softening diagrams: tri-linear (a) and exponential (b).

The exponential softening diagram proposed by Cornelissen et al. (1986) (see Figure 4.6(b)) is defined by

$$\frac{\sigma_n^{cr}(\epsilon_n^{cr})}{f_{ct}} = \begin{cases} \left(1 + \left(c_1 \frac{\epsilon_n^{cr}}{\epsilon_{n,ult}^{cr}} \right)^3 \right) \exp\left(-c_2 \frac{\epsilon_n^{cr}}{\epsilon_{n,ult}^{cr}} \right) - \frac{\epsilon_n^{cr}}{\epsilon_{n,ult}^{cr}} (1 + c_1^3) \exp(-c_2) & \text{if } 0 < \epsilon_n^{cr} < \epsilon_{n,ult}^{cr} \\ 0 & \text{if } \epsilon_n^{cr} \geq \epsilon_{n,ult}^{cr} \end{cases} \quad (4.34)$$

where $c_1 = 3.0$ and $c_2 = 6.93$. The ultimate crack normal strain, $\epsilon_{n,ult}^{cr}$, is obtained from,

$$\epsilon_{n,ult}^{cr} = \frac{1}{k} \frac{G_f}{f_{ct} h} \quad (4.35)$$

where

$$k = \left[\frac{1}{c_2} \left[1 + 6 \left(\frac{c_1}{c_2} \right)^3 \right] - \left[\frac{1}{c_2} + c_1^3 \left(\frac{1}{c_2} + \frac{3}{c_2^2} + \frac{6}{c_2^3} + \frac{6}{c_2^4} \right) + \frac{1}{2} (1 + c_1^3) \right] \right] \exp(-c_2) \quad (4.36)$$

The mode I stiffness modulus is calculated with the following expression

$$D_I^{cr} = f_{ct} \left[3 \left(c_1 \frac{\epsilon_n^{cr}}{\epsilon_{n,ult}^{cr}} \right)^2 \frac{c_1}{\epsilon_{n,ult}^{cr}} \exp \left(-c_2 \frac{\epsilon_n^{cr}}{\epsilon_{n,ult}^{cr}} \right) + \exp \left(-c_2 \frac{\epsilon_n^{cr}}{\epsilon_{n,ult}^{cr}} \right) \left(-c_2 \frac{\epsilon_n^{cr}}{\epsilon_{n,ult}^{cr}} \right) \left[1 + \left(c_1 \frac{\epsilon_n^{cr}}{\epsilon_{n,ult}^{cr}} \right)^3 \right] - \frac{1 + c_1^3}{\epsilon_{n,ult}^{cr}} \exp(-c_2) \right] \quad (4.37)$$

The concrete fracture energy, G_f , is the energy required to propagate a tensile crack of unit area. Generally, G_f is assumed to be a material parameter and according to the CEB-FIB (1993) it can be estimated from the concrete compressive strength, f_c , and maximum aggregate size.

In the smeared crack approach, the fracture zone is distributed in a certain width of the finite element, which is designated crack band-width, h , as indicated in Figure 4.7. In this model a constant strain distribution in the width h is assumed. To assure mesh objectivity, the crack band-width must be mesh dependent. Several researchers have proposed different ways to estimate h (Bazant and Oh 1983, Rots et al 1985, Leibengood et al. 1986, Oñate et al. 1987, Dahlblom et al. 1990, Oliver et al. 1990, Cervenka et al. 1990, Rots 1992, Feenstra 1993). In the present numerical model, the crack band-width can be estimated in three different ways: equal to the square root of the area of the finite element, equal to the square root of the area of the integration point or equal to a constant value. To avoid *snap-back instability*, the crack band-width is subjected to the following constraint (de Borst 1991),

$$h \leq \frac{G_f E_c}{b f_{ct}^2} \quad (4.38)$$

where $b = \max\{k_i\}$ for tri-linear softening diagram and $b = k(c_2 + (1 + c_1^3)\exp(-c_2))$ for exponential softening diagram.

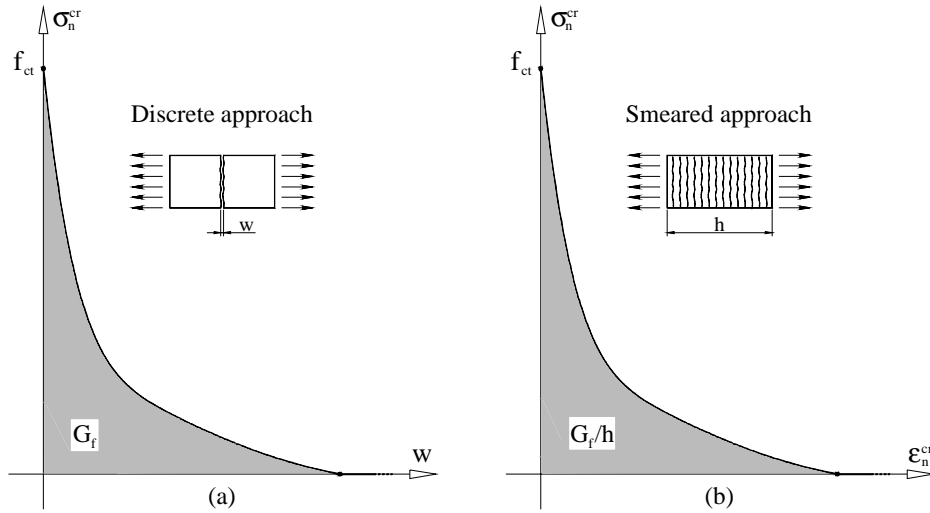


Figure 4.7 – Two distinct approaches to model the tensile-softening diagram: (a) discrete and (b) smeared crack models.

Applying the strain decomposition concept to the incremental shear strain, yields

$$\Delta\gamma = \Delta\gamma^{cr} + \Delta\gamma^{co} \quad (4.39)$$

or,

$$\frac{1}{\beta G_c} = \frac{1}{D_{II}^{cr}} + \frac{1}{G_c} \quad (4.40)$$

resulting

$$D_{II}^{cr} = \frac{\beta}{1 - \beta} G_c \quad (4.41)$$

The parameter β is called the shear retention factor and its value depends on the crack normal strain and on the ultimate crack normal strain (Rots 1988, Póvoas 1991, Barros 1995),

$$\beta = \left(1 - \frac{\varepsilon_n^{cr}}{\varepsilon_{n,ult}^{cr}} \right)^{p_1} \quad (4.42)$$

In this equation p_1 is a parameter that, currently, can assume the values of 1, 2 or 3 (Barros 1995). When $\varepsilon_n^{cr} = 0$ (closed crack) a full interlock is assumed. For a fully open crack ($\varepsilon_n^{cr} \geq \varepsilon_{n,ult}^{cr}$) the shear retention factor is equal to zero, resulting in a null shear stiffness modulus that corresponds to a negligible aggregate interlock.

4.2.2 Multi-fixed smeared crack concept

In the previous sections the concept of the fixed smeared crack model was described. In this model only one fixed smeared crack was allowed to form at each integration point. To be capable of simulating the formation of more than one fixed smeared crack, as well as to be not restricted to the particular case of two orthogonal cracks (Azevedo 1985, Póvoas 1991), the formulation was extended, resulting in the multi-fixed smeared crack model.

To deal with the eventual formation of n_{cr} cracks at each integration point, the generalized crack transformation matrix, \underline{T}^{cr} , and the crack constitutive matrix, \underline{D}^{cr} , adopt the following format

$$\underline{T}^{cr} = \left[\underline{T}_1^{cr}(\theta_1) \quad \underline{T}_2^{cr}(\theta_2) \quad \dots \quad \underline{T}_{n_{cr}}^{cr}(\theta_{n_{cr}}) \right]^T \quad (4.43)$$

$$\underline{D}^{cr} = \begin{bmatrix} \underline{D}_1^{cr} & \underline{0} & \dots & \underline{0} \\ \underline{0} & \underline{D}_2^{cr} & \dots & \underline{0} \\ \dots & \dots & \dots & \dots \\ \underline{0} & \underline{0} & \dots & \underline{D}_{n_{cr}}^{cr} \end{bmatrix} \quad (4.44)$$

In these matrices, $\underline{T}_i^{cr}(\theta_i)$ and \underline{D}_i^{cr} correspond to the crack transformation matrix and to the crack constitutive matrix of the i -th crack, respectively. Matrix \underline{D}^{cr} is diagonal since the sub-matrices \underline{D}_i^{cr} have null off-diagonal terms (see Section 4.2.1.5).

4.2.2.1 Crack initiation

Cracking occurs when the maximum principal stress exceeds the concrete uniaxial tensile strength, f_{ct} . After crack initiation, and assuming that the shear retention factor is non-null, i.e., the crack shear stresses can be transferred between the crack lips, the values and the orientation of the principal stresses can change during the loading process. For this reason the maximum principal stress in the concrete between cracks can also exceed f_{ct} . In the present work a new crack is initiated when the following two conditions are satisfied simultaneously:

- the maximum principal stress, σ_I , exceeds the uniaxial tensile strength, f_{ct} ;
- the angle between the direction of the existing cracks and the direction of σ_I , $\bar{\theta}_I$, exceeds the value of a predefined threshold angle, α_{th} .

Typically, the threshold angle varies between 30 and 60 degrees (de Borst and Nauta 1985). When the second condition is not verified (which means that the new crack is not initiated) the tensile strength is updated in order to avoid inconsistencies in the crack initiation process. With this strategy the updated tensile strength can significantly exceed the original concrete tensile strength (Rots 1988).

4.2.2.2 Crack evolution history

In a previously cracked integration point, the coupling between non-orthogonal cracks is simulated with fracture parameters associated to the new cracks. The fracture energy available for the next crack, G_f^{next} , is calculated with (Barros 1995)

$$G_f^{next} = (G_f - G_{f,a}) \left(\frac{\alpha}{\pi/2} \right)^{p_2} + G_{f,a} \quad (4.45)$$

where p_2 is a parameter that, currently, can assume the values of 1, 2 or 3, α is the angle (in radians) between the next and the previous crack and $G_{f,a}$ is the available fracture energy of the previous crack. Its value is calculated subtracting the fracture energy consumed by the previous crack, $G_{f,c}^{prev}$, from the concrete fracture energy (see Figure 4.8),

$$G_{f,a} = G_f - G_{f,c}^{prev} \quad (4.46)$$

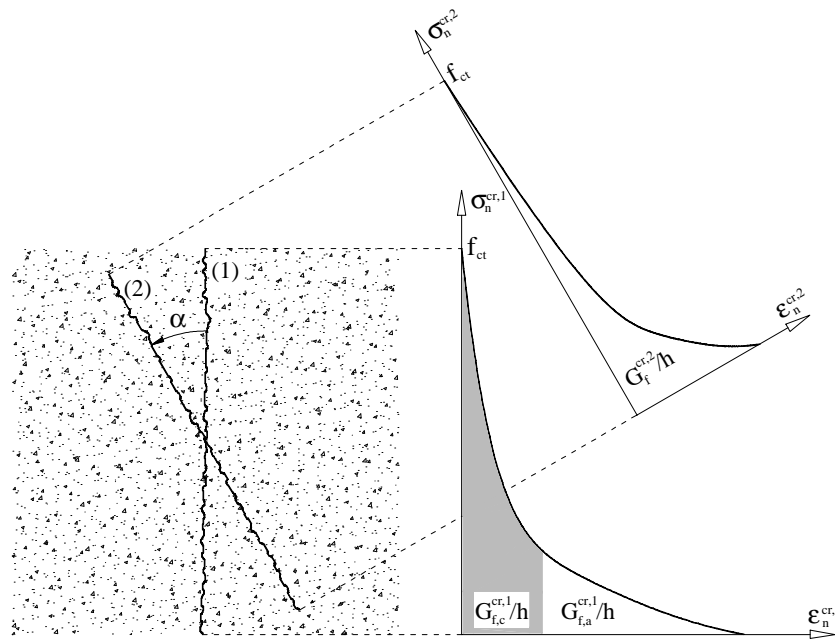


Figure 4.8 – Fracture energy available for the next crack.

4.2.3 Algorithmic aspects

In a multi-fixed smeared crack model, the consideration of all the crack status changes that may occur during the loading process of a concrete element, requires the implementation of several computational procedures. Otherwise the model becomes unreliable and inefficient for practical use (de Borst and Nauta 1985, Rots 1988, Crisfield and Wills 1989,

Barros 1995, Hofstetter and Mang 1995). The implementation of these algorithms in the FEMIX computer code is described below.

4.2.3.1 Stress update

When the strain field in a cracked integration point is submitted to an increment defined by $\Delta \underline{\varepsilon}_m$, the stress state of the integration point is also modified and must be updated ($\underline{\sigma}_m$).

The incremental relationship (4.17) can be written in terms of total stresses,

$$\underline{\sigma}_{\ell,m}^{cr} = \underline{T}_m^{cr} \underline{\sigma}_m \quad (4.47)$$

This equation is equivalent to

$$\underline{\sigma}_{\ell,m-1}^{cr} + \Delta \underline{\sigma}_{\ell,m}^{cr} = \underline{T}_m^{cr} (\underline{\sigma}_{m-1} + \Delta \underline{\sigma}_m) \quad (4.48)$$

Including (4.21) in (4.48) yields

$$\underline{\sigma}_{\ell,m-1}^{cr} + \Delta \underline{\sigma}_{\ell,m}^{cr} = \underline{T}_m^{cr} \left(\underline{\sigma}_{m-1} + \underline{D}^{co} \left(\Delta \underline{\varepsilon}_m - \left[\underline{T}_m^{cr} \right]^T \Delta \underline{\varepsilon}_{\ell,m}^{cr} \right) \right) \quad (4.49)$$

Equation (4.49) can be written as

$$\underline{\sigma}_{\ell,m-1}^{cr} + \Delta \underline{\sigma}_{\ell,m}^{cr} \left(\Delta \underline{\varepsilon}_{\ell,m}^{cr} \right) + \underline{T}_m^{cr} \underline{D}^{co} \left[\underline{T}_m^{cr} \right]^T \Delta \underline{\varepsilon}_{\ell,m}^{cr} - \underline{T}_m^{cr} \underline{\sigma}_{m-1} - \underline{T}_m^{cr} \underline{D}^{co} \Delta \underline{\varepsilon}_m = \underline{0} \quad (4.50)$$

where $\Delta \underline{\sigma}_{\ell,m}^{cr}$ depends on $\Delta \underline{\varepsilon}_{\ell,m}^{cr}$. The components of the incremental crack strain vector, $\Delta \underline{\varepsilon}_{\ell,m}^{cr}$, are the unknown variables of the nonlinear equations (4.50). This vector contains the two local strain components of the active cracks, i.e., non-closed cracks. To solve this equation two different methods were implemented: the Newton-Raphson and the fixed-point iteration methods (Chapra and Canale 1998). The methods exhibiting quadratic convergence, such as the Newton-Raphson method, are usually very efficient, but in some cases the solution cannot be obtained. In these cases the Newton-Raphson method is

replaced with the fixed-point iteration method which exhibits linear convergence. In the following algorithms the first member of equation (4.50) is referred to as a function f of $\Delta \underline{\underline{\varepsilon}}_{\ell,m}^{cr}$,

$$\underline{\underline{f}}(\Delta \underline{\underline{\varepsilon}}_{\ell,m}^{cr}) = \underline{\underline{\sigma}}_{\ell,m-1}^{cr} + \Delta \underline{\underline{\sigma}}_{\ell,m}^{cr}(\Delta \underline{\underline{\varepsilon}}_{\ell,m}^{cr}) + \underline{\underline{T}}_m^{cr} \underline{\underline{D}}^{co} [\underline{\underline{T}}_m^{cr}]^T \Delta \underline{\underline{\varepsilon}}_{\ell,m}^{cr} - \underline{\underline{T}}_m^{cr} \underline{\underline{\sigma}}_{m-1}^{cr} - \underline{\underline{T}}_m^{cr} \underline{\underline{D}}^{co} \Delta \underline{\underline{\varepsilon}}_m \quad (4.51)$$

With this assumption, equation (4.50) becomes $\underline{\underline{f}}(\Delta \underline{\underline{\varepsilon}}_{\ell,m}^{cr}) = \underline{\underline{0}}$.

Figure 4.9 shows the flowchart of the Newton-Raphson method adapted to the solution of (4.50). The calculation of the initial solution (step (2) in Figure 4.9) is performed with equation (4.50), considering $\Delta \underline{\underline{\sigma}}_{\ell,m}^{cr}(\Delta \underline{\underline{\varepsilon}}_{\ell,m}^{cr})$ equal to $\underline{\underline{D}}_{m-1}^{cr} \Delta \underline{\underline{\varepsilon}}_{\ell,m}^{cr}$, where $\underline{\underline{D}}_{m-1}^{cr}$ is the tangential crack constitutive matrix of the previous converged stress state.

In step 3 $Toler = 10^{-6} f_c$, where f_c is the concrete compressive strength. The symbol $\| \cdot \|_{\infty}$ means the infinite norm of the vector, i.e., the maximum absolute value found in vector $\underline{\underline{f}}$. The first derivatives of $\underline{\underline{f}}$ in order to the incremental crack strain vector can be defined as

$$\frac{\partial \underline{\underline{f}}(\Delta \underline{\underline{\varepsilon}}_{\ell,m}^{cr})}{\partial \Delta \underline{\underline{\varepsilon}}_{\ell,m}^{cr}} = \underline{\underline{D}}_m^{cr} + \hat{\underline{\underline{D}}}_m^{cr} + \underline{\underline{T}}_m^{cr} \underline{\underline{D}}^{co} [\underline{\underline{T}}_m^{cr}]^T \quad (4.52)$$

where

$$\hat{\underline{\underline{D}}}_m^{cr} = \begin{bmatrix} \hat{\underline{\underline{D}}}_{1,m}^{cr} & \underline{\underline{0}} & \dots & \underline{\underline{0}} \\ \underline{\underline{0}} & \hat{\underline{\underline{D}}}_{2,m}^{cr} & \dots & \underline{\underline{0}} \\ \dots & \dots & \dots & \dots \\ \underline{\underline{0}} & \underline{\underline{0}} & \dots & \hat{\underline{\underline{D}}}_{n_{cr},m}^{cr} \end{bmatrix} \quad (4.53)$$

and

$$\hat{\underline{D}}_{i,m}^{cr} = \begin{bmatrix} 0 & 0 \\ \frac{\partial \Delta \tau_{t,m}^{cr}}{\partial \Delta \varepsilon_{n,m}^{cr}} \Big|_i & 0 \end{bmatrix} \quad (4.54)$$

When equation (4.42) is adopted to define (4.41) the non-null term of (4.54) is

$$\frac{\partial \Delta \tau_{t,m}^{cr}}{\partial \Delta \varepsilon_{n,m}^{cr}} = \frac{\left(1 - \frac{\varepsilon_{n,m-1}^{cr} + \Delta \varepsilon_{n,m}^{cr}}{\varepsilon_{n,ult}^{cr}}\right)^{p_1} G_c p_1}{\varepsilon_{n,ult}^{cr} \left(1 - \frac{\varepsilon_{n,m-1}^{cr} + \Delta \varepsilon_{n,m}^{cr}}{\varepsilon_{n,ult}^{cr}}\right) \left(1 - \left(1 - \frac{\varepsilon_{n,m-1}^{cr} + \Delta \varepsilon_{n,m}^{cr}}{\varepsilon_{n,ult}^{cr}}\right)^{p_1}\right)} \Delta \gamma_{t,m}^{cr} - \frac{\left(\left(1 - \frac{\varepsilon_{n,m-1}^{cr} + \Delta \varepsilon_{n,m}^{cr}}{\varepsilon_{n,ult}^{cr}}\right)^{p_1}\right)^2 G_c p_1}{\left(1 - \left(1 - \frac{\varepsilon_{n,m-1}^{cr} + \Delta \varepsilon_{n,m}^{cr}}{\varepsilon_{n,ult}^{cr}}\right)^{p_1}\right)^2 \varepsilon_{n,ult}^{cr} \left(1 - \frac{\varepsilon_{n,m-1}^{cr} + \Delta \varepsilon_{n,m}^{cr}}{\varepsilon_{n,ult}^{cr}}\right)} \Delta \gamma_{t,m}^{cr} \quad (4.55)$$

When the convergence is not obtained using the Newton-Raphson method, the fixed-point iteration method, shown in Figure 4.10 is tried.

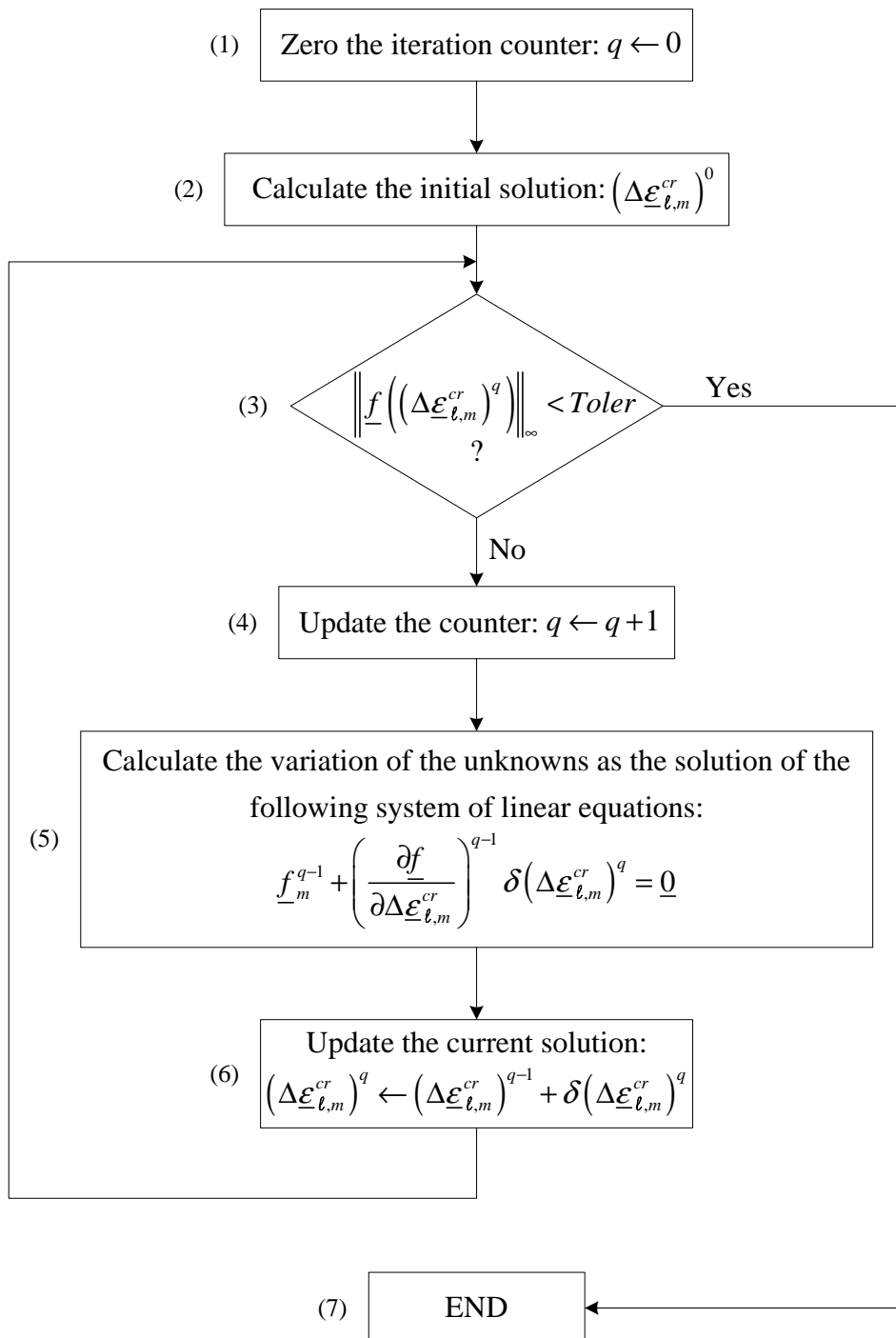


Figure 4.9 – Flowchart of the Newton-Raphson method.

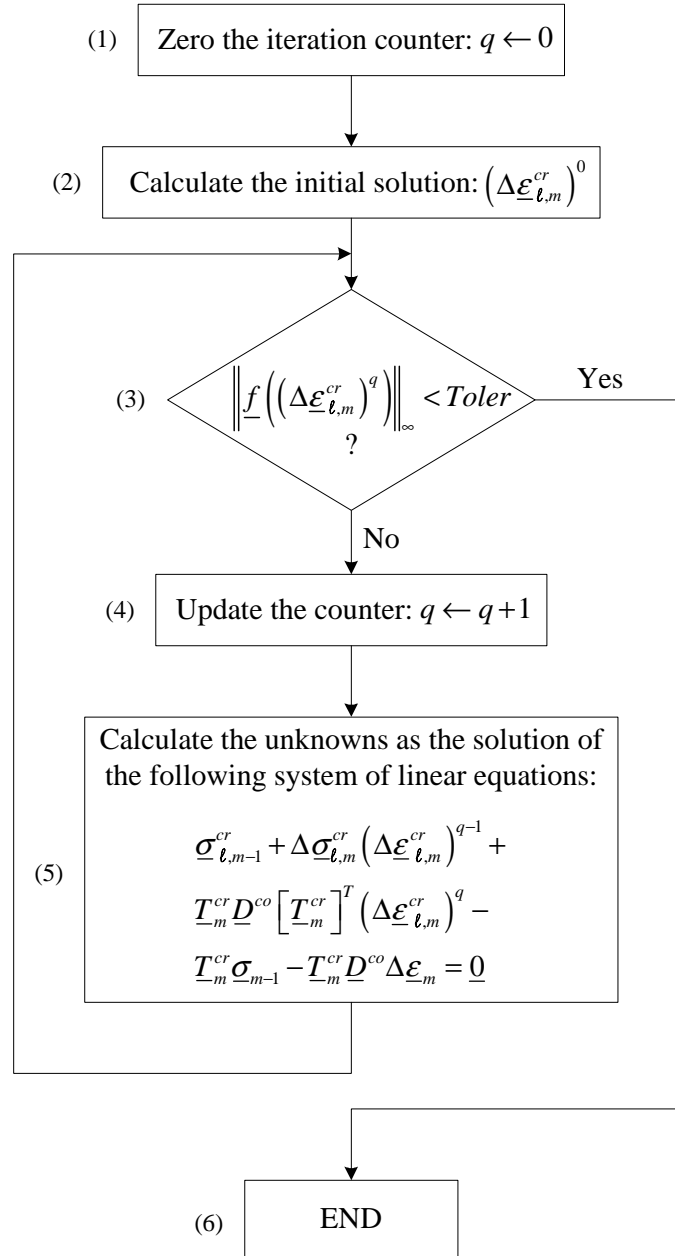


Figure 4.10 – Fixed-point iteration method.

4.2.3.2 Crack status

Depending on the followed $\sigma_n^{cr} - \varepsilon_n^{cr}$ path, a crack can assume one of six crack statuses as shown in Figure 4.11. The first (1) is named *initiation* and corresponds to the crack initiation. The *opening* status occurs when the crack is in the softening branch (2). In the present model a secant branch is assumed to simulate the unloading (3) and the reloading (5) phases. The *closing* status designates the unloading phase while the *reopening* status is attributed to the crack in the reloading phase. This assumption does not correspond to the

most realistic approach, since cyclic tests reveal the occurrence of a hysteretic behavior (Hordijk 1991). Since the present model was developed to simulate the behavior of concrete structures under monotonic loading, this simple approach is sufficiently accurate. If a crack closes, i.e., $\varepsilon_n^{cr} = 0$, the crack status receives the designation of *closed* (4). The *fully open* (6) status occurs when in the crack the mode I fracture energy is fully exhausted.

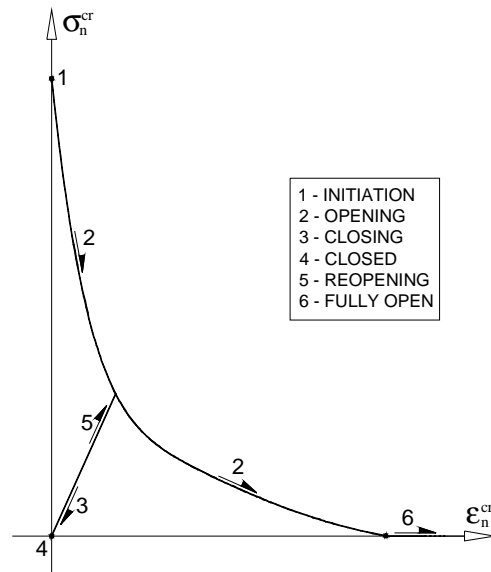


Figure 4.11 – Crack status.

The stress update procedure described in the previous section is only applied to the active cracks, i.e., when $\varepsilon_n^{cr} > 0$. When a crack initiates ($\sigma_t > f_{ct}$ and $\bar{\theta}_t \geq \alpha$), when a crack closes ($\varepsilon_n^{cr} < 0$) or when a closed crack reopens ($\sigma_n^{cr} > 0$), the incremental strain vector $\Delta \underline{\varepsilon}$ must be successively decomposed in order to accurately simulate the crack status evolution (see Figure 4.12). These three crack status changes were named critical crack status changes. This decomposition is necessary since the content of \underline{D}^{cr} and \underline{T}^{cr} matrices depend on the number of active cracks. For instance, when a new crack is formed the size of these matrices must be extended in order to accommodate new terms (see equations (4.43) and (4.44)).

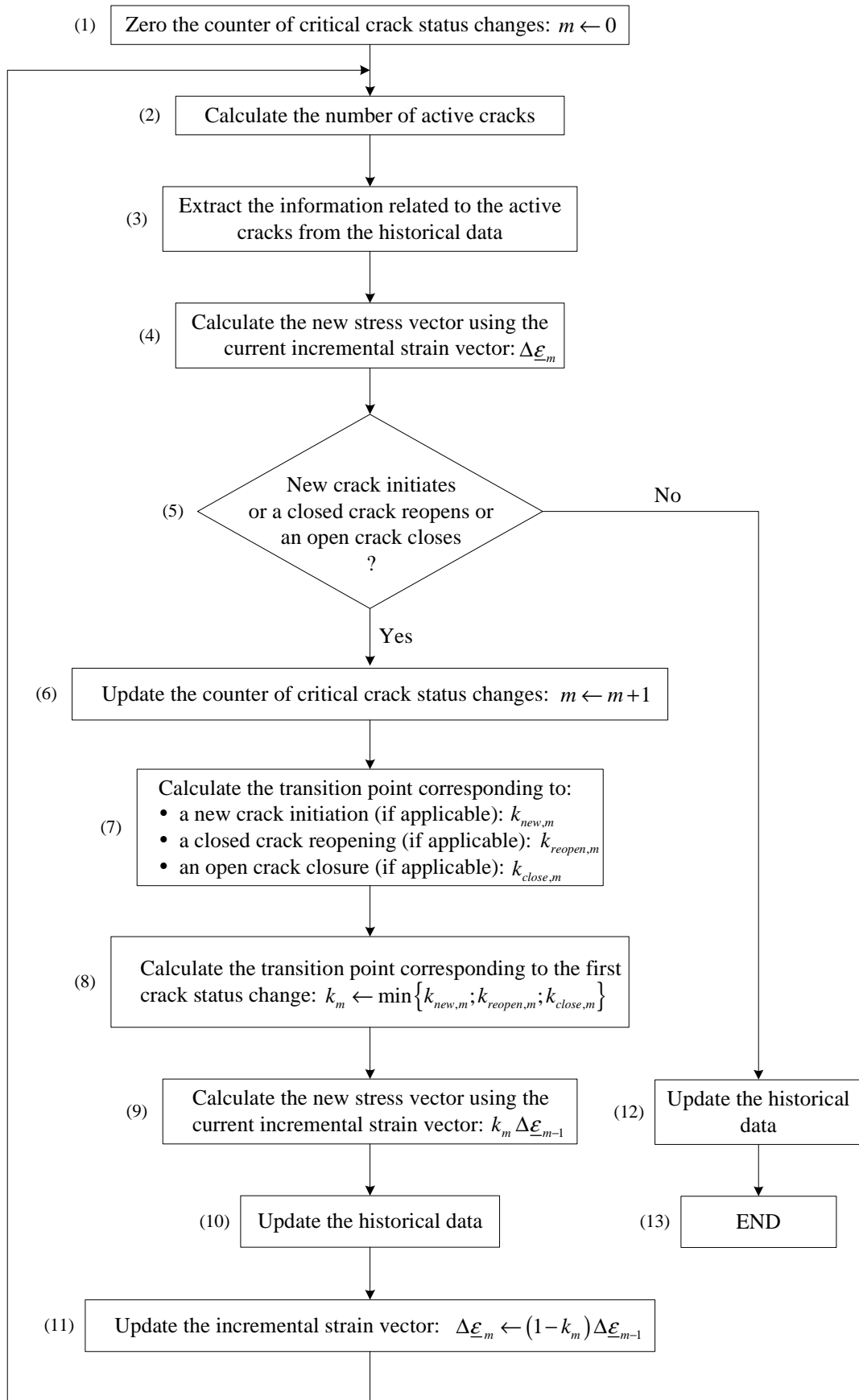


Figure 4.12 – Algorithm used for the decomposition of the incremental strain vector.

The calculation of the number of active cracks (step (2) in Figure 4.12) is based on the content of the database containing the historical data. This database stores, for each integration point and for each iteration of the incremental-iterative procedure, all the critical parameters such as the stress and strain vectors, the number of cracks, the crack stress and strain vectors, the crack statuses, the crack orientation and data associated with the crack evolution history.

The stress update procedure, described in the Section 4.2.3.1, is performed in step (4) of Figure 4.12. When one of the critical crack status changes occurs, the current incremental strain vector, $\Delta \underline{\varepsilon}$, must be decomposed.

To calculate the transition point corresponding to crack initiation, $k_{new,m}$, to a closed crack reopening, $k_{reopen,m}$, or to an open crack closure, $k_{close,m}$, two algorithms were implemented: the Newton-Raphson method (Figure 4.13) and the bisection method (Figure 4.14). The latter one is used when the former fails. Table 4.2 contains the definition of the function $f(k)$, the initial solution and the parameter *Toler* of the critical crack status changes. These functions and parameters are used in the algorithms shown in Figure 4.13 and Figure 4.14.

Table 4.2 – Definition of the function f used in the algorithms shown in Figure 4.13 and Figure 4.14, and the respective initial solution and convergence criterion parameter.

	Critical crack status changes		
	New crack initiation	Closed crack reopening	Open crack closure
$f(k)$	$f_{ct} - \sigma_I(k)$	$\sigma_n^{cr}(k)$	$\varepsilon_n^{cr}(k)$
k^0	$\frac{f_{ct} - \sigma_I^{p-1}}{\sigma_I(\Delta \underline{\varepsilon}^p) - \sigma_I^{p-1}}$	0.5	$1 - \frac{\varepsilon_{n,m}^{cr}}{\varepsilon_{n,m}^{cr} - \varepsilon_{n,m-1}^{cr}}$
<i>Toler</i>	$10^{-6} f_c$	$10^{-6} f_c$	10^{-6}

Besides the crack initiation conditions described in Section 4.2.2.1 (tensile strength and threshold angle), an additional check is required. When a new crack is initiating, $k_{new,m}$ is calculated (see Figure 4.12). At this phase, the new crack is only considered as a

potential crack. At the end of the first part of the incremental strain vector, $k_{new,m}\Delta\underline{\varepsilon}_{m-1}$, the crack normal stress, σ_n^{cr} , is equal to the current tensile strength, f_{ct} , and its crack normal strain, ε_n^{cr} , has a null value (point 1 in Figure 4.11). For the remaining part of the incremental strain vector, $(1-k_{new,m})\Delta\underline{\varepsilon}_{m-1}$, the potential crack is already considered in equation (4.50). To become a definitive crack, $\Delta\varepsilon_n^{cr}$ of the potential crack must be positive during the evaluation of equation (4.50). If this condition is not fulfilled, the crack initiation procedure is aborted and the tensile strength is replaced with the value of the current maximum principal stress.

After the determination of the transition point corresponding to the first critical crack status change (step 7 in Figure 4.12), the stress vector is calculated, and the historical data of the cracks and the incremental strain vector are updated. The decomposition of the incremental strain vector ends when no more critical crack status changes occur (see Figure 4.12).

In this section, m is the counter of critical crack status changes, requiring a decomposition of the vector $\Delta\underline{\varepsilon}$. In Table 4.3 the meaning of “previous iteration” $m-1$ is clarified.

Table 4.3 – Meaning of $m-1$ (previous iteration).

m value	Algorithmic strategy (PD or PI)	Meaning of $m-1$
$m = 0$	Path dependent	Previous Newton-Raphson iteration
	Path independent	Previous converged combination
$m > 0$	Path dependent or path independent	Previous iteration in the algorithm of Figure 4.12

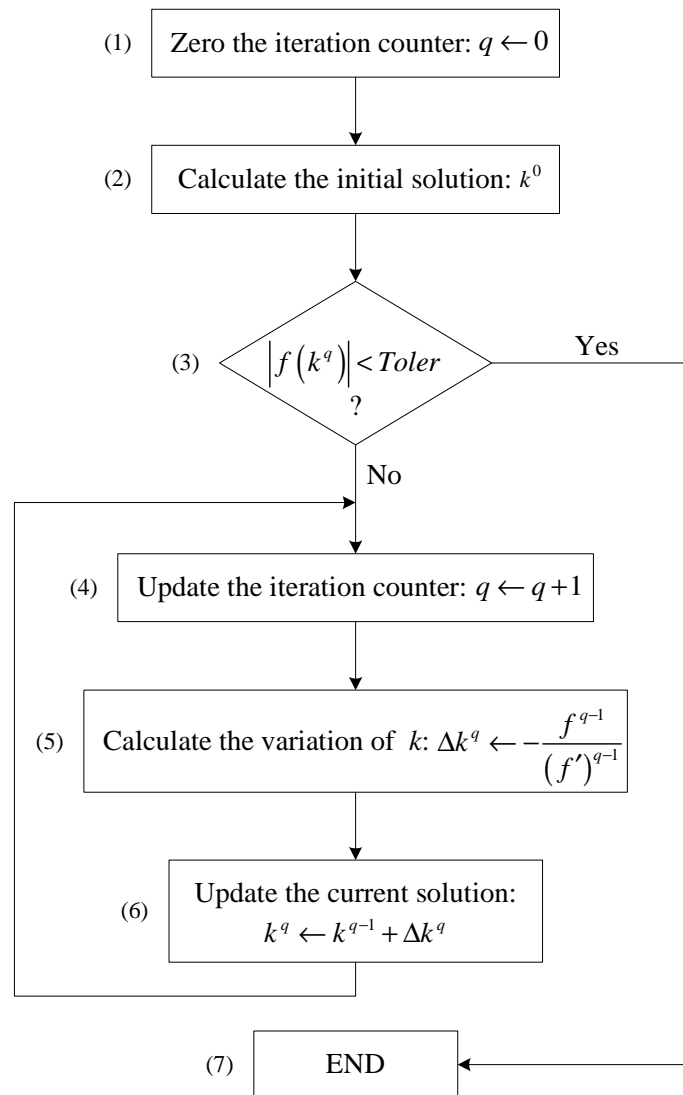


Figure 4.13 – Calculation of the transition point by the Newton-Raphson method.

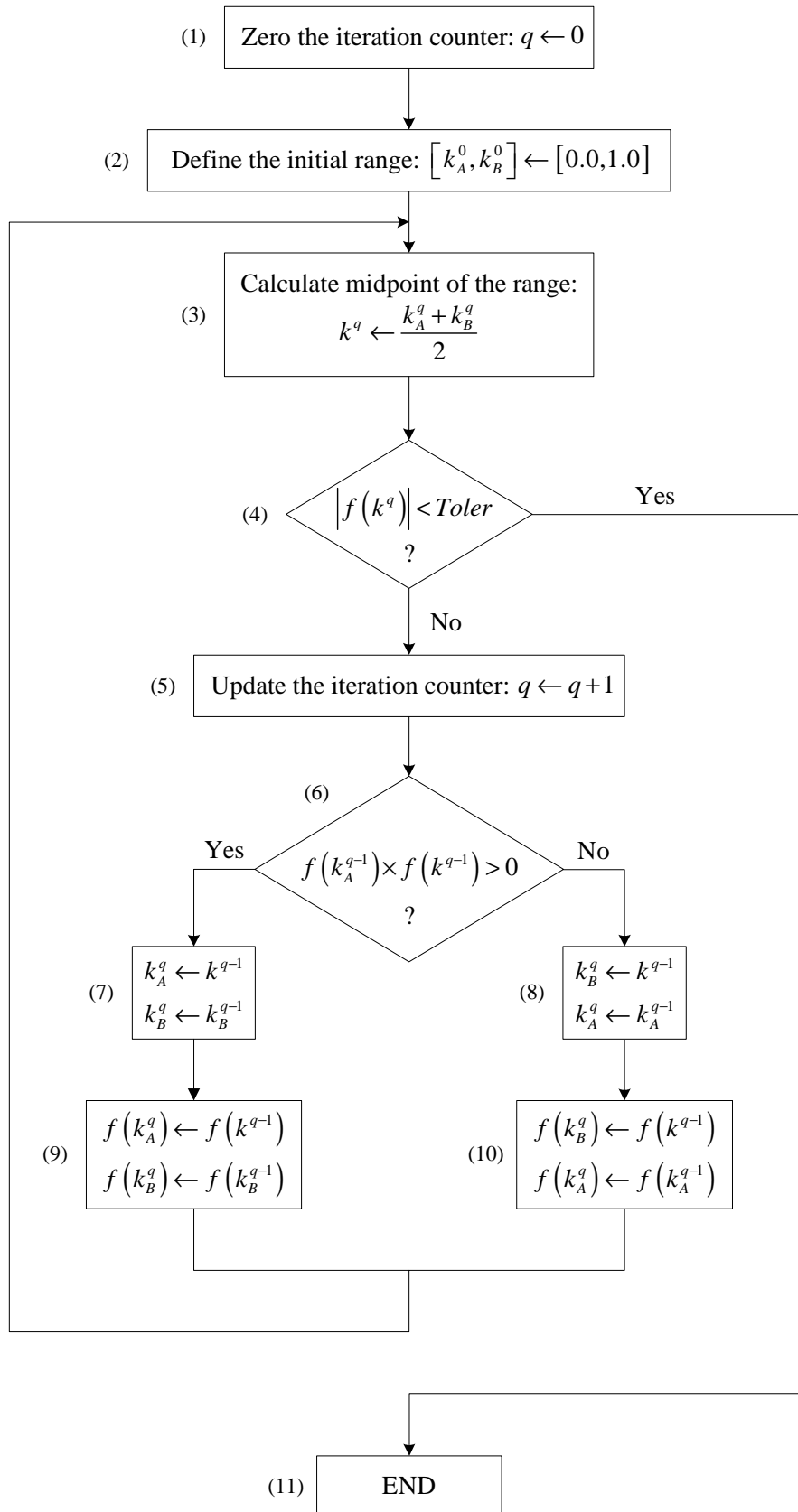


Figure 4.14 – Calculation of the transition point by the bisection method.

4.2.3.3 Singularities

When two fully open orthogonal cracks occur at an integration point, it can be shown that, in the system of nonlinear equations (4.50), the shear equations related to these cracks are linearly dependent. This situation can be illustrated with the following example.

Considering two orthogonal cracks, being one horizontal ($\theta_1 = 90^\circ$) and the other vertical ($\theta_2 = 0^\circ$), and considering that both are *fully open*. In this case the variation of the crack stress vector, $\Delta \underline{\sigma}_\ell^{cr}$, is null. Assuming that in the previous state $\underline{\sigma}_{\ell,m-1}^{cr} = \underline{T}_m^{cr} \underline{\sigma}_{m-1}$, equation (4.50) leads to

$$\underline{T}_m^{cr} \underline{D}^{co} \left[\underline{T}_m^{cr} \right]^T \Delta \underline{\varepsilon}_{\ell,m}^{cr} - \underline{T}_m^{cr} \underline{D}^{co} \Delta \underline{\varepsilon}_m = \underline{0} \quad (4.56)$$

resulting in

$$\begin{cases} \Delta \varepsilon_n^{cr,1} = \Delta \varepsilon_2 \\ +\Delta \gamma_t^{cr,1} - \Delta \gamma_t^{cr,2} = -\Delta \gamma_{12} \\ \Delta \varepsilon_n^{cr,2} = \Delta \varepsilon_1 \\ -\Delta \gamma_t^{cr,1} + \Delta \gamma_t^{cr,2} = +\Delta \gamma_{12} \end{cases} \quad (4.57)$$

where $\Delta \varepsilon_n^{cr,1}$, $\Delta \gamma_t^{cr,1}$, $\Delta \varepsilon_n^{cr,2}$ and $\Delta \gamma_t^{cr,2}$ are the normal and shear crack strain variations of the crack 1 and 2, respectively. The system of equations (4.57) cannot be solved since the second and fourth equations are linearly dependent. A physical interpretation of this situation is presented in Figure 4.15. The crack normal strain variations can be obtained directly from the global strain variations.

The solution of (4.50) for the case of fully open orthogonal cracks requires the introduction of the following additional condition

$$\Delta \gamma_t^{cr,i} + \Delta \gamma_t^{cr,j} = 0 \quad (4.58)$$

where $\Delta \gamma_t^{cr,i}$ and $\Delta \gamma_t^{cr,j}$ are the crack shear strain variations of a pair of orthogonal cracks.

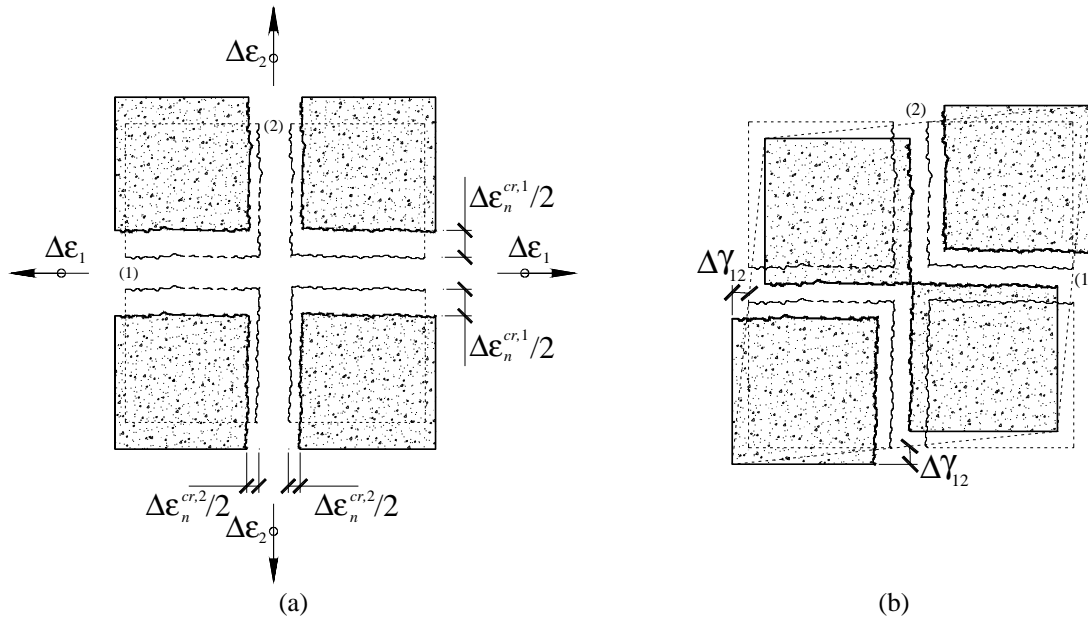


Figure 4.15 – Crack strain variation: (a) normal strain and (b) shear strain.

To calculate the stiffness matrix of an element, \underline{K} , the constitutive matrix, \underline{D} , is required. The calculation of \underline{D} of a cracked concrete integration point requires the inversion of the matrix that results from the evaluation of the following expression (see Section 4.2.1.4, equation (4.27))

$$\underline{D}' = \underline{D}^{cr} + \underline{T}^{cr} \underline{D}^{co} \left[\underline{T}^{cr} \right]^T \quad (4.59)$$

When an integration point has two fully open orthogonal cracks, \underline{D}^{cr} is null resulting in a singular \underline{D}' matrix. To overcome this problem the following residual value is assigned to \underline{D}^{cr} ,

$$D_{II}^{cr} = 10^{-6} G_c \quad (4.60)$$

4.2.4 Model appraisal

The performance of the developed multi-fixed smeared crack model is assessed using results published by other researchers. Since the concrete plastic deformation is not considered in the formulation described, the example selected to validate the model exhibit a linear behavior in compression.

Three-point bending tests are commonly used to evaluate the concrete tensile strength and the fracture energy (RILEM 1985). The tests carried out by Kormeling and Reihnardt (1983) are simulated using the implemented numerical model. The adopted mesh (see Figure 4.16) is composed of 4-node Lagrangian plane stress elements with 2×2 Gauss-Legendre integration scheme. In order to obtain a well-defined crack pattern at mid-span, 1×2 Gauss-Legendre integration rule is used in the elements that cross the center line.

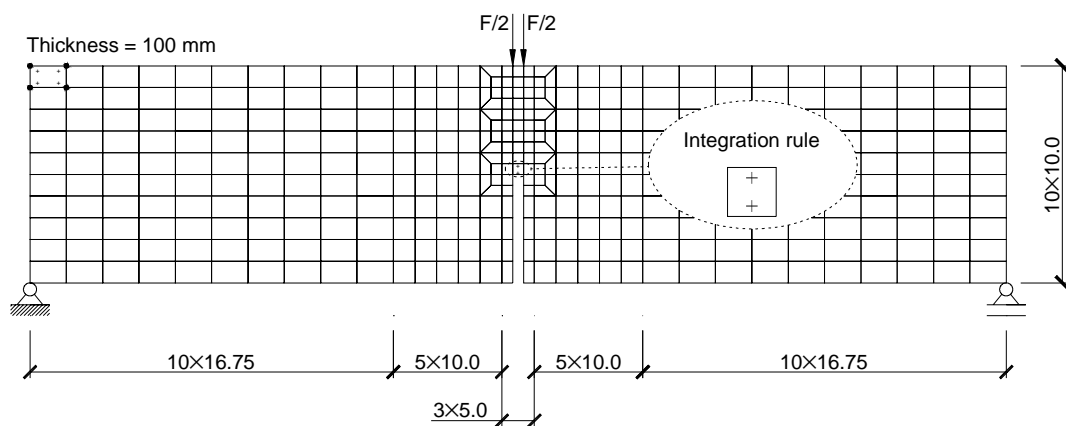


Figure 4.16 – Notched beam: geometry, mesh, loading configuration and support conditions. Note: all dimensions are in millimeters.

The concrete properties used in the present simulation are listed in Table 4.4. Three different types of tensile-softening diagrams were used: linear, tri-linear and exponential. The beam weight is included in the simulation.

Figure 4.17 shows the response obtained using the three different types of tensile-softening diagrams described above. The experimental results are also displayed. It can be observed that all numerical simulations have the same pre-peak response, up to 1050 kN. The maximum numerical peak load is obtained with the linear softening diagram. The tri-linear and the exponential tensile-softening diagrams lead to an identical response in the post-peak phase, in good agreement with the experimental results.

Figure 4.18 shows the crack pattern at the final stage, for the case of tri-linear diagram. A well-defined crack above the notch can be observed. Spurious cracks with *closing* status were formed in the neighborhood of the fracture surface.

Table 4.4 – Concrete properties used in the simulation of the three point bending test.

Density	$\rho = 2.4 \times 10^{-6} \text{ N/mm}^3$
Poisson's ratio	$\nu_c = 0.20$
Initial Young's modulus	$E_c = 20000.0 \text{ N/mm}^2$
Compressive strength	$f_c = 48.0 \text{ N/mm}^2$
Tensile strength	$f_{ct} = 2.4 \text{ N/mm}^2$
Tri-linear softening parameters	$\xi_1 = 0.4$; $\alpha_1 = 0.6$; $\xi_2 = 0.8$; $\alpha_2 = 0.2$
Fracture energy	$G_f = 0.113 \text{ N/mm}$
Parameter defining the mode I fracture energy available to the new crack	$p_1 = 2$
Shear retention factor	<i>Exponential</i> ($p_2 = 2$)
Crack band-width	<i>Square root of the area of the element</i>
Threshold angle	$\alpha_{th} = 30^\circ$

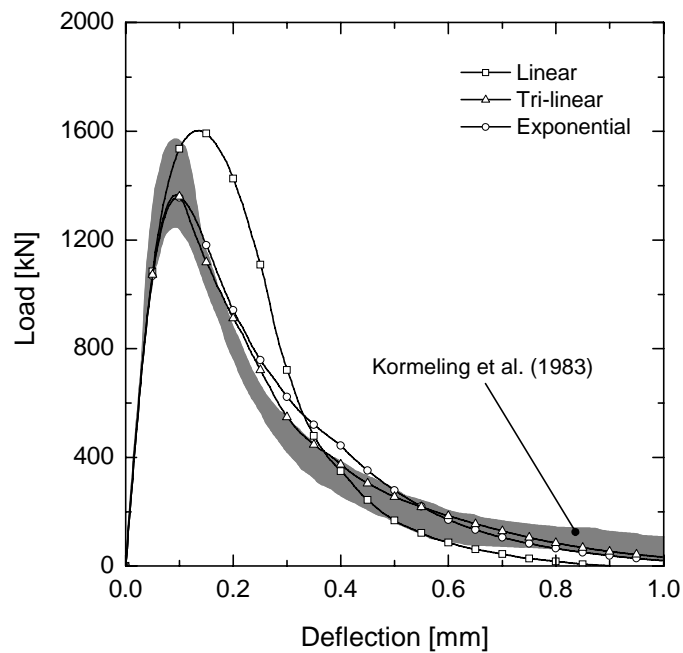


Figure 4.17 – Influence of the type of tensile-softening diagram on the load-deflection response.

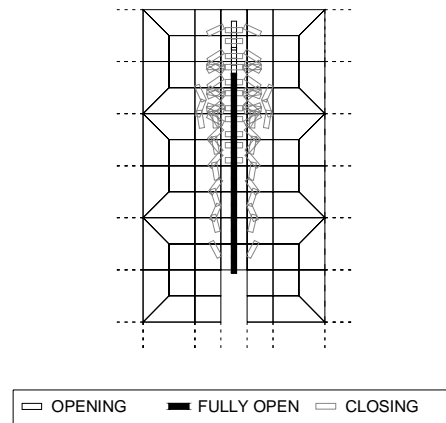


Figure 4.18 – Numerical crack pattern at the final stage using the tri-linear diagram.

4.3 PLASTICITY

The plasticity theory has been used by many researchers in the simulation of the behavior of structures built with materials exhibiting irreversible deformations, such as concrete (Chen 1982), soils (Chen and Mizuno 1990) or masonry (Lourenço 1996). An extensive study of this subject can be found in the literature (Lemaitre and Caboche 1985, Lubliner 1990, Crisfield 1997, Simo and Hughes 1998). In the simulation of the concrete in compression, a model based on the plasticity theory is adopted. This model is described in the following sections. Results available in the literature are used to assess the performance of the model.

4.3.1 Basic assumptions

The basic assumption of the plasticity theory, in the context of small strains, is the decomposition of the incremental strain, $\Delta \underline{\underline{\varepsilon}}$, in an elastic reversible part, $\Delta \underline{\underline{\varepsilon}}^e$, and an irreversible or plastic part, $\Delta \underline{\underline{\varepsilon}}^p$:

$$\Delta \underline{\underline{\varepsilon}} = \Delta \underline{\underline{\varepsilon}}^e + \Delta \underline{\underline{\varepsilon}}^p \quad (4.61)$$

The elastic constitutive matrix, $\underline{\underline{D}}^e$, is used to obtain the incremental stress vector, $\Delta \underline{\underline{\sigma}}$,

$$\Delta \underline{\sigma} = \underline{D}^e \Delta \underline{\varepsilon}^e = \underline{D}^e (\Delta \underline{\varepsilon} - \Delta \underline{\varepsilon}^p) \quad (4.62)$$

Plasticity based models depend on the concepts of yield surface, flow rule and hardening (or softening) law. The yield surface, defined in the stress space, limits the elastic behavior domain. In general, this surface is a function of the stress state in a point, $\underline{\sigma}$, and of some internal variables, \underline{a} and κ , that define the evolution of the yield surface. The general equation of the yield surface is

$$f(\underline{\sigma}, \underline{a}, \kappa) = 0 \quad (4.63)$$

The back-stress vector, \underline{a} , locates the origin of the yield surface and κ is the scalar hardening parameter, which defines the amount of hardening or softening.

Depending on the evolution of the yield surface during the loading process, three basic hardening types can be defined (see Figure 4.19): isotropic hardening (Odqvist 1933), kinematic hardening (Prager 1955) and mixed hardening (Hodge 1957). The internal variables involved in these hardening rules are indicated in Table 4.5.

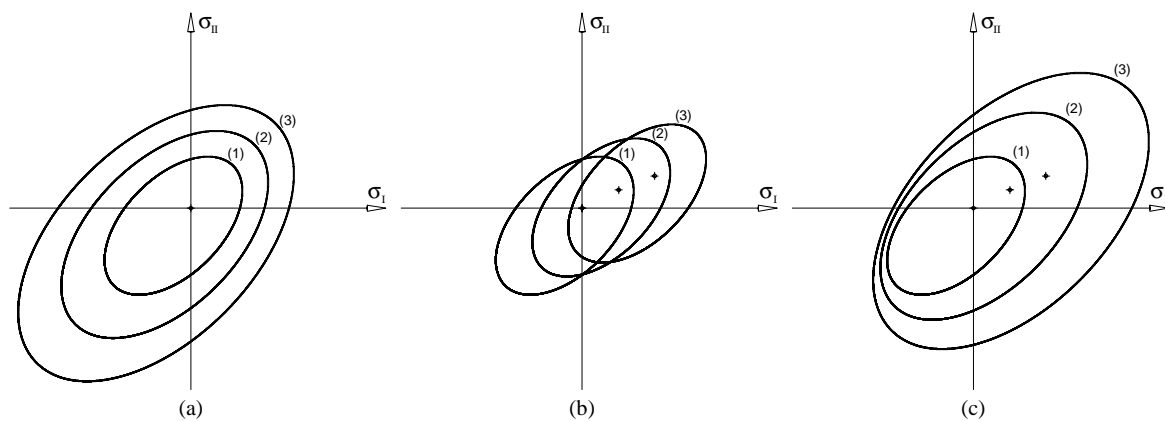


Figure 4.19 – Basic hardening rules: (a) isotropic hardening, (b) kinematic hardening and (c) mixed hardening.

Table 4.5 – Basic hardening rules.

Hardening rule	Variables involved
No hardening (ideal plasticity)	$f(\underline{\sigma})$
Isotropic hardening (Figure 4.19(a))	$f(\underline{\sigma}, \kappa)$
Kinematic hardening (Figure 4.19(b))	$f(\underline{\sigma}, \underline{a})$
Mixed hardening (Figure 4.19(c))	$f(\underline{\sigma}, \underline{a}, \kappa)$

In the geometric representation shown in Figure 4.19 \underline{a} defines the location of the origin of the yield surface whereas κ controls the size and shape of the yield surface. Good results can be obtained with the isotropic hardening when loading is monotonic. However, more complex hardening rules are required when the material is submitted to cyclic loading. Since the aim of the present model is to simulate the behavior of concrete structures under monotonic loading, the back-stress vector will not be considered as a yield surface parameter. With these assumptions the yield condition adopted for the present model is the following

$$f(\underline{\sigma}, \kappa) = 0 \quad (4.64)$$

The evolution of the plastic strain is given by the following flow rule

$$\Delta \underline{\varepsilon}^p = \Delta \lambda \frac{\partial g}{\partial \underline{\sigma}} \quad (4.65)$$

where $\Delta \lambda$ is a non-negative scalar termed plastic multiplier and g is the plastic potential function in the stress space. When g and f coincide, the flow rule is named associated. Otherwise, a non-associated flow rule is obtained. The yield function and the plastic multiplier are constrained by the following conditions

$$f \leq 0, \Delta \lambda \geq 0 \text{ and } \Delta \lambda f = 0 \quad (4.66)$$

The variation of the hardening parameter, $\Delta \kappa$, coincides with the equivalent plastic strain variation $\Delta \varepsilon^{eps}$ (strain hardening) or with the plastic work variation ΔW^p (work

hardening). When the first hypothesis holds ($\Delta\kappa = \Delta\varepsilon^{eps}$), the hardening parameter is defined by

$$\Delta\kappa = \Delta\varepsilon^{eps} = c\sqrt{(\Delta\underline{\varepsilon}^p)^T \Delta\underline{\varepsilon}^p} \quad (4.67)$$

The assumption of $c = \sqrt{2/3}$ assures that the plastic strain in the loading direction of a uniaxial test is equal to the equivalent plastic strain variation, i.e., $\Delta\varepsilon^{eps} = \Delta\varepsilon_1^p$ and $\Delta\varepsilon_2^p = \Delta\varepsilon_3^p = -\Delta\varepsilon_1^p/2$ (Owen and Hinton 1980).

The equivalent plastic strain variation can also be defined as a function of the plastic work per unit volume, ΔW^p , resulting

$$\Delta\kappa = \Delta\varepsilon^{eps} = \frac{\Delta W^p}{\bar{\sigma}} = \frac{1}{\bar{\sigma}} \underline{\sigma}^T \Delta\underline{\varepsilon}^p \quad (4.68)$$

where $\bar{\sigma}$ is the uniaxial yield stress which depends on the hardening parameter, and is currently named hardening law. When the variation of the hardening parameter is defined with the work hardening hypothesis ($\Delta\kappa = \Delta W^p$), the following relation holds

$$\Delta\kappa = \Delta W^p = \underline{\sigma}^T \Delta\underline{\varepsilon}^p \quad (4.69)$$

4.3.2 Integration of the elasto-plastic constitutive equations

The integration of the elasto-plastic constitutive equations over a finite step in a consistent manner is one of the main challenges in computational plasticity. At the previous step $n-1$, the stress state and the internal variables are known ($\underline{\sigma}_{n-1}$, κ_{n-1} , $\underline{\varepsilon}_{n-1}$, $\underline{\varepsilon}_{n-1}^p$), and the main task is the calculation of the current values of these variables when a strain variation occurs, $\Delta\underline{\varepsilon}_n$. This problem can be solved with an implicit Euler backward integration algorithm. The stability and accuracy of this algorithm has been demonstrated by several researchers (Ortiz and Popov 1985, de Borst and Feenstra 1990, Schellekens and de Borst 1990). The algorithm has two phases: an elastic predictor phase and a plastic

corrector phase. In the former null plastic flow is assumed, which leads to a discrete set of equations

$$\begin{cases} \underline{\sigma}_n^e = \underline{\sigma}_{n-1} + \underline{D}^e \Delta \underline{\varepsilon}_n \\ \kappa_n = \kappa_{n-1} \\ f_n = f(\underline{\sigma}_n^e, \kappa_n) = 0 \end{cases} \quad (4.70)$$

When the elastic trial stress, $\underline{\sigma}_n^e$, lies outside the yield surface, plastic flow must be considered and the plastic corrector phase of the algorithm is used to find an admissible stress state. Otherwise, the load step is considered linear elastic. The algorithm used to find an admissible stress state is named return-mapping algorithm and consists in the solution of the following system of nonlinear equations,

$$\begin{cases} \left[\underline{D}^e \right]^{-1} (\underline{\sigma}_n - \underline{\sigma}_n^e) + \Delta \lambda_n \left(\frac{\partial g}{\partial \underline{\sigma}} \right)_n = \underline{0} \\ \kappa_n - \kappa_{n-1} - \Delta \kappa_n = 0 \\ f_n(\underline{\sigma}_n, \kappa_n) = 0 \end{cases} \quad (4.71)$$

The first equation of the system of nonlinear equations is obtained from the equation

$$\underline{\sigma}_n = \underline{\sigma}_{n-1} + \underline{D}^e (\Delta \underline{\varepsilon}_n - \Delta \underline{\varepsilon}_n^p) = \underline{\sigma}_n^e - \underline{D}^e \Delta \underline{\varepsilon}_n^p \quad (4.72)$$

where $\Delta \underline{\varepsilon}_n^p$ is replaced with the right-hand side of equation (4.65). The Newton-Raphson method is used to solve the system of nonlinear equations (4.71), where $\underline{\sigma}_n$, κ_n and $\Delta \lambda_n$ are the unknowns.

4.3.3 Evaluation of the tangent operator

As indicated in Section 4.1.1, the Newton-Raphson method is used to calculate the solution of the system of nonlinear equations resulting from the nonlinear finite element analysis.

The nonlinear problem is converted into a sequence of linear iterations until convergence is reached, as shown in Figure 4.1. The linearized form of the equations depends on a tangent stiffness matrix, \underline{K}_T , which plays a crucial role in the performance and robustness of the Newton-Raphson method. In the context of the mathematical plasticity, and according to Simo and Taylor (1985), the tangent stiffness matrix must be obtained by consistent linearization of the stress update resulting from the return-mapping algorithm at the end of the iteration i .

The elasto-plastic consistent tangent constitutive matrix can be determined from the total differentials $d\underline{\sigma}_n$, $d\underline{\varepsilon}_n^p$ and df_n (Hofstetter and Mang 1995) or from part of the Jacobian matrix used in the Newton-Raphson method of the return-mapping algorithm (Lourenço 1996).

4.3.4 Elasto-plastic concrete model

Several elasto-plastic models have been proposed to simulate the concrete behavior. These models differ from each other, mainly, in the shape of the yield surface and in the hardening and flow rules. The model described in this section is suitable to simulate the concrete compressive behavior under monotonic loading, admitting that the tensile stresses do not exceed the concrete tensile strength.

4.3.4.1 Yield surface

The yield surface proposed by Owen and Figueiras (1983) was adopted in the present model. Its main characteristic is the consideration of parabolic meridians. This yield surface is defined with the following equation

$$f(\underline{\sigma}, \kappa) = (\underline{\sigma}^T \underline{P} \underline{\sigma})^{1/2} + \underline{q}^T \underline{\sigma} - \bar{\sigma}(\kappa) = 0 \quad (4.73)$$

where \underline{P} is the projection matrix, given by

$$\underline{P} = \begin{bmatrix} a & b & 0 \\ b & a & 0 \\ 0 & 0 & c \end{bmatrix} \quad (4.74)$$

and \underline{q} is the projection vector defined by

$$\underline{q} = d\underline{q}_1 = d[1 \ 1 \ 0]^T \quad (4.75)$$

The parameters a , b , c and d can be obtained with

$$a = \left(\frac{A}{2}\right)^2 + B, \quad b = \left(\frac{A}{2}\right)^2 - \frac{B}{2}, \quad c = 3B, \quad d = \frac{A}{2} \quad (4.76)$$

where the scalars A and B assume the values that result from the fitting process between the present model and the experimental results obtained by Kupfer et al. (1969). In these circumstances, A and B assumes the values of (Owen and Figueiras 1983)

$$A = 0.355 \text{ and } B = 1.355 \quad (4.77)$$

Figure 4.20 represents the initial and the limit yield surfaces. This initial yield surface is the limiting surface for elastic behavior. Experimental results obtained by Kupfer et al. (1969) are also included.

4.3.4.2 Hardening behavior

Figure 4.21 represents the relationship between the yield stress, $\bar{\sigma}$, and the hardening parameter, κ , used to simulate the hardening and softening phases of the concrete behavior. Three points define the transitions between branches of the curve. The location of these points is obtained from uniaxial compression tests: $\bar{\sigma}_0 = \alpha_0 f_c$, $\bar{\sigma}_p = f_c$ and $\bar{\sigma}_{\text{lim}} = 0.5 f_c$. The equivalent plastic strain corresponding to the peak compressive strength, κ_p , with the following equation

$$\kappa_p = \varepsilon_{c1} - f_c/E_c \quad (4.78)$$

where ε_{c1} is the total strain at the peak compressive strength. Parameter α_0 defines the beginning of the plastic behavior. In most cases, α_0 can assume the value 0.3.

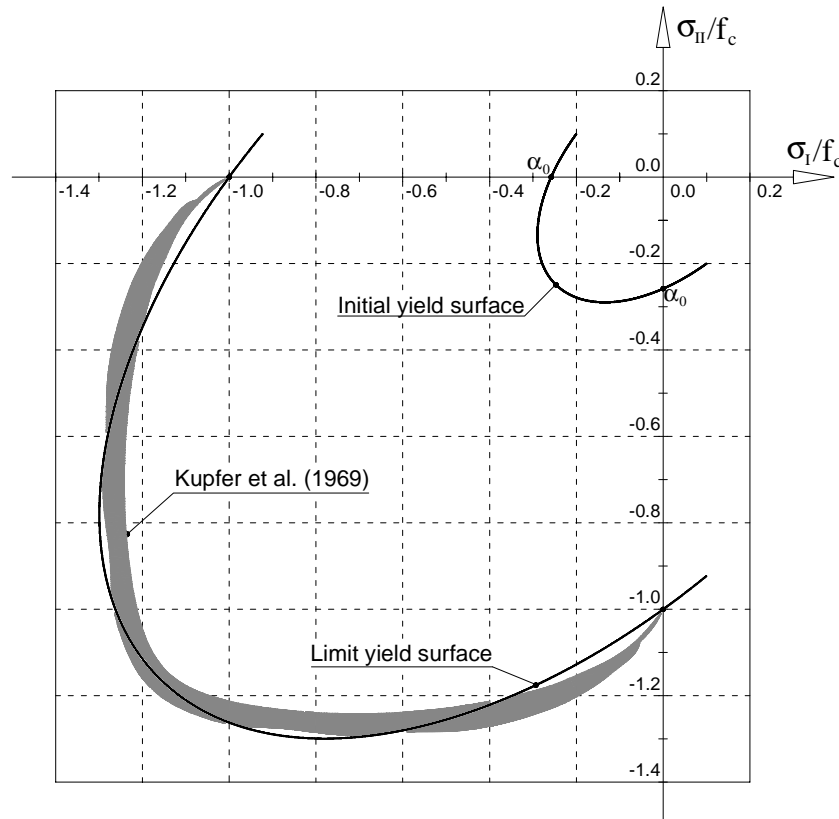


Figure 4.20 – Yield surfaces for concrete.

For the hardening branch, $\bar{\sigma}_1(\kappa)$, the relationship used by Lourenço (1996) was adopted, whereas for the softening phase, $\bar{\sigma}_2(\kappa)$ and $\bar{\sigma}_3(\kappa)$, the post-peak relationship proposed by CEB-FIB (1993) for the uniaxial compressive behavior was used. The expressions of the hardening and softening behavior relationships are included in APPENDIX C.

The plastic strain variation is described by the following expression which is assumed to be valid when an associated flow rule is considered

$$\Delta \underline{\varepsilon}^p = \Delta \lambda \frac{\partial g}{\partial \underline{\sigma}} = \Delta \lambda h_c \frac{\partial f}{\partial \underline{\sigma}} \quad (4.79)$$

The scalar function h_c is included in this equation in order to amplify the contribution of $\Delta \lambda \partial f / \partial \underline{\sigma}$ to $\Delta \underline{\varepsilon}^p$. Function h_c depends on the hydrostatic pressure, p , and reads (ABAQUS 2002)

$$h_c = h_c(\underline{\sigma}) = 1 + c_0 \left(\frac{p}{f_c} \right)^2 \quad (4.80)$$

A value of 6.056 for c_0 was obtained based on the condition that under biaxial compression, with equal compressive stress in both directions, the plastic strain at failure is, according to Kupfer et al. (1969), approximately 1.28 times the plastic strain at failure under uniaxial compression.

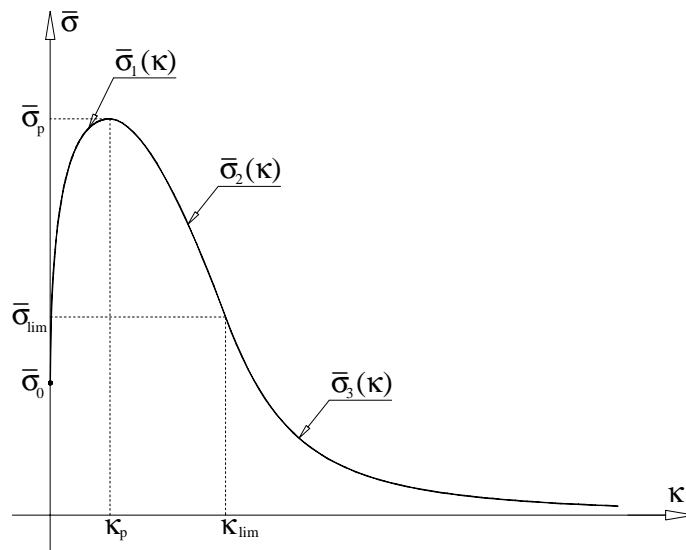


Figure 4.21 – Hardening and softening relationships for concrete.

4.3.4.3 Return-mapping algorithm

Assuming the strain-hardening hypothesis, $\Delta \kappa = \Delta \lambda$ (Cachim 1999, Abaqus 2002), the system of nonlinear equations (4.71) can be reduced to the following pair of equations,

$$\begin{cases} \underline{f}_{1,n} = [\underline{D}^e]^{-1} (\underline{\sigma}_n - \underline{\sigma}_n^e) + \Delta \kappa_n h_{c,n} \left(\frac{\partial f}{\partial \underline{\sigma}} \right)_n = \underline{0} \\ \underline{f}_{2,n} = f(\underline{\sigma}_n, \kappa_n) = 0 \end{cases} \quad (4.81)$$

Figure 4.22 shows the return-mapping algorithm currently implemented in the computer code. The pair of norms defined in step (4) is given by

$$\|\underline{r}_n^q\| = \left[\begin{array}{l} \left\| [\underline{D}^e]^{-1} (\underline{\sigma}_n^q - \underline{\sigma}_n^e) + \Delta \kappa_n^q h_{c,n}^q \left(\frac{\partial f}{\partial \underline{\sigma}} \right)_n^q \right\|_{\infty} \\ |f(\underline{\sigma}_n^q, \kappa_n^q)| \end{array} \right] \quad (4.82)$$

where the superscript q corresponds to the iteration counter. The Jacobian matrix used in step (6) is defined by the following four blocks

$$\begin{aligned} \underline{J} &= \begin{bmatrix} \frac{\partial f_1}{\partial \underline{\sigma}} & \frac{\partial f_1}{\partial \kappa} \\ \frac{\partial f_2}{\partial \underline{\sigma}} & \frac{\partial f_2}{\partial \kappa} \end{bmatrix} \\ &= \begin{bmatrix} [\underline{D}^e]^{-1} + \Delta \kappa \left(\frac{\partial f}{\partial \underline{\sigma}} \left(\frac{\partial h_c}{\partial \underline{\sigma}} \right)^T + h_c \frac{\partial^2 f}{\partial \underline{\sigma}^2} \right) & h_c \frac{\partial f}{\partial \underline{\sigma}} \\ \left(\frac{\partial f}{\partial \underline{\sigma}} \right)^T & \frac{\partial f}{\partial \kappa} \end{bmatrix} \end{aligned} \quad (4.83)$$

where

$$\begin{aligned} \frac{\partial f}{\partial \underline{\sigma}} &= \frac{\underline{P} \underline{\sigma}}{(\underline{\sigma}^T \underline{P} \underline{\sigma})^{1/2}} + \underline{q}; & \frac{\partial^2 f}{\partial \underline{\sigma}^2} &= \frac{\underline{P}}{(\underline{\sigma}^T \underline{P} \underline{\sigma})^{1/2}} - \frac{\underline{P} \underline{\sigma} \underline{\sigma}^T \underline{P}}{(\underline{\sigma}^T \underline{P} \underline{\sigma})^{3/2}} \\ \frac{\partial h_c}{\partial \underline{\sigma}} &= 2c_0 \frac{p}{f_c^2} \underline{q}_1; & \frac{\partial f}{\partial \kappa} &= -\frac{d\bar{\sigma}}{d\kappa} = -h \end{aligned} \quad (4.84)$$

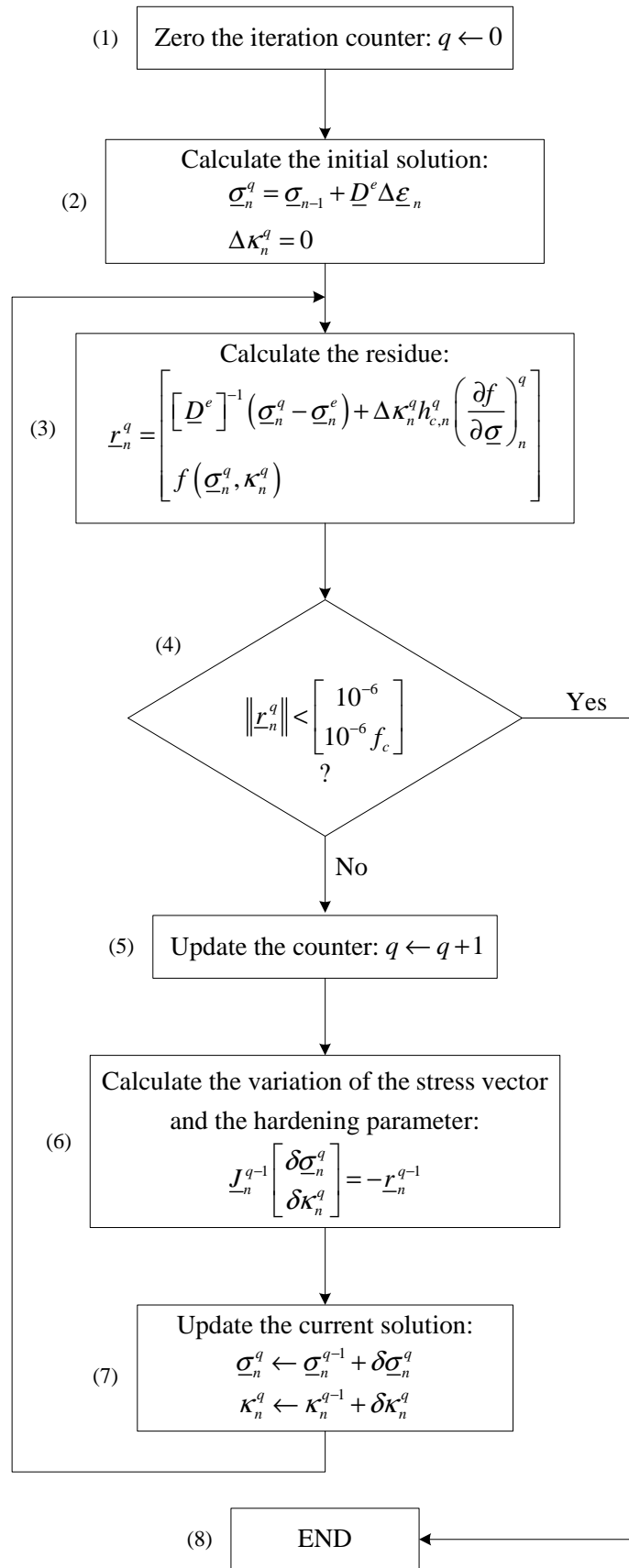


Figure 4.22 – Return-mapping algorithm of the elasto-plastic model.

4.3.4.4 Consistent tangent operator

The consistent tangent constitutive matrix adopted in the present numerical model is deduced in APPENDIX D, resulting

$$\underline{D}^{ep} = \underline{H} - \frac{\underline{H} \frac{\partial f}{\partial \underline{\sigma}} \left(\frac{\partial f}{\partial \underline{\sigma}} \right)^T \underline{H}}{h + \left(\frac{\partial f}{\partial \underline{\sigma}} \right)^T \underline{H} \frac{\partial f}{\partial \underline{\sigma}}} \quad (4.85)$$

where

$$\underline{H} = \left(\left[D^e \right]^{-1} + h_c \Delta \lambda \frac{\partial^2 f}{\partial \underline{\sigma}^2} \right)^{-1} \quad (4.86)$$

4.3.5 Model appraisal

The performance and the accuracy of the developed elasto-plastic model are assessed using results available from the literature. All the selected examples are governed by the compressive behavior.

4.3.5.1 Uniaxial compressive tests

The uniaxial compressive tests 3B2-4 to 3B2-6, carried out by Van Mier (1984), were selected for a comparison with the proposed model. One single 4-node Lagrangian plane stress finite element with 1×1 Gauss-Legendre integration scheme is used to simulate the experimental results. The dimensions of the finite element coincides with those of specimen (200×200×200 mm³). Table 4.6 shows the adopted concrete properties. The numerical and the experimental results are compared in Figure 4.23.

Up to peak stress, the model matches with high accuracy the experimental results. In the softening phase, and for strains higher than 4.5 %, the model estimates a residual strength that is lower than those experimentally obtained. This indicates that the softening

branch of the uniaxial compressive behavior proposed by CEB-FIB (1993), mainly the second softening branch, $\bar{\sigma}_3(\kappa)$, may not be suitable to reproduce this type of test.

Table 4.6 – Concrete properties used in the simulation of the uniaxial compressive test.

Poisson's ratio	$\nu_c = 0.20$
Initial Young's modulus	$E_c = 33344.0 \text{ N/mm}^2$
Compressive strength	$f_c = 43.24 \text{ N/mm}^2$
Strain at peak compression stress	$\varepsilon_{c1} = 2.7 \times 10^{-3}$
Parameter defining the initial yield surface	$\alpha_0 = 0.3$

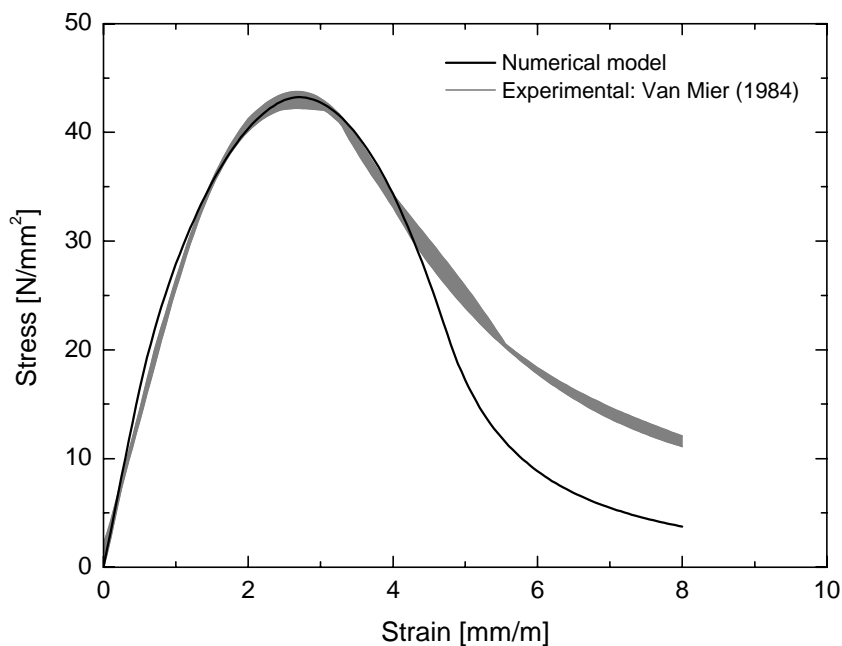


Figure 4.23 – Stress-strain relationships: experimental and numerical results.

4.3.5.2 Biaxial compressive test

To evaluate the importance of the h_c parameter in the flow rule, the biaxial compressive tests carried out by Kupfer et al. (1969) were selected. One single 4-node Lagrangian plane stress element with 1×1 Gauss-Legendre integration scheme is used in the numerical model. Table 4.7 shows the properties adopted for the concrete and for the yield surface. In

Figure 4.24 the numerical simulations with $c_0 = 0$ ($h_c = 1.0$) and $c_0 = 6.056$ are compared with the experimental results.

Table 4.7 – Concrete properties used in the simulation of the biaxial compressive test.

Poisson's ratio	$\nu_c = 0.20$
Initial Young's modulus	$E_c = 30180.0 \text{ N/mm}^2$
Compressive strength	$f_c = 32.06 \text{ N/mm}^2$
Strain at peak compression stress	$\epsilon_{c1} = 2.2 \times 10^{-3}$
Parameter defining the initial yield surface	$\alpha_0 = 0.3$

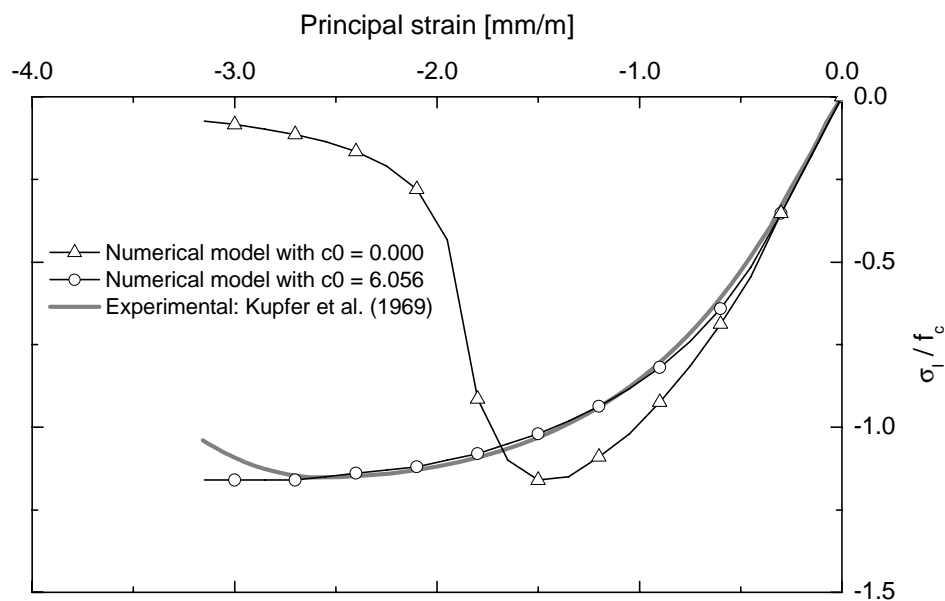


Figure 4.24 – Influence of the c_0 parameter in numerical response.

The results shown in Figure 4.24 indicate that the response obtained with $c_0 = 0$ is stiffer in the hardening phase and too brittle after the peak stress. A good agreement with the experimental results is obtained with $c_0 = 6.056$.

4.4 ELASTO-PLASTIC MULTI-FIXED SMEARED CRACK MODEL

In the present section an elasto-plastic multi-fixed smeared crack model is proposed. This model corresponds to the coupling of the multi-fixed smeared crack model described in Section 4.2 and the elasto-plastic model presented in Section 4.3. In the following sections the implemented model is described.

4.4.1 Yield surface

Two types of yield surface are combined in the proposed numerical model: the Rankine criterion (described in Section 4.2.1.5) for concrete in tension, and the Owen and Figueiras (1983) yield surface (described in Section 4.3.4.1) for concrete in compression. Figure 4.25 represents the initial and the limit yield surfaces. Experimental results from Kupfer et al. (1969) are also included.

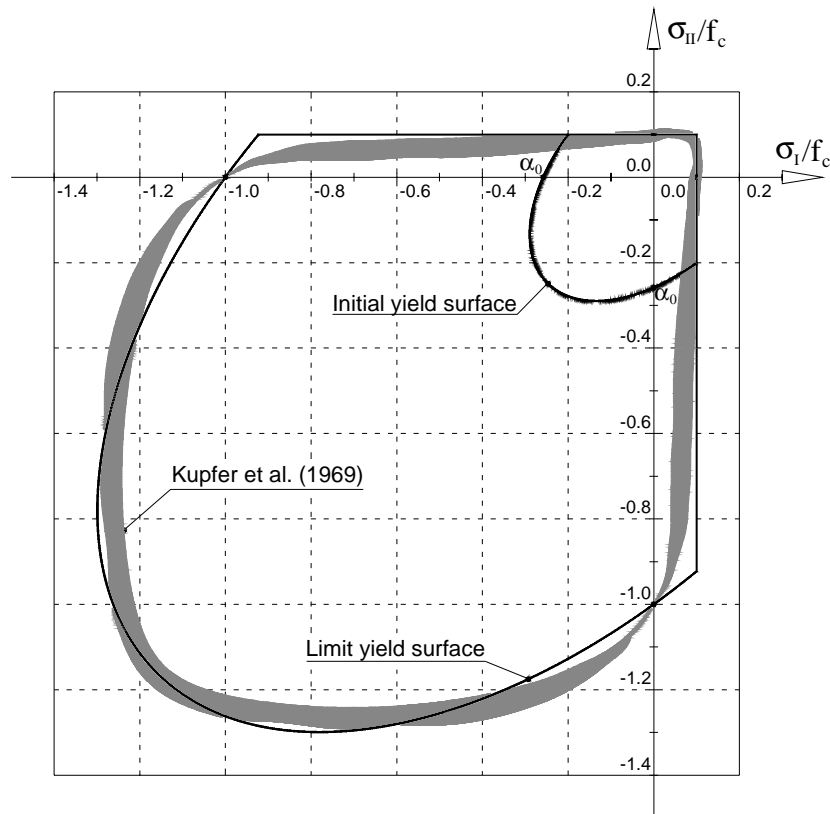


Figure 4.25 – Yield surface adopted in the elasto-plastic multi-fixed smeared crack model.

4.4.2 Integration of the constitutive equations

The incremental strain vector is decomposed in an incremental crack strain vector, $\Delta \underline{\underline{\varepsilon}}^{cr}$, and an incremental strain vector of the concrete between cracks, $\Delta \underline{\underline{\varepsilon}}^{co}$. This vector is decomposed in an elastic reversible part, $\Delta \underline{\underline{\varepsilon}}^e$, and an irreversible or plastic part, $\Delta \underline{\underline{\varepsilon}}^p$, resulting

$$\Delta \underline{\underline{\varepsilon}} = \Delta \underline{\underline{\varepsilon}}^{cr} + \Delta \underline{\underline{\varepsilon}}^{co} = \Delta \underline{\underline{\varepsilon}}^{cr} + \Delta \underline{\underline{\varepsilon}}^e + \Delta \underline{\underline{\varepsilon}}^p \quad (4.87)$$

The constitutive equations of the present model follow the multi-fixed smeared crack model and the elasto-plastic model and are deduced in the following sections.

4.4.2.1 Constitutive equations from the multi-fixed smeared crack model

The incremental stress vector can be computed from the incremental elastic strain vector,

$$\Delta \underline{\underline{\sigma}}_m = \underline{\underline{D}}^e \Delta \underline{\underline{\varepsilon}}_m^e \quad (4.88)$$

Incorporating (4.88) into (4.48) leads to

$$\underline{\underline{\sigma}}_{\ell,m-1}^{cr} + \Delta \underline{\underline{\sigma}}_{\ell,m}^{cr} = \underline{\underline{T}}_m^{cr} \left(\underline{\underline{\sigma}}_{m-1} + \underline{\underline{D}}^e \Delta \underline{\underline{\varepsilon}}_m^e \right) \quad (4.89)$$

Substituting (4.87) into (4.89) yields

$$\underline{\underline{\sigma}}_{\ell,m-1}^{cr} + \Delta \underline{\underline{\sigma}}_{\ell,m}^{cr} = \underline{\underline{T}}_m^{cr} \underline{\underline{\sigma}}_{m-1} + \underline{\underline{T}}_m^{cr} \underline{\underline{D}}^e \left(\Delta \underline{\underline{\varepsilon}}_m - \Delta \underline{\underline{\varepsilon}}_m^p \right) - \underline{\underline{T}}_m^{cr} \underline{\underline{D}}^e \left[\underline{\underline{T}}_m^{cr} \right]^{-T} \Delta \underline{\underline{\varepsilon}}_{\ell,m}^{cr} \quad (4.90)$$

and including (4.79) in (4.90) results in

$$\begin{aligned} & \underline{\underline{\sigma}}_{\ell,m-1}^{cr} + \Delta \underline{\underline{\sigma}}_{\ell,m}^{cr} \left(\Delta \underline{\underline{\varepsilon}}_{\ell,m}^{cr} \right) + \underline{\underline{T}}_m^{cr} \underline{\underline{D}}^e \left[\underline{\underline{T}}_m^{cr} \right]^{-T} \Delta \underline{\underline{\varepsilon}}_{\ell,m}^{cr} - \underline{\underline{T}}_m^{cr} \underline{\underline{\sigma}}_{m-1} - \\ & \underline{\underline{T}}_m^{cr} \underline{\underline{D}}^e \left(\Delta \underline{\underline{\varepsilon}}_m - \Delta \lambda_m h_{c,m} \left(\frac{\partial f}{\partial \underline{\underline{\sigma}}} \right)_m \right) = \underline{\underline{0}} \end{aligned} \quad (4.91)$$

4.4.2.2 Constitutive equations from the elasto-plastic model

The incremental elastic strain vector, $\Delta \underline{\boldsymbol{\varepsilon}}_m^e$, multiplied by the elastic constitutive matrix, $\underline{\boldsymbol{D}}^e$, is used to update the stress vector, which leads to

$$\underline{\boldsymbol{\sigma}}_m = \underline{\boldsymbol{\sigma}}_{m-1} + \underline{\boldsymbol{D}}^e \Delta \underline{\boldsymbol{\varepsilon}}_m^e \quad (4.92)$$

Including (4.87) and (4.79) in (4.92) yields to

$$\underline{\boldsymbol{\sigma}}_m = \underline{\boldsymbol{\sigma}}_{m-1} + \underline{\boldsymbol{D}}^e \left(\Delta \underline{\boldsymbol{\varepsilon}}_m - \Delta \underline{\boldsymbol{\varepsilon}}_m^{cr} \right) - \Delta \lambda_m h_{c,m} \underline{\boldsymbol{D}}^e \left(\frac{\partial f}{\partial \underline{\boldsymbol{\sigma}}} \right)_m \quad (4.93)$$

This equation can be written in a more suitable format as

$$\left[\underline{\boldsymbol{D}}^e \right]^{-1} \left(\underline{\boldsymbol{\sigma}}_m - \underline{\boldsymbol{\sigma}}_{m-1} - \underline{\boldsymbol{D}}^e \left(\Delta \underline{\boldsymbol{\varepsilon}}_m - \Delta \underline{\boldsymbol{\varepsilon}}_m^{cr} \right) \right) + \Delta \lambda_m h_{c,m} \left(\frac{\partial f}{\partial \underline{\boldsymbol{\sigma}}} \right)_m = \underline{\mathbf{0}} \quad (4.94)$$

or

$$\left[\underline{\boldsymbol{D}}^e \right]^{-1} \left(\underline{\boldsymbol{\sigma}}_m - \underline{\boldsymbol{\sigma}}_{m-1} - \underline{\boldsymbol{D}}^e \left(\Delta \underline{\boldsymbol{\varepsilon}}_m - \left[\underline{\boldsymbol{T}}_m^{cr} \right]^T \Delta \underline{\boldsymbol{\varepsilon}}_{l,m}^{cr} \right) \right) + \Delta \lambda_m h_{c,m} \left(\frac{\partial f}{\partial \underline{\boldsymbol{\sigma}}} \right)_m = \underline{\mathbf{0}} \quad (4.95)$$

4.4.2.3 Return-mapping algorithm

Equations (4.91), (4.95) and (4.73) define the system of nonlinear equations that corresponds to the return-mapping algorithm of the present model. Assuming $\Delta \kappa = \Delta \lambda$ (see Section 4.3.4.3) this system becomes

$$\left\{ \begin{array}{l}
 \underline{f}_{1,m} = \underline{\sigma}_{\ell,m-1}^{cr} + \Delta \underline{\sigma}_{\ell,m}^{cr} (\Delta \underline{\varepsilon}_{\ell,m}^{cr}) + \underline{T}_m^{cr} \underline{D}^e \left[\underline{T}_m^{cr} \right]^T \Delta \underline{\varepsilon}_{\ell,m}^{cr} - \underline{T}_m^{cr} \underline{\sigma}_{m-1} - \\
 \quad \underline{T}_m^{cr} \underline{D}^e \left(\Delta \underline{\varepsilon}_m - \Delta \kappa_m h_{c,m} \left(\frac{\partial f}{\partial \underline{\sigma}} \right)_m \right) = \underline{0} \\
 \underline{f}_{2,m} = \left[\underline{D}^e \right]^{-1} \left(\underline{\sigma}_m - \underline{\sigma}_{m-1} - \underline{D}^e \left(\Delta \underline{\varepsilon}_m - \left[\underline{T}_m^{cr} \right]^T \Delta \underline{\varepsilon}_{\ell,m}^{cr} \right) \right) + \Delta \kappa_m h_{c,m} \left(\frac{\partial f}{\partial \underline{\sigma}} \right)_m = \underline{0} \\
 \underline{f}_{3,m} = f(\underline{\sigma}_m, \kappa_m) = 0
 \end{array} \right. \quad (4.96)$$

In the system of nonlinear equations (4.96) the unknowns are $\Delta \underline{\varepsilon}_{\ell,m}^{cr}$, $\underline{\sigma}_m$ and κ_m . Figure 4.26 shows the return-mapping algorithm implemented in the present computer code. The determination of the initial solution is based on the assumption of null plastic flow (see step 2). The residual vector defined in step (3) is given by

$$\underline{r}_m = \left[\underline{f}_{1,m} \quad \underline{f}_{2,m} \quad \underline{f}_{3,m} \right]^T \quad (4.97)$$

and the corresponding norms (step 4) are defined as

$$\|\underline{r}_m\| = \left[\|\underline{f}_{1,m}\|_{\infty} \quad \|\underline{f}_{2,m}\|_{\infty} \quad \|\underline{f}_{3,m}\| \right]^T \quad (4.98)$$

The Jacobian matrix of step (6) is composed of nine blocks

$$\underline{J} = \begin{bmatrix} \frac{\partial \underline{f}_1}{\partial \Delta \underline{\varepsilon}_{\ell}^{cr}} & \frac{\partial \underline{f}_1}{\partial \underline{\sigma}} & \frac{\partial \underline{f}_1}{\partial \kappa} \\ \frac{\partial \underline{f}_2}{\partial \Delta \underline{\varepsilon}_{\ell}^{cr}} & \frac{\partial \underline{f}_2}{\partial \underline{\sigma}} & \frac{\partial \underline{f}_2}{\partial \kappa} \\ \frac{\partial \underline{f}_3}{\partial \Delta \underline{\varepsilon}_{\ell}^{cr}} & \frac{\partial \underline{f}_3}{\partial \underline{\sigma}} & \frac{\partial \underline{f}_3}{\partial \kappa} \end{bmatrix} \quad (4.99)$$

being

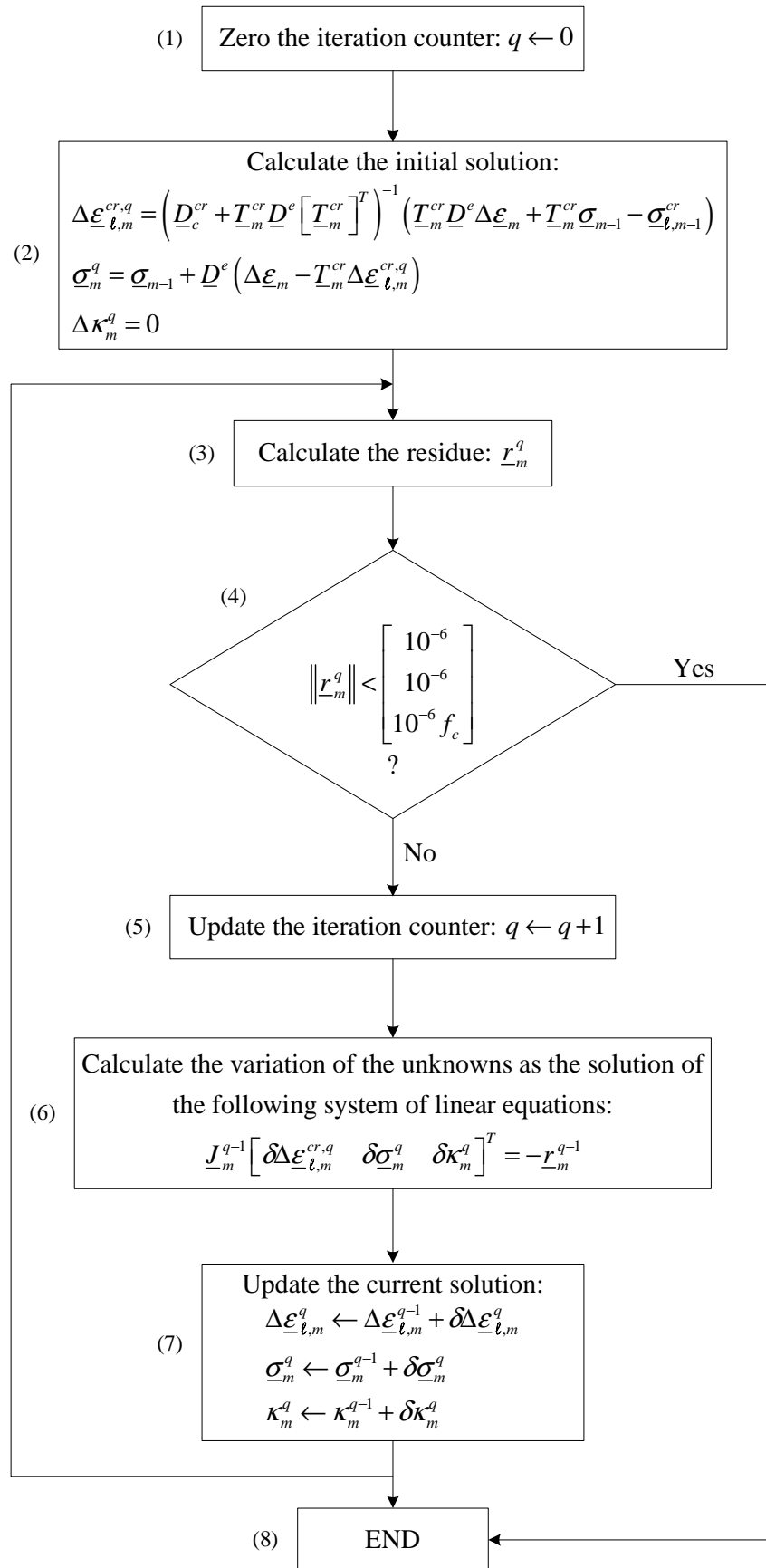


Figure 4.26 – Return-mapping algorithm of the elasto-plastic multi-fixed smeared crack model.

$$\frac{\partial f_1}{\partial \Delta \underline{\varepsilon}_l^{cr}} = \frac{\partial \Delta \underline{\sigma}_l^{cr}}{\partial \Delta \underline{\varepsilon}_l^{cr}} + \underline{T}^{cr} \underline{D}^e \left[\underline{T}^{cr} \right]^T$$

$$\frac{\partial f_1}{\partial \underline{\sigma}} = \underline{T}^{cr} \underline{D}^e \Delta \kappa \left(\frac{\partial f}{\partial \underline{\sigma}} \left(\frac{\partial h_c}{\partial \underline{\sigma}} \right)^T + h_c \frac{\partial^2 f}{\partial \underline{\sigma}^2} \right) \quad (4.100)$$

$$\frac{\partial f_1}{\partial \kappa} = \underline{T}^{cr} \underline{D}^e \left(h_c + \Delta \kappa \frac{\partial h_c}{\partial \kappa} \right) \frac{\partial f}{\partial \underline{\sigma}}$$

$$\frac{\partial f_2}{\partial \Delta \underline{\varepsilon}_l^{cr}} = \left[\underline{T}^{cr} \right]^T$$

$$\frac{\partial f_2}{\partial \underline{\sigma}} = \left[\underline{D}^e \right]^{-1} + \Delta \kappa \left(h_c \frac{\partial^2 f}{\partial \underline{\sigma}^2} + \frac{\partial f}{\partial \underline{\sigma}} \left(\frac{\partial h_c}{\partial \underline{\sigma}} \right)^T \right) \quad (4.101)$$

$$\frac{\partial f_2}{\partial \kappa} = \left(h_c + \Delta \kappa \frac{\partial h_c}{\partial \kappa} \right) \frac{\partial f}{\partial \underline{\sigma}}$$

$$\frac{\partial f_3}{\partial \Delta \underline{\varepsilon}_l^{cr}} = \underline{0}^T$$

$$\frac{\partial f_3}{\partial \underline{\sigma}} = \left(\frac{\partial f}{\partial \underline{\sigma}} \right)^T \quad (4.102)$$

$$\frac{\partial f_3}{\partial \kappa} = \frac{\partial f}{\partial \kappa}$$

These derivatives are defined in Sections 4.2.3.1 and 4.3.4.3. In the present model $\partial h_c / \partial \kappa = 0$.

4.4.2.4 Method proposed by de Borst and Nauta

An additional algorithm was implemented to be used when the algorithm of Figure 4.26 fails. This algorithm was proposed by de Borst and Nauta (1985). In the method proposed by de Borst and Nauta the constitutive equations of the smeared crack model and the constitutive equations of the elasto-plastic model are solved separately. To solve the constitutive equations of the smeared crack model, the procedure described in Section 4.2.3 is used, replacing $\Delta \underline{\varepsilon}$ by $\Delta \underline{\varepsilon} - \Delta \underline{\varepsilon}^p$. The constitutive equations of the elasto-plastic model

are solved using the procedure described in Section 4.3.4, replacing $\Delta \underline{\varepsilon}$ by $\Delta \underline{\varepsilon} - \Delta \underline{\varepsilon}^{cr}$. Figure 4.27 shows the implemented algorithm. The determination of the initial solution is based on the assumption of null plastic flow (see step 2). The solution is reached when the yield surface is not violated (step 4).

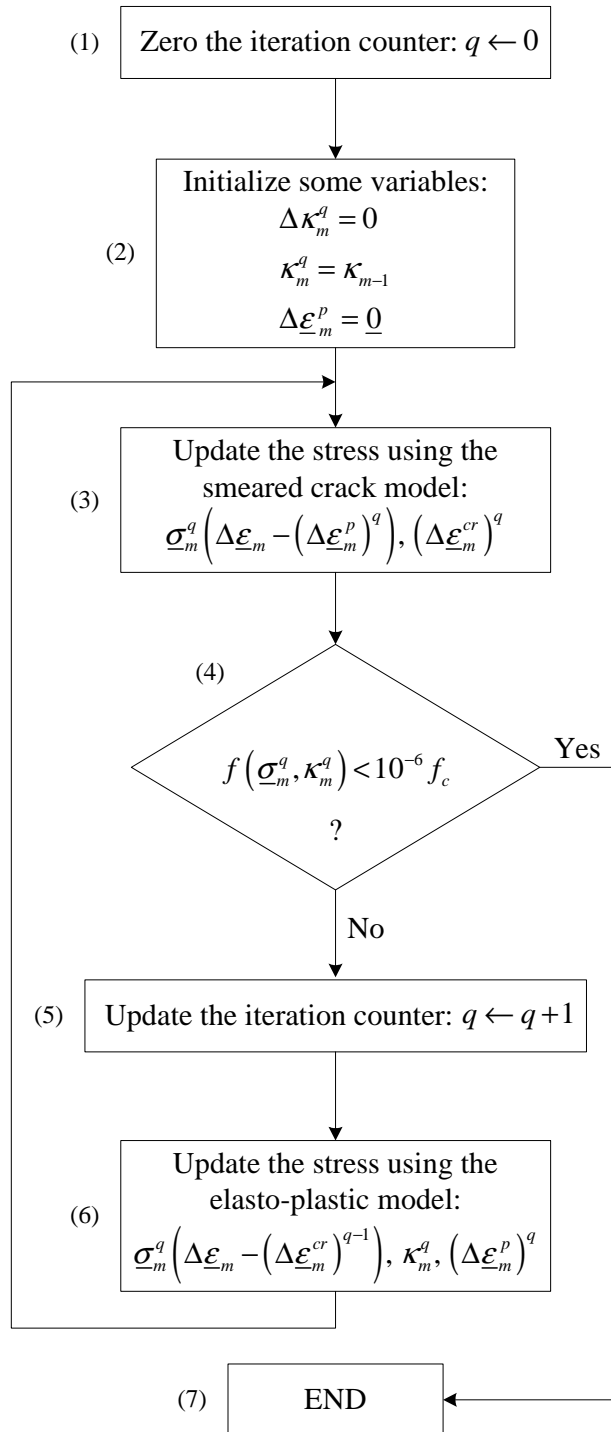


Figure 4.27 – Method proposed by de Borst and Nauta (1985).

4.4.3 Consistent tangent operator

The elasto-plastic cracked consistent tangent operator, \underline{D}^{epcr} , can be calculated from the elasto-plastic consistent tangent constitutive matrix \underline{D}^{ep} (see Section 4.3.4.4) and from the constitutive matrix of cracked concrete, \underline{D}^{crco} (see Section 4.2.1.4). The incremental stress vector, $\Delta\sigma$, is obtained with

$$\Delta\sigma = \underline{D}^{ep} \Delta\epsilon^{ep} \quad (4.103)$$

where \underline{D}^{ep} is the elasto-plastic consistent tangent constitutive matrix, and $\Delta\epsilon^{ep}$ is the incremental elasto-plastic strain vector, which includes the elastic and the plastic variations of the strain vector ($\Delta\epsilon^e + \Delta\epsilon^p$). Incorporating equation (4.87) into (4.103) and using (4.14) yields

$$\Delta\sigma = \underline{D}^{ep} \left(\Delta\epsilon - [\underline{T}^{cr}]^T \Delta\epsilon_{\ell}^{cr} \right) \quad (4.104)$$

Pre-multiplying equation (4.104) by \underline{T}^{cr} and substituting (4.17) and (4.20) in the left side of (4.104), an expression that evaluates the incremental crack strain vector from the incremental cracked concrete strain vector is obtained,

$$\Delta\epsilon_{\ell}^{cr} = \left(\underline{D}^{cr} + \underline{T}^{cr} \underline{D}^{ep} [\underline{T}^{cr}]^T \right)^{-1} \underline{T}^{cr} \underline{D}^{ep} \Delta\epsilon \quad (4.105)$$

Including (4.105) in (4.104) the constitutive law for cracked concrete is obtained

$$\Delta\sigma = \left(\underline{D}^{ep} - \underline{D}^{ep} [\underline{T}^{cr}]^T \left(\underline{D}^{cr} + \underline{T}^{cr} \underline{D}^{ep} [\underline{T}^{cr}]^T \right)^{-1} \underline{T}^{cr} \underline{D}^{ep} \right) \Delta\epsilon \quad (4.106)$$

or

$$\Delta\sigma = \underline{D}^{epcr} \Delta\epsilon \quad (4.107)$$

where \underline{D}^{epcr} is the consistent tangent constitutive matrix for the elasto-plastic cracked concrete

$$\underline{D}^{epcr} = \underline{D}^{ep} - \underline{D}^{ep} \left[\underline{T}^{cr} \right]^T \left(\underline{D}^{cr} + \underline{T}^{cr} \underline{D}^{ep} \left[\underline{T}^{cr} \right]^T \right)^{-1} \underline{T}^{cr} \underline{D}^{ep} \quad (4.108)$$

4.4.4 Model appraisal

The first part of this section describes some numerical tests that have the main purpose of evaluating the performance of the model under cyclic loading, inducing different crack statuses and irreversible deformations. In the second part, the performance of the developed elasto-plastic multi-fixed smeared crack model is assessed using results available from the literature.

The numerical tests were performed using one single 4-node Lagrangian plane stress element with 1×1 Gauss-Legendre integration scheme. Table 4.8 shows the adopted parameters. Three numerical tests were selected from all that were carried out during the developing phase of the model. In the remaining part of this section a description of these tests is performed.

Table 4.8 – Concrete properties used in the simulation of the numerical tests.

Poisson's ratio	$\nu_c = 0.20$
Initial Young's modulus	$E_c = 33550.0 \text{ N/mm}^2$
Compressive strength	$f_c = 38.0 \text{ N/mm}^2$
Strain at peak compression stress	$\varepsilon_1 = 2.2 \times 10^{-3}$
Parameter defining the initial yield surface	$\alpha_0 = 0.3$
Tensile strength	$f_{ct} = 2.9 \text{ N/mm}^2$
Type of softening diagram	<i>Exponential</i>
Fracture energy	$G_f = 0.5 \text{ N/mm}$
Shear retention factor	<i>Exponential ($p_2 = 2$)</i>
Crack band-width	<i>Square root of the area of the element</i>

4.4.4.1 Traction-compression-traction (TCT) numerical test

In the first uniaxial test, the element is, initially, submitted to a tensile force up to the formation of a single crack (steps 1 and 2 in Figure 4.28(a)). With the purpose of inducing plastic deformation under compression, compressive forces are applied (step 3 and 4). In the beginning of the compressive softening phase response, the loading direction is reversed causing a return to the crack-opening process (steps 5 and 6). The loading procedure is terminated at step 7, which corresponds to a complete dissipation of the fracture energy (*fully open crack status*).

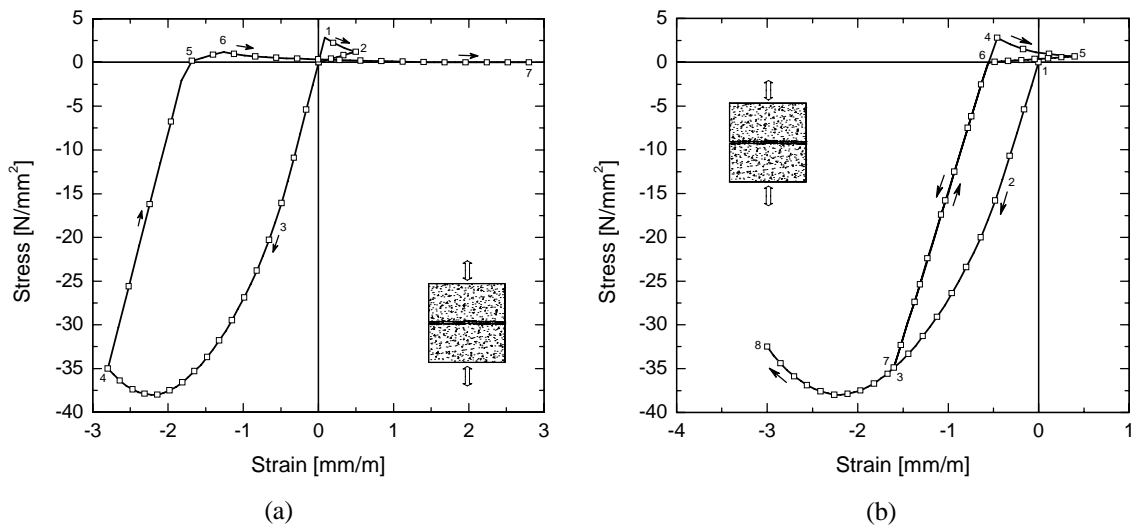


Figure 4.28 – Numerical tests: (a) TCT test; (b) CTC test.

4.4.4.2 Compression-traction-compression (CTC) numerical test

This uniaxial test consists in, firstly, submitting the element to a compressive force up to the occurrence of plastic deformation under compression (steps 1, 2 and 3 in Figure 4.28(b)). Afterwards, loading is reversed and is increased up to crack formation (step 4) and crack propagation (step 5). At the tensile softening phase loading is again reversed until the compressive softening response is reached.

4.4.4.3 Biaxial numerical test

The biaxial test consists in the application of biaxial tensile forces up to the formation of two orthogonal cracks (step 1 in Figure 4.29). Afterwards, loading in x_1 direction is reversed in order to induce compressive forces with the same direction. In x_2 direction the load continues its progression in the same direction until total dissipation of the fracture energy (step 2 and 3 in Figure 4.29). In step 4, the concrete reaches a compressive softening phase (x_1 direction) and the crack orthogonal to x_2 direction remains with *fully open* status. Figure 4.29 shows the obtained response in terms of x_1 and x_2 normal stresses.

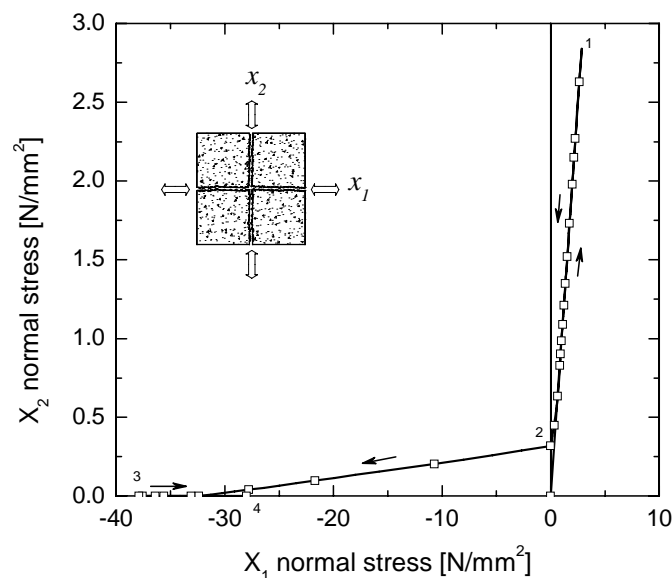


Figure 4.29 – Biaxial numerical test.

4.4.4.4 Beam failing by shear

Figure 4.30 shows the finite element mesh adopted in the simulation of the behavior of the beam tested by Walraven (1978). Due to its load and properties the beam failed by shear. In the simulation, 8-node Serendipity plane stress elements with 3×3 Gauss-Legendre integration scheme are used. Table 4.9 includes the main properties of the concrete. The properties of the elasto-perfect-plastic steel reinforcement located in the bottom side of the beam are: Young modulus's $E_s = 210000 \text{ N/mm}^2$; yield stress $f_{sy} = 440 \text{ N/mm}^2$.

Some researchers have already used this test with the aim of assessing the performance of other models (de Borst and Nauta 1985, Póvoas 1991, Barros 1995). The obtained results indicate that the simulation of beams failing by shear is a difficult task.

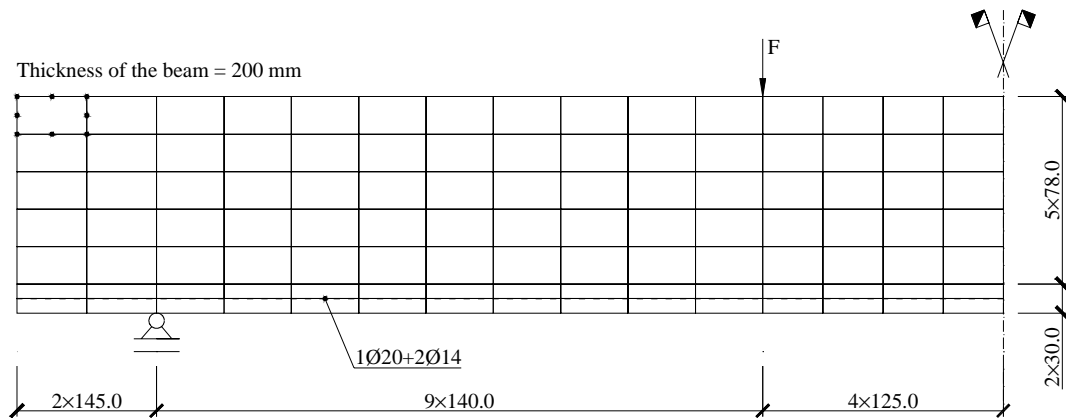


Figure 4.30 – Finite element mesh of the moderately deep beam. Note: all dimensions are in millimeters.

Table 4.9 – Concrete properties used in the simulation of the beam failing by shear.

Poisson's ratio	$\nu_c = 0.20$
Initial Young's modulus	$E_c = 28000.0 \text{ N/mm}^2$
Compressive strength	$f_c = 20.0 \text{ N/mm}^2$
Strain at peak compression stress	$\varepsilon_{c1} = 2.2 \times 10^{-3}$
Parameter defining the initial yield surface	$\alpha_0 = 0.3$
Tensile strength	$f_{ct} = 2.5 \text{ N/mm}^2$
Tri-linear softening diagram parameters	$\xi_1 = 0.01$; $\alpha_1 = 0.45$; $\xi_2 = 0.05$; $\alpha_2 = 0.10$
Fracture energy	$G_f = 0.06 \text{ N/mm}$
Parameter defining the mode I fracture energy available to the new crack	$p_1 = 2$
Shear retention factor	<i>Exponential</i> ($p_2 = 2$)
Crack band-width	<i>Square root of the area of the integration point</i>
Threshold angle	$\alpha_{th} = 30^\circ$

Figure 4.31 and Figure 4.32 show the experimental and the numerical crack pattern obtained, respectively. A shear crack near the middle of the shear-span of the represented

part of the beam can be easily identified. Due to the perfect bond assumed between the reinforcement and the concrete, the numerical model has predicted the formation of cracks at the reinforcement level, which were not observed in the experimental test. Figure 4.33 includes all cracks and the plastic zones. In some integration points, the concrete is cracked and exhibits plastic deformation, simultaneously.

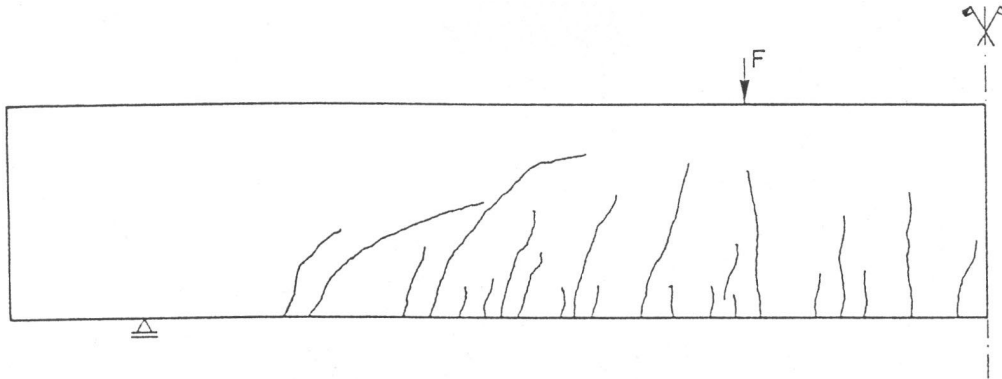


Figure 4.31 – Experimental crack pattern at impending failure (de Borst and Nauta 1985).

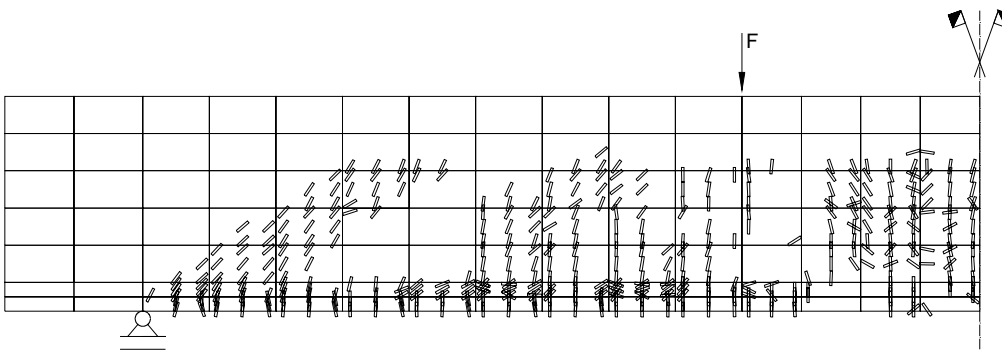


Figure 4.32 – Numerical crack pattern at the final stage (only cracks with *opening* status are included).

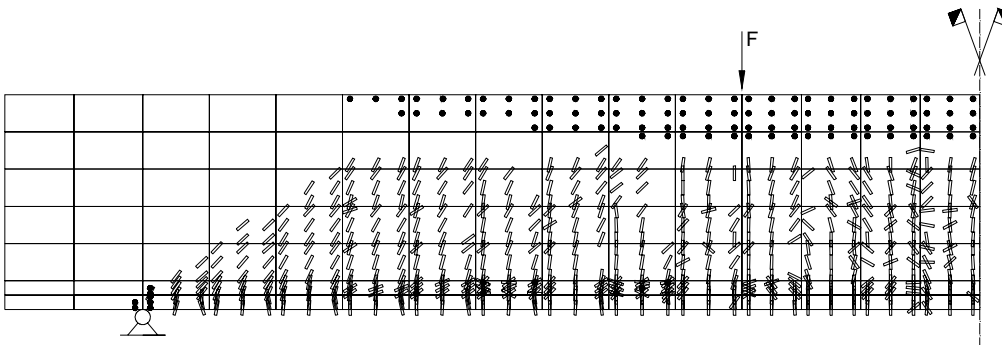


Figure 4.33 – Numerical crack pattern (all cracks) and plastic zones (represented by circles) at the final stage.

Figure 4.34 shows the relationship between the load and the deflection at mid-span, for both the experimental test and the numerical analysis. A good agreement can be observed with the exception of the ultimate load, which is higher in the numerical simulation. The reason for this behavior is the non-shear failure obtained with the numerical model.

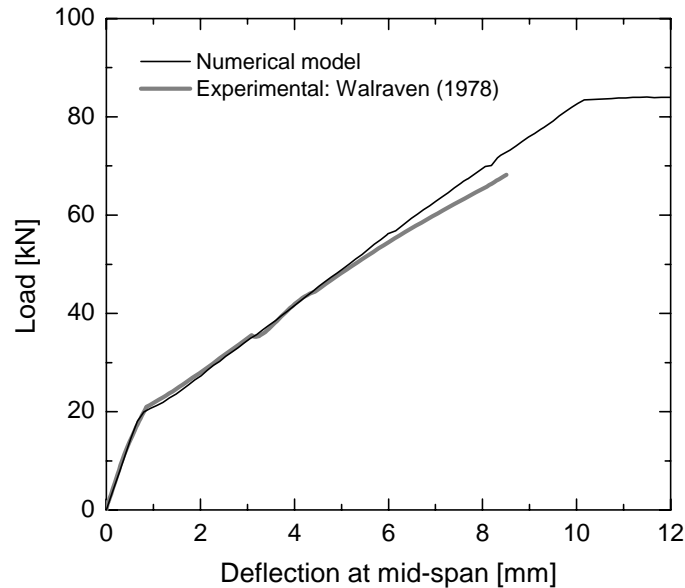


Figure 4.34 – Load vs. deflection at mid-span: experimental and numerical results.

4.5 LINE INTERFACE FINITE ELEMENT

In this section a finite element formulation for interface elements is presented. Interface elements can be divided into two classes: the continuous interface elements and the nodal or point interface elements (Schellekens 1990). The latter, to a certain extent, are identical to spring elements (Ngo and Scordelis 1967). The stiffness matrix of a continuous interface element can be numerically or lumped integrated. The first approach is used in the present work. A description of nodal interface elements and lumped continuous interface elements can be found elsewhere, e.g., Ngo and Scordelis (1967) or Schellekens (1990).

4.5.1 Finite element formulation

The four and six-node 2D line interface elements used in the present work are schematically represented in Figure 4.35. The nodal coordinates defining the mean line (dashed line in Figure 4.35) define the local coordinate system (x'_1, x'_2) and are calculated by means of a linear interpolation between the bottom and top nodal coordinates. The first axis of the local coordinate system, x'_1 , is tangent to the mean line, and the second, x'_2 , is normal to the same line. In the local coordinate system, x'_i , the continuous displacement field is

$$\underline{u}' = [u'_{B1} \quad u'_{B2} \quad u'_{T1} \quad u'_{T2}]^T \quad (4.109)$$

where u'_{Bi} is the i -th component of the displacement field in the bottom line of the finite element, and u'_{Ti} has the same meaning but corresponds to the top line.

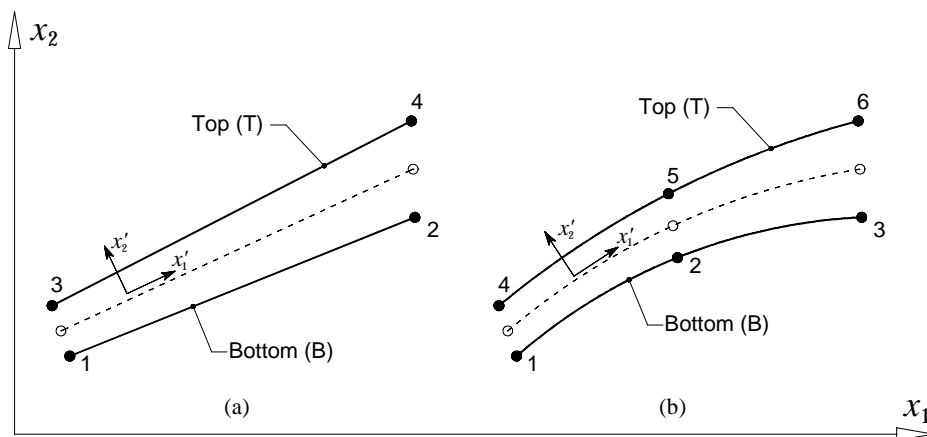


Figure 4.35 – 2D line interface elements: (a) linear 4-node; (b) quadratic 6-node.

In this section the expressions of the stiffness matrix and of the internal equivalent nodal forces are determined taking the 6-node element as an example. The treatment of the 4-node element would be similar. The final expressions are applicable to line interface elements with any even number of nodes.

The nodal displacements, in the local coordinate system, of the element represented in Figure 4.35(b) are grouped in the following vector

$$\underline{a}' = [a'_{11} \quad a'_{12} \mid a'_{21} \quad a'_{22} \mid a'_{31} \quad a'_{32} \mid a'_{41} \quad a'_{42} \mid a'_{51} \quad a'_{52} \mid a'_{61} \quad a'_{62}]^T \quad (4.110)$$

where a'_{ij} is the displacement of node i in the x'_j direction. The continuous displacement field is obtained from the element nodal displacements using the interpolation

$$\underline{u}' = \underline{N} \underline{a}' \quad (4.111)$$

where \underline{N} is the matrix of the element shape functions. Equation (4.111), in expanded format, reads

$$\begin{bmatrix} u'_{B1} \\ u'_{B2} \\ u'_{T1} \\ u'_{T2} \end{bmatrix} = \begin{bmatrix} N_1 & 0 & N_2 & 0 & N_3 & 0 & 0 & 0 & 0 & 0 & 0 & 0 \\ 0 & N_1 & 0 & N_2 & 0 & N_3 & 0 & 0 & 0 & 0 & 0 & 0 \\ 0 & 0 & 0 & 0 & 0 & 0 & N_1 & 0 & N_2 & 0 & N_3 & 0 \\ 0 & 0 & 0 & 0 & 0 & 0 & 0 & N_1 & 0 & N_2 & 0 & N_3 \end{bmatrix} \begin{bmatrix} a'_{11} \\ a'_{12} \\ a'_{21} \\ a'_{22} \\ a'_{31} \\ a'_{32} \\ a'_{41} \\ a'_{42} \\ a'_{51} \\ a'_{52} \\ a'_{61} \\ a'_{62} \end{bmatrix} \quad (4.112)$$

where N_i is the i -th shape function of a quadratic 3-node unidimensional element (Zienkiewicz and Taylor 1989). The components of the relative displacement vector, $\Delta \underline{u}'$, can be obtained from the \underline{u}' vector

$$\begin{aligned}
\Delta \underline{u}' &= \begin{bmatrix} \Delta u'_1 \\ \Delta u'_2 \end{bmatrix} = \begin{bmatrix} u'_{T1} - u'_{B1} \\ u'_{T2} - u'_{B2} \end{bmatrix} \\
&= \begin{bmatrix} -1 & 0 & 1 & 0 \\ 0 & -1 & 0 & 1 \end{bmatrix} \begin{bmatrix} u'_{B1} \\ u'_{B2} \\ u'_{T1} \\ u'_{T2} \end{bmatrix} \\
&= \underline{L} \underline{u}'
\end{aligned} \tag{4.113}$$

Substituting (4.111) into (4.113) results

$$\begin{aligned}
\Delta \underline{u}' &= \underline{L} \underline{N} \underline{a}' \\
&= \underline{B} \underline{a}'
\end{aligned} \tag{4.114}$$

where

$$\underline{B} = \underline{L} \underline{N} \tag{4.115}$$

which, in expanded format, reads

$$\underline{B} = \begin{bmatrix} -N_1 & 0 & -N_2 & 0 & -N_3 & 0 & N_1 & 0 & N_2 & 0 & N_3 & 0 \\ 0 & -N_1 & 0 & -N_2 & 0 & -N_3 & 0 & N_1 & 0 & N_2 & 0 & N_3 \end{bmatrix} \tag{4.116}$$

The constitutive behavior of the interface element is simulated with the following stress-relative displacement relationship

$$\underline{\sigma}' = \begin{bmatrix} \sigma'_1 \\ \sigma'_2 \end{bmatrix} = \underline{D} \Delta \underline{u}' \tag{4.117}$$

where σ'_1 and σ'_2 are the tangential and normal stress components of $\underline{\sigma}'$, and \underline{D} is the constitutive matrix

$$\underline{D} = \begin{bmatrix} D_t & 0 \\ 0 & D_n \end{bmatrix} \tag{4.118}$$

with D_t and D_n being the tangential and normal stiffness. For accurate simulations of nonlinear phenomena in concrete structures, such as crack propagation in concrete or slipping between reinforcement and concrete, appropriate laws defining D_t and D_n must be used.

From the principle of virtual work (PVW), the internal work is

$$W_{\text{int}} = \int_S \delta(\Delta \underline{u}')^T \underline{\sigma}' dS \quad (4.119)$$

where $\delta(\Delta \underline{u}')^T$ is the virtual relative displacement vector. The element nodal displacement vector in the local coordinate system (see Figure 4.35), \underline{a}' , can be obtained from the element nodal displacement vector in the global coordinate system, \underline{a} ,

$$\underline{a}' = \underline{T} \underline{a} \quad (4.120)$$

where \underline{T} is the appropriated transformation matrix. Replacing (4.120) into (4.114) yields

$$\Delta \underline{u}' = \underline{B} \underline{a}' = \underline{B} \underline{T} \underline{a} \quad (4.121)$$

and substituting (4.121) into (4.117) leads to

$$\underline{\sigma}' = \underline{D} \underline{B} \underline{T} \underline{a} \quad (4.122)$$

Substituting (4.121) and (4.122) into (4.119) yields

$$\begin{aligned} W_{\text{int}} &= \int_S \delta \underline{a}'^T \underline{T}^T \underline{B}^T \underline{D} \underline{B} \underline{T} \underline{a} dS \\ &= \delta \underline{a}'^T \int_S \underline{T}^T \underline{B}^T \underline{D} \underline{B} \underline{T} dS \underline{a} \end{aligned} \quad (4.123)$$

The work produced by the external forces due to virtual displacements is given by

$$W_{ext} = \delta(\underline{a}')^T \underline{F}' \quad (4.124)$$

where

$$\underline{F}' = \underline{T} \underline{F} \quad (4.125)$$

Substituting (4.120) and (4.125) into (4.124) yields

$$\begin{aligned} W_{ext} &= \delta \underline{a}^T \underline{T}^T \underline{T} \underline{F} \\ &= \delta \underline{a}^T \underline{F} \end{aligned} \quad (4.126)$$

From the PVW, $W_{ext} = W_{int}$, resulting

$$\int_S \underline{T}^T \underline{B}^T \underline{D} \underline{B} \underline{T} dS \underline{a} = \underline{F} \quad (4.127)$$

or

$$\underline{K} \underline{a} = \underline{F} \quad (4.128)$$

with

$$\underline{K} = \int_S \underline{T}^T \underline{B}^T \underline{D} \underline{B} \underline{T} dS \quad (4.129)$$

In (4.128), \underline{K} , is the element stiffness matrix and \underline{F} is the load vector.

To avoid erroneous oscillations in the stress field, an appropriate integration scheme must be selected (Rots 1988, Schellekens 1992). In the present study the interface elements are integrated with the Gauss-Lobatto integration scheme.

4.5.2 Model appraisal

The results obtained in the series fcm70_Lb80_M of the pullout-bending tests described in Chapter 2 are used to evaluate the performance of the developed line interface element. The pullout-bending test is considered a plane stress problem. Figure 4.36 shows the finite element mesh adopted in the simulation, where 4-node Lagrangian plane stress elements with 2×2 Gauss-Legendre integration scheme are used to simulate the concrete beam and the steel hinge. The CFRP is simulated with 2D frame elements. Linear elastic behavior is assumed for these materials, with properties obtained in the experimental program. To connect the CFRP to concrete, 4-node line interface elements with two-point Gauss-Lobatto integration rule are used. The bond stress-slip relationship obtained for the series fcm70_Lb80_M is used to model the tangential stiffness of the interface elements (see Section 3.3),

$$\sigma'_1 = D_t \Delta u_1 = \begin{cases} 18.2 \left(\frac{s}{0.35} \right)^{0.19} & \text{if } s \leq 0.35 \\ 18.2 \left(\frac{s}{0.35} \right)^{-0.27} & \text{if } s > 0.35 \end{cases} \quad (4.130)$$

Assuming that the normal stiffness of the interface element has marginal effect on the bonding behavior between CFRP and concrete, a constant value of 10^6 N/mm^3 is attributed to D_n . The load is applied by direct displacement-control at the loaded point.

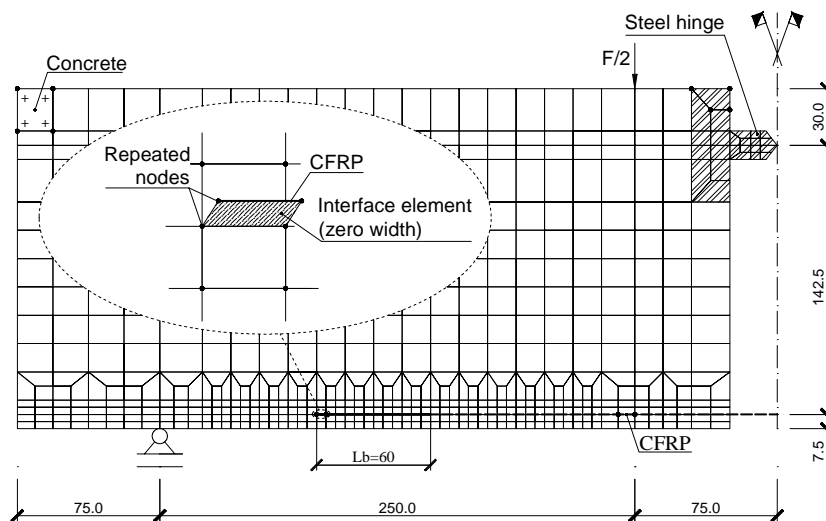


Figure 4.36 – Finite element model. Note: all dimensions are in millimeters.

In Figure 4.37 the relationship between the pullout force and the loaded end slip obtained numerically is compared with the results registered experimentally. As expected, a good agreement is observed.

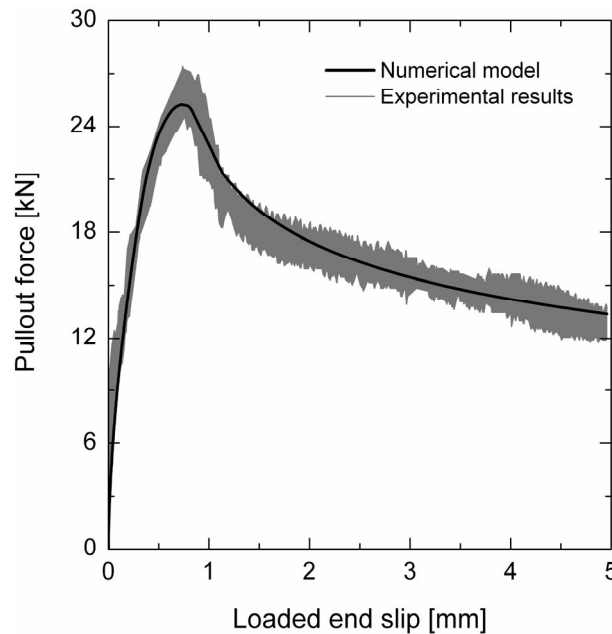


Figure 4.37 – Pullout force vs. loaded end slip: experimental and numerical results.

4.6 SUMMARY AND CONCLUSIONS

The present chapter described the developed tools whose purpose is the numerical simulation of concrete structures strengthened with near-surface mounted CFRP laminate strips.

The Newton-Raphson method as an iterative technique for the solution of nonlinear finite element problems was briefly presented. The proposed numerical tools are implemented in a finite element computer code whose main characteristics were briefly described.

The formulation of the developed elasto-plastic multi-fixed smeared crack model was described in detail. This model has two independent yield surfaces: one for concrete in tension and the other for concrete in compression. The former controls crack initiation and propagation and the latter controls the plastic behavior of compressed concrete. The

incremental strain vector $\Delta \underline{\varepsilon}$ is decomposed in order to accurately simulate the crack status evolution. The post-cracking behavior of concrete depends on the tension-softening diagram. In the developed computer code several alternatives for this diagram are available. Fully implicit Euler backward integration schemes are used to integrate the constitutive equations. Data available in the literature was used to show that the developed model can predict, with enough accuracy, the nonlinear behavior of concrete structures.

A finite element formulation for interface elements, whose purpose is the simulation of the CFRP-concrete interface, was presented. The tangential component of the corresponding constitutive matrix is based on the relationship obtained in the analytical analysis performed in Chapter 3. The developed interface element was validated by means of a comparison with the experimental results presented in Chapter 2.

CHAPTER 5

NUMERICAL APPLICATIONS

The applications described in this chapter assess the ability of the developed numerical tools in the simulation of the main features observed in the experimental tests of reinforced concrete structures strengthened with near-surface mounted CFRP laminate strips. Aspects such as crack initiation, stiffness degradation, yield initiation in the rebars, load carrying capacity and crack patterns will also be focused. The importance of modeling the bond-slip behavior at the CFRP-concrete interface in this type of structures is investigated. Two groups of reinforced concrete beams are analyzed. The first group is composed of beams with flexural strengthening, whereas the second group deals with shear-strengthened beams. Both groups of beams were tested in the Laboratory of the Structural Division of the Civil Engineering Department of the University of Minho, Portugal.

5.1 CONCRETE PROPERTIES

The previously described concrete constitutive model requires the definition of a considerable number of material properties. These properties must characterize the concrete used in the structures to be analyzed, in order to assure numerical simulations with enough accuracy. These aspects are treated in the following sections.

5.1.1 Uniaxial behavior of plain concrete

Figure 5.1(a) shows the typical stress-strain response of a concrete specimen under uniaxial compressive loading. Up to approximately 30 % of the compressive strength, f_c , the concrete exhibits a linear elastic behavior. From this stress level up to the peak load, a gradual decrease of the stiffness is observed. After the peak stress, the stiffness becomes negative and the descending branch of the stress-strain curve characterizes the softening behavior of concrete under uniaxial compressive loading. According to van Mier et al. (1997), the concrete compressive strength depends on the type of test machine loading platens and the slenderness of the specimen, h/d , where h is the height of the specimen

and d is either the diameter of a cylinder specimen or the width of a prism, depending on which type of geometry is used. When the friction between platen and specimen is high, a decrease of the h/d ratio causes an increase of the concrete compressive strength. In contrast, when the friction is low, the concrete compressive strength measured in prisms or cylinders is independent of the h/d ratio. When low-friction platens are used, the pre-peak branch of the compressive stress-strain curve is also independent of the slenderness of the specimen. However, in the post-peak branch and for all loading systems, the ductility is significantly increased with the decrease of the h/d ratio. According to van Mier et al. (1997), the post-peak behavior seems to be a mixture of material and structural behavior.

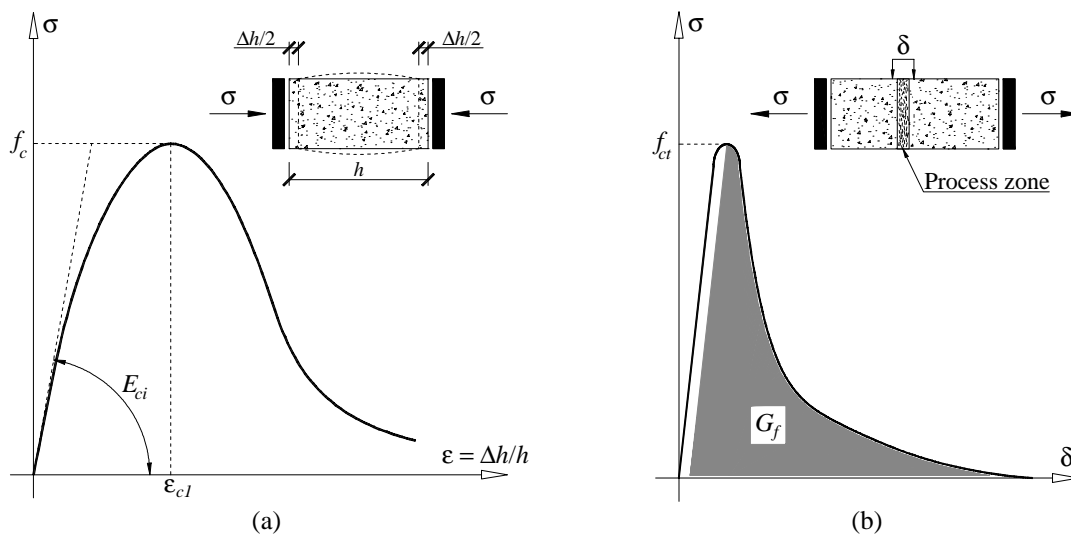


Figure 5.1 – (a) Stress-strain response of concrete under uniaxial compressive loading. (b) Stress-displacement response of concrete under uniaxial tensile loading.

The characterization of the concrete used in most experimental programs is scarce and is commonly limited to the determination of the uniaxial compressive strength, which is based on direct compression tests, with cylinders of 150 mm diameter and 300 mm height. With these tests, the mean value of the uniaxial compressive strength, f_{cm} , is evaluated. The characteristic compressive strength, f_{ck} , can be estimated with the following expression (CEB 1993)

$$f_{ck} = f_{cm} - 8 \text{ [MPa]} \quad (5.1)$$

Young's modulus of concrete, E_{ci} , is defined as the initial slope of the uniaxial compressive stress-strain diagram (see Figure 5.1(a)). The values of E_{ci} for normal weight concrete can be estimated from (CEB 1993)

$$E_{ci} = 9979 f_{cm}^{1/3} \text{ [MPa]} \quad (5.2)$$

Following the recommendations of CEB-FIB (1993), the strain value at the peak stress, ε_{cl} , is considered constant and equal to 0.0022.

Poisson's ratio of concrete, ν_c , ranges between 0.1 and 0.2. In the numerical simulations of the present chapter a Poisson's ratio of 0.15 is adopted.

Figure 5.1(b) shows the stress-displacement curve obtained in a uniaxial tensile test. Up to approximately 90 % of the maximum tensile strength, f_{ct} , the concrete behaves as a linear elastic material. At this stage, strains and micro-cracks start to localize in a narrow zone, named process zone, and afterwards a continuous macro-crack is developed. The width of the macro-crack increases and the stiffness reduces rapidly until the macro-crack cannot transfer any tensile stress. The post-peak branch of the stress-displacement curve is usually named softening branch.

The tensile strength is influenced by the shape and surface texture of the aggregates and may be reduced substantially by environmental effects. The lower and upper values of the characteristic tensile strength, $f_{ct,\min}$ and $f_{ct,\max}$, respectively, can be estimated from the characteristic compressive strength, f_{ck} (CEB 1993)

$$f_{ct,\min} = 0.20 f_{ck}^{2/3} \text{ [MPa]} \quad (5.3)$$

$$f_{ct,\max} = 0.40 f_{ck}^{2/3} \text{ [MPa]} \quad (5.4)$$

and the mean value of the tensile strength is given by (CEB 1993)

$$f_{cm} = 0.30 f_{ck}^{2/3} \text{ [MPa]} \quad (5.5)$$

In the present study, the values of the tensile strength adopted in the numerical simulations vary between $f_{ct,min}$ and f_{ctm} .

The fracture energy of plain concrete, G_f , is the energy required to propagate a tensile crack of unit area. In Figure 5.1(b), G_f corresponds to the area under the post-peak branch of the stress-displacement curve and is commonly assumed as a material parameter. In the absence of experimental data, G_f may be estimated from (CEB 1993)

$$G_f = 0.2 G_{f0} f_{cm}^{0.7} \text{ [Nmm/mm}^2\text{]} \quad (5.6)$$

where G_{f0} is the base value of fracture energy, which depends on the maximum aggregate size, d_{max} . When d_{max} is equal to 8 mm, 16 mm or 32 mm, the value of G_{f0} is 0.025 Nmm/mm², 0.030 Nmm/mm² or 0.058 Nmm/mm², respectively.

Tri-linear diagrams are used in the present study to model the concrete tensile-softening behavior (see Figure 4.6). For the case of plain concrete, the parameters ξ_1 , α_1 , ξ_2 and α_2 must be carefully selected in order to accurately simulate the concrete post-cracking behavior.

5.1.2 Uniaxial behavior of reinforced concrete

Uniaxial compressive behavior of reinforced concrete is commonly simulated with the uniaxial compressive model used for plain concrete, which was previously discussed. Concrete cracking is also an influential phenomenon governing the tensile behavior of reinforced concrete elements. Figure 5.2 illustrates the force-displacement diagram of a tensile test. When the load increases, the existing cracks localized in narrow bands evolve and a number of primary macro-cracks are formed. Due to the existence of bond between

concrete and reinforcement, a gradual redistribution of the internal forces from the concrete to the reinforcement occurs, inducing the formation of secondary cracks. This process of stress redistribution and crack formation ends when the crack pattern stabilizes. It is clear that the stiffness of the tensile member is increased with reference to the rebar by the stiffness of the concrete. This effect is usually referred to in the literature as tension-stiffening and depends on the reinforcement ratio, the stress level at the rebar, the characteristics of the surface of the rebar, the angle between the rebar and the crack, as well as the fracture concrete properties and the type of loading (Barros 1995).

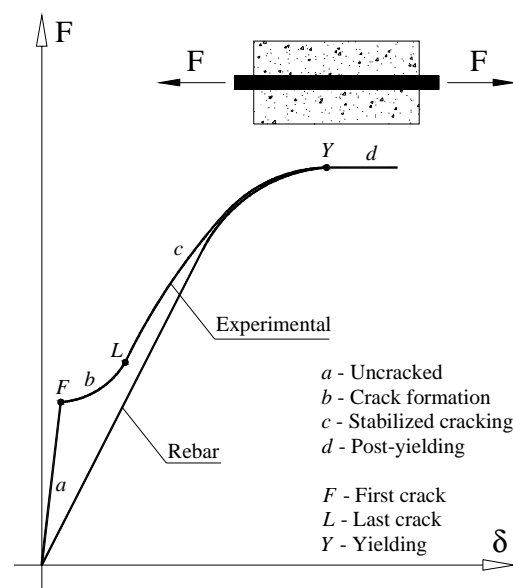


Figure 5.2 – Behavior of a reinforced concrete tensile member.

Previous research has revealed that the most appropriate tension-stiffening models must be based on a stress-strain diagram that considers the following aspects: crack stabilization, reinforcement yielding at the crack, member strain at point Y of Figure 5.2 equal to the reinforcement yield strain (Barros 1995). In the present work, the diagram represented in Figure 4.6 is used to model the tension-stiffening effect, since an appropriate choice of values for the parameters ξ_1 , α_1 , ξ_2 and α_2 leads to a model that satisfies the desired characteristics.

At the cross section level, only the concrete area surrounding the reinforcement is affected by the tension-stiffening phenomenon. This area is usually referred to in the

literature as the effective tension area, $A_{eff} = h_{eff}b$ (see Figure 5.3), where h_{eff} can be estimated according to the following CEB-FIB (1993) recommendation

$$h_{eff} = \min\{2.5(h-d), (h-x)/3\} \quad (5.7)$$

In this equation d is the distance between the top surface of the beam (zone in compression) and the centroid of the reinforcement in tension, and x is the distance between the neutral axis and the top surface of the beam. Since x is only known during the analysis process, the relation $h_{eff} = 2.5(h-d)$ is adopted in the present work.

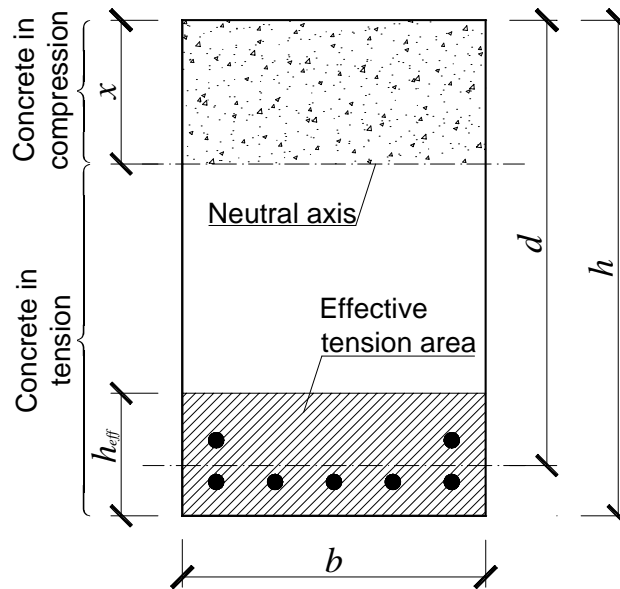


Figure 5.3 – Effective tension area of a beam.

5.2 STEEL REINFORCEMENT PROPERTIES

The material properties of the steel reinforcement are commonly determined using standard tensile tests. The obtained stress-strain diagram is usually replaced with an idealized relationship, as shown Figure 5.4. This figure represents the adopted uniaxial constitutive model of the rebars. The curve (under compressive or tensile loading) is composed of four branches (see equation (5.9)). In order to define the four branches three points $PT1 = (\varepsilon_{sy}, \sigma_{sy})$, $PT2 = (\varepsilon_{sh}, \sigma_{sh})$ and $PT3 = (\varepsilon_{su}, \sigma_{su})$ and the parameter p are required.

Typically, the value of the parameter p varies between 1.0 and 4.0. Unloading and reloading linear branches with slope E_s are assumed in the present approach. Defining E_s as

$$E_s = \sigma_{sy} / \varepsilon_{sy} \tag{5.8}$$

the curve is given by

$$\sigma(s) = \begin{cases} E_s \varepsilon_s & \text{if } \varepsilon_s \leq \varepsilon_{sy} \\ E_{sy} (\varepsilon_s - \varepsilon_{sh}) + \sigma_{sh} & \text{if } \varepsilon_{sy} < \varepsilon_s \leq \varepsilon_{sh} \\ \sigma_{su} + (\sigma_{sh} - \sigma_{su}) \left(\frac{\varepsilon_{su} - \varepsilon_s}{\varepsilon_{su} - \varepsilon_{sh}} \right)^p & \text{if } \varepsilon_{sh} < \varepsilon_s \leq \varepsilon_{su} \\ 0 & \text{if } \varepsilon_s > \varepsilon_{su} \end{cases} \tag{5.9}$$

where

$$E_{sy} = (\sigma_{sh} - \sigma_{sy}) / (\varepsilon_{sh} - \varepsilon_{sy}) \tag{5.10}$$

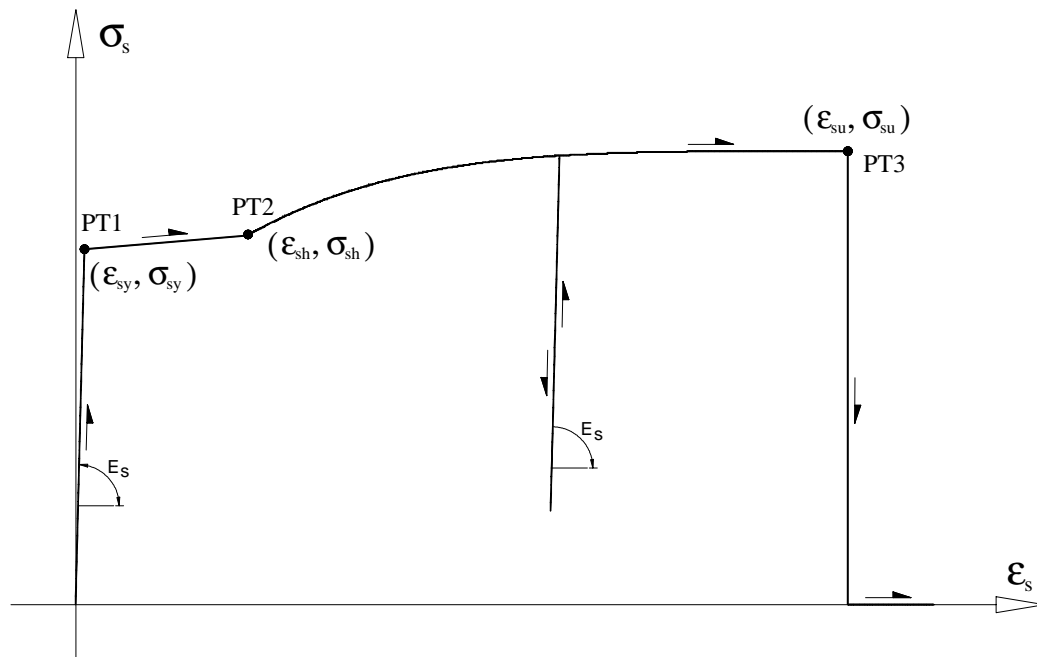


Figure 5.4 – Uniaxial constitutive model of the rebars.

5.3 MODELING OF BEAMS WITH FLEXURAL STRENGTHENING

In this section the simulation of the experimental tests carried out by Barros and Fortes (2002) is presented. The main purpose of this experimental program was to assess the ability of the NSM strengthening technique as a means of increasing the flexural capacity of reinforced concrete beams. Two distinct analyses are performed: in the former a perfect bond between the CFRP and concrete is assumed, while in the latter slip can occur.

Figure 5.5 to Figure 5.7 show the geometry, finite element mesh, loading configuration and support conditions adopted in this study. The reference beams (V1, V2, V3 and V4) are simulated with the setup shown in Figure 5.5, whereas Figure 5.6 and Figure 5.7 present the setup adopted for the strengthened beams (V1R1, V2R2, V3R2 and V4R3) assuming perfect bond and allowing slip at the CFRP-concrete interface, respectively (see Chapter 1). The height of each beam is indicated in Figure 1.5. In order to simulate the concrete part of the specimen, 8-node Serendipity plane stress elements with 3×3 Gauss-Legendre integration scheme are used. The longitudinal and transverse steel reinforcements, as well as the CFRP laminates, are simulated with 3-node quadratic embedded cable elements with two Gauss-Legendre integration points. When slip is allowed at the CFRP-concrete interface, the CFRP laminates are simulated with 3-node quadratic cable elements with two Gauss-Legendre integration points, and the CFRP-concrete interface is discretized with 6-node quadratic interface elements with two Gauss-Lobatto integration points.

Table 5.1 includes the concrete properties used in the numerical simulations. From the mean value of the experimentally obtained compressive strengths, f_{cm} , all the other parameters were estimated according to the expressions indicated in Section 5.1. In order to simulate the post-cracking behavior of reinforced concrete, a tri-linear tension-stiffening diagram is used. The material that exhibits this type of behavior is located in the first rows of each finite element mesh, counting from the bottom of the beam (see Figure 5.5 to Figure 5.7). In the parts of the mesh where no longitudinal reinforcement is present (upper rows), a tri-linear tension-softening diagram is used. The total height of the finite element rows where the material is treated as reinforced concrete is defined by the parameter h_{eff} (see Figure 5.3). In the cases where CFRP reinforcement is also present, the post-cracking

behavior of concrete must be treated differently. Therefore, a realistic tension-stiffening model for the simulation of the post-cracking behavior of these elements should also take into account the properties of the CFRP materials. In the present work, the tri-linear stress-strain diagram, represented in Figure 4.6, is used to simulate the post-cracking behavior of reinforced concrete elements strengthened with CFRP materials. The main advantage of this diagram is the possibility of changing the values of ξ_1 , α_1 , ξ_2 and α_2 , thus providing enough flexibility in order to model the most important aspects of the tension-stiffening effect. Since no previous research could be found regarding the selection of appropriate values for the referred parameters, several attempts were made with the aim of fitting the numerical results with the experimental results, in terms of global beam behavior.

All the parameters that define the material model of the rebars (longitudinal and transverse reinforcements) and CFRP laminates are included in Table 5.2. These parameters were estimated by Barros and Fortes (2004).

In the experimental program carried out by Barros and Fortes (2002), and in the pullout-bending tests performed in this work, the geometry of the slits and the obtained properties of the epoxy adhesive are not coincident. In the present numerical analysis the following relationship is adopted to simulate the nonlinear behavior of the CFRP-concrete interface

$$\tau(s) = \begin{cases} 16 \left(\frac{s}{0.3} \right)^{0.2} & \text{if } s \leq 0.3 \\ 16 \left(\frac{s}{0.3} \right)^{-0.3} & \text{if } s > 0.3 \end{cases} \quad (5.11)$$

In order to evaluate the influence of the occurrence of slip on the global behavior of the beams, the $\tau-s$ relationship should allow a large contribution of the slip phenomenon. Therefore, the smallest value found in the results of the analytical modeling described in Chapter 3 was attributed to parameter τ_m . The values of the other parameters of the $\tau-s$ relationship were selected taking into account the values obtained in the experimental program described in Chapter 2 and considering the width of the slits of the analyzed

beams. Assuming that the normal stiffness of the interface elements has a marginal effect on the bonding behavior, a constant value of 10^6 N/mm^3 is attributed to D_n .

In all the numerical simulations the load is applied by direct displacement-control at the loaded point.

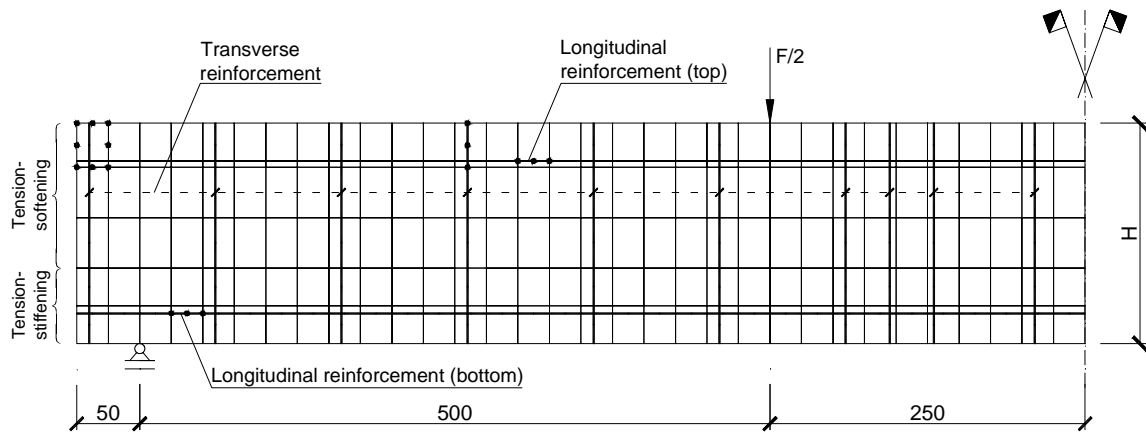


Figure 5.5 – Geometry, mesh, loading and support conditions of reinforced concrete beams. Note: all dimensions are in millimeters.

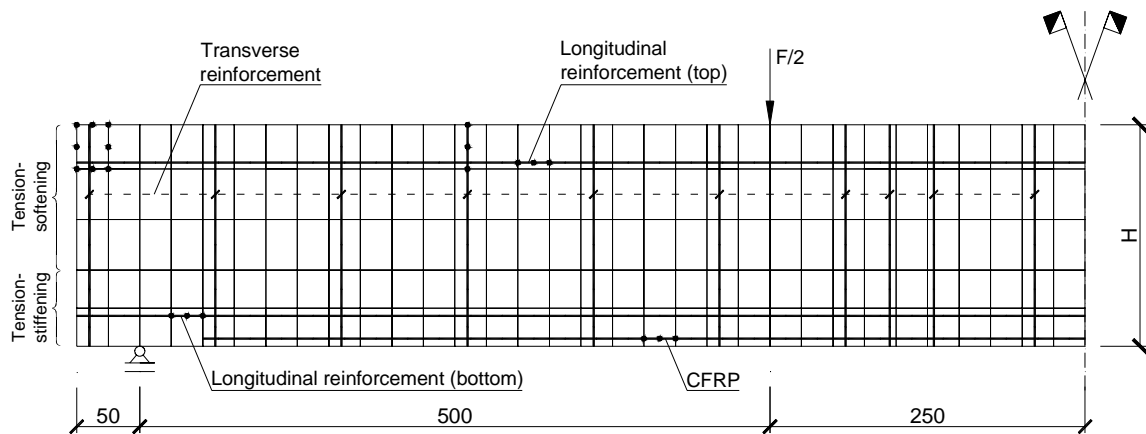


Figure 5.6 – Geometry, mesh, loading and support conditions of reinforced concrete beams strengthened with CFRP laminate strips. Perfect bond between the CFRP and concrete is assumed. Note: all dimensions are in millimeters.

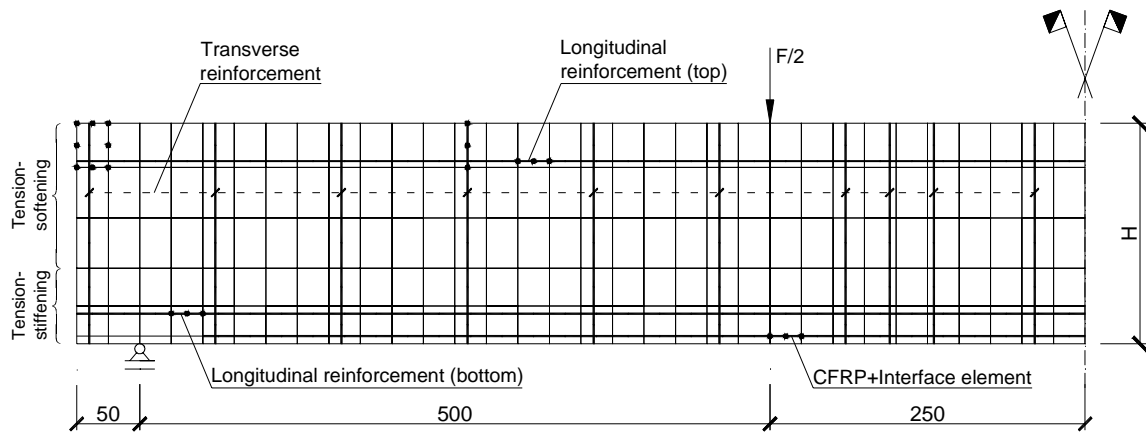


Figure 5.7 – Geometry, mesh, loading and support conditions of reinforced concrete beams strengthened with CFRP laminate strips. Bond-slip at the CFRP-concrete interface is modeled. Note: all dimensions are in millimeters.

Table 5.1 – Concrete properties used in the simulation of beams with flexural strengthening.

Poisson's ratio	$\nu_c = 0.15$
Initial Young's modulus	$E_c = 35757 \text{ N/mm}^2$
Compressive strength	$f_c = 46.0 \text{ N/mm}^2$
Strain at peak compression stress	$\varepsilon_{c1} = 2.2 \times 10^{-3}$
Parameter defining the initial yield surface	$\alpha_0 = 0.3$
Tri-linear tension-softening diagram	$f_{ct} = 3.0 \text{ N/mm}^2$; $G_f = 0.087 \text{ N/mm}$ $\xi_1 = 0.02$; $\alpha_1 = 1/3$; $\xi_2 = 0.48$; $\alpha_2 = 1/6$
Tri-linear tension-stiffening diagram of the beams V1, V2, V3 and V4	$f_{ct} = 3.0 \text{ N/mm}^2$; $G_f = 0.24 \text{ N/mm}$ $\xi_1 = 0.05$; $\alpha_1 = 0.5$; $\xi_2 = 0.8$; $\alpha_2 = 0.4$
Tri-linear tension-stiffening diagram of the beams V1R1, V2R2, V3R2 and V4R3	$f_{ct} = 3.0 \text{ N/mm}^2$; $G_f = 0.7 \text{ N/mm}$ $\xi_1 = 0.1$; $\alpha_1 = 0.6$; $\xi_2 = 0.45$; $\alpha_2 = 0.3$
Parameter defining the mode I fracture energy available to the new crack	$p_1 = 2$
Shear retention factor	<i>Exponential</i> ($p_2 = 2$)
Crack band-width	<i>Square root of the area of the element</i>
Threshold angle	$\alpha_{th} = 60^\circ$

Table 5.2 – Reinforcement properties used in the simulation of beams with flexural strengthening.

Reinforcement	$(\epsilon_{sy}; \sigma_{sy})$	$(\epsilon_{sh}; \sigma_{sh})$	$(\epsilon_{su}; \sigma_{su})$	p
Ø3	$(8.97 \times 10^{-4}; 175)$	$(1.44 \times 10^{-1}; 288)$	$(1.44 \times 10^{-1}; 288)$	1.0
Ø6	$(3.50 \times 10^{-3}; 700)$	$(5.00 \times 10^{-3}; 760)$	$(3.17 \times 10^{-2}; 800)$	1.0
Ø8	$(2.62 \times 10^{-3}; 524)$	$(3.00 \times 10^{-2}; 554)$	$(1.50 \times 10^{-1}; 614)$	2.6
CFRP	$(17.1 \times 10^{-3}; 2700)$	$(17.1 \times 10^{-3}; 2700)$	$(17.1 \times 10^{-3}; 2700)$	1.0

Note: all stresses are in megapascal.

Figure 5.8(a) to Figure 5.11(a) show the relationship between deflection at beam mid-span and load, for both the experimental tests and the numerical analyses (assuming perfect bond). The main aspects observed in the experimental tests of the reference beams (V1, V2, V3 and V4), such as crack initiation, stiffness degradation, yield initiation of rebars, and load carrying capacity are well simulated. The exception occurred in beam V3, where the model has predicted a crack initiation load greater than the experimentally observed one. A possible reason for this discrepancy is a slight damage of beam V3 that might have occurred before the test. Due to some difficulties in the convergence of the Newton-Raphson iterative procedure, the predicted ultimate deflection was lower than the one obtained experimentally in the reference beams.

The numerical simulation of the strengthened beams (V1R1, V2R2, V3R2 and V4R3), assuming perfect bond at the CFRP-concrete interface, has also reproduced the main aspects observed in the experimental tests. However, the numerical model did not predict the maximum load carrying capacity obtained experimentally, due to the non-convergence of the Newton-Raphson iterative procedure at a load level of about 90% of the experimental maximum load carrying capacity. For all the strengthened beams, the maximum difference between the numerically obtained ultimate load and the experimentally observed maximum load did not exceed 12 % of the latter.

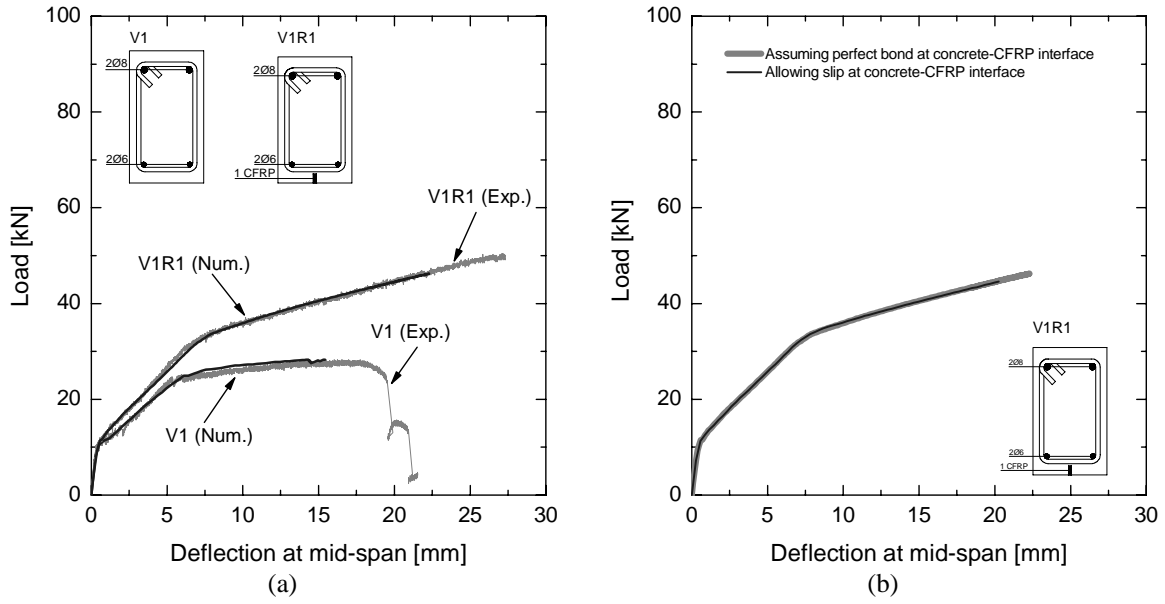


Figure 5.8 – (a) Load vs. deflection at mid-span obtained experimentally and numerically (assuming perfect bond) for the beams V1 and V1R1. (b) Load vs. deflection at mid-span obtained numerically assuming perfect bond and allowing slip at the CFRP-concrete interface.

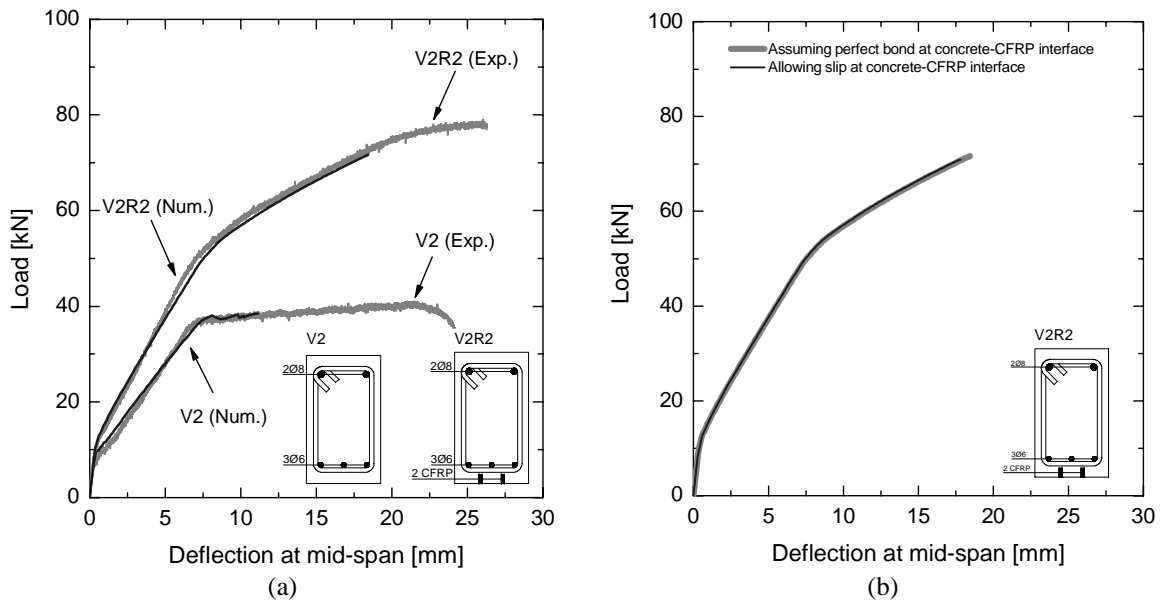


Figure 5.9 – (a) Load vs. deflection at mid-span obtained experimentally and numerically (assuming perfect bond) for the beams V2 and V2R2. (b) Load vs. deflection at mid-span obtained numerically assuming perfect bond and allowing slip at the CFRP-concrete interface.

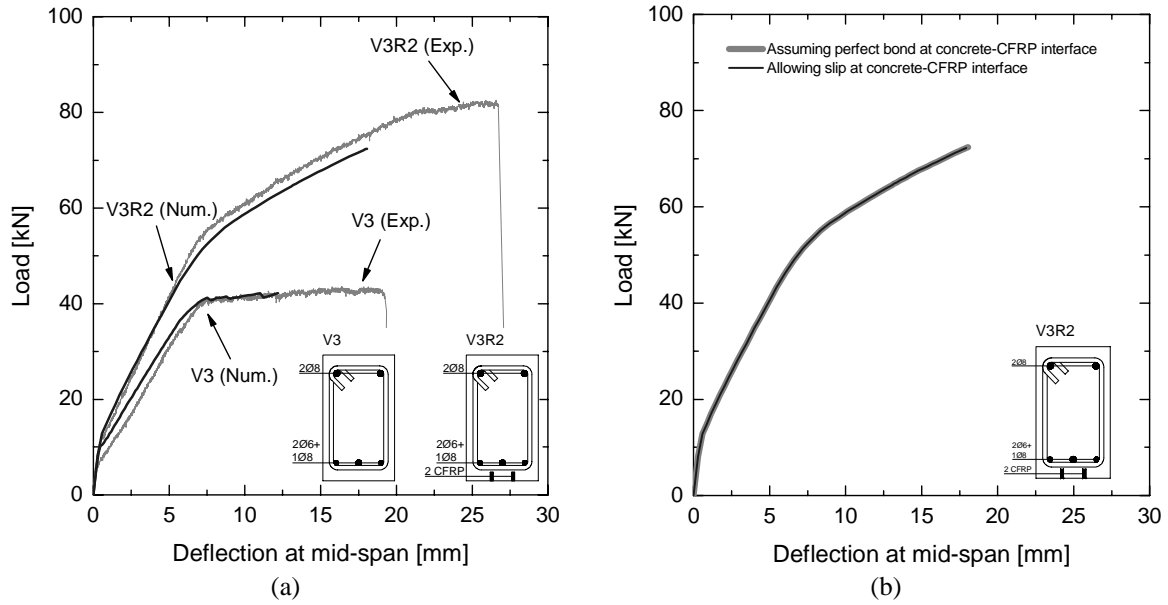


Figure 5.10 – (a) Load vs. deflection at mid-span obtained experimentally and numerically (assuming perfect bond) for the beams V3 and V3R2. (b) Load vs. deflection at mid-span obtained numerically assuming perfect bond and allowing slip at the CFRP-concrete interface.

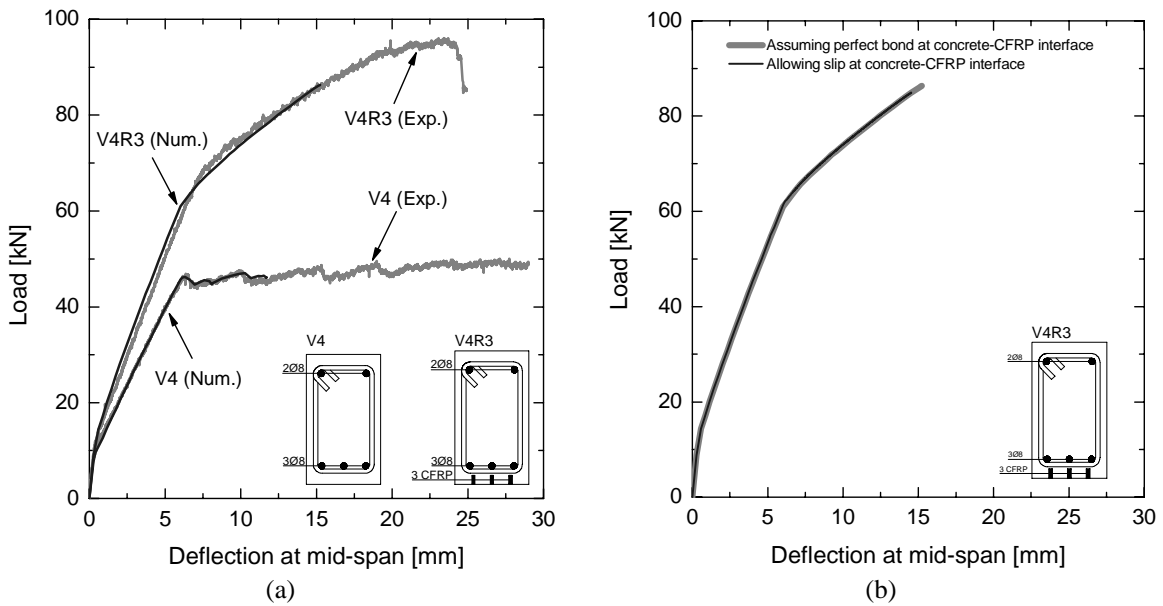


Figure 5.11 – (a) Load vs. deflection at mid-span obtained experimentally and numerically (assuming perfect bond) for the beams V4 and V4R3. (b) Load vs. deflection at mid-span obtained numerically assuming perfect bond and allowing slip at the CFRP-concrete interface.

Figure 5.8(b) to Figure 5.11(b) depict the numerical relationship between the load and deflection at mid-span, for the assumption of perfect bond and allowing slip at the CFRP-concrete interface. Modeling the bond-slip behavior at the CFRP-concrete interface did not contribute to an increase of the maximum deflection obtained in the analyses with

perfect bond, thus indicating that in this type of beams the slip between the CFRP and concrete has a marginal contribution to the global response. This can also be inferred from the observed failure modes of the tested beams (Barros and Fortes 2004), since the main cause of failure was the detachment of a concrete layer composed of the concrete cover and fragments of concrete located above the longitudinal tensile rebars.

In the beams tested by Barros and Fortes (2002) the strains in the CFRP were also recorded. Two strain gages (1 and 2) were located as indicated in Figure 5.12. A third strain gage was placed at the specimen mid-span. In Figure 5.12 the strains recorded in the strain gages 1 and 2 are compared with the values obtained from the numerical model, assuming perfect bond between the CFRP and the concrete. The evolution of the strain with the load is well predicted up to the point where convergence could no longer be obtained. In the remaining strengthened beams (V1R1, V3R3 and V4R3) the numerical model produced results with similar characteristics.

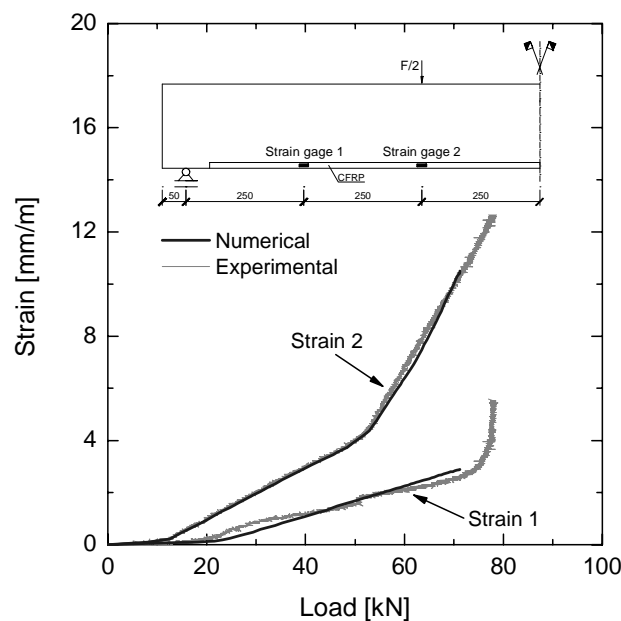


Figure 5.12 – Comparison between numerical and experimental CFRP strains in the test of beam V2R2.

Figure 5.13(a) represents the distribution of the CFRP strain in beam V2R2 at three distinct load levels: crack initiation, onset of rebar yielding and last converged combination. As expected, the CFRP strains at crack initiation are marginal. When the

rebars yield, the CFRP strain varies linearly with x , from $x = 0$ mm to $x = 450$ mm, and remains constant in the pure bending zone. For higher load levels, the strain in the shear span varies nonlinearly with x . In the pure bending zone the strain distribution is almost constant.

The bond stress distribution in the last converged combination is presented in Figure 5.13(b) for the beam V2R2. The bond stress decreases significantly in the range 0 mm to 100 mm. The bond stress oscillations are caused by the presence of flexural cracks. The maximum bond stress does not exceed the bond strength considered in the $\tau - s$ relationship and the slip is always lower than 0.3 mm.

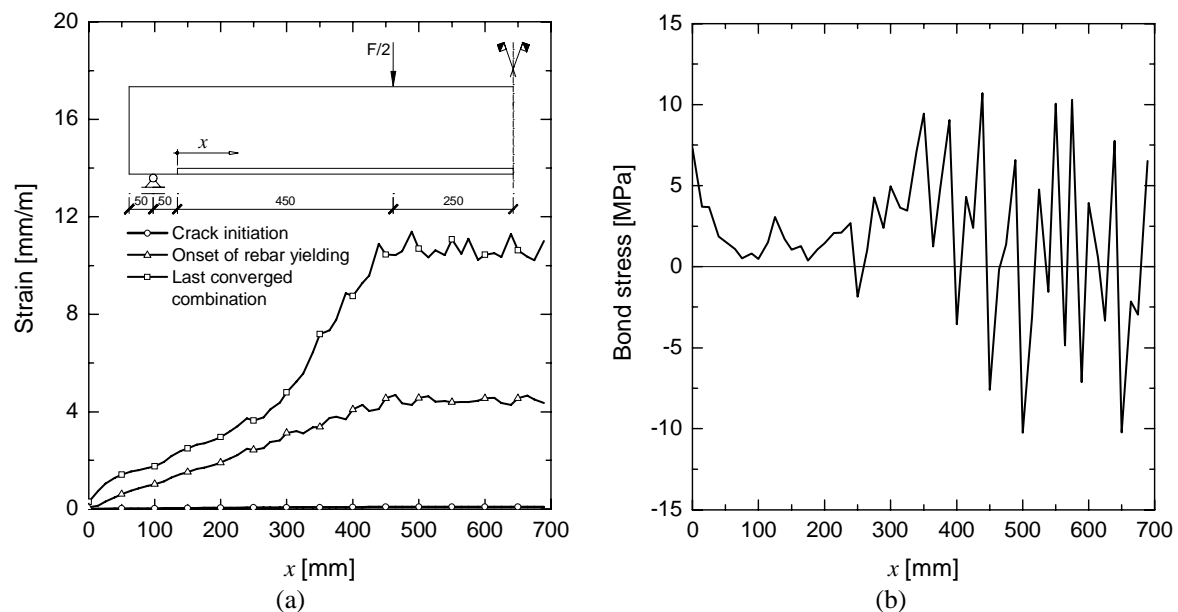


Figure 5.13 – Numerical results obtained at the CFRP level in the beam V2R2: (a) evolution of the CFRP strain along the longitudinal axis of the CFRP; (b) evolution of the bond stress along the longitudinal axis of the CFRP.

5.4 MODELING OF SHEAR-STRENGTHENED BEAMS

The performance of the NSM technique as a means of increasing the shear strength of reinforced concrete beams was experimentally assessed by Barros and Dias (2003), being the beams composing the VA series selected for the numerical simulation described below.

Figure 5.14 to Figure 5.17 show the geometry, finite element mesh, loading configuration and support conditions adopted in this study. In order to simulate the concrete part of the specimen, 8-node Serendipity plane stress elements with 3×3 Gauss-Legendre integration scheme are used. The longitudinal and transverse steel reinforcements, as well as the CFRP laminates, are simulated with 3-node quadratic embedded cable elements with two Gauss-Legendre integration points. The assumption of perfect bond between the reinforcement and concrete is adopted.

The concrete properties adopted in the present analyses are included in Table 5.3. From the mean value of the experimentally obtained compressive strengths, f_{cm} , all the other parameters were estimated according to the expressions indicated in Section 5.1. Since the longitudinal steel reinforcement ratio is high, the effect of the tension-stiffening is negligible (Massicotte et al. 1990). For this reason the post-cracking behavior of concrete is simulated with a tri-linear tension-softening diagram. Two distinct numerical analyses are performed for the beams VAE-30, VACI-30 and VACV-20, considering two values of the threshold angle, 30° or 60°.

Table 5.4 includes the properties of the rebars and CFRP reinforcements. Preliminary finite element numerical simulations with the beam VAE-30 have questioned the values of properties indicated by Barros and Dias (2003) for the Ø10 rebars (yield stress of 464 MPa). In fact, the numerical results have pointed out that the maximum load obtained experimentally can only be reached when the yield stress of the Ø10 rebars is approximately equal to 600 MPa. This value of the yield stress was confirmed by a layer model whose purpose is the determination of the moment-curvature relationship of a reinforced concrete cross section (Ribeiro et al. 2003). According to Barros and Dias, the cause of this discrepancy might have been the heterogeneity of the Ø10 rebars used in the tensile tests and in the beams. Consequently, in the present numerical simulations the properties of the Ø10 rebars are those indicated in Table 5.4.

In all the numerical simulations the load is applied by direct displacement-control at the point located in the lower right corner of the mesh.

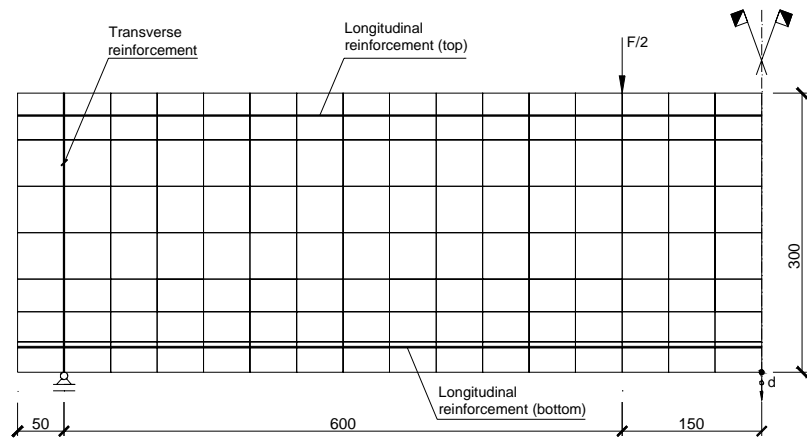


Figure 5.14 – Geometry, mesh, loading configuration and support conditions of the beam VA10. Note: all dimensions are in millimeters.

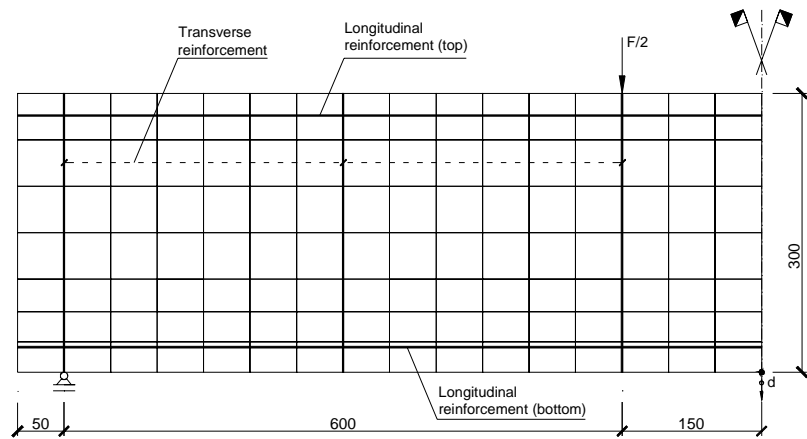


Figure 5.15 – Geometry, mesh, loading configuration and support conditions of the beam VAE-30. Note: all dimensions are in millimeters.

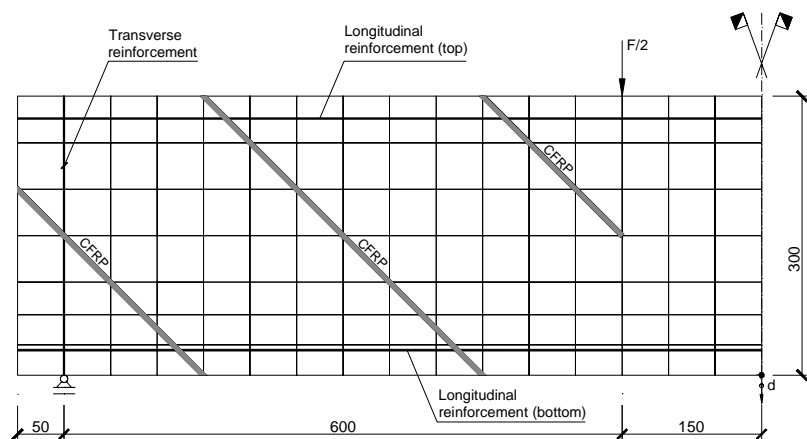


Figure 5.16 – Geometry, mesh, loading configuration and support conditions of the beam VACI-30. Note: all dimensions are in millimeters.

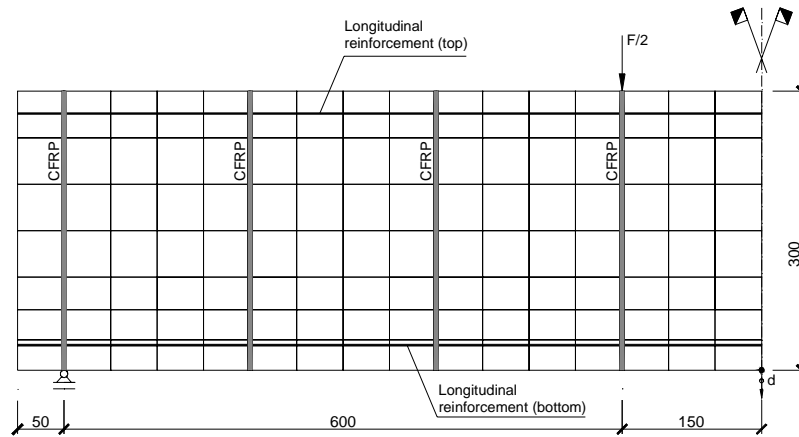


Figure 5.17 – Geometry, mesh, loading configuration and support conditions of the beam VACV-20. Note: all dimensions are in millimeters.

Table 5.3 – Concrete properties used in the simulation of shear-strengthened beams.

Poisson's ratio	$\nu_c = 0.15$
Initial Young's modulus	$E_c = 36567 \text{ N/mm}^2$
Compressive strength	$f_c = 49.2 \text{ N/mm}^2$
Strain at peak compression stress	$\epsilon_{c1} = 2.2 \times 10^{-3}$
Parameter defining the initial yield surface	$\alpha_0 = 0.3$
Tri-linear tension-softening diagram	$f_{ct} = 3.0 \text{ N/mm}^2$; $G_f = 0.09 \text{ N/mm}$ $\xi_1 = 0.1$; $\alpha_1 = 0.5$; $\xi_2 = 0.3$; $\alpha_2 = 0.2$
Parameter defining the mode I fracture energy available to the new crack	$p_1 = 0.5$
Shear retention factor	<i>Linear</i> ($p_2 = 1$)
Crack band-width	<i>Square root of the area of the element</i>
Threshold angle	$\alpha_{th} = 30^\circ$ or $\alpha_{th} = 60^\circ$

Table 5.4 – Reinforcement properties used in the simulation of shear-strengthened beams.

Reinforcement	$(\epsilon_{sy}; \sigma_{sy})$	$(\epsilon_{sh}; \sigma_{sh})$	$(\epsilon_{su}; \sigma_{su})$	P
Ø6 (Transverse reinforcement)	$(2.70 \times 10^{-3}; 540)$	$(1.0; 540)$	$(1.0; 540)$	1.0
Ø6 (Longitudinal reinforcement)	$(3.11 \times 10^{-3}; 622)$	$(1.0; 622)$	$(1.0; 622)$	1.0
Ø10	$(3.00 \times 10^{-3}; 600)$	$(1.0; 600)$	$(1.0; 600)$	1.0
CFRP	$(14.7 \times 10^{-3}; 2200)$	$(14.7 \times 10^{-3}; 2200)$	$(14.7 \times 10^{-3}; 2200)$	1.0

Note: all stresses are in megapascal.

Figure 5.18 and Figure 5.19 show the relationship between the load and the deflection at mid-span, for both the experimental test and the numerical simulations. For the beams VAE-30, VACI-30 and VACV-20, the numerical simulations with values of the threshold angle equal to 30° and 60° are included in these figures.

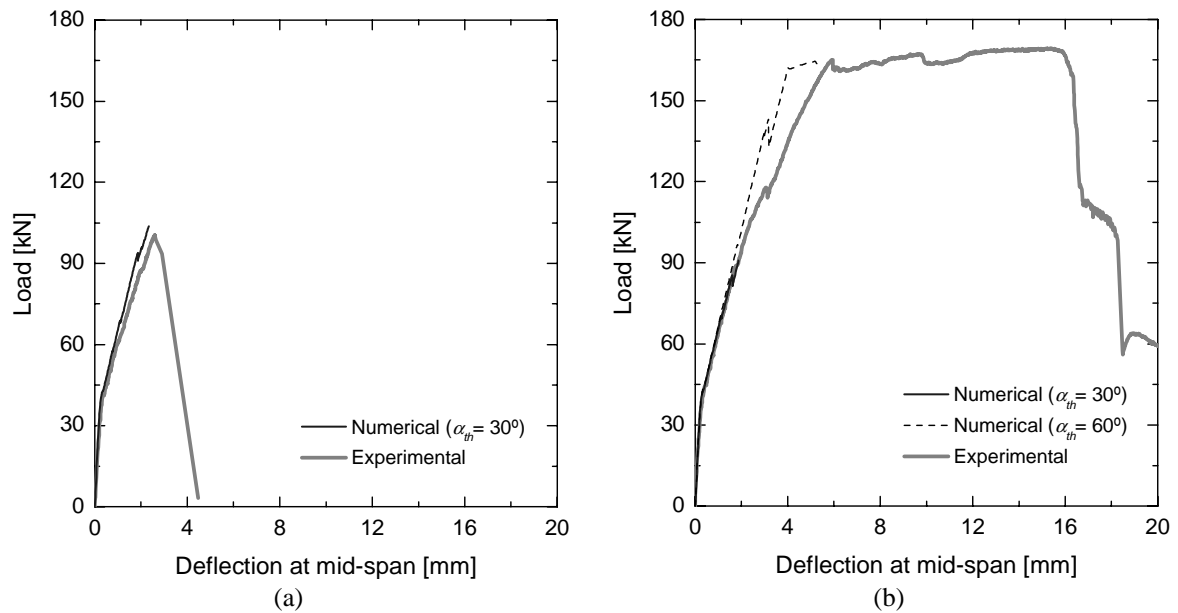


Figure 5.18 – Load vs. deflection at mid-span obtained experimentally and numerically for the beams VA10 (a) and VAE-30 (b).

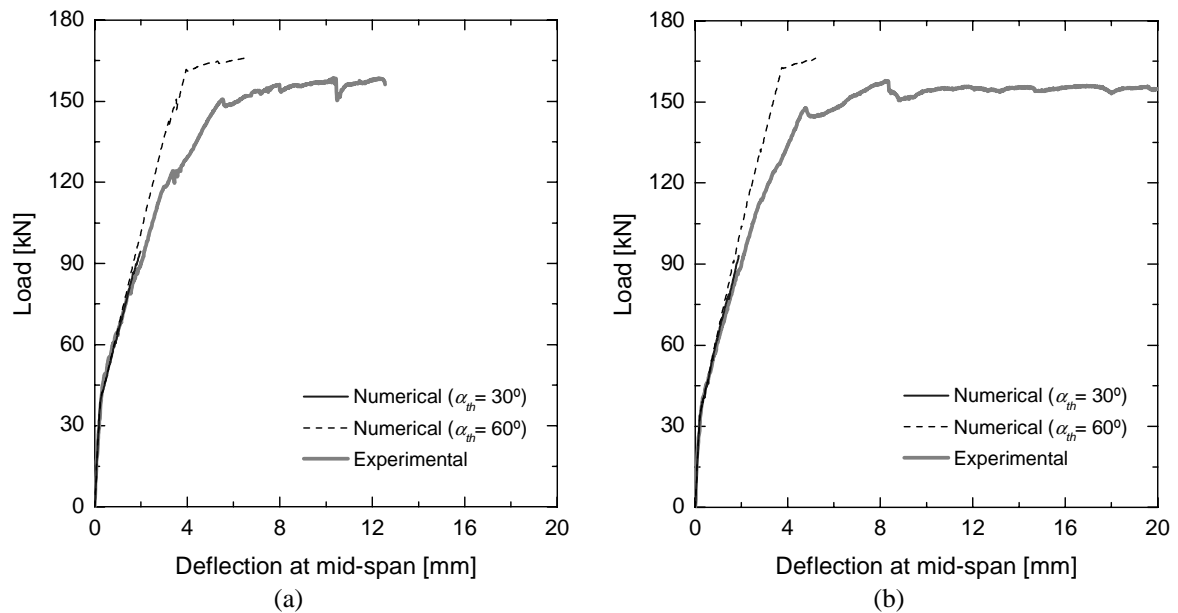


Figure 5.19 – Load vs. deflection at mid-span obtained experimentally and numerically for the beams VACV-20 (a) and VACI-30 (b).

In the beam VA10, a good agreement between the numerical and experimental results is obtained. The crack initiation, the ultimate load and the beam deformability are well predicted. The numerical analysis was terminated when the iterative Newton-Raphson procedure failed to converge.

Figure 5.20 shows the numerical crack pattern at the last converged combination of the beam VA10. In this figure only the cracks with the *opening* and *fully open* statuses are represented. The experimental crack pattern at impending failure of the beam VA10 is depicted in Figure 5.21. It can be observed that the beam failed by shear due to the occurrence of large deformations in the main shear crack indicated in the figure. This crack is well predicted by the numerical model, since a well defined shear crack band is formed in a location that coincides with the observed experimental shear crack and has the same orientation. In this shear crack band several cracks have a *fully open* status. According to Barros (1995), the type of numerical crack pattern indicated in Figure 5.20 occurs when the shear failure is imminent. However, numerical convergence is too difficult to obtain at this stage, since several cracks are forming and, simultaneously, existent cracks are changing their status.

When a 30° threshold angle is adopted, the numerical simulation of the beam VAE-30, which has transverse reinforcement (see Figure 1.7), did not converge for a load level close to the failure load of the beam VA10, which has no transverse reinforcement (see Figure 1.7). For the available numerical results, the relationship between the load and the deflection at mid-span accurately fits the experimental data as shown in Figure 5.18(b). At the last converged combination, the numerical model accurately reproduces the experimentally observed crack pattern (see Figure 5.22(a) and Figure 5.23).

When a 30° threshold angle is considered, the Newton-Raphson algorithm does not converge in an intermediate combination that corresponds to the evolution of the shear crack band. This non-convergence is due to the formation of several cracks and to the simultaneous occurrence of a significant number of critical crack status changes in the existing cracks.

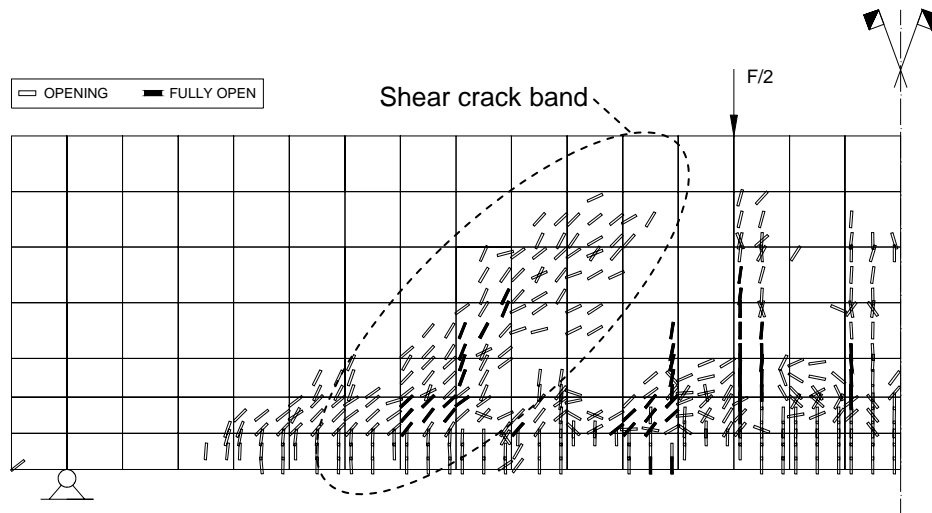


Figure 5.20 – Numerical crack pattern of the beam VA10 at the last converged combination.

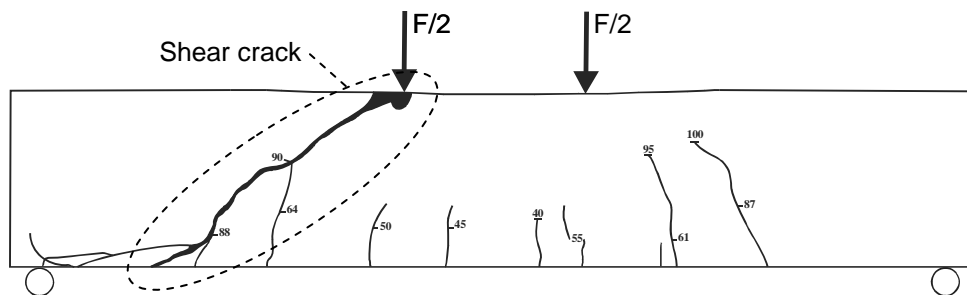


Figure 5.21 – Experimental crack pattern of the beam VA10 at impending failure (Dias and Barros 2004).

In the calculation of the internal equivalent nodal forces, the numerical model decomposes the incremental strain vector $\Delta \underline{\epsilon}$ in order to accurately simulate the crack status evolution (see Section 4.2.3.2). When the contribution of the shear stress to the stress vector is high, the principal stresses significantly change their orientation and the maximum principal stress can exceed the concrete tensile strength. In this case, if a new crack is formed at an integration point, in general, existent cracks tend to change their status, which causes the decomposition of the strain increment vector. This aspect also contributes to the numerical instabilities, since the calculation of the stiffness matrix depends on the crack statuses attributed at the end of the previous evaluation of the internal equivalent nodal forces, which can be considerably distinct from the crack statuses at the end of the previous combination. In order to avoid this type of numerical instability the number of critical crack status changes should be limited. This strategy was not investigated in the present work.

Figure 5.18(b) also includes the numerical analysis with a 60° threshold angle. In this analysis, a new crack can only be formed when the principal stress exceeds the concrete tensile strength and the angle between the direction of the existing cracks and the direction of the principal stress surpasses 60° . For this reason the response is stiffer than the one experimentally observed and stiffer than the numerical response with a 30° threshold angle. In the analysis with a 60° threshold angle, the stress in the longitudinal reinforcement reaches the yield stress, in agreement with the experiments. However, the numerical crack pattern does not accurately match the experimental crack pattern (see Figure 5.22(b)). In fact, in the numerical model, all cracks in *fully open* status are located in the pure bending zone and the shear crack band is formed closer to the support of beam.

The results of the numerical simulations performed with the VACI-30 and VACV-20 beams are similar to those described for the beam VAE-30. Similar numerical difficulties were encountered in the simulations performed with a 30° threshold angle.

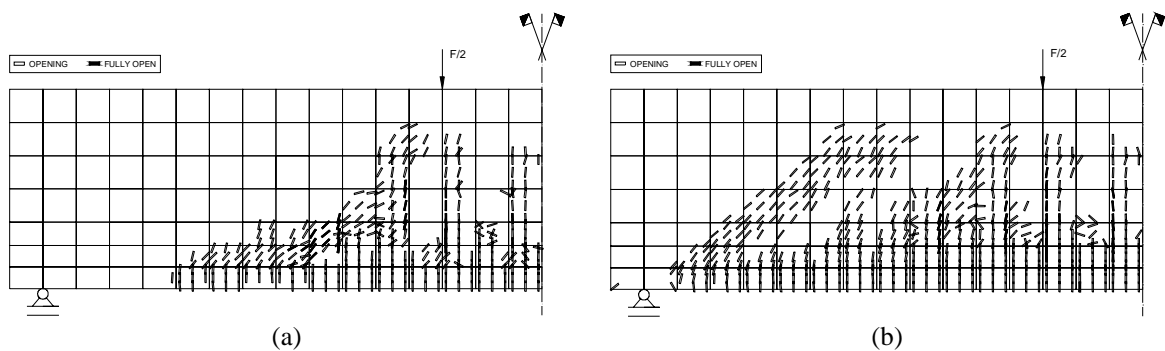


Figure 5.22 – Numerical crack pattern of the beam VAE-30, at the last converged combination, obtained with a threshold angle equal to 30° (a) and equal to 60° (b).

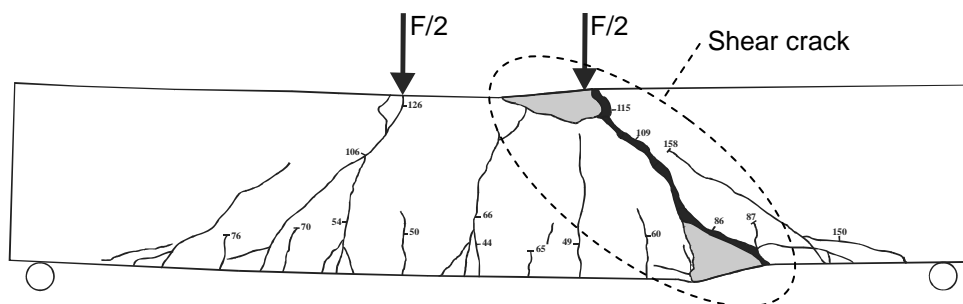


Figure 5.23 – Experimental crack pattern of the beam VAE-30 at impending failure (Dias and Barros 2004).

5.5 SUMMARY AND CONCLUSIONS

The numerical tools described in Chapter 4, whose purpose is the simulation of the behavior of reinforced concrete beams strengthened with NSM CFRP laminate strips, are applied to some examples, which were presented in this chapter. These examples include a pair of experimental programs, whose numerical simulation is used as a validation of the proposed tools. The first group comprises the analysis of reinforced concrete beams with flexural strengthening, whereas the second group deals with shear-strengthened reinforced concrete beams.

In the numerical simulation of beams with flexural strengthening two distinct types of analyses were considered in terms of the characterization of the CFRP-concrete interface: the assumption of perfect bond and the possibility of the occurrence of slip at the CFRP-concrete interface. With the exception of the maximum load carrying capacity, both approaches predicted with high accuracy the main features observed in the experimental tests. In the numerical simulation of the strengthened beams, and due to numerical instabilities, convergence could not be obtained when the load level was about 90 % of the maximum load recorded in the experiments. Since modeling the CFRP-concrete interface has not improved the accuracy of the numerical simulation, it seems that sliding between CFRP and concrete has a negligible effect in the global response.

In the numerical simulation of the reinforced concrete beams shear-strengthened with NSM CFRP laminate strips, perfect bond between CFRP and concrete was assumed. In the analysis of these types of beams, the influence of the value of the threshold angle was investigated. Using a 30° threshold angle, the crack pattern and the force-deflection relationship were predicted with higher accuracy than in the case of a 60° threshold angle. In the former analyses more cracks are formed, causing a significant decrease of the beam stiffness after its cracking load. However, the presence of three cracks in some integration points and the occurrence of more than one critical crack status change during the calculation of the internal equivalent nodal forces led to some numerical instabilities. These numerical instabilities caused the non-convergence of the Newton-Raphson iterative procedure at a load level close to the failure load of the reference beam. The analysis with a 60° threshold angle predicted with high accuracy the maximum load registered in the experimental tests, but the numerical response was stiffer than the one registered

experimentally. The crack patterns numerically predicted did not exactly match the experimental results, since the most prominent shear crack was located closer to the beam support than the shear failure crack experimentally observed.

CHAPTER 6

SUMMARY AND CONCLUSIONS

The near-surface mounted (NSM) strengthening technique has been used to increase the load carrying capacity of concrete structures. This technique consists in the insertion of CFRP laminate strips into pre-cut slits opened in the concrete cover of the elements to be strengthened. The laminates are bonded to concrete using an epoxy adhesive. The present work is a contribution to a better knowledge of the behavior of concrete structures strengthened with NSM CFRP laminate strips. The carried out study was composed of an experimental, an analytical and a numerical part.

Experimental research

In order to assess the bond performance between the CFRP and concrete using the NSM technique, pullout-bending tests under monotonic and cyclic loading were carried out. The influence of bond length, concrete strength, and load history was analyzed.

The bond test setup used in the carried out experimental program is adequate for the evaluation of the bond performance between CFRP laminate strips and concrete. Strain gages on the CFRP were used in order to accurately measure its tensile stress. The measured slip includes the contribution of the CFRP-adhesive and adhesive-concrete interfaces, as well as the deformation of the epoxy adhesive layer. A physical interpretation of the evolution of the pullout force, slip at the free end and slip at the loaded end was given based on the presumed micro-mechanisms.

Some parameters were determined to characterize the bond performance of the pullout-bending tests, such as the peak pullout force, the loaded end slip and the bond strength. According to the observations, these parameters were significantly influenced by the bond length, whereas the concrete strength had a negligible effect. In the case of the cyclic tests, the envelope of the pullout force *versus* slip relationships and the curve obtained in the homologous monotonic tests had similar shape.

Analytical modeling

A numerical method, which uses the results obtained in the experimental program, was developed with the purpose of determining an analytical local bond stress-slip relationship ($\tau - s$) for the NSM technique. This method solves the differential equation that governs the slip evolution of the CFRP laminate strip in the context of the NSM strengthening technique. The method takes into account the distribution of the slip and the bond stress along the bond length. The developed numerical method was also used in the evaluation of the CFRP anchorage length required in both service and ultimate limit state analyses. In the numerical method the slip concept is the sliding between CFRP and concrete.

The obtained $\tau - s$ relationship depends on the bond length, since the slip measured in the pullout-bending tests includes the contribution of the CFRP-adhesive and adhesive-concrete interfaces, as well as the deformation of the epoxy adhesive layer.

Numerical modeling

In order to simulate the behavior of concrete structures strengthened with NSM CFRP laminate strips some numerical tools were developed. These tools were implemented in a computer code named FEMIX, which is a general purpose finite element software system. The simulation of the concrete behavior was based on a developed elasto-plastic multi-fixed smeared crack model. A line interface finite element and a constitutive model for the simulation of the nonlinear behavior of the interface between CFRP and concrete were developed. The ability of the numerical tools used in the simulation of the behavior of reinforced concrete beams strengthened with NSM CFRP laminate strips was assessed by means of experimental results obtained in beams with flexural strengthening and in shear-strengthened beams.

In the numerical simulation of the beams with flexural strengthening two distinct approaches were considered for the modeling of the CFRP-concrete interface: perfect bond and possibility of occurrence of slip. In this type of strengthened beams, the modeling of the slip between CFRP and concrete did not significantly contribute to the accuracy of the numerical simulation. The numerical model predicted with high accuracy the main features

of the behavior registered in the experimental tests. However, the predicted maximum load carrying capacity was about 90 % of the corresponding experimental observation.

In the numerical simulations of the beams shear-strengthened with NSM CFRP laminate strips, perfect bond between CFRP and concrete was assumed. In the analysis of this type of beams the influence of the value of the threshold angle was investigated. When a 30° threshold angle was adopted, the numerical model simulated the experimental results with high accuracy up to a load level close to the failure load of the reference beam. However, due to numerical instabilities, the simulations did not progress any further. When a 60° threshold angle was adopted the model predicted accurately the maximum load carrying capacity, but the response was stiffer than the corresponding experimental observation.

Suggestions for future work

In retrospect, the objectives pre-established for the present work were successfully attained. The carried out experimental research contributed to increase the knowledge of the bond behavior between CFRP and concrete, in the context of the NSM strengthening technique. The aim of the numerical strategy was the determination of an analytical local bond stress-slip relationship for the NSM technique. And, finally, finite element numerical tools were developed to simulate the behavior of reinforced concrete structures strengthened with the NSM technique. However, further research is still needed in all the investigated areas.

A new test setup should be created with the aim of measuring the slip in the CFRP-adhesive and adhesive-concrete interfaces, as well as the deformation of the epoxy adhesive layer. With this new test, the influence of the thickness of the epoxy adhesive and of the bond length on the bond behavior should be clarified.

Using the results obtained with this new test, a different $\tau - s$ relationship would be determined. With this purpose, the numerical method described in Chapter 3 should be adjusted in order to take into account all the contributions to the slip. The exhaustive search used in the determination of the parameters that define the $\tau - s$ relationship should

be replaced with an optimization procedure in order to increase the global efficiency of this task.

The numerical instabilities observed in the constitutive model of the concrete should be investigated. The presence of three cracks in some integration points and the occurrence of more than one critical crack status change during the calculation of the internal equivalent nodal forces caused some numerical instabilities. In order to investigate the influence of this aspect the maximum number of critical crack status changes should be limited. These numerical instabilities might also be related with the simulation of the mode II fracture. In fact, in the developed model, when a crack is opening the incremental crack shear stress decreases, but the total crack shear stress increases, causing the formation of spurious cracks. In order to verify whether these instabilities are related to the shear inconsistency, a strain-softening relationship for the mode II fracture should be implemented.

The extension of the multi-fixed smeared crack model from 2D to 3D is straightforward. The 3D model can be useful in the context of the NSM strengthening technique, since recent research has shown that the failure mode of shear-strengthened beams is not in agreement with the plane stress assumptions, requiring a treatment of the whole structure as a three-dimensional solid.

REFERENCES

- ABAQUS (2002). ABAQUS Theory Manual – version 6.3, US. [available in CD-ROM]
- ACI (1991). “Fracture mechanics of concrete: concepts, models and determination of material properties (Reapproved 1999).” *Technical committee document 446.1R-91*, American Concrete Institute (ACI), Committee 446, 146 pp.
- ACI (1997). “Finite element analysis of fracture in concrete structures: state-of-the-art.” *Technical committee document 446.3R-97*, American Concrete Institute (ACI), Committee 446, 33 pp.
- ACI (2002). “Guide for the design and construction of externally bonded FRP systems for strengthening concrete structures.” *Technical committee document 440.2R-02*, American Concrete Institute (ACI), Committee 440, 45 pp.
- Alkhrdaji, T., Nanni, A., Chen, G., and Barker, M. (1999). “Upgrading the transportation infrastructure: solid RC decks strengthened with FRP.” *Concrete International*, 21(10), 37-41.
- Al-Zahrani, M.M. (1995). “Bond behavior of fiber reinforced plastic (FRP) reinforcements with concrete.” *PhD Thesis*, Department of Civil and Environmental Engineering, Pennsylvania State University, University Park, Pennsylvania, US.
- ASCE (1982). “State of the art report on finite element analysis of reinforced concrete.” American Society of Civil Engineers (ASCE), ASCE Task Committee on FEA of RC Structures of the Structural Division Committee on Concrete and Masonry Structures, New York, US, 553 pp.
- Asplund, S.O. (1949). “Strengthening bridge slabs with grouted reinforcement.” *Journal of the American Concrete Institute*, 20(6), 397-406.
- Azevedo, A.F.M. (1985). “Análise não linear de estruturas planas de betão armado pelo método dos elementos finitos. *Nonlinear analysis of plane reinforced concrete structures by the finite element method.*” *MSc Thesis*, Faculty of Engineering, University of Porto, Portugal. [in Portuguese]

- Azevedo, A.F.M., and Barros, J.A.O. (1990). "Análise comparativa de métodos directos e iterativos na resolução de grandes sistemas de equações lineares. *Comparative analysis of direct and iterative methods for the solution of large systems of linear equations.*" *Proceedings of Segundas Jornadas Portuguesas de Engenharia de Estruturas*, Laboratório Nacional de Engenharia Civil, Lisbon, Portugal. [in Portuguese]
- Azevedo, A.F.M., Barros, J.A.O., Sena-Cruz, J.M., and Gouveia, A.V. (2003). "Software no ensino e no projecto de estruturas. *Educational software for the design of structures.*" *Proceedings of III Congresso de Luso-Moçambicano de Engenharia*, J.S. Gomes, C.F. Afonso, C.C. António and A.S. Matos (eds.), Maputo, Mozambique, 81-92. [in Portuguese]
URL: http://www.civil.uminho.pt/jsenacruz/Publications/CP.N-009-2003_CLME2003.pdf
- Bakis, C.E., Uppuluri, V.S., Nanni, A., and Boothby, T.E. (1998). "Analysis of bonding mechanics of smooth and lugged FRP rods embedded in concrete." *Composite Science and Technology*, Elsevier, 58, 1307-1319.
- Barros, J.A.O. (1995). "Comportamento do betão reforçado com fibras. Análise experimental e simulação numérica. *Behavior of fiber reinforced concrete. Experimental analysis and numerical simulation.*" *PhD Thesis*, Faculty of Engineering, University of Porto, Portugal. [in Portuguese]
- Barros, J.A.O., and Dias, S.J.E. (2003). "Shear strengthening of reinforced concrete beams with laminate strips of CFRP." *Proceedings of the International Conference of Composites in Construction*, D. Bruno, G. Spadea, and N. Swamy (eds.), Cosenza, Italy, 289-294.
- Barros, J.A.O., and Figueiras, J.A. (1999). "Flexural behavior of steel fiber reinforced concrete: testing and modeling." *Journal of Materials in Civil Engineering*, ASCE, 11(4), 331-339.
- Barros, J.A.O., and Fortes, A.S. (2002). "Concrete beams reinforced with carbon laminates bonded into slits." *Proceedings of the 5th Congreso de Métodos Numéricos en Ingeniería*, Madrid, Spain, 16 pp. [available in CD-ROM].
- Barros, J.A.O., and Fortes, A. (2004). "Flexural strengthening of concrete beams with CFRP laminates bonded into slits." *Cement and concrete composites*. [in press]

- Barros, J.A.O., Ferreira, D.R.S.M., and Lourenço, P.B. (2000). "Comportamento de pilares de betão armado reforçados com laminados de fibras de carbono. *Behavior of reinforced concrete columns strengthened with CFRP laminate strips.*" *Proceedings of Betão Estrutural 2000*, J.A. Figueiras, A. Serra Neves, A.M. Bastos, E. Cansado de Carvalho, J. Almeida, and P.B. Lourenço (eds.), Porto, 393-402. [in Portuguese]
- Bartos, P. (1982). "Bond in concrete." *Proceeding of the International Conference on Bond in Concrete*, P. Bartos (ed.), Paisley, Scotland, UK.
- Bathe, K.J. (1996). "Finite element procedures." *Prentice-Hall*, New Jersey, US.
- Bazant, Z.P., and Gambarova, P. (1980). "Rough cracks in reinforced concrete." *Journal of Structural Division*, ASCE, 106(4), 819-842.
- Bazant, Z.P., and Oh, B.H. (1983). "Crack band theory for fracture of concrete." *Materials and Structures*, RILEM, 16(93), 155-177.
- Bittencourt, T., Ingrassia, A.R., and Llorca, J. (1992). "Simulation of arbitrary, cohesive crack propagation." *Proceedings of the Conference Fracture Mechanics of Concrete Structures*, Z. Bazant (ed.), Elsevier, New York, 339-350.
- Blaschko, M., and Zilch, K. (1999). "Rehabilitation of concrete structures with CFRP strips glued into slits." *Proceedings of the 12th International Conference on Composite Materials*, Paris, France, 7 pp. [available in CD-ROM]
- Cachim, P.B. (1999). "Experimental and numerical analysis of the behavior of structural concrete under fatigue loading with applications to concrete pavements." *PhD Thesis*, Faculty of Engineering, University of Porto, Portugal.
- CEB (1982). "Bond action and bond behaviour of reinforcement. State-of-the-art report." *Bulletin d'Information No. 151*, Comité Euro-International du Béton (CEB), Göteborg, Sweden.
- CEB-FIB (1993). "CEB-FIP Model Code 1990 - Design Code." *Thomas Telford*, Lausanne, Switzerland.
- Cervenka, V., Pukl, H. and Eligehausen R. (1990). "Computer simulation of anchoring technique and design of concrete structures." *Proceedings of the 2nd International Conference on Computer Aided Analysis and Design of Concrete Structures*, N. Bicanic and H. Mang (eds.), Zell am See, Austria, 1-19.

- Chapra, S.C., and Canale, R.P. (1998). "Numerical methods for engineers (Third edition)." *WCB/McGraw-Hill*, Singapore.
- Chen, W.F. (1982). "Plasticity in reinforced concrete." *McGraw-Hill*, New York, US.
- Chen, W.F., and Han, D.J. (1988). "Plasticity for structural engineers." *Springer-Verlag*, New York, US.
- Chen, W.F., and Mizuno, E. (1990). "Non-linear analysis in soil mechanics. Theory and implementation." *Elsevier*, Amsterdam, The Netherlands.
- Cornelissen, H.A.W., Hordijk, D.A., and Reinhardt, H.W. (1986). "Experimental determination of crack softening characteristics of normal weight and lightweight concrete." *Heron*, Fracture Mechanics and Structural Aspects of Concrete, 31(2), 45-56.
- Cosenza, E., Manfredi, G., and Realfonzo, R. (1997). "Behavior and modeling of bond of FRP rebars to concrete." *Journal of Composites for Construction*, ASCE, 1(2), 40-51.
- Crisfield, M.A. (1991). "Non-linear finite element analysis of solids and structures. Volume 1: essentials." *John Wiley & Sons*, Chichester, England.
- Crisfield, M.A. (1997). "Non-linear finite element analysis of solids and structures. Volume 2: advanced topics." *John Wiley & Sons*, Chichester, England.
- Crisfield, M.A., and Wills, J. (1989). "Analysis of R/C panels using different concrete models." *Journal of Engineering Mechanics*, ASCE, 115(3), 578-597.
- Cunha, P.A.S.C.M. (2004). "Análise experimental e numérica do comportamento à tracção de betão reforçado com fibras aço. *Experimental and numerical analysis of the steel fiber reinforced concrete behavior.*" *MSc Thesis*, Civil Engineering Department, University of Minho, Portugal. [in Portuguese]
- Dahlblom, O., and Ottosen, N.S. (1990). "Smearred crack analysis using generalized fictitious crack model." *Journal of Engineering Mechanics*, ASCE, 116(1), 55-76.
- de Borst, R. (1991). "Computational methods in non-linear solid mechanics. Part 2: physical non-linearity." *Report No. 25-2-91-2-06*, Delft University of Technology, The Netherlands, 174 p.

- de Borst, R., and Feenstra, P.H. (1990). "Studies in anisotropic plasticity with reference to Hill criterion." *International Journal of Numerical Methods in Engineering*, 29, 315-336.
- de Borst, R., and Nauta, P. (1985). "Non-orthogonal cracks in smeared finite element model." *Engineering Computations Journal*, 2, 35-46.
- De Lorenzis, L. (2002). "Strengthening of RC structures with near-surface mounted FRP rods." *PhD Thesis*, University of Lecce, Italy.
- De Lorenzis, L., Nanni, A., and La Tegola, A. (2000). "Flexural and shear strengthening of reinforced concrete structures with near-surface mounted FRP rods." *Proceedings of the 3rd International Conference on Advanced Composite Materials in Bridges and Structures*, J. Humar, and A.G. Razaqpur (eds.), Ottawa, Canada, 521-528.
- De Lorenzis, L., Rizzo, A., and La Tegola, A. (2002). "A modified pull-out test for bond of near-surface mounted FRP rods in concrete." *Journal of Composites Part B: Engineering*, Elsevier, 33(8), 589-603.
- Dias, S.J.E., and Barros, J.A.O. (2004). "CFRP no reforço ao corte de vigas de betão armado: investigação experimental e modelos analíticos. *CFRP for the shear strengthening of reinforced concrete beams: experimental research and analytical models.*" Report No. 04-DEC/E-08, Civil Engineering Department, University of Minho, Portugal, 109 pp. [in Portuguese]
- Eligehausen, R., Popov, E.P., and Bertero, V.V. (1983) "Local bond stress-slip relationships of deformed bars under generalized excitations." Report No. UCB/EERC-83/23, Earthquake Engineering Research Center, College of Engineering, University of California, Berkeley, California, US, 162 pp.
- Emmons, P., Thomas, J., and Sabnis, G.M. (2001). "New strengthening technology developed – Blue circle cement silo repair and upgrade." *Proceedings of the International Workshop on Structural Composites for Infrastructure Applications*, T. Rizk (ed.), Cairo, Egypt, 97-107.
- Ezeldin, A., and Balaguru, P. (1989). "Bond behavior of normal and high strength fiber reinforced concrete." *Material Journal*, ACI, 86, 515-524.

- Feenstra, P.H. (1993). "Computational aspects of biaxial stress in plain and reinforced concrete." *PhD Thesis*, Delft University of Technology, The Netherlands.
- Feenstra, P.H., de Borst, R., and Rots, J.G. (1990). "Stability analysis and numerical evaluation of crack dilatancy models." *Proceedings of the 2nd International Conference on Computer Aided Analysis and Design of Concrete Structures*, SCI-C 1990, Vol. 2.
- Ferreira, D.R.S.M. (2001). "Pilares de betão armado reforçados com laminados de fibras de carbono. *Reinforced concrete columns strengthened with CFRP laminate strips.*" *MSc Thesis*, Civil Engineering Department, University of Minho, Portugal. [in Portuguese]
- FIB (2000). "Bond of reinforcement in concrete." *Bulletin No. 10*, The International Federation for Structural Concrete (FIB), State-of-the-art report prepared by Task Group Bond Models (former CEB Task Group 2.5), Lausanne, Switzerland, 427 pp.
- FIB (2001). "Externally bonded FRP reinforcement for RC structures." *Bulletin No. 14*, The International Federation for Structural Concrete (FIB), Report prepared by Task Group 9.3 FRP reinforcement for concrete structures, Lausanne, Switzerland, 130 pp.
- Focacci, F., Nanni, A., and Bakis, C.E. (2000). "Local bond-slip relationship for FRP reinforcement in concrete." *Journal of Composites for Construction*, ASCE, 4(1), 24-31.
- Freitas, F., Barros, J.A.O., and Fonseca, P. (1998). "Manual do utilizador do equipamento SENTUR – release 1.0 *User manual of the SENTUR equipment release 1.0*" Report, Civil Engineering Department, University of Minho, Portugal. [in portuguese]
- Girard, C., and Bastien, J. (2002). "Finite-element bond-slip model for concrete columns under cyclic loads." *Journal of Structural Engineering*, ASCE, 128(12), 1502-1510.
- Henriques, A.A., Silva, P.A.S.C.M., and Oliveria, L. (2001). "Computational modeling of nonlinear behaviour of concrete structures strengthened by FRP." *Proceedings of the International Conference Composites in Construction*, J.A. Figueiras, L. Juvandes, and R. Faria (eds.), Porto, Portugal, 629-634.
- Hill, R. (1950). "The mathematical theory of plasticity." *Oxford University Press*, London.

- Hillerborg, A., Modéer, M., and Petersson, P.E. (1976). "Analysis of crack formation and crack growth in concrete by means of fracture mechanics and finite elements." *Cement and Concrete Research*, 6, 773-782.
- Hodge, P.G. (1957). Discussion [of Prager (1956)]. *Journal of Applying Mechanics*, 23, 482-484.
- Hofstetter, G., and Mang, H.A. (1995). "Computational mechanics of reinforced concrete structures." *Friedr. Vieweg & Sohn Verlagsgesellschaft mbH*, Germany.
- Hogue, T., Cornforth, R.C., and Nanni, A. (1999). "Myriad convention center floor system reinforcement." *Proceedings of the 4th International Symposium on Fiber Reinforced Polymer Reinforcement for Reinforced Concrete Structures*, C.W. Dolan, S. Rizkalla, and A. Nanni (eds.), Baltimore, Maryland, US, ACI SP-188, 1145-161.
- Hordijk, D.A. (1991). "Local approach to fatigue of concrete." *PhD Thesis*, Delft University of Technology, The Netherlands.
- Ingraffea, A.R., Gerstle, W.H., Gergely, P., and Saouma, V. (1984) "Fracture mechanics of bond in reinforced concrete." *Journal of Structural Engineering*, ASCE, 110(4), 871-898.
- ISO 527-5 (1997). "Plastics – Determination of tensile properties – Part 5: Test conditions for unidirectional fibre-reinforced plastic composites." *International Organization for Standardization (ISO)*, Genève, Switzerland.
- Karsan, I.D., and Jirsa, J.O. (1969). "Behavior of concrete under compressive loadings." *Journal of the Structural Division*, ASCE, 95 (ST12), 2543-2563.
- Kormeling, H.A., and Reinhardt, H.W. (1983). "Determination of the fracture energy of normal concrete and epoxy modified concrete." *Report No. 5-83-18*, Stevin Laboratory, Delft University of Technology, The Netherlands.
- Kreyszig, E. (1993). "Advanced engineering mathematics (Seventh edition)." *John Wiley & Sons*, New York, US.
- Kupfer, H., Hilsdorf, H.K., and Rusch, H. (1969). "Behavior of concrete under biaxial stresses." *ACI Journal*, 66(8), 656-666.
- Larralde, J., and Silva-Rodriguez, R. (1993). "Bond and slip of FRP rebars in concrete." *Journal of Materials in Civil Engineering*, ASCE, 5(1), 30-40.

- Leibengood, L., Darwin, D., and Dodds, R.H. (1986). "Parameters affecting FE analysis of concrete structures." *Journal of Structural Engineering*, ASCE, 112, 326-341.
- Lemaitre, J., and Caboche, J.L. (1985). "Mécanique des matériaux solides." *Dunod*, Paris, France.
- Litton, R.W. (1974). "A contribution to the analysis of concrete structures under cyclic loading." *PhD Thesis*, University of California, Berkeley, US.
- Lourenço, P.B. (1996). "Computational strategies for masonry structures." *PhD Thesis*, Delft University of Technology, The Netherlands.
- Lubliner, J. (1990). "Plasticity theory." *Macmillan Company*, New York, US.
- Lundgren, K., and Gylltoft, K. (2000). "A model for the bond between concrete and reinforcement" *Magazine of Concrete Research*, 52(1), 53-63.
- Malvar, L. (1995). "Tensile and bond properties of GFRP reinforcing bars." *ACI Material Journal*, 92(3), 276-2985.
- Massicotte, B., Elwi, A.E., and MacGregor, J.G. (1990). "Tension-stiffening model for planar reinforced concrete members." *Journal of Structural Engineering*, ASCE, 116(11), 3039-3058.
- Mehlhorn, G., Kollegger, J., Keuser, M., and Kolmar, W. (1985). "Nonlinear contact problems - A finite element approach implemented in ADINA." *Computers & Structures*, Elsevier, 21(1/2), 69-80.
- Mukhopadhyaya, P., and Swamy, N. (2001). "Interface shear stress: a new design criterion for plate debonding." *Journal of Composites for Construction*, ASCE, 5(1), 35-43.
- Ngo, D., and Scordelis, A.C. (1967). "Finite element analysis of reinforced concrete beams." *Journal of the American Concrete Institute*, 64(3), 152-163.
- Nguyen, D.M., Chan, T.K., and Cheong, H.K. (2001). "Brittle failure and bond development length of CFRP concrete beams." *Journal of Composites for Construction*, ASCE, 5(1), 12-17.
- NP 1379 (1976). "Inertes para argamassas e betões - análise granulométrica." *Instituto Português da Qualidade*, Lisbon, Portugal, 3 pp. [in Portuguese]

- NP-EN 196-1 (1987). "Métodos de ensaio de cimentos." *Comite europeu de normalisation* (CEN), Bruxelles, Belgium. [in Portuguese]
- Odqvist, F.K.G. (1933). "Die verfestigung von flusseisenahnlichen korpen. Ein beitrage zur plastizitiitstheorie." *Zeit. Angew. Math. Und Mech.*, 13, 360-3.
- Oliver, J., Cervera, M., Oller, S., and Lubliner, J. (1990). "Isotropic damage models and smeared crack analysis of concrete." *Proceedings of the 2nd International Conference on Computer Aided Analysis and Design of Concrete Structures*, N. Bicanic, and H. Mang (eds.), Pineridge Press Ltd, 945-957.
- Oñate, E., Oller, S., Oliver, J., and Lubliner, J. (1987). "A constitutive model for cracking of concrete based on the incremental theory of plasticity." *Proceedings of the International Conference in Computational Plasticity-Models, Software and Applications*, D.R. Owen, E. Hinton, and E. Oñate (eds.), Barcelona, Spain, 1311-1329.
- Ortiz, M., and Popov, E.P. (1985). "Accuracy and stability of integration algorithms for elastoplastic constitutive equations." *International Journal of Numerical Methods in Engineering*, 29, 1561-1576.
- Otter, D., and Naaman, A.E. (1986). "Steel fibre reinforced concrete under static and cyclic compressive loading." *RILEM Symposium FRC 86, Developments in Fibre Reinforced Cement and Concrete*, 1, Sheffield, England, paper 3.10.
- Owen, D.R.J., and Figueiras, J.A. (1983). "Anisotropic elasto-plastic finite element analysis of thick and thin plates and shells." *International Journal for Numerical Methods in Engineering*, 19, 323-350.
- Owen, D.R.J., and Hinton, E. (1980). "Finite elements in plasticity. Theory and practice." *Pineridge Press Limited*, Swansea, UK.
- Pantuso, A., Neubauer, U. and Rostasy, F.S. (2000). "Effects of thermal mismatch between FRP and concrete on bond." *Proceedings of the 4th ConFibreCrete Meeting*, Lille, France.
- Póvoas, R.H.C.F. (1991) "Modelos não-lineares de análise e dimensionamento de estruturas laminares de betão incluindo efeitos diferidos. *Nonlinear models for the analysis and design of concrete laminate structures including time dependent*

- effects.” *PhD Thesis*, Faculty of Engineering, University of Porto, Portugal. [in Portuguese]
- Prager, W. (1955). “The theory of plasticity: a survey of recent achievements.” *Proceedings of the Institute of Mechanical Engineers*, London, England, 169, 41-57.
- Ribeiro, A.F. (2004). “Modelos de fenda discreta na simulação do comportamento em flexão de betão reforçado com fibras de aço. *Discrete crack models for the simulation of the flexural behavior of steel fiber reinforced concrete.*” *MSc Thesis*, Civil Engineering Department, University of Minho, Portugal. [in Portuguese]
- Ribeiro, A.F., Cunha, V.M.C.F., Barros, J.A.O., and Antunes, J.A.B. (2003). “Modelo de secção para dimensionamento à flexão de estruturas de betão: formulação e manual do programa DOCROS. *Cross section layer model for the design of concrete structures: formulation and manual of the program DOCROS.*” *Report No. 03-DEC/E-25*, Civil Engineering Department, University of Minho, Portugal, 59 pp. [in Portuguese]
- RILEM (1982). “Bond test for reinforcement steel. 1. Beam test.”, *TC9-RC*.
- RILEM (1985). “Determination of the fracture energy of mortar and concrete by means of three-point bending tests on notched beams. Draft Recommendation, 50-FMC Committee Fracture Mechanics of Concrete.” *Materials and Structures*, RILEM, 85(85), 285-290.
- Rossi, P. (1998) “Les bétons de fibres métalliques.” *Presses de l’École National des Ponts et Chaussées*, Paris, France. [in French].
- Rots, J.G. (1988). “Computational modeling of concrete fracture.” *PhD Thesis*, Delft University of Technology, The Netherlands.
- Rots, J.G. (1992). “Removal of finite elements in smeared crack analysis.” *Proceedings of the 3rd International Conference on Computational Plasticity, Fundamentals and Applications*, D.R.J. Owen, E. Oñate, and E. Hinton (eds.), Pineridge Press, 669-680.
- Rots, J.G., Nauta, P., Kusters; G.M.A., and Blaawendraad, J. (1985). “Smeared crack approach and fracture localization in concrete.” *HERON*, 30(1), 1-48.

- Schellekens, J.C.J. (1990). "Interface elements in finite element analysis." *Report No. 25-2-90-5-17 (TU-Delft)*, Delft University of Technology, The Netherlands, 82 pp.
- Schellekens, J.C.J. (1992). "Computational strategies for composite structures." *PhD Thesis*, Delft University of Technology, The Netherlands.
- Schellekens, J.C.J., and de Borst, R. (1990). "The use of the Hoffmann yield criterion in finite element analysis of anisotropic composites." *Computers & Structures*, Elsevier, 37(6), 1087-1096.
- Sena-Cruz, J.M., and Barros, J.A.O. (2002). "Caracterização experimental da ligação de laminados de CFRP inseridos no betão de recobrimento. *Experimental characterization of CFRP laminates bonded into concrete cover.*" *Report No. 02-DEC/E-15*, Civil Engineering Department, University of Minho, Portugal, 54. pp. [in Portuguese]
URL: http://www.civil.uminho.pt/jsenacruz/Publications/TR-002-2004_04-DEC-E-04.pdf
- Sena-Cruz, J.M., Barros, J.A.O., and Faria, R.M.C.M. (2001). "Assessing the embedded length of epoxy bonded carbon laminates by pull-out bending tests." *Proceedings of the International Conference Composites in Construction*, J.A. Figueiras, L. Juvandes, R. Faria, A. Torres Marques, A. Ferreira, J. Barros and J. Appleton (eds.), Porto, Portugal, 217-222.
URL: http://www.civil.uminho.pt/jsenacruz/Publications/CP.I-003-2001_CCC2001.pdf
- Sena-Cruz, J.M., Barros, J.A.O., and Gettu, R. (2004). "Bond behavior of near-surface mounted CFRP laminate strips under monotonic and cyclic loading." *Report No. 04-DEC/E-04*, Civil Engineering Department, University of Minho, Portugal, 55 pp.
URL: http://www.civil.uminho.pt/jsenacruz/Publications/TR-002-2004_04-DEC-E-04.pdf
- Silva, P.A.S.C.M. (1999). "Modelação e análise de estruturas de betão reforçadas com FRP. *Modeling and analysis of concrete structures strengthened with FRP.*" *MSc Thesis*, Faculty of Engineering, University of Porto, Portugal. [in Portuguese]
- Simo, J.C., and Hughes, T.J.R. (1988). "Elastoplasticity and viscoplasticity – Computational aspects." *Springer*, New York, US.

- Simo, J.C., and Hughes, T.J.R. (1998). "Computational inelasticity." *Springer-Verlang*, New York, US.
- Simo, J.C., and Taylor, R.L. (1985). "Consistent tangent operators for rate independent elasto-plasticity." *Computer Methods in Applied Mechanics and Engineering*, 48, 101-118.
- Sinha, B.P., Gerstle, K.H., and Tulin, L.G. (1964). "Stress-strain relations for concrete under cyclic loading." *ACI Journal*, 61(2), 195-210.
- Stang, H., and Aarre, T. (1992). "Evaluation of crack width in FRC with conventional reinforcement." *Cement & Concrete Composites*, Elsevier, 14(2), 143-154.
- Täljsten, B., and Carolin, A. (2001). "Concrete beams strengthened with near-surface mounted CFRP laminates." *Proceeding of FRPRCS-5*, C. Burgoyne (ed.), Cambridge, UK, 107-116.
- Täljsten, B., Carolin, A., and Nordin, H. (2003). "Concrete structures strengthened with near-surface mounted reinforcement of CFRP." *Advances in Structural Engineering*, 6(3), 201-213.
- Tan, K., Tumialan, G., and Nanni, A. (2002). "Evaluation of CFRP systems for the strengthening of RC slabs." *Report No. CIES 02-38*, Center for Infrastructure Engineering Studies, University of Missouri-Rolla, Rolla, Missouri, US, 121 pp.
- Tassios, T.P. (1979). "Properties of bond between concrete and steel under load cycles idealizing seismic actions." *Proceedings of the AICAP-CEB Symposium*, CEB Bulletin No. 131, 67-122.
- Tepfers, R. (1998). "Bond between FRP-bars and concrete." *Report No. 98:3*, Division of Building Technology, Chalmers University of Technology, Gothenburg, Sweden, 16 pp.
- Toutanji, H., and Balaguru, P. (1998). "Durability characteristics of concrete columns wrapped with fiber tow sheets." *Journal of Materials in Civil Engineering*, ASCE, 10(1), 52-57.
- Tumialan, G., Tinazzi, D., Myers, J., and Nanni, A. (1999). "Field evaluation of masonry walls strengthened with FRP composites at the Malcolm Bliss Hospital." *Report*

- No. CIES 99-8*, Center for Infrastructure Engineering Studies, University of Missouri-Rolla, Rolla, Missouri, US.
- UNE-EN 933-1 (1998). “Ensayos para determinar las propiedades geométricas de los áridos. Parte 1: Determinación de la granulometría de las partículas. Métodos del tamizado.” *AENOR – Asociación Española de Normalización y Certificación*, 16 pp. [in Spanish]
- Van Mier, J.G.M. (1984). “Strain-softening of concrete under multiaxial loading conditions.” *PhD Thesis*, Delft University of Technology, The Netherlands.
- Van Mier, J.G.M. et al. (1997). “Strain-softening of concrete in uniaxial compression.”, *Report of the Round Robin Test carried out by RILEM TC 148-SSC, Materials and Structures*, RILEM, 30, 195-209.
- Walraven, J.C. (1978). “The influence of depth on the shear strength of light-weight concrete beams without shear reinforcement.” *Report No. 5-78-4*, Stevin Laboratory, Delft University of Technology, Delft, The Netherlands.
- Warren, G.E. (1998). “Waterfront repair and upgrade, advanced technology demonstration Site No. 2: Pier 12, NAVSTA San Diego.” *Report No. SSR-2419-SHR*, Naval Facilities Engineering Service Center, Port Hueneme, California, US.
- Warren, G.E. (2000). “Waterfront repair and upgrade, advanced technology demonstration Site No. 3: NAVSTA Bravo 25, Pearl Harbour.” *Report No. SSR-2567-SHR*, Naval Facilities Engineering Service Center, Port Hueneme, California, US.
- Wong, R.S.Y., and Vecchio, F.J. (2003). “Towards modeling of reinforced concrete members with externally bonded fiber-reinforced polymer composites.” *Structural Journal*, ACI, 100(1), 47-55.
- Yan, X., Miller, B., Nanni, A., and Bakis, C.E. (1999). “Characterization of CFRP bars used as near-surface mounted reinforcement.” *Proceedings of the 8th International Structural Faults and Repair Conference*, M.C. Forde (ed.), Edinburgh, Scotland, Engineering Technics Press, 10 pp. [available in CD-ROM]
- Zienkiewicz, O.C., and Taylor, R.L. (1989). “The finite element method (Fourth edition) Volume 1, Basic formulation and linear problems.” *McGraw-Hill*, Berkshire, England.

Zienkiewicz, O.C., and Taylor, R.L. (1991). "The finite element method (Fourth edition) Volume 2, Solid and fluid mechanics, dynamics and non-linearity." *McGraw-Hill*, Berkshire, England.

APPENDIX A

EXPERIMENTAL RESULTS

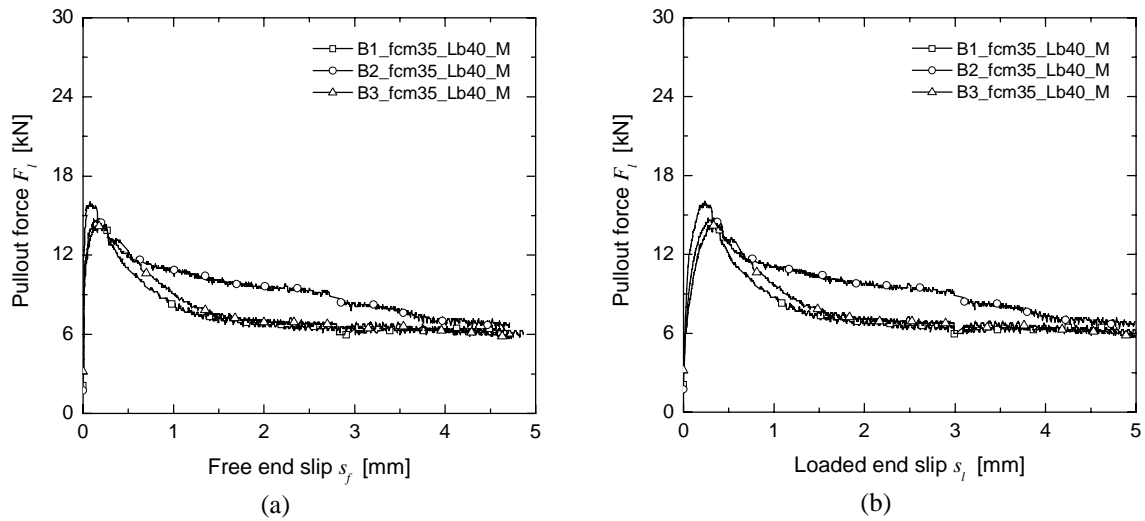


Figure A.1 – Pullout force vs. free end slip (a) and vs. loaded end slip (b), of the fcm35_Lb40_M series.

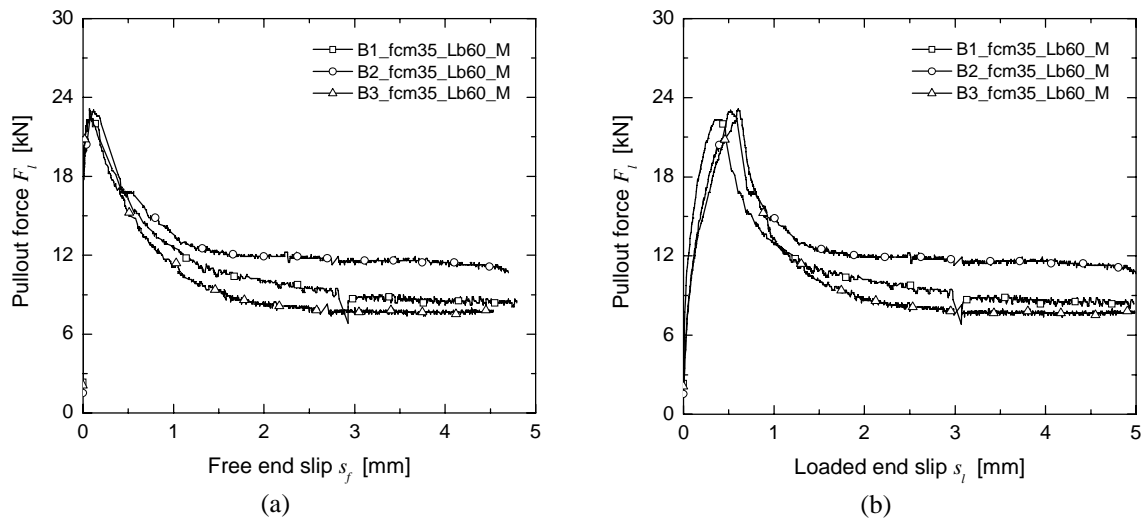


Figure A.2 – Pullout force vs. free end slip (a) and vs. loaded end slip (b), of the fcm35_Lb60_M series.

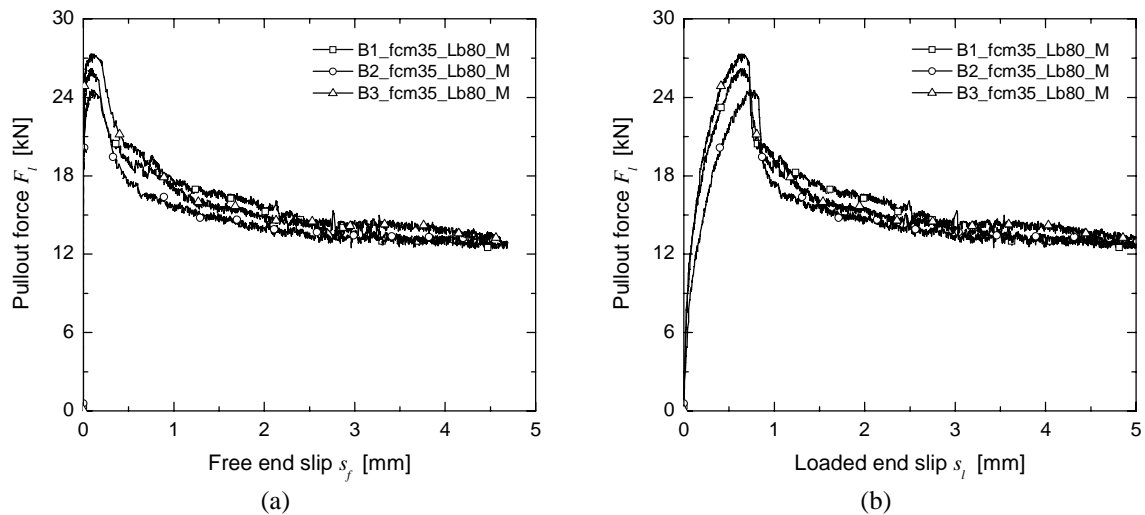


Figure A.3 – Pullout force vs. free end slip (a) and vs. loaded end slip (b), of the fcm35_Lb80_M series.

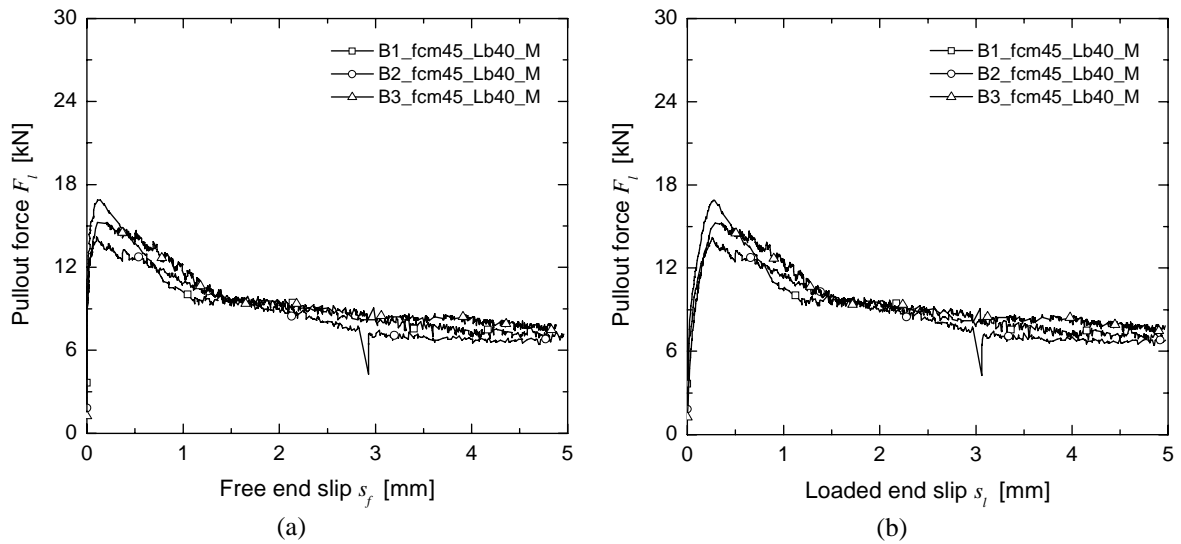


Figure A.4 – Pullout force vs. free end slip (a) and vs. loaded end slip (b), of the fcm45_Lb40_M series.

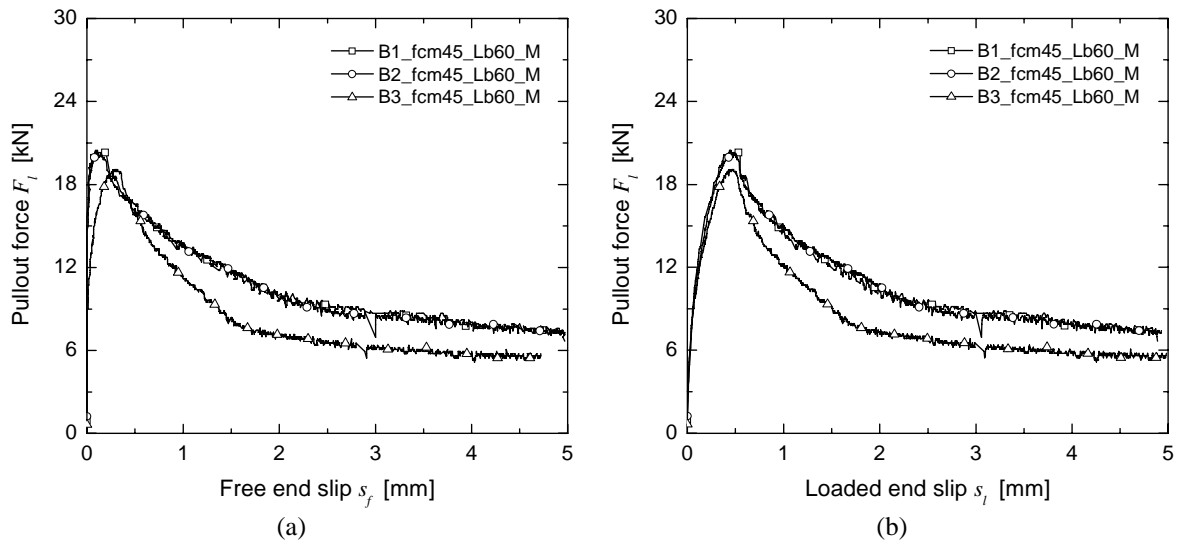


Figure A.5 – Pullout force vs. free end slip (a) and vs. loaded end slip (b), of the fcm45_Lb60_M series.

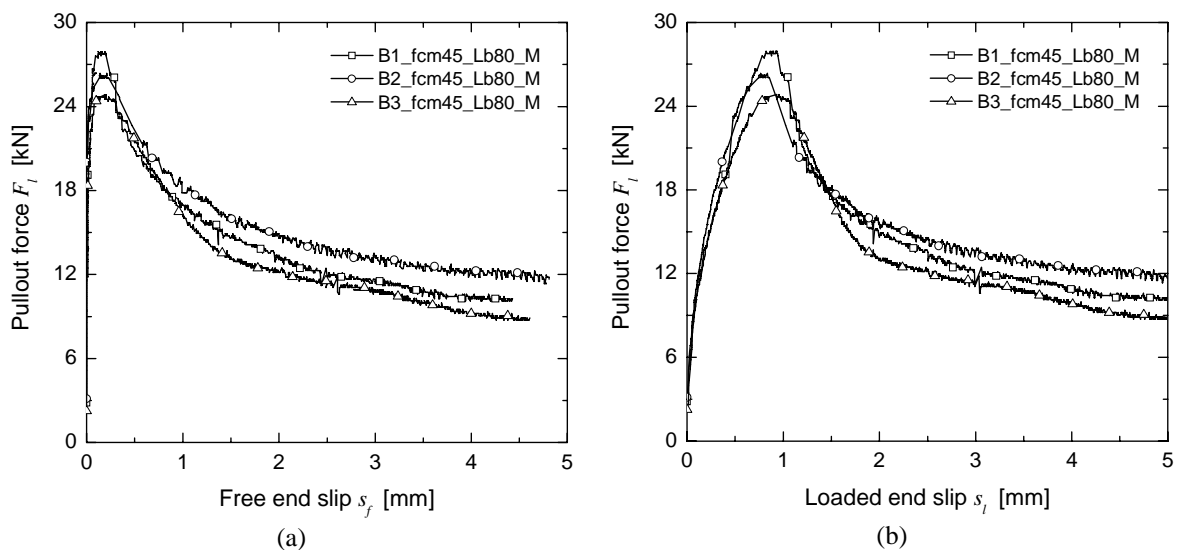


Figure A.6 – Pullout force vs. free end slip (a) and vs. loaded end slip (b), of the fcm45_Lb80_M series.

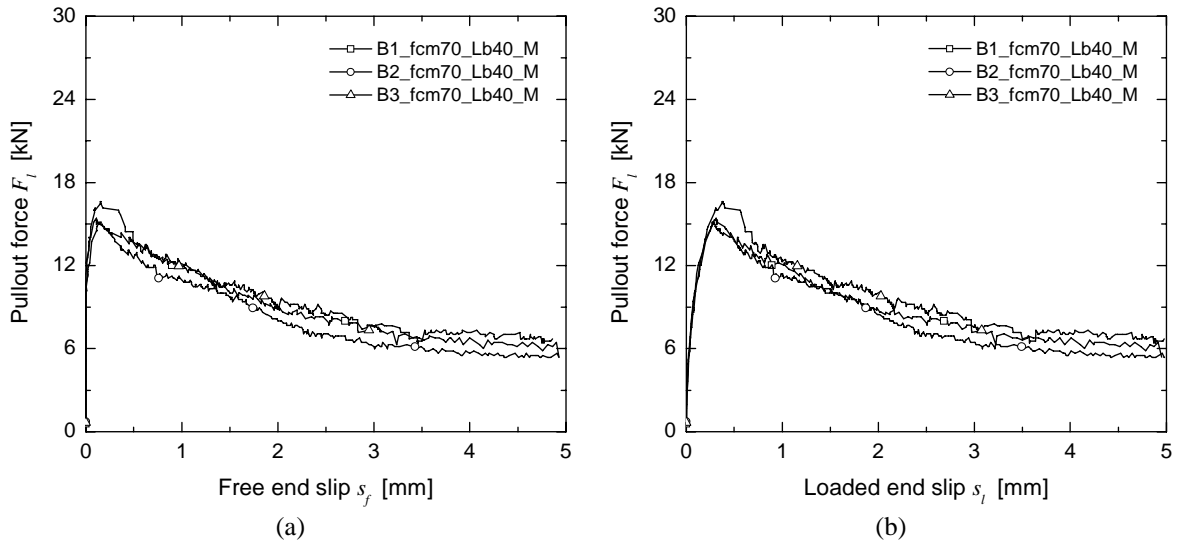


Figure A.7 – Pullout force vs. free end slip (a) and vs. loaded end slip (b), of the fcm70_Lb40_M series.

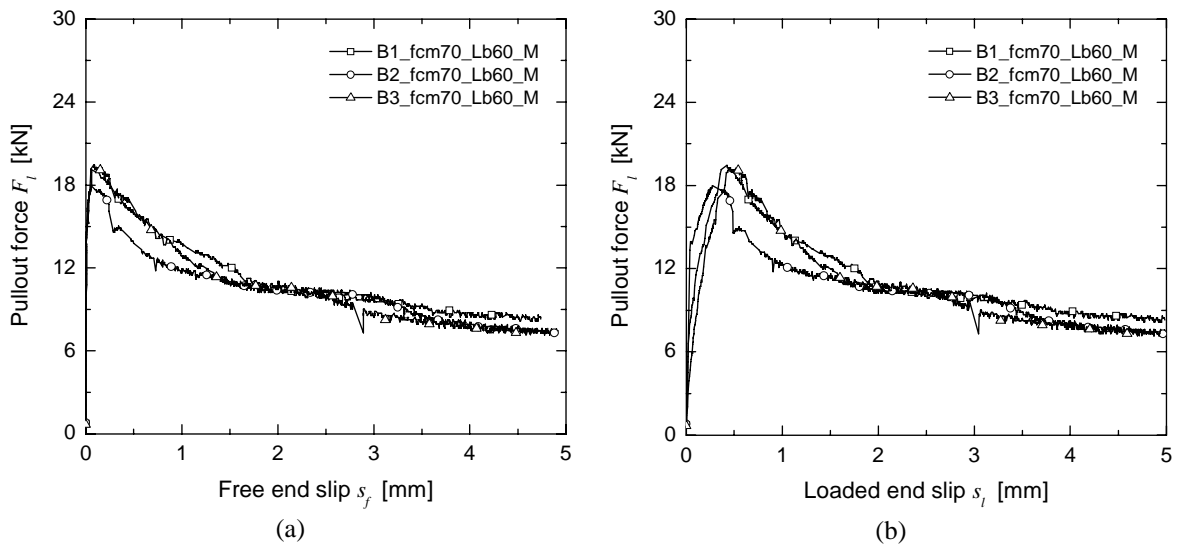


Figure A.8 – Pullout force vs. free end slip (a) and vs. loaded end slip (b), of the fcm70_Lb60_M series.

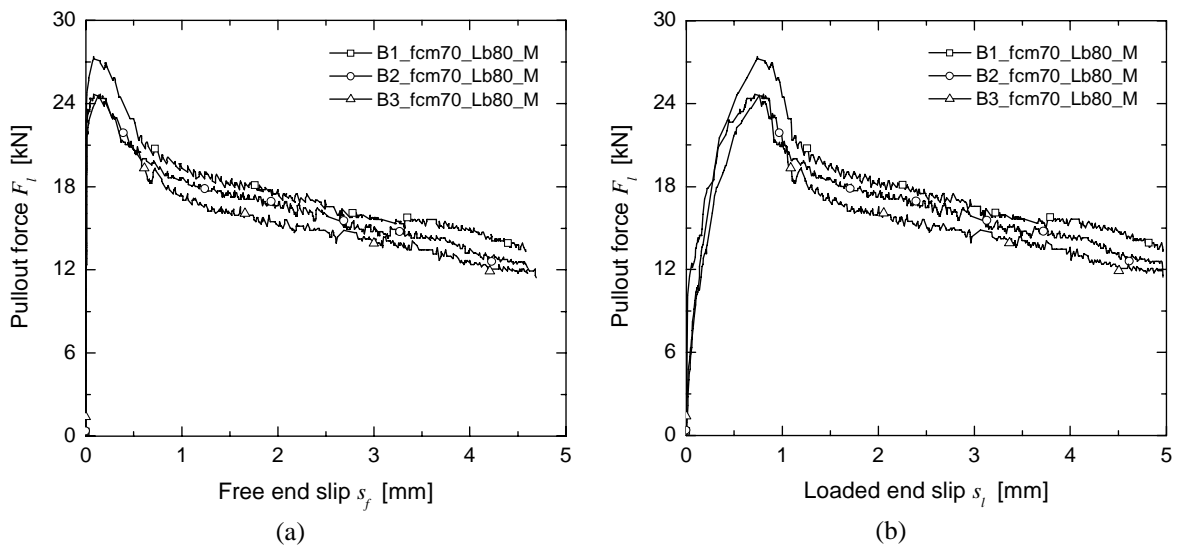


Figure A.9 – Pullout force vs. free end slip (a) and vs. loaded end slip (b), of the fcm70_Lb80_M series.

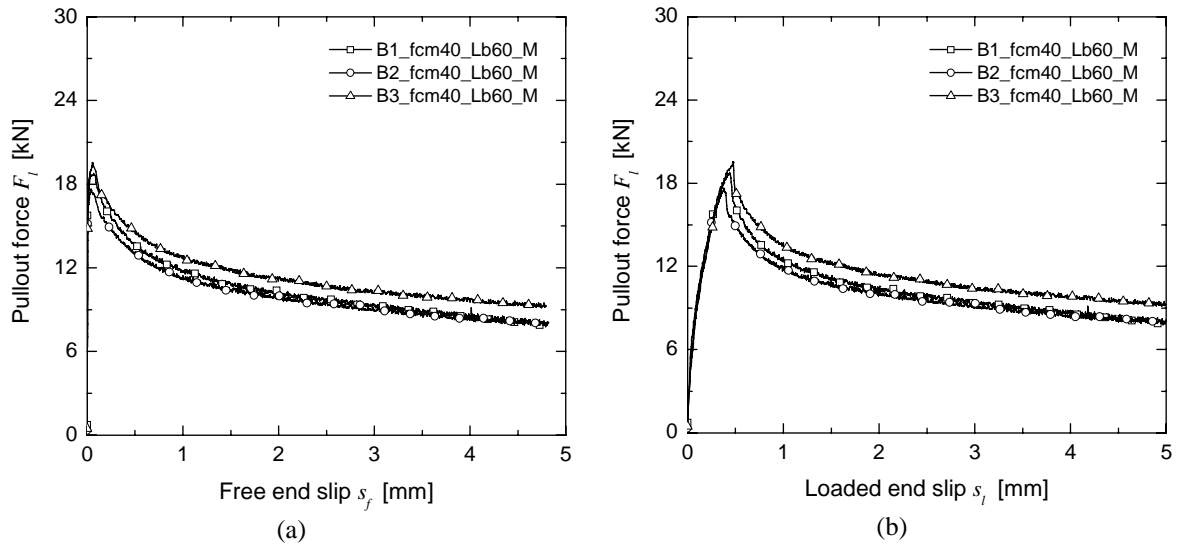


Figure A.10 – Pullout force vs. free end slip (a) and vs. loaded end slip (b), of the fcm40_Lb60_M series.

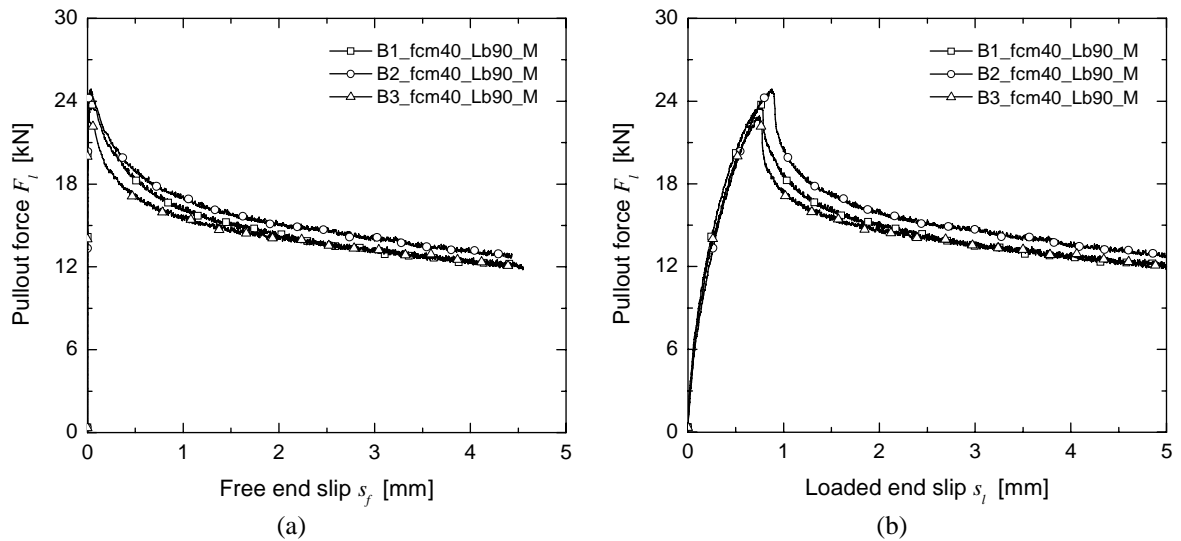


Figure A.11 – Pullout force vs. free end slip (a) and vs. loaded end slip (b), of the fcm40_Lb90_M series.

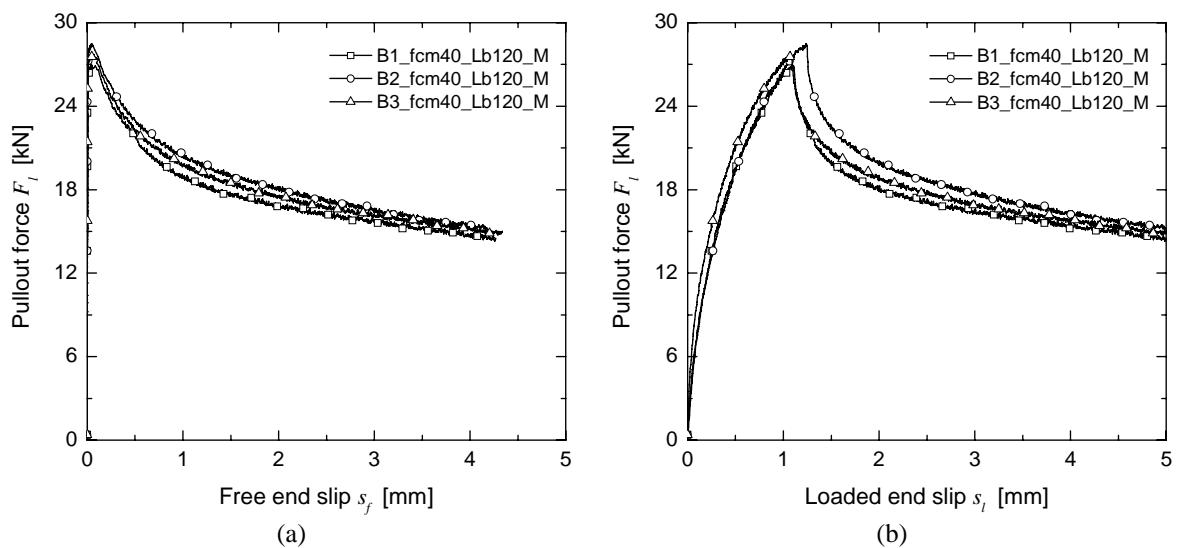


Figure A.12 – Pullout force vs. free end slip (a) and vs. loaded end slip (b), of the fcm40_Lb120_M series.

APPENDIX B

RUNGE-KUTTA-NYSTRÖM METHOD

The Runge-Kutta-Nyström (RKN) method (Kreyszig 1993) computes the solution of $y'' = f(x, y, y')$ using the initial values $y(x_0) = y_0$, $y'(x_0) = y'_0$ at equidistant points $x_1 = x_0 + h$, $x_2 = x_0 + 2h$, ..., $x_N = x_0 + Nh$, h the step length and N the number of steps. Figure B.1 shows the corresponding algorithm.

The following functions are used in the present study: $y'' = d^2s/dx^2$; $f(x, y, y') = 2/(t_f E_f) \tau(s)$. The first point of the effective bond length, L_{ef} , is $x_0 = 0$ and the last one is $x_N = L_{ef}$. The effective bond length was divided in 100 segments of equal width ($N = 100$).

The initial values are the free end slip, $y(x_0) = s_f$, and the laminate strain at the free end, $y'(x_0) = (ds/dx)_0 = \varepsilon_f(x=0) = 0$. According to the algorithm represented in Figure B.1, the loaded end slip, $y(x_N) = s_l$, and the laminate strain at the loaded end, $y'(x_N) = \varepsilon_f(x_N)$, are calculated.

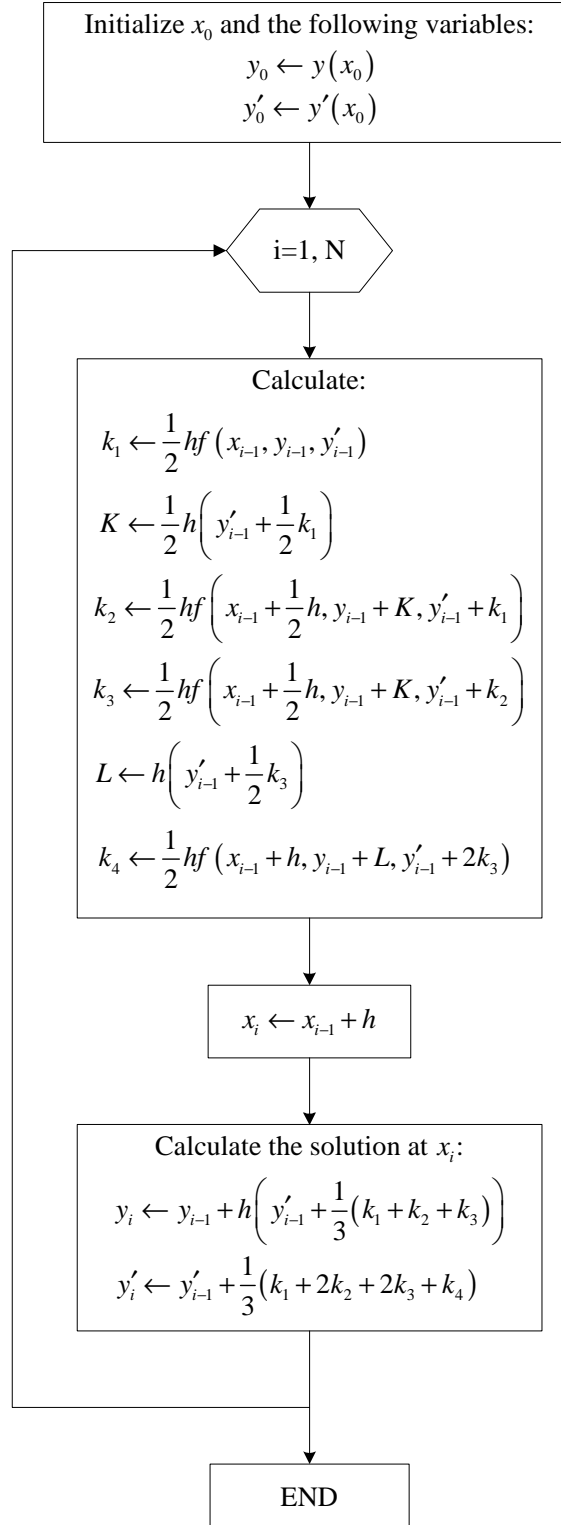


Figure B.1 – Runge-Kutta-Nyström algorithm.

APPENDIX C

HARDENING/SOFTENING LAW FOR CONCRETE

The expression that defines the hardening behavior is the following (see also Figure 4.21)

$$\bar{\sigma}_1(\kappa) = \bar{\sigma}_0 + (\bar{\sigma}_p - \bar{\sigma}_0) \left(\frac{2\kappa}{\kappa_p} - \frac{\kappa^2}{\kappa_p^2} \right)^{1/2} \quad (\text{C.1})$$

The first branch of the softening phase is defined by

$$\bar{\sigma}_2(\kappa) = \frac{-H + \sqrt{H^2 - 4GI}}{2G} \quad (\text{C.2})$$

where

$$\begin{aligned} G &= \frac{C}{E_c} + \frac{Bf_c}{E_c^2} \\ H &= 1 - A \frac{f_c}{E_c} + \left(C + 2B \frac{f_c}{E_c} \right) \kappa \\ I &= Bf_c \kappa^2 - Af_c \kappa \end{aligned} \quad (\text{C.3})$$

and

$$\begin{aligned} A &= \frac{E_c}{f_c} \\ B &= \frac{1}{\varepsilon_{c1}^2} \\ C &= \left(\frac{E_c \varepsilon_{c1}}{f_c} - 2 \right) / \varepsilon_{c1} \end{aligned} \quad (\text{C.4})$$

The second branch of the softening phase is defined by

$$\bar{\sigma}_3(\kappa) = \bar{\sigma}_3^3 \frac{D}{E_c^2} + \bar{\sigma}_3^2 \left(\frac{F}{E_c} + \frac{2D\kappa}{E_c} \right) + \bar{\sigma}_3 (D\kappa^2 + F\kappa) - f_c = 0 \quad (\text{C.5})$$

where

$$D = \left(\frac{\xi}{\varepsilon_{c,\text{lim}}/\varepsilon_{c1}} - \frac{2}{(\varepsilon_{c,\text{lim}}/\varepsilon_{c1})^2} \right) \frac{1}{\varepsilon_{c1}^2} \quad (\text{C.6})$$

$$F = \left(\frac{4}{\varepsilon_{c,\text{lim}}/\varepsilon_{c1}} - \xi \right) \frac{1}{\varepsilon_{c1}}$$

and

$$\xi = \frac{4 \left[\left(\frac{\varepsilon_{c,\text{lim}}}{\varepsilon_{c1}} \right)^2 \left(\frac{E_c \varepsilon_{c1}}{f_c} - 2 \right) + 2 \frac{\varepsilon_{c,\text{lim}}}{\varepsilon_{c1}} - \frac{E_c \varepsilon_{c1}}{f_c} \right]}{\left[\frac{\varepsilon_{c,\text{lim}}}{\varepsilon_{c1}} \left(\frac{E_c \varepsilon_{c1}}{f_c} - 2 \right) - 1 \right]^2} \quad (\text{C.7})$$

$$\varepsilon_{c,\text{lim}} = \varepsilon_{c1} \left\{ \frac{1}{2} \left(\frac{1}{2} \frac{E_c \varepsilon_{c1}}{f_c} + 1 \right) + \left[\frac{1}{4} \left(\frac{1}{2} \frac{E_c \varepsilon_{c1}}{f_c} + 1 \right)^2 - \frac{1}{2} \right]^{1/2} \right\}$$

Finally, ε_{c1} is the strain at the uniaxial peak compressive stress, f_c , and E_c is the initial Young's modulus of concrete.

APPENDIX D

CONSISTENT TANGENT OPERATOR

The derivation of the consistent tangent constitutive matrix requires the determination of the total differentials $d\underline{\sigma}_n$, $d\underline{\varepsilon}_n^p$ and df_n (Simo and Hughes 1988), obtained from the constitutive equation (4.72), the plastic flow (4.79) and the yield condition (4.73), respectively, resulting

$$d\underline{\sigma} = \underline{D}^e (d\underline{\varepsilon} - d\underline{\varepsilon}^p) \quad (\text{D.1})$$

$$d\underline{\varepsilon}^p = h_c d\lambda \frac{\partial f}{\partial \underline{\sigma}} + h_c \Delta\lambda \frac{\partial^2 f}{\partial \underline{\sigma}^2} d\underline{\sigma} \quad (\text{D.2})$$

$$df = \left(\frac{\partial f}{\partial \underline{\sigma}} \right)^T d\underline{\sigma} - \frac{\partial \bar{\sigma}}{\partial \kappa} d\kappa = 0 \quad (\text{D.3})$$

Incorporating equation (D.2) into (D.1) yields

$$d\underline{\sigma} = \underline{H} \left(d\underline{\varepsilon} - h_c d\lambda \frac{\partial f}{\partial \underline{\sigma}} \right) \quad (\text{D.4})$$

where

$$\underline{H} = \left(\left[\underline{D}^e \right]^{-1} + h_c \Delta\lambda \frac{\partial^2 f}{\partial \underline{\sigma}^2} \right)^{-1} \quad (\text{D.5})$$

Including equation (D.4) in equation (D.3), results

$$\left(\frac{\partial f}{\partial \underline{\sigma}} \right)^T \underline{H} d\underline{\varepsilon} - h_c d\lambda \left(\frac{\partial f}{\partial \underline{\sigma}} \right)^T \underline{H} \frac{\partial f}{\partial \underline{\sigma}} - \frac{\partial \bar{\sigma}}{\partial \kappa} d\kappa = 0 \quad (\text{D.6})$$

and assuming the strain hardening hypotheses ($d\lambda = d\kappa$), leads to

$$d\lambda = \frac{\left(\frac{\partial f}{\partial \underline{\sigma}}\right)^T \underline{H}}{\frac{\partial \bar{\sigma}}{\partial \kappa} + h_c \left(\frac{\partial f}{\partial \underline{\sigma}}\right)^T \underline{H} \frac{\partial f}{\partial \underline{\sigma}}} d\underline{\varepsilon} \quad (\text{D.7})$$

Substituting this equation into (D.4) yields

$$d\underline{\sigma} = \left(\underline{H} - \frac{h_c \underline{H} \frac{\partial f}{\partial \underline{\sigma}} \left(\frac{\partial f}{\partial \underline{\sigma}}\right)^T \underline{H}}{\frac{\partial \bar{\sigma}}{\partial \kappa} + h_c \left(\frac{\partial f}{\partial \underline{\sigma}}\right)^T \underline{H} \frac{\partial f}{\partial \underline{\sigma}}} \right) d\underline{\varepsilon} \quad (\text{D.8})$$

or

$$d\underline{\sigma} = \left(\underline{H} - \frac{h_c \underline{H} \frac{\partial f}{\partial \underline{\sigma}} \left(\frac{\partial f}{\partial \underline{\sigma}}\right)^T \underline{H}}{h + h_c \left(\frac{\partial f}{\partial \underline{\sigma}}\right)^T \underline{H} \frac{\partial f}{\partial \underline{\sigma}}} \right) d\underline{\varepsilon} \quad (\text{D.9})$$

where h is the hardening modulus. Finally, the consistent tangent stiffness matrix, \underline{D}^{ep} , is given by

$$\underline{D}^{ep} = \underline{H} - \frac{h_c \underline{H} \frac{\partial f}{\partial \underline{\sigma}} \left(\frac{\partial f}{\partial \underline{\sigma}}\right)^T \underline{H}}{h + h_c \left(\frac{\partial f}{\partial \underline{\sigma}}\right)^T \underline{H} \frac{\partial f}{\partial \underline{\sigma}}} \quad (\text{D.10})$$